Establishment of Stable Isotope-Resolved Metabolomics as Test System to Assess Membrane-Associated Drug Targets in Cancer

Dissertation

der Mathematisch-Naturwissenschaftlichen Fakultät

der Eberhard Karls Universität Tübingen

zur Erlangung des Grades eines

Doktors der Naturwissenschaften

(Dr. rer. nat.)

vorgelegt von

Marcel Nicolai Lackner

aus Bad Windsheim

Tübingen

2025

Gedruckt mit Genehmigung der Mathematisch-Naturwissenschaftlichen Fakultät der Eberhard Karls Universität Tübingen.

Tag der mündlichen Qualifikation:	28.01.2026
Dekan:	Prof. Dr. Thilo Stehle
1. Berichterstatter/-in:	Prof. Dr. med. Matthias Schwab
2. Berichterstatter/-in:	Prof. Dr. Michael Lämmerhofer

List of Contents

List of Abbreviations

2-PG	2-phosphoglycerate
2-HG	2-hydroxyglutarate
3H3MG	3-hydroxy-3-methylglutarate
3-PG	3-phosphoglycerate
µM	Micromolar
ACN	Acetonitrile
AmAc	Ammonium acetate
AMBIC	Ammonium bicarbonate
AMP	Adenosine monophosphate
ADP	Adenosine diphosphate
ATP	Adenosine triphosphate
ATTC	American Type Culture Collection
BSA	Bovine serum albumin
CCD	charge-coupled device
CMP	Cytidine monophosphate
CMP-NANA	Cytidine monophosphate N-acetylneuraminate
CV	Coefficient of variation
DMSO	Dimethylsulfoxide
DNA	Deoxyribonucleic acid
EC	Energy charge
ECM	Extracellular matrix
EIC	Extracted ion chromatogram
ESI	Electrospray ionization
FBS	Fetal bovine serum
FC	Fold change
F16BP	Fructose 1,6-bisphosphate
F6P	Fructose 6-phosphate
G1P	Glucose 1-phosphate
G6P	Glucose 6-phosphate
GC	Gas chromatography
GSH	Glutathione
GSSG	Oxidized glutathione
h	hour
HILIC	Hydrophilic interaction liquid chromatography
HPLC	High performance liquid chromatography
i.d.	Inner diameter
IS	Internal standard
kDa	Kilo Dalton
LC	Liquid chromatography
LC-QTOF-MS	Liquid chromatography quadrupole time-of-flight mass spectrometry
LoA	Level of assignment

MeOH	Methanol
mDa	Millidalton
mM	Millimolar
MS	Mass spectrometry
MSI	Metabolomics Standard Initiative
MS/MS	Tandem mass spectrometry
m/z	Mass over charge
NA	Not assigned
NAA	N-acetylaspartate
NANA	N-acetylneuraminate
Nm	Nanometer
PBS	Phosphate buffered saline
PCA	Perchloric acid
PEP	Phosphoenolpyruvate
ppm	Parts per million
PTEN	Phosphatase and tension homolog
OXPHOS	Oxidative phosphorylation
QC	Quality control
RT	Retention time
SIRM	Stable isotope resolved metabolomics
UMP	Uridine monophosphate
UDP	Uridine diphosphate
UDP-GlcNAc	Uridine diphosphate N-acetylglucosamine
UTP	Uridine triphosphate
TCA cycle	Tricarboxylic acid- cycle
TIC	Total ion chromatogram
TNBC	Triple negative breast cancer
TQ-MS	Triple quadrupole mass spectrometry

List of Figures

List of Tables

Zusammenfassung

Stable isotope-resolved metabolomics (SIRM) ist ein leistungsstarkes Verfahren, um Einblicke in den Krebsstoffwechsel zu gewinnen, Drug-Targets zu charakterisieren und potenzielle neue Biomarker für die Diagnose oder Prognose von Krebs zu entdecken. Das Ziel dieser Arbeit war es, SIRM als Testplattform zu etablieren, um die Stoffwechselaktivität von Krebszellen zu bewerten und medikamenteninduzierte Stoffwechselveränderungen durch einen PI3Kβ selektiven Inhibitor (AZD8186) zu charakterisieren. Die Arbeit gliederte sich in folgende Teile: **(I)** Etablierung und Optimierung eines Protokolls für die Probenvorbereitung. Dabei wurden das Quenchen des Metabolismus, die Lagerungsstabilität der Proben, das Waschen der Zellkulturen vor der Zellernte und die präanalytische Normalisierung untersucht. **(II)** Im weiteren Verlauf wurde eine PTEN (Phosphatase and Tensin homolog) Wildtyp triple-negative Mammakarzinom (TNBC) Zelllinie und eine PTEN-Null TNBC Zelllinie funktionell charakterisiert. Dies ermöglichte die Dosisfindung von AZD8186 und war eine wichtige Voraussetzung, um den Einfluss der PI3Kβ-Inhibition auf die Aktivitäten des Stoffwechselweges mittels SIRM zu untersuchen. **(III)** Die SIRM-Plattform wurde auf Basis des [U-^{13}C]-Glukose Tracers und einer Kombination aus der Datenanalyse durch „*targeted isotopologue-feature extraction*“ sowie „*non-targeted feature extraction*“ durch X^{13}CMS entwickelt. Die *non-targeted feature extraction* identifizierte signifikante Unterschiede in der Isotopenanreicherung von metabolischen Signaturen (d.h. Features) zwischen den unbehandelten und den AZD8186 behandelten Zellen („*untargeted differential tracing*“). **(IV)** Die etablierte Plattform wurde anschließend genutzt, um mithilfe [U-^{15}N]- und [U-^{13}C, ^{15}N]-Glutamin-Tracern Veränderungen in Stoffwechselflüssen außerhalb des zentralen Stoffwechsels zu ermitteln. Dies umfasste beispielsweise die Purin- und Pyrimidin-Nukleotidbiosynthese, den Aminosäurestoffwechsel und den Hexosamin-Biosyntheseweg. **(V)** Zuletzt wurden die Zelllinien HCC70 und MDA-MB-468 mittels *untargeted differential tracing* untersucht. Es konnten isotopenangereicherte Features identifiziert werden, die in Gegenwart von AZD8186 sowohl gemeinsam als auch zelllinienspezifisch signifikant verändert waren.

(I) Basierend auf der Bestimmung des Energieladung (EC) sowie den Konzentrationen der adenylierten Ribonukleotiden (ARs) und Zwischenprodukten der Glykolyse ergab das Waschen mit eiskaltem 1x konzentriertem PBS, gefolgt vom Quenchen mit tiefkaltem 80% MeOH (-80 °C), die höchste Metabolitausbeute und einem EC von 0.94. Die Proben blieben im Extraktionslösemittel drei Wochen stabil. Im Vergleich dazu führte eine Trockenlagerung nach Verdampfen des Extraktionslösemittels zu einer leichten, aber nicht signifikanten Abnahme der AR-Konzentration. Hinsichtlich der präanalytischen Normalisierung (DNS-Konzentration vs. Zellzahl) war die Normalisierung anhand der Zellzahl robuster (CV_{mean} = 6%) im Vergleich zur Normalisierung anhand der DNS (CV_{mean} > 20%).

(II) In der TNBC Zelllinie MDA-MB-468 konnte eine konzentrationsabhängige Abnahme der AKT-Phosphorylierung (Thr_{308} und Ser_{473}) durch die Inhibierung der PI3Kβ gezeigt werden. Dies deutet auf eine Beeinträchtigung der nachgelagerten Signalkaskade von pAKT hin. Untersuchungen des metabolischen Phänotyps durch quantitative Metabolomics-Analysen und extrazelluläre Flux-Analyse bestätigte eine verringerte Glykolyse, eine verminderte Aktivität des Citrat-Zyklus und der oxidativen Phosphorylierung sowie eine signifikante

Abnahme der Sekretion von Laktat in Gegenwart von AZD8186. Dosisoptimierungsexperimente zeigten, dass eine Inhibitorkonzentration von 0.5 µM sowohl die Glykolyse- als auch die Citrat-Zyklus-Aktivität verringerte und das Zellwachstum für bis zu drei Tage hemmte. Hohe zelluläre Aufnahmeraten von Glukose und Glutamin wurden unabhängig von der PI3Kβ-Hemmung festgestellt, was die Verwendung von isotopenmarkierter Glukose und Glutamin als geeignete Tracer-Substrate für den Aufbau des SIRM-Workflows bestätigte.

(III) Basierend auf dem optimierten Protokoll für die Probenvorbereitung wurde der SIRM-Workflow von Zellkultur bis zur Datenanalyse und Visualisierung mittels der Statistik-Software R entwickelt. Dieser Workflow wurde auf die MDA-MB-468 Zelllinie angewandt, die über einen Zeitraum von bis zu 24 Stunden mit 0.5 µM AZD8186 oder dem Vehikel behandelt wurde. Das *untargeted differential tracing* ergab 286 isotopenangereicherte Features, die zwischen der Vehikel-Kontrollgruppe und den behandelten Zellen signifikant verändert waren. Davon konnten 19 Features bekannten Verbindungen bzw. Stoffwechselwegen zugeordnet werden. Weitere 11 Features wurden anhand des Abgleichs von Fragment-Spektren mit Datenbanken und Referenzsubstanzen eindeutig identifiziert. Die strukturell identifizierten Metaboliten wurden in den bestehenden Workflow der *targeted isotopologue-feature extraction* integriert, um die Isotopeninkorporation durch die natürlichen Isotopenhäufigkeit zu korrigieren, die Testperformance zu bewerten und Veränderungen der Stoffwechselaktivitäten durch PI3Kβ-Inhibition zu untersuchen. Die intrazelluläre Anreicherung der Isotope war für die meisten Isotopologe in technischen Replikaten mit einer RSD von unter 10 % sehr gut reproduzierbar. Die Reproduzierbarkeit eines zweiten SIRM-Experiments zeigte eine starke Korrelation der intrazellulären Isotopenanreicherung (Pearson $R^2 > 0,99$). Darüber hinaus wurden signifikante Veränderungen in der Stoffwechselaktivität durch die PI3Kβ-Inhibition festgestellt. Neben den bereits bekannten Veränderungen im Zentralstoffwechsel wurden ebenfalls Veränderungen in weiteren Stoffwechselwegen, wie der Pyrimidin- oder der Hexosamin-Stoffwechsel, entdeckt. Alle identifizierten Stoffwechselwege sind Teil wichtiger metabolischer Prozesse, die mit dem Krebsstoffwechsel und möglichen Therapieansätzen in Verbindung stehen.

(IV) Die Verwendung von [U-^{15}N]- und [U-^{13}C,^{15}N]-Glutamin mittels der *targeted isotopologue-feature extraction* zeigte auffällige Auswirkungen im Zusammenhang mit der PI3Kβ-Inhibition bei Metaboliten des Hexosamin-Biosynthesewegs, den adenylierten Ribonukleotiden und einer veränderten Isotopenanreicherung innerhalb der Zwischenprodukte des Citrat-Zyklus (d. h. Succinat, Fumarat und Malat). Diese Ergebnisse deuten auf vorwiegend oxidative Effekte hin, während die Auswirkungen des Inhibitors auf die glutaminolytische Aktivität begrenzt waren. Ein Vergleich der Ergebnisse aus *untargeted differential tracing* mit [U- ^{13}C,^{15}N] Glutamin und [U-^{13}C] Glucose zeigte nur eine geringe Überlappung (6,9%) der isotopenangereicherten Features, die bei der Inhibition von PI3Kβ signifikant verändert waren. Die Mehrheit der Features (>20 %) war hingegen nur für markiertes Glutamin vorhanden.

(V) Unter Verwendung von [U-^{13}C]-Glukose als Tracer und *untargeted differential tracing* wurden 521 und 417 isotopenangereicherte Features gefunden, die sich zwischen der Kontrolle und der Behandlung mit AZD8186 in HCC70- bzw. MDA-MB-468-Zellen signifikant unterschieden. In der HCC70-Zelllinie lag die Verteilung der Features bei 49% in der

Kontrollgruppe, 16% in der behandelten Gruppe und 35% der Features fand sich in beiden Gruppen. Im Vergleich dazu zeigt die MDA-MB-468 Zelllinie eine nahezu gleichmäßige Verteilung von ~30% in den drei Gruppen. Der Vergleich der Datensätze aus dem *untargeted differential tracing* der HCC70- und der MDA-MB-468-Zellen ergab, dass 162 Features in beiden Zelllinien vorkamen. Darüber hinaus konnten 20 Features strukturell identifiziert werden, die dem zentralen Kohlenstoffstoffwechsel, dem Aminosäurestoffwechsel, der Ribonukleotidbiosynthese und dem Hexosaminweg angehören.

Zusammenfassend wurde in dieser Arbeit SIRM als Untersuchungsplattform etabliert, mit der Veränderungen in der Aktivität von Stoffwechselwegen untersucht werden können. Dabei war diese Plattform weder auf den untersuchten PI3K-Signalweg begrenzt noch auf die spezifische Inhibierung der PI3Kβ in TNBC-Zelllinien. Die Plattform kann wesentlich zu Fortschritten in der Krebsforschung beitragen und die Entwicklung neuer Behandlungsstrategien für Patienten ermöglichen.

Summary

Stable isotope-resolved metabolomics (SIRM) is a powerful technique to gain insights into cancer metabolism, characterize drug targets and discover novel biomarkers for potential diagnosis and prognosis. The scope of this work was to establish SIRM as a test system to assess cancer metabolic network activities *in vitro* and to enable the characterization of drug induced alterations in the absence and presence of the selective PI3Kβ inhibitor AZD8186. The work entailed **(I)** the establishment and optimization of a sample preparation workflow including assessment of metabolism quenching, sample storage and stability, cell washing and pre-analytical normalization, and **(II)** the functional characterization of a PTEN (phosphatase and tensin homolog) wildtype and a PTEN-null triple-negative breast cancer (TNBC) cell line to enable dose finding of AZD8186 as a prerequisite for studying the effect of PI3Kβ inhibition on metabolic pathway activities using SIRM. The SIRM platform was established with **(III)** [U-^{13}C] glucose as tracer including a combination of targeted isotopologue feature extraction with a non-targeted routine based on X^{13}CMS to enable identification of isotope-enriched features that are significantly altered between control and treatment conditions (i.e., untargeted differential tracing). The platform was further applied using **(IV)** [U-^{15}N] and [U-^{13}C, ^{15}N] glutamine to assess altered metabolic fluxes in lower parts of central metabolism (e.g. purine and pyrimidine nucleotide biosynthesis, amino acid metabolism, hexosamine pathway). Lastly, **(V)** employing untargeted differential tracing, differences in AZD8186-induced enrichment of labeled isotopes between the epithelial cancer cell line HCC70 and MDA-MB-468 were investigated, thereby demonstrating isotope-enriched features that were significantly altered in the presence of AZD8186 both jointly and uniquely for each cell line.

(I) Based on the determination of the adenylated energy charge (EC) as well as quantitative levels of adenylated ribonucleotides (ARs) and glycolytic intermediates, washing with ice-cold 1x PBS followed by quenching with ultra-cool 80% MeOH (-80 °C) resulted in the highest metabolite yield and an EC of 0.94. Samples were found to be stable for three weeks in extraction solvent, while solvent evaporation resulted in a slight but non-significant reduction of AR levels. With respect to the preanalytical normalization (DNA concentration vs. cell count), normalization by cell count was shown to be more robust (CV_{mean} = 6%) compared to normalization by DNA (CV_{mean} > 20%).

(II) In the MDA-MB-468 cell line, a concentration-dependent decrease in AKT phosphorylation (Thr_{308} and Ser_{473}) was observed upon inhibition of PI3Kβ, indicating impaired signaling downstream of pAKT. Investigation of the metabolic phenotype by quantitative metabolomics and real-time metabolic flux analysis confirmed reduced glycolysis, TCA cycle activity and OXPHOS, as well as significant reduction of lactate secretion in the presence of AZD8186. Dose optimization experiments showed that an inhibitor concentration of 0.5 µM reduced glycolysis and TCA cycle activity and inhibited cell growth for up to three days of treatment. High cellular uptake rate of glucose und glutamine were detected independently of PI3Kβ inhibition, supporting the use of stable isotope labeled glucose and glutamine as suitable tracer substrates for establishing the SIRM workflow.

(III) Based on the optimized sample preparation, a SIRM workflow from cell culture to data analysis and visualization in the statistical software R was developed. The workflow was

applied to MDA-MB-468 cells treated for up to 24h with 0.5 µM AZD8186 or vehicle. Untargeted differential tracing revealed 286 isotope-enriched features that were significantly altered between vehicle control and treatment, of which 19 features could be attributed to known compounds from targeted pathways. The other 11 features were unambiguously identified based on data-dependent MS/MS spectra and reference substances. The structurally identified metabolites were integrated into the existing targeted isotopologue feature extraction workflow to enable natural abundance correction, evaluation of assay performance and assessment of drug-induced changes in pathway activities. Label incorporation was highly reproducible for the majority of isotopologues in technical replicates with a RSD below 10%. The inter-day repeatability of a second label experiment showed strong correlation (Pearson $R^2 > 0.99$) between tracer incorporation on different days. Finally, prominent pathway activity alterations upon PI3Kβ inhibition were identified. Besides pathways in central metabolism known to be changed, the workflow revealed additional pathways that were altered in the presence of the inhibitor, like pyrimidine metabolism or hexosamine pathway. All pathways identified represent key metabolic processes associated with cancer metabolism and therapy.

(IV) While ^{13}C labeled glucose is commonly used for monitoring glycolytic rates and TCA cycle activity, information on metabolic changes within parts of the central carbon metabolism downstream of pyruvate or fueling the TCA cycle *via* glutamine oxidation cannot be captured. The use of [U-^{15}N] and [U-^{13}C,^{15}N] glutamine employing targeted isotopologue feature extraction showed prominent effects associated with PI3Kβ inhibition in metabolites of the hexosamine pathway, the adenylated ribonucleotides, and altered isotope enrichment within TCA cycle intermediates (i.e. succinate, fumarate, and malate). These results suggested predominantly oxidative effects whereas the metabolic consequence of the inhibitor on glutaminolytic activity was limited. Comparison of the results of untargeted differential tracing using [U-^{13}C,^{15}N] glutamine with those of [U-^{13}C] glucose revealed only small overlap (6.9%) of isotope-enriched features that were significantly altered upon inhibition of PI3Kβ while the majority of features (>20%) were unique to labeled glutamine, providing complementary information on pathway changes.

(V) Using [U-^{13}C] glucose and performing untargeted differential tracing, 521 and 417 isotope-enriched features were found to be significantly altered between control and treatment with AZD8186 in HCC70 and MDA-MB-468 cells, respectively. For the HCC70 cell line, the distribution of features was found to be 49% in the control, 16% in the treated and 35% in the shared proportion compared to an almost even distribution of ~30% within the MDA-MB-468 cell line. Data alignment from the non-targeted analysis showed that 162 features were found in both cell lines. 20 features were identified based on structurally known compounds belonging to the central carbon metabolism, amino acid metabolism, ribonucleotide biosynthesis and the hexosamine pathway.

Overall, this work established a SIRM platform that allowed to investigate changes in metabolic pathway activities that is not limited to the PI3K signalling pathway, nor to the PI3Kβ inhibition in TNBC cell lines. This platform can substantially contribute to advances in cancer research and may enable the development of novel treatment strategies for patients.

1. Introduction

Cancer was the second leading cause of death in Germany in 2023, accounting for 22.4% of all deaths (Statistisches Bundesamt 2025). The lifetime risk of developing cancer is 1 in 2, and the probability of dying is 1 in 4 for women and 1 in 5 for men, respectively (Haberland et al. 2010). It is well established that genetic predispositions (e.g., BRCA1/2 and TP53), lifestyle factors (e.g. smoking, alcohol), and environmental factors (e.g. air pollution, radiation) can promote the development of cancer. Nevertheless, tumorigenesis is complex and has been a major focus of research for over a century (Weinstein and Case 2008). Cancer occurs in more than 100 different types and is not restricted to any organ or part of the body. One of the most common types of cancer is adenocarcinoma, which arises from abnormal growth of epithelial cells. Important examples include breast, pancreatic, prostate, and colon carcinomas. These adenocarcinomas accounted for nearly one-third of cancer related deaths in Germany in 2023 (Statistisches Bundesamt 2024).

1.1. The Phosphatidylinositol 3-kinase (PI3K) pathway and its role in human cancer

While non-tumor cells tightly regulate their proliferation by e.g., cytokines or hormones docking to membrane-associated receptors, cancer cells can overcome this ligand-mediated dependence by constitutive activation of signaling pathways downstream of such receptors as a result of somatic mutations. A key example of aberrantly activated signaling pathways is the phosphatidylinositol 3-kinase (PI3K) pathway which is commonly activated in human tumors (Lawrence et al. 2014).

This signaling pathway is conserved across yeast and mammalian cells and interconnects many intracellular processes including proliferation and survival (Cantley 2002; Engelman 2009; Gao et al. 2011). Furthermore, the PI3K pathway plays a crucial role in the cell metabolism where it governs glucose and amino acid metabolism (Zhang et al. 2019), *de novo* synthesis of acetyl-CoA (Dibble et al. 2022) or nucleotide biosynthesis (Wang et al. 2009). Signaling is directed by the PI3K lipid kinases that facilitate the transformation of phosphatidylinositol 4,5-bisphosphate (PIP_2) to the second messenger phosphatidylinositol 3, 4,5-trisphosphate (PIP_3) at the plasma membrane. Three different classes of PI3K have been identified and are categorized based on their sequence or substrate specificity (Figure 1) (Engelman et al. 2006; Nürnberg and Beer-Hammer 2019). Class I PI3Ks are further subdivided into class IA or IB according to their coupled receptor (Cantley 2002; Engelman et al. 2006). Class IA PI3Ks are coupled with a receptor tyrosine kinase (RTK), whereas class IB PI3Ks are linked to G-protein coupled receptors (GPCR). Both classes are heterodimers with a catalytic (i.e. Class IA, p110; Class IB p110 γ) and a regulatory subunit (i.e. Class IA, p85α,

p85β, p55δ; Class IB, p84, p87) wherein the catalytic subunit of Class IA is expressed as three different isoforms (i.e. p110α, β, δ) (Nürnberg and Beer-Hammer 2019; Chalhoub and Baker 2009). The phosphatase and tensin homolog (PTEN) tightly regulates this activation and signal relay by dephosphorylation of the second messenger (PIP_3) under physiological conditions (Figure 1) (Chalhoub and Baker 2009; Fruman et al. 2017; Hoxhaj and Manning 2020; Nürnberg and Beer-Hammer 2020). Activation of the PI3Ks and subsequent production of PIP_3 leads to the recruitment of AKT to the plasma membrane with subsequent site specific phosphorylation at the $Threonine_{308}$ and $Serine_{473}$ residue by PDK1 (phosphoinositide-dependent kinase 1) and mTORC2 (mammalian target of rapamycin complex 2), respectively (Hoxhaj and Manning 2020; Manning and Toker 2017). Upon phosphorylation of AKT further downstream effectors are activated driving major cellular functions e.g. proliferation, metabolism, and growth.

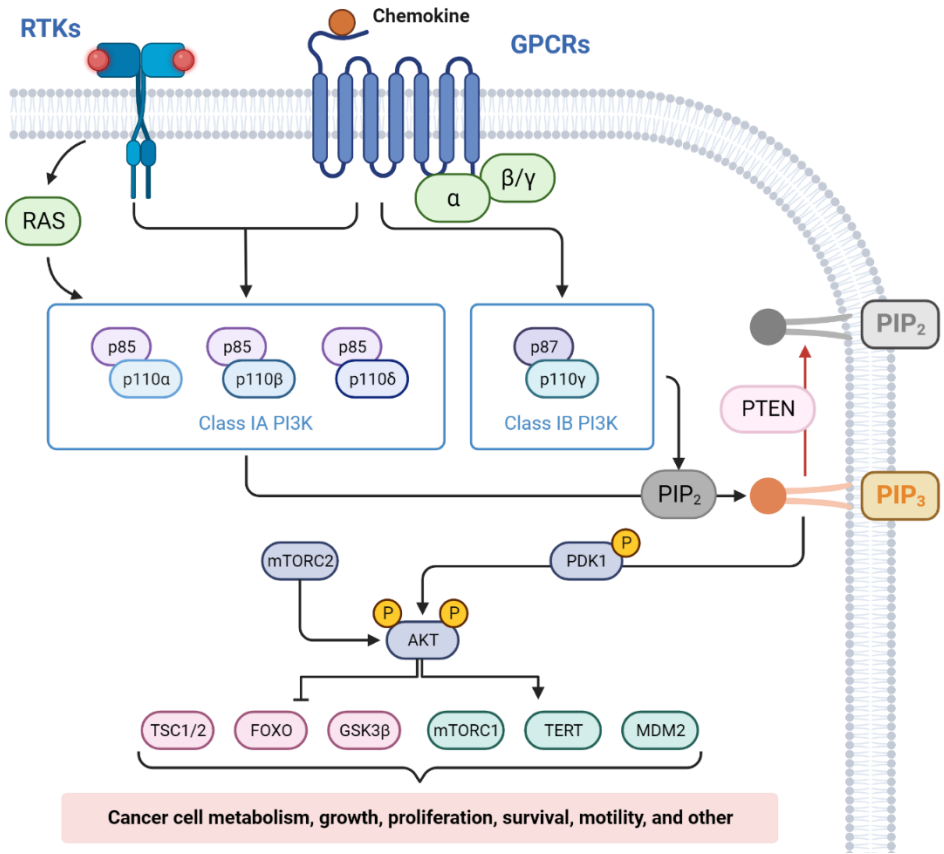

Figure 1: Schematic illustration of the PI3K signaling cascade. Phosphorylation of PIP2 by signaling through different classes of PI3Ks and corresponding regulation by PTEN. PIP3 drives the activation of AKT via phosphorylation by PDK and mTORC2 with subsequent signal relay to govern cellular functions. Adapted from Chalhoub and Baker 2009; Janku et al. 2018; Sun and Meng 2020; Vidal et al. 2022**.** Created with BioRender.com

1.1.1 Selective inhibition of the PI3K signaling pathway in cancer therapy

Due to their central role within cancer cell physiology, PI3Ks have become a rational target for therapeutic intervention and meanwhile several PI3K inhibitors have been approved for the treatment of different malignancies (Vanhaesebroeck et al. 2021). As the PI3K signaling pathway is also important for normal physiological processes in various tissues, therapeutic intervention has proven to be difficult. Drug resistance or drug toxicities are just some of the obstacles that need to be overcome (Mishra et al. 2021; Vanhaesebroeck et al. 2021). PI3K inhibitors can be classified into pan (targeting all PI3K isoforms), isoform-specific and dual PI3K/mTOR inhibitors (Mishra et al. 2021). While pan and dual inhibitors displayed more drug toxicities, targeting specific isoforms of the PI3Ks seems to be an alternative in order to circumvent safety concerns (Wang et al. 2015; Vanhaesebroeck et al. 2021; Mishra et al. 2021).

1.1.2 Isoform specific inhibition of PI3Kβ in triple negative breast cancer

In this context it has been shown, that inactivation of PTEN drives tumorigenesis while at the same time a wide range of tumors become dependent on the PI3Kβ isoform (Jia et al. 2008; Wee et al. 2008). This has led to the development of isoform-specific inhibitors, especially for tumors with low PTEN expression and limited treatment options. Triple negative breast cancers (TNBC) are tumors in question for this therapy, since almost 30% of TNBC carry a PTEN mutation. Additionally, missing hormone receptors limit therapeutic interventions and is further topped by their aggressiveness, tendency to relapse and overall poor survival (Cocco et al. 2020; Jung et al. 2018; Pascual and Turner 2019). A retrospective cohort study found a 5-year survival rate of approximately 75% for TNBC compared to 86.5% for non-TNBC in Germany (Schwentner et al. 2012). Furthermore, metastatic TNBC has a significantly lower 5-year survival rate of 10.81% compared to ~33% in non-TNBC cases (Hsu et al. 2022). As selective inhibition of PI3Kβ with AZD8186 led to promising results in PTEN-null tumors *in vitro* and breast tumor xenografts in mice, it was also investigated in a clinical setting (Barlaam et al. 2015; Hancox et al. 2015; Hansen et al. 2017; Lynch et al. 2017; Lynch et al. 2018; Choudhury et al. 2022). Despite these findings the clinical development was discontinued displaying the need for novel approaches that can contribute to a better understanding of disease development and modes of drug action (Vanhaesebroeck et al. 2021).

1.2. Metabolomics as a tool to study cancer cell metabolism and cancer drug targets

1.2.1 The complexity of the metabolome

The metabolome is the result of complex interactions between the genome, transcriptome, and proteome and represents the closest link to the phenotype. The functional element of the metabolome are small molecules, so called metabolites that are produced or consumed in wide networks of biochemical reactions. These metabolites have a molecular weight between 50 Da and 1500 Da and cover a wide range of compound classes including amino acids and carbohydrates, lipids, vitamins, nucleotides, fatty acids and others (Cortes et al. 2017). Moreover, they differ in their physicochemical properties, their subcellular location or as well as intracellular concentrations (i.e. subcellular metabolite pools). This variety is emphasized by the more than 200.000 metabolite entries in the Human Metabolome database (Wishart et al. 2022) in comparison to the 20.000 protein coding genes in the human genome (Piovesan et al. 2019).

1.2.2 Altered cell metabolism in cancer

The concept of cancer as a metabolic disease is not new but rather has gained momentum over the last years (Coller 2014; Gyamfi et al. 2022; Seyfried et al. 2014; Wishart 2015). The so called “Warburg effect” (Warburg 1924) is well-known in cancer research and is a proven example on how the metabolic phenotype is altered across different tumor types (Potter et al. 2016). A variety of cancer cells (e.g. breast, lung, and colorectal cancer) demonstrate increased glycolytic activity with subsequent lactate fermentation instead of oxidative phosphorylation *via* the tricarboxylic acid cycle (TCA cycle) under aerobic conditions (Potter et al. 2016; Warburg 1924). Interestingly, the most frequently mutated gene TP53 is altered in ~ 50% of all cancers (Baugh et al. 2018; Levine and Oren 2009), while an elevated glycolytic activity has been demonstrated in > 90% of cancer types by ^{18}flurodeoxyglucose (^{18}FDG) uptake in positron emission tomography (PET) in clinical applications (Epstein et al. 2017). Increased glycolytic activity is not the only characteristic of tumors but altered metabolic pathway activities or even single metabolites have been shown to be involved in carcinogenesis. As an example, 2-Hydroxyglutarate contributes to the development of brain tumor (Dang et al. 2009) and has also been shown to modulate gene expression across other tumor types (e.g. acute myeloid leukemia, pancreatic cancer, and colorectal cancer) (Gupta et al. 2021; Ježek 2020; Tabata et al. 2023). TCA cycle intermediates (i.e. fumarate and succinate) have also been implicated in certain tumors including renal cell carcinoma and paragangliomas (Bayley and Devilee 2010; Yang et al. 2012). The accumulation of these metabolites stabilizes the hypoxia induced factor (HIF) transcription factor complex, leading to

the upregulation of glucose transport and glycolysis, as well as the activation of oncogenic target genes (Bayley and Devilee 2010; Isaacs et al. 2005; Yang et al. 2012). Likewise, amino acids (e.g. glutamine, serine, and glycine) have been associated with carcinogenesis, as they participate in crucial anabolic pathways i.e. biosynthesis of proteins, ribonucleotides, or redox homeostasis (Baysal et al. 2000; Dang et al. 2009; Gyamfi et al. 2022; Khatami et al. 2019; Sciacovelli and Frezza 2016; Tomlinson et al. 2002; Vettore et al. 2020; Vučetić et al. 2017). These and other metabolites are nowadays more commonly referred to as oncometabolites (Kumar and Misra 2019). The presence of these metabolites at elevated non-physiological levels can lead to aberrant changes in signaling pathways, support anabolic metabolism for maintaining proliferative activity, or even protect against chemotherapeutic drugs (Collins et al. 2017; Kumar and Misra 2019; Sen et al. 2016).

1.2.3 Metabolomics approaches

Metabolites are the product of all complex interactions between genes, proteins, and environmental influences (e.g. microbiome) and are capable of depicting the functional state of a diseased or healthy biological system. Consequently, the investigation of the entire metabolome and associated pathway activities can provide a more comprehensive and deeper understanding of disease development, progression, or drug response. The investigation of the metabolome (i.e. characterization, identification and quantification) in a biological system is often referred to metabolomics and is most commonly performed by spectroscopic (e.g. nuclear magnetic resonance (NMR)) or spectrometric approaches like mass spectrometry (Wang et al. 2010). Over the last decades, metabolomics has established itself as a crucial tool in biomedical research and clinical applications (Kaushik and DeBerardinis 2018; López-López et al. 2018) leading to an increased interest in metabolomics and its applications (Tolstikov et al. 2020). In this work, metabolomics was performed by mass spectrometry and thus are explained further.

1.2.4 Platforms in mass spectrometry-based metabolomics

Metabolites are not readily detected by a mass spectrometer but have to undergo several stages during analysis prior detection. This process sequence is typically comprised of the generation, separation, and detection of charged molecules and can be achieved by various means in mass spectrometry (Meyer et al. 2022). In general, these charged molecules, so called ions, are brought into the gas phase by the ion source and guided through a magnetic or electric field. These ions are then separated in the mass analyzer according to their mass to charge ratio (m/z), where ultimately filtered ions are registered as current on a detector which allows for the plotting of a mass spectrum. Additionally, samples can be subjected to chromatographic separation prior ionization, which allows for better resolution of compounds

with identical or similar masses or reduces ion suppression caused by matrix effects. To enable chromatographic separation, mass spectrometers can be coupled with gas chromatography (GC-MS) or (ultra) high performance liquid chromatography, respectively ([U]HPLC-MS).

1.2.4.1. GC-MS

The principle of GC relies on the volatility of compounds and their interaction with the stationary phase while being passed through the stationary phase with a carrier gas. Most applications nowadays use capillary columns that have the stationary phase coated onto the inner wall, typically polysiloxane polymers or polyethylene glycols (PEG) (Rahman et al. 2015). Typically, GC is employed for highly volatile compounds or alternatively metabolites can be made volatile through derivatization procedures. For the modification of functional groups that might intervene with the volatility of the compounds, common protocols use trimethylsilylation or tert-butydimethylsilylation as derivatization reactions (Fiehn 2016). Compared to LC-MS, GC-MS is in particular suited for the analysis of molecules with smaller molecular weights <650 Da (Fiehn 2016). In addition, GC-MS offers high repeatability and well-established libraries for compound identifications. On the contrary, thermolabile and nonvolatile compounds are not suitable for GC-MS analysis, whilst time consuming sample preparation due to the chemical derivatization procedure and a larger degree of fragmentation due to harsh ionization conditions (electron impact ionization) are also considered disadvantages compared to LC-MS.

1.2.4.2. HPLC-MS

The application of HPLC-MS especially in combination with electro-spray ionization (ESI) as soft ionization method, has become the most commonly employed approach in metabolomic research (Gowda and Djukovic 2014; Schrimpe-Rutledge et al. 2016). Unlike GC-MS, there is generally no need for chemical modification in LC-MS analysis, and analytes with a wider range of physicochemical properties (i.e. polar non-polar, molecular weight, nonvolatile) compared to GC-MS can be analyzed (Agin et al. 2016). In liquid chromatography, the analytes are dissolved in the mobile phase and undergo interactions with the stationary phase due to their physicochemical properties and thus are retained differently on the column. In turn, analytes of interest are separated from unwanted compounds or interferences leading to the desired increase in selectivity and specificity. The selectivity of the chromatography is mainly determined by the stationary phase of the column, with additional contributions from the mobile phase. Most commonly applied separation techniques employ reversed phase liquid chromatography (RPLC) and hydrophilic interaction liquid chromatography (HILIC). While nonpolar and weakly polar molecules can be efficiently separated on RPLC columns, polar compounds are typically not easily retained or resolved on these columns and can be

alternatively analyzed by ion pairing liquid chromatography (IPLC) which enables the analysis of polar compounds on conventional reveres phase columns as well (Knee et al. 2013). Alternatively, HILIC columns are the preferred choice for the analysis of polar metabolites (Tang et al. 2016). HILIC can be regarded as a subtype of normal-phase liquid chromatography (NPLC) with a polar stationary phase but mobile phases similar to those employed in RPLC which are typically organic solvents miscible with water e.g. acetonitrile. The proposed retention mechanism is based on the interaction of analytes with the polar stationary phase and the highly organic mobile phase (Alpert 1990). Moreover, the polar stationary phase enables the generation of an immobilized water interface leading to partitioning of the analytes between this interface and the mobile phase (Harrieder et al. 2022). Additionally, further interactions between analyte, mobile phase, and stationary phase can occur e.g. adsorption of the analyte to the surface of the stationary phase (Buszewski and Noga 2012). Not only different retention mechanisms drive the selection of HILIC columns, but also the composition of the stationary phase can be adjusted towards the corresponding need. Here, stationary phases can be grouped into four categories (i.e. anionic, cationic, uncharged, and zwitterionic (Contrepois et al. 2015)). Especially, immobilization of a positively and negatively charged chemical group onto silica-bonded stationary phases makes the employment of zwitterionic columns appealing as due to the combination of ionic and polar interactions the selectivity is further improved (Jandera and Janás 2017).

1.2.5 Approaches in MS based metabolomics

Two complementary approaches can be applied to assess the metabolome of samples - targeted metabolomics that commonly make use of e.g. triple quadrupole MS (TQ-MS) or GC-MS instruments. On the other hand, untargeted metabolomics is typically performed on high resolution mass spectrometers such as e.g. Quadrupole Time of Flight mass spectrometers (QToF).

1.2.5.1. Targeted metabolomics

Targeted metabolomics analyzes chemically characterized compounds that can be attributed to known biochemical reactions or pathways (e.g. glycolysis, TCA cycle, or amino acid biosynthesis). This approach is hypothesis driven and corresponding target analytes are validated by chromatographic and fragment characteristics from corresponding analytical standards. This allows for tailored method development and optimization regarding accuracy, precision and detection sensitivity within the instrument. Established targeted methods have been successfully applied for the screening of more than twenty inborn errors of metabolism in newborns like phenylketonuria or β-hydroxy-β-methylglutaric acidemia already since the late 90s (Matsumoto and Kuhara 1996). Other targeted applications include the detection of

potential biomarkers for heart failure and diabetes (Ahmad et al. 2016; Guasch-Ferré et al. 2016; Wang et al. 2018). The identification of oncometabolites and the possibility of monitoring cancer progression underlines the valuable addition of targeted metabolomics to cancer research (Han et al. 2021). While targeted metabolomics is often applied in hypothesis-driven research, the biased selection of only a preselected panel of metabolites may overlook a significant portion of metabolites of potential biological relevance in pathophysiology and/or drug response.

1.2.5.2. Untargeted metabolomics

In order to overcome the limitations of targeted metabolomics, the hypothesis generating approach of untargeted metabolomics can be employed. This method aims at a comprehensive and unbiased analysis of the metabolome within a given sample or matrix. By the nature of this approach, metabolites are typically not annotated at first and thus are referred to so called metabolic features. The goal of any untargeted metabolomics experiment is to detect a high number of features in order to cover a broad range of biochemically diverse compounds. Metabolic feature levels can only be quantified relatively, which is typically achieved by bioinformatical data analysis pipeline e.g. Metaboanalyst (Pang et al. 2022). Here, statistically significantly (p-value) and relevantly (fold- change) altered features are determined (e.g. by volcano plot) followed by their structural assignment based on accurate mass or by comparing its fragment spectra with mass spectral libraries e.g. HMBD (Wishart et al. 2022), METLIN (Smith et al. 2005), MassBank (Horai et al. 2010). Additionally, computational tools exist that enable metabolite identification based on *in silico* fragmentation e.g. MS Finder (Tsugawa et al. 2016), and SIRIUS (Dührkop et al. 2019). Although accurate mass is one important parameter for successful feature annotation, some features will not be identified with 100% certainty. Due to the fact that even a mass accuracy of less than 1 ppm produces a significant amount of valid chemical structures (Kind and Fiehn 2006). In this context, the Metabolomic Standard Initiative (MSI) has proposed four levels of metabolite identification to classify these unknown features and provide a standardized reporting procedure (Sumner et al. 2007). These levels include known compound (Level 1), putatively annotated compound (Level 2), putatively characterized compound classes (Level 3), and lastly unknown compounds (Level 4). Ultimately, after identification of new compounds or compound classes, the hypothesis can be cross validated by the targeted approach.

1.3. Stable Isotope resolved Metabolomics (SIRM)

1.3.1 Steady state metabolomics vs. SIRM

Steady state metabolomics aims at the absolute quantitation of known metabolites within specific pathways (i.e. targeted approach) or relative quantitation of metabolic features in an untargeted fashion at a specific time point in a biological system. While this approach has been widely used for the discovery of metabolic biomarkers or the evaluation of therapy responses (Wang et al. 2011; Wei et al. 2013; Debik et al. 2019; Martín-Blázquez et al. 2019), it displays a rather static picture of the metabolome that does not provide information about pathway dynamics (i.e. increased or decreased consumption or production, respectively), especially in the context of a wide metabolic network. To fully understand the regulation of aberrant cancer cell metabolism, knowledge of the intracellular flux throughout the different metabolic pathways is desired, which in addition can provide valuable insights into metabolic changes related to cancer drug treatment. Here, mass spectrometry based stable isotope resolved metabolomics (SIRM) has established itself as a powerful complementary tool as it enables monitoring of pathway activities.

1.3.2 Definitions and experimental approaches relevant for SIRM

1.3.2.1. Terminology in stable isotope resolved metabolomics

Isotopes are atoms with equal number of protons but varying numbers of neutrons. Stable isotopes occur naturally with an element specific abundance (Table 1) and can be further distinguished from non-stable isotopes (i.e. radioactive) as they do not decay over time. While their chemical properties are comparable, the presence of naturally occurring heavy isotopes needs to be addressed when stable isotope labeled substrates (so called tracer substrates) are applied in biological systems. To this end, enrichment of any compound is corrected for its natural abundance in order to accurately determine the extent of incorporation of labeled isotopes into metabolic products (Fernandez et al. 1996).

Table 1: Abundance of naturally occurring stable isotopes. Adapted from Wolfe 2005

Element	Stable isotope	Natural abundance [%]	Mass [g/mol]
Hydrogen	^{1}H	99.985	1.0078
	^{2}H	0.015	2.0141
Carbon	^{12}C	98.89	12.0000
	^{13}C	1.11	13.0034
Nitrogen	^{14}N	99.63	14.0031
	^{15}N	0.37	15.0001

Isotopic enrichment within molecules *via* enzymatic reactions from the employed tracer results in a gain of molecular mass. These labeled “versions” of a compound, so called isotopologues, have the identical sum formula as the unlabeled parent molecule but differ in their isotopic composition and thus in their molecular mass. Typically, these isotopologues are referred to as “m+n isotopologue”, where the unlabeled molecule is denoted as m+0 isotopologue while the maximum number of isotopologues is given by the number of atoms (i.e. ”n”) that can be replaced by its stable isotopic counterpart. For example, glycine with a sum formula of $C_2H_5NO_2$, can have three isotopologues for the carbon atoms resulting in m+0, m+1 and m+2 isotopologues (Figure 2 A). While isotopologues do not provide any information related to the position of an isotope within a molecule, isotopomers do. Isotopomers can contribute to a better understanding of enzymatic reactions. However, obtaining structural information through mass spectrometry is challenging, therefore complementary techniques such as nuclear magnetic resonance (NMR) spectrometry are often required (Fan and Lane 2016; Gowda and Raftery 2019). In general, isotopomers have the same elemental and isotopic composition as corresponding isotopologues. However, the position of the isotope within the molecule is different. In the case of glycine, one ^{13}C atom can be incorporated at two different positions, resulting in a m+1 isotopologue with two distinct isotopomers (Figure 2 A).

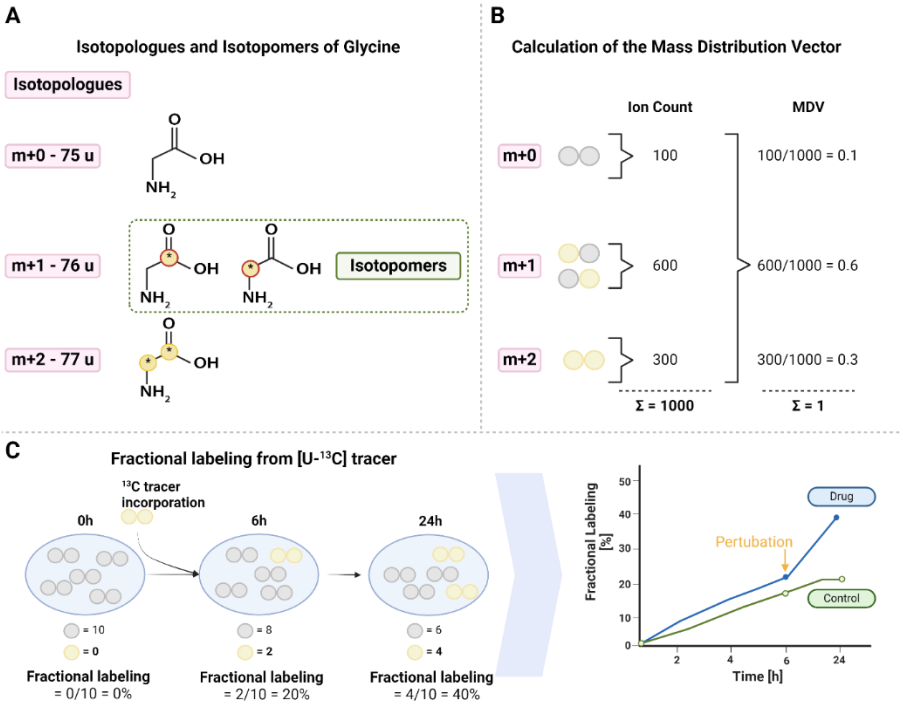

Figure 2: Illustration of glycine isotopologues, MDV calculation, and fractional labeling after ^{13}C incorporation. Adapted from Buescher et al. 2015 and Weindl 2015. A: Isotopologues and isotopomers are exemplarily shown for glycine. B: Schematic display of the calculation of the mass distribution vector (MDV) for glycine using generic ion intensities. C: Calculation of fractional labeling upon ^{13}C tracer incorporation. Fractional labeling as measure to compare relative abundance of heavy isotopes in the same compound for different biological conditions. Created with BioRender.com

The stable isotopic enrichment of compounds by an administered stable isotope tracer is visualized by its labeling pattern and is calculated from the mass distribution vector (MDV). The MDV corresponds to the fractional abundance of corresponding isotopologues normalized to the sum of all isotopologues, in which the sum of all isotopologues fractions is set to 1 or 100%, respectively (Figure 2 B) (Buescher et al. 2015).

Although the labeling pattern represented by the MDV is an important measure to infer specific pathway activities, the relative abundance of the heavy isotope in the overall pool of a compound is just as important. In this work, this parameter is referred to as fractional labeling and defined by Equation 3 (2.2.6.1). In the case of fully labeled substrates, the fractional labeling describes how much of a tracer contributes to the formation of a labeled intermediate (Buescher et al. 2015). It becomes helpful when the extent of isotopic enrichment needs to be compared across multiple compounds or biological conditions. In further detail, ^{13}C incorporation into the molecular structure of glycine leads to a pool of different isotopologues from unlabeled m+0 to fully labeled m+2 isotopologues (Figure 2 C). Fractional labeling now displays the overall percentage of the glycine metabolite pool that incorporated any ^{13}C atoms into its structure based on the normalized (i.e. corrected for natural abundance) fractional abundance of the MDV.

1.3.2.2. *General approach in SIRM experiments*

Typically, performing SIRM experiments involves feeding of a labeled tracer substrate to an organism of interest (e.g. plants, cell culture or *in vivo* models etc.). The tracer is subsequently taken up and enzymatically metabolized leading to incorporation of the stable isotopes into metabolites (Figure 3). Dependent on specific pathways or enzyme activities, rearrangement of the stable isotopes within the endogenous metabolite pool occurs. Mass spectrometric analysis determines the relative abundances of isotopologues within the molecule and allows for the calculation of the MDV. The resulting labeling patterns are used to infer specific pathways, qualitatively assess relative changes in activities and even monitor substrate fluxes (Antoniewicz 2018; Buescher et al. 2015). This principle holds true for any stable isotope-labeled substrate and is not limited to ^{13}C labeled substrates.

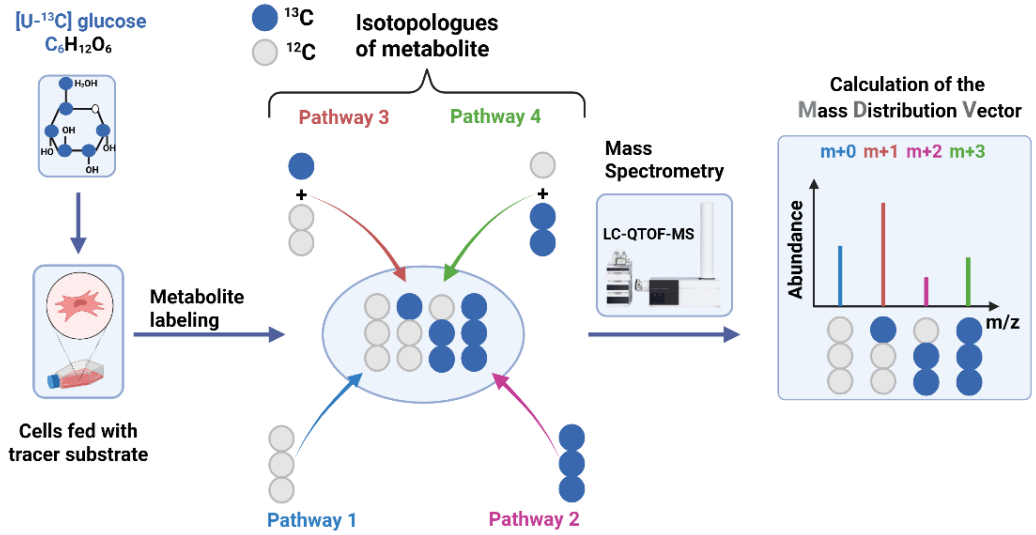

Figure 3: Scheme of ^{13}C tracing from [U-^{13}C] glucose in cultured cells with pathway specific rearrangement of stable isotopes in a fictional metabolite. MDV calculation based on isotopologue abundances determined by LC-QTOF. Created with BioRender.com

1.3.2.3. *Selection of suitable tracer substrates*

Attributing specific labeling patterns in metabolites to certain pathways and enzymatic activities is a key characteristic of SIRM experiments. However, the identification of pathways of interest prior to starting labeling experiments is of outmost importance, as the employed tracer also has a major impact on the measured labeling pattern of metabolites. There is a large panel of tracers at hand that enable the investigation of several pathways and metabolic reactions (Jang et al. 2018), reaching from applications in glycolytic pathways to the biosynthesis of amino acids and ribonucleotides. For example, in the context of glycolytic activity, positionally labeled glucose (e.g. [1,3-^{13}C] glucose) can provide additional information in regard to the exploration of the non-oxidative and the oxidative PPP (Lee et al. 1998). Likewise palmitic acid as unsaturated fatty acid is a suitable tracer substrate for the investigation of fatty acid oxidation

and fueling of the energy metabolism in cancer cells (Carracedo et al. 2013). In this work the focus will only be on glucose (i.e. [U-^{13}C] glucose) and glutamine tracers (i.e. [U-^{13}C] and [U-^{15}N] glutamine, respectively) since cancer cells demonstrate the highest uptake rates for glucose followed by glutamine (Hosios et al. 2016; Jain et al. 2012).

1.3.3 Interpretation of ^{13}C/^{15}N tracer incorporation within different metabolic pathways

In typical isotopic labeling experiments, the labeling fraction of corresponding isotopologues (glycine as example shown in Figure 2) is plotted for results interpretation. In the following chapters, different routes of ^{13}C/^{15}N labeled precursors and their routes of incorporation will be displayed for all pathways relevant for this work (Figure 4). These comprise glycolysis (1.3.3.1), TCA cycle (1.3.3.2), biosynthesis of ribonucleotides (1.3.3.4) and nucleotide sugars (1.3.3.5), and amino acid biosynthesis (1.3.3.6). Understanding the "flow" of carbon and nitrogen atoms through the different metabolic routes will be pivotal for results interpretation of this thesis based on MDV plots and the dynamics of tracer incorporation for different labeling times.

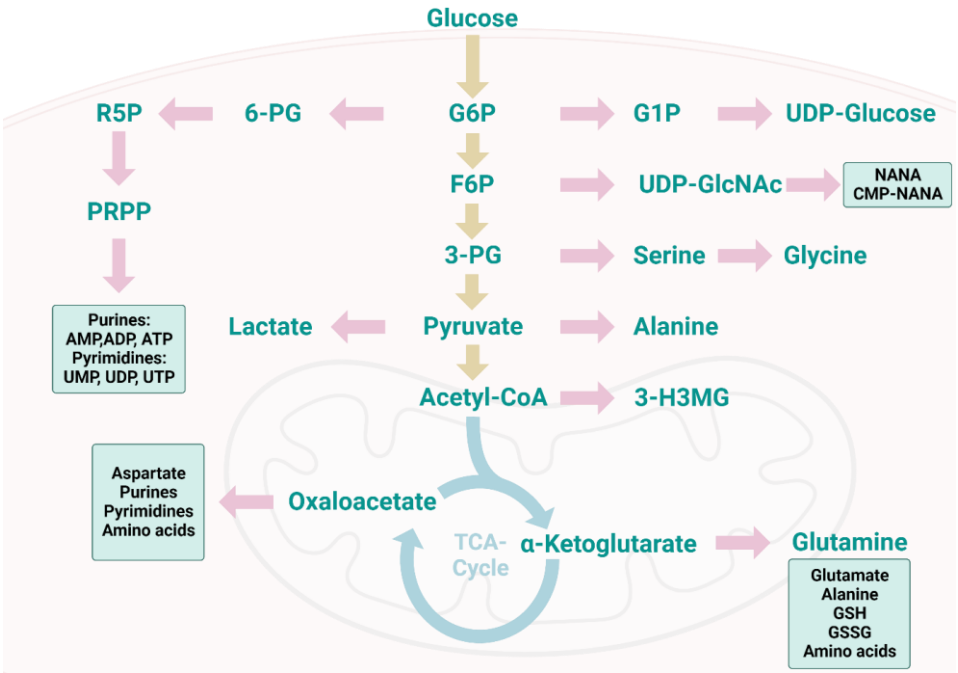

Figure 4: Overview of intermediates and corresponding pathway origins relevant to this work. Glycolysis: Glucose, glucose-6-phosphate (G6P), fructose-6-phosphate (F6P), 3-phosphoglycerate (3-PG), glucose-1-phosphate (G1P), pyruvate; PPP: 6-phosphogluconate (6-PG), ribose-5-phosphate (R5P); TCA cycle: Acetyl-CoA, α-ketoglutarate, oxaloacetate; Amino acids: Glutamine, alanine, serine, glycine, aspartate; Nucleotide sugars: Uridine diphosphate N-acetylglucosamine (UDP-GlcNAc), UDP-glucose, N-acetylneuraminate (NANA), cytidine monophosphate N-acetylneuraminic acid (CMP-NANA); Mevalonate pathway: 3-hydroxy-3-methylglutarate (3-H3MG); *De novo* ribonucleotide biosynthesis: Phosphoribosyl pyrophosphate (PRPP), adenosine mono/di/triphosphate (AMP, ADP, ATP), uridine mono/di/triphosphate (UMP, UDP, UTP). Created with BioRender.com

1.3.3.1. Tracer incorporation along glycolysis and PPP

In terms of labeling patterns for the glycolytic breakdown of [U-^{13}C] glucose the hexose phosphates will mostly display the fully labeled m+6 isotopologue (Figure 5). However, in presence of unlabeled glucose or feeding a mixture of [U-^{13}C] glucose and unlabeled glucose, reversibility of fructose-bisphosphate aldolase can be seen as m+3 isotopologue in fructose-1,6-bisphosphate (F16BP), whereas fructose bisphosphatase activity (F16BP → G6P) can be monitored *via* the m+3 isotopologue in G6P (Jang et al. 2018). Within the irreversible oxidative branch of the PPP the 6-phosphogluconate (6-PG) incorporates six ^{13}C carbons originating from G6P *via* glucose-6-phosphate dehydrogenase and 6-phosphogluconate dehydrogenase activity (Polat et al. 2021), thus producing the fully labeled m+6 isotopologue. The decarboxylation reaction from 6-PG to ribulose 5-phosphate will form the m+5 isotopologue in corresponding intermediates of the PPP. Furthermore, ribose 5-phosphate provides the ribose backbone for purine and pyrimidines after being converted to phosphoribosyl pyrophosphate (PRPP) *via* the PRPP synthase (Engelking 2015) and is an essential building block for the biosynthesis of ribonucleotides (1.3.3.4).

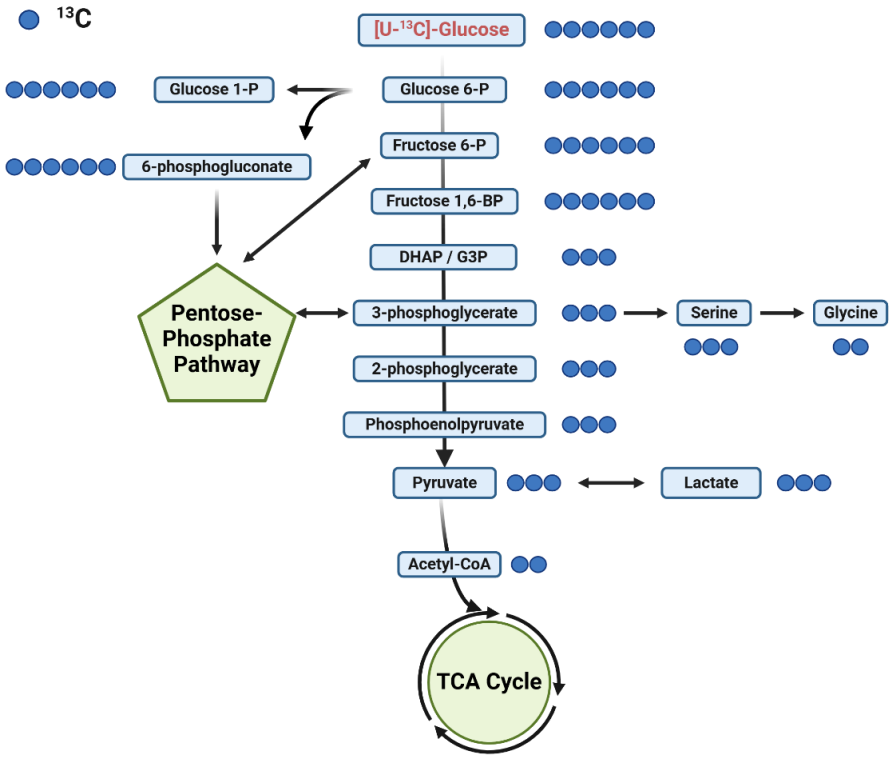

Figure 5: Glycolytic breakdown of [U-^{13}C] glucose. Created with BioRender.com

Fructose-bisphosphate aldolase produces the triose phosphates dihydroxyacetone phosphate (DHAP) and glyceraldehyde 3-phosphate (G3P) from F16BP. Here, 3-phosphoglycerate (3-PG) is formed *via* multiple reactions from G3P. Labeling of these triose phosphates will mostly show m+3 isotopologues (Gkiouli et al. 2019). However, it is worth mentioning that gluconeogenetic activity can result in labeling of triose phosphates originating from tracer incorporation within the TCA cycle due to phosphoenolpyruvate carboxykinase activity (PEPCK), yielding m+2 isotopologues in PEP and 3-PG. 3-PG also provides the necessary carbons for the *de novo* biosynthesis of serine and glycine (Choi and Coloff 2019) illustrated in Figure 6. Here, serine typically displays the m+3 isotopologue and donates one carbon to the one-carbon-metabolism. Consequently, glycine will show the m+2 isotopologue (Gkiouli et al. 2019).

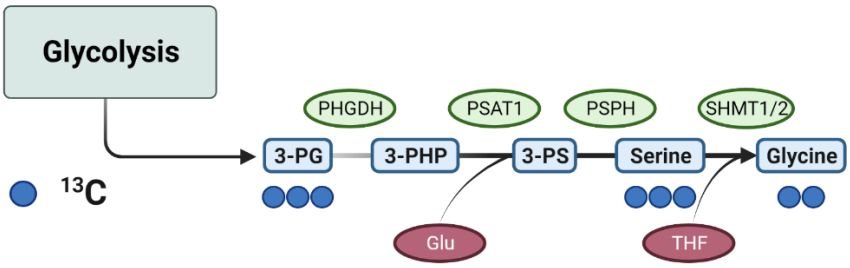

Figure 6: *De novo* biosynthesis of serine and glycine from [U-^{13}C] glucose *via* 3-phosphoglycerate (3-PG). Phosphoglycerate dehydrogenase (PHGDH) produces 3-phosphohydroxypyruvate (3-PHP) from 3-PG. 3-phosphoserine (3-PS) is synthesized from 3-PHP and glutamate (Glu) *via* the enzyme phosphoserine aminotransferase 1 (PSAT1). Phosphoserine phosphatase (PSPH) produces serine and subsequently glycine *via* serine hydroxymethyltransferase 1/2 (SHMT1/2) and tetrahydrofolate (THF) (Choi and Coloff 2019). Created with BioRender.com

The fully labeled 3-PG (i.e. m+3) is converted to fully labeled phosphoenolpyruvate (PEP) *via* 2-phosphoglycerate and the enzymes phosphoglycerate mutase and enolase, respectively. Lastly, pyruvate kinase drives the conversion of PEP to pyruvate. The transition from glycolysis to TCA cycle is mediated by the pyruvate decarboxylase producing fully labeled acetyl-CoA (m+2) from pyruvate. On the contrary, pyruvate can also undergo fermentation to lactate *via* lactate dehydrogenase-A (LDHA) in a reductive reaction (San-Millán and Brooks 2017). In this case, lactate will display the m+3 isotopologue obtained from the pyruvate carbon structure.

1.3.3.2. Analysis of the TCA cycle

Employment of [U-^{13}C] glucose results in continuous ^{13}C incorporation in TCA cycle intermediates after glycolytic breakdown. Expected labeling patterns from key metabolites of TCA are visualized for three consecutive rounds of the TCA cycle (Figure 7). After the breakdown of glucose during glycolysis and decarboxylation to $^{13}C_2$-acetyl-CoA *via* PDH, two ^{13}C-carbons enter the TCA cycle into the first round producing m+2 citric acid *via* citrate synthase in combination with unlabeled oxaloacetate (OAA). Upon isomerization of citrate to cis-aconitate and isocitrate, m+2 α-ketoglutarate is produced *via* isocitrate dehydrogenase

(IDH). Intermediates located downstream of α-ketoglutarate will also incorporate these two labeled carbons in their structure yielding isotopologues of m+2 (Figure 7 A). By the end of the first round, oxaloacetate incorporated two ^{13}C atoms.

Transitioning from round one to round two, m+2 labeled oxaloacetate now incorporates again $^{13}C_2$ labeled acetyl-CoA, yielding citric acid as M+4. Depending on the positional incorporation of the ^{13}C atoms from acetyl-CoA into citrate, the following metabolites will display either m+3 or m+4 isotopologues (Figure 7 B). In case of transaminase activity, glutamate will display identical labeling patterns as α-ketoglutarate, likewise for the amino acid aspartate which can be converted from OAA. By the beginning of the third round, citrate will display the m+5 isotopologue. In turn, oxidative decarboxylation of m+5 citrate by IDH will produce either fully labeled α-ketoglutarate (i.e. m+5) or the m+4 isotopologue. Fully labeled and m+4 isotopologues of succinate, fumarate and malate are a result of α-ketoglutarate dehydrogenase activity, decarboxylating the α-ketoglutarate (Figure 7 C).

Aside from these forward reactions, pyruvate anaplerosis allows fueling of the TCA cycle *via* the enzyme pyruvate carboxylase (PC) and can be followed as m+3 intermediates up-stream of succinate (i.e. fumarate, malate, oxaloacetate, and aspartate) (Figure 7 D). However, it should be noted that fumarate reductase activity can mask the PC activity by mirroring labeling patterns in succinate. In this cases the m+3 and m+4 isotopologue of α-ketoglutarate can provide additional reassurance, as the decarboxylation reaction from α-ketoglutarate to succinate is considered to be irreversible (Buescher et al. 2015). Furthermore, gluconeogenesis occurs *via* the enzymatic activity of PEPCK and uses oxaloacetate as substrate, thus producing labeling patterns (i.e. m+1, m+2 isotopologues) in PEP not typically anticipated upon incubation with [U-^{13}C] glucose tracer breakdown (i.e. m+3 isotopologue) (Gkiouli et al. 2019).

Although the TCA cycle in itself is a loop of metabolic reactions, intermediates can be exported to participate in the biosynthesis of other molecules like amino acids and lipid synthesis (DeBerardinis and Chandel 2016; Martínez-Reyes and Chandel 2020). For example, the combination of oxaloacetate with glutamate *via* the enzyme aspartate transaminase produces the amino acid aspartate, essential for the biosynthesis of ribonucleotides.

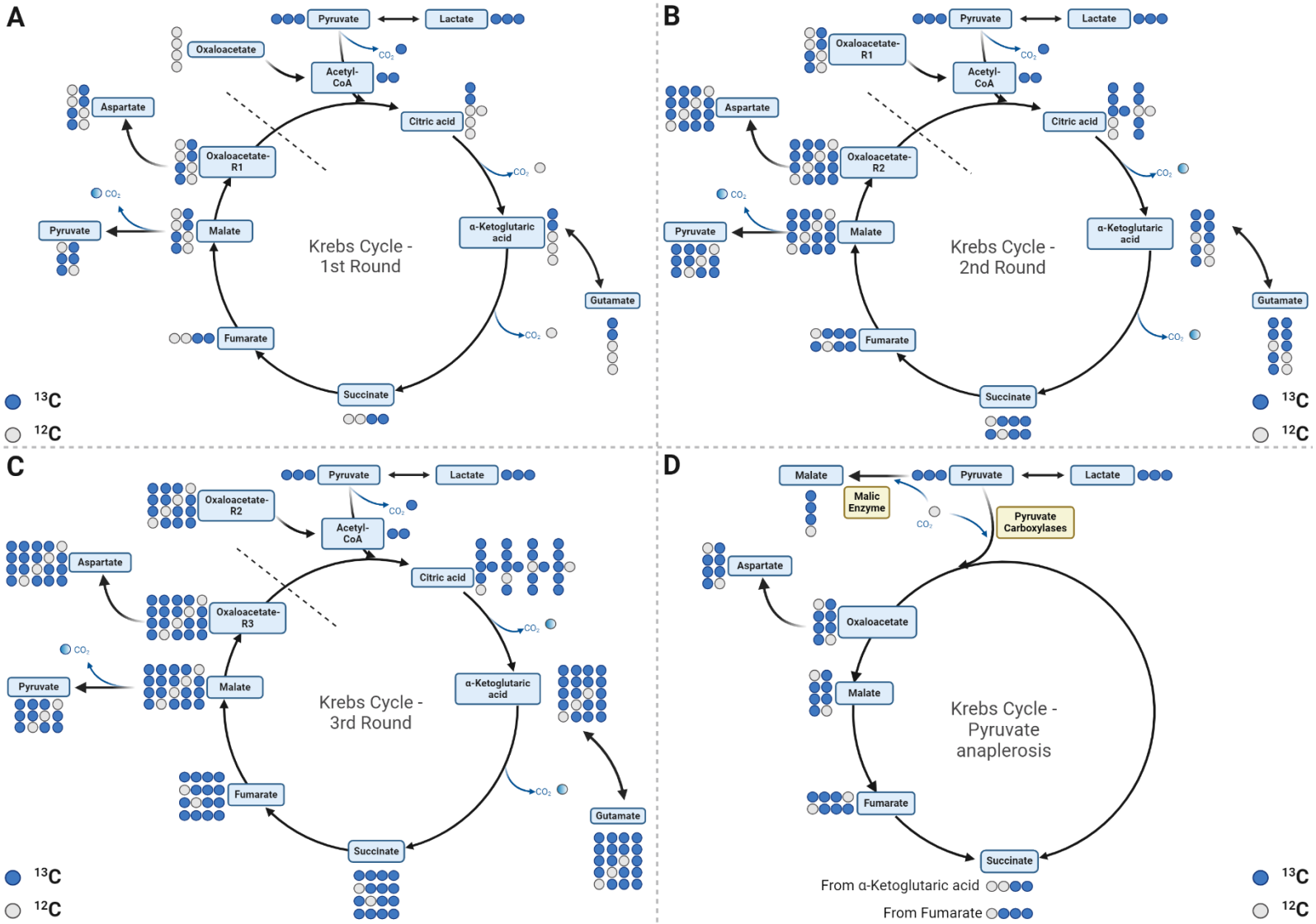

Figure 7: Schematic display of ^{13}C tracer incorporation into TCA cycle intermediates upon [U-^{13}C] glucose breakdown with three consecutive rounds of tracer incorporation (A through C) and pyruvate anaplerosis *via* pyruvate carboxylase activity (D). Adapted from Buescher et al. 2015. Created with BioRender.com

1.3.3.3. Glutamine anaplerosis of the TCA cycle via [U-^{13}C] glutamine

Anaplerosis of the TCA cycle can also occur *via* carbon contribution from the amino acid glutamine. In this case, glutaminolytic activity is best resolved by the employment of [U-^{13}C] glutamine. Here, glutamine is firstly converted to glutamate by glutaminase or branched-chain amino transferases (BCAT1/2) and subsequently to α-ketoglutarate *via* glutamate dehydrogenase (Choi and Coloff 2019; Errera and Greenstein 1949; Greenstein and Price 1949). This reaction is also reversible *via* transaminase enzymes. Correspondingly, uniformly labeled ^{13}C glutamine will produce a fully labeled m+5 isotopologue in α-ketoglutarate. Oxidative decarboxylation of fully labeled α-ketoglutarate is noticeable as m+4 isotopologues in downstream intermediates such as succinate, fumarate, malate, and aspartate (Figure 8).

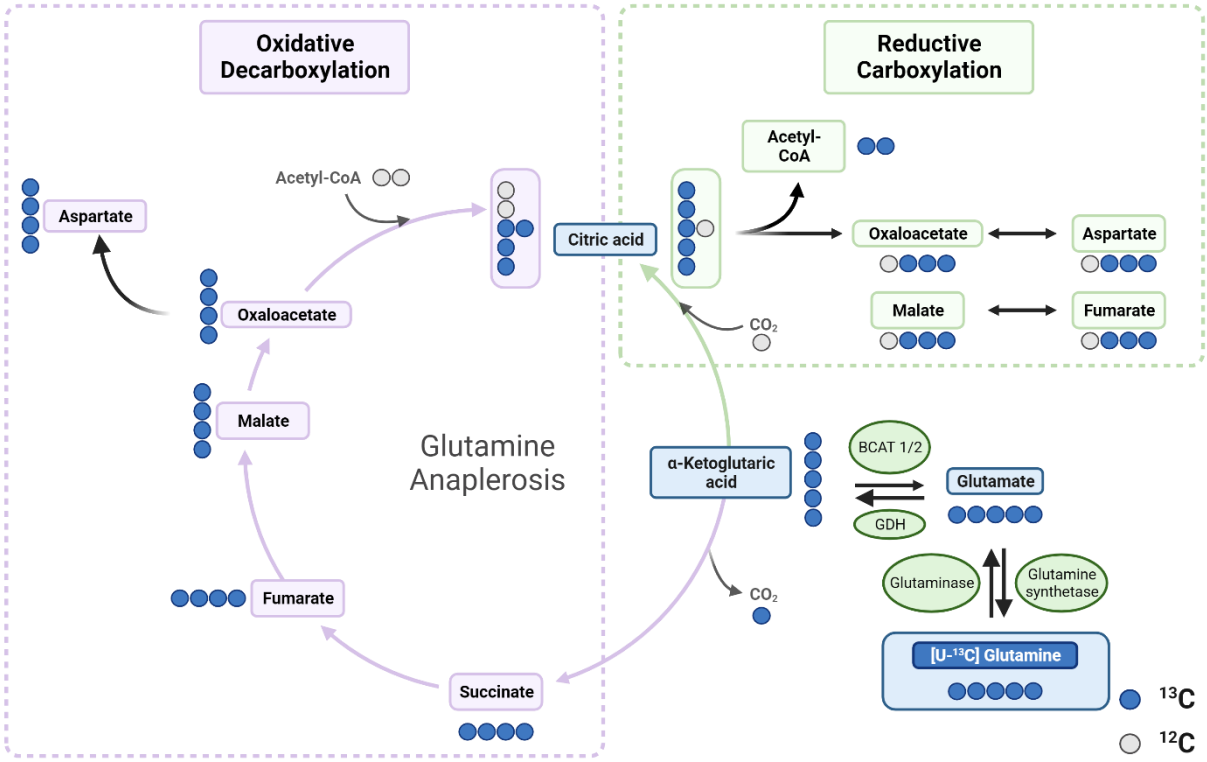

Figure 8: Glutamine anaplerosis from [U-^{13}C] glutamine and ^{13}C incorporation into TCA cycle intermediates by glutaminase and glutamate dehydrogenase (GDH) activity. Biosynthesis of glutamate from α-ketoglutarate *via* branched chain amino transferase activity (BCAT 1/2). *De novo* glutamine biosynthesis from glutamate by glutamine synthetase activity. Created with BioRender.com

On the contrary, reductive carboxylation activity *via* IDH can be monitored by the m+5 isotopologue in aconitate and citrate, respectively. This reaction is crucial under hypoxic conditions and impaired mitochondrial activity for the production of citrate and has been shown for tumor cells (Mullen et al. 2011; Wise et al. 2011). Furthermore, there are different isoforms of IDH, with IDH1 located in the cytosol and IDH2 in the mitochondria. Mutations within the IDH2 isoform lead to elevated formation of the oncometabolite 2-hydroxyglutarate (2-HG) directly from α-ketoglutarate. 2-HG that has been associated with the formation and progression of malignant gliomas (Dang et al. 2009). In turn, this activity also produces a

different labeling pattern in the intermediates upstream of citrate. Here, reductive carboxylation activity is noticeable as m+3 isotopologue in oxaloacetate, malate, fumarate, and aspartate.

1.3.3.4. Biosynthesis of ribonucleotides

Glycolysis and TCA cycle play a crucial role in the *de novo* biosynthesis of adenylated ribonucleotides. Purine nucleotides are synthesized from ribose-5-phosphate and require the amino acids glycine, aspartate, and glutamine in their formation process from phosphoribosyl pyrophosphate (PRPP) to inosine monophosphate (IMP) (Engelking 2015). Using [U-^{13}C] glucose those metabolite moieties can be explored by stable isotope metabolomics and assigned according to their respective carbon contribution in resulting purine rings (Figure 9). Typical labeling patterns will show the m+5 isotopologue as ribose moiety obtained from PRPP after pentose phosphate pathway. Further isotopologues m+6 or m+7 are a combination of the m+5 isotopologue and carbon contributions from TCA cycle derived CO_2, folate metabolism, or glycine. Labeling patterns resulting in isotopologues larger than m+8 are generally a combination of aforementioned isotopologue distributions.

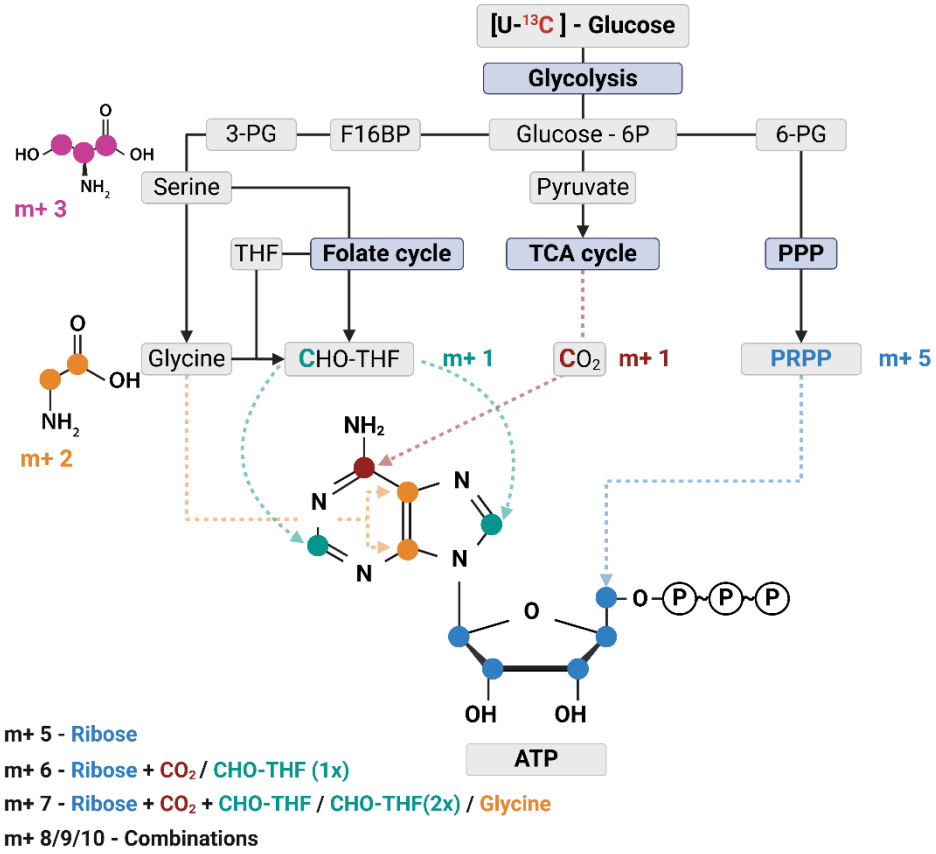

Figure 9: ^{13}C tracer incorporation from [U-^{13}C] glucose into purines, schematically illustrated by the adenylated ribonucleotide adenosine triphosphate (ATP). Created with BioRender.com

1.3.3.5. Biosynthesis of nucleotide sugars

The biosynthesis of the nucleotide sugars UDP-glucose and UDP-GlcNAc is also closely linked to the glycolysis and the ribonucleotide synthesis (Figure 5 and Figure 9). It is schematically displayed for UDP-glucose in Figure 10 to demonstrate [$^{13}C_6$] glucose derived carbon incorporation into different molecular subunits. These comprise the m+6 isotopologue derived from G1P and the m+11 isotopologue reflecting G1P + ribose (derived from PPP). The latter combines with orotate originating from aspartate to produce UTP with isotopologues m+5, m+6, m+7 and m+8. Within the final product UDP-glucose, the UTP-derived labels are reflected as the m+12, m+13 and m+14 isotopologues. Correspondingly, m+5, m+6 isotopologues and the sum of both (i.e. m+11) are distinctive isotopologues for these compounds. Nevertheless, amino acids (i.e. aspartate) also contribute to the formation of these compounds, thus yielding isotopologue patterns exceeding the m+12 isotopologue.

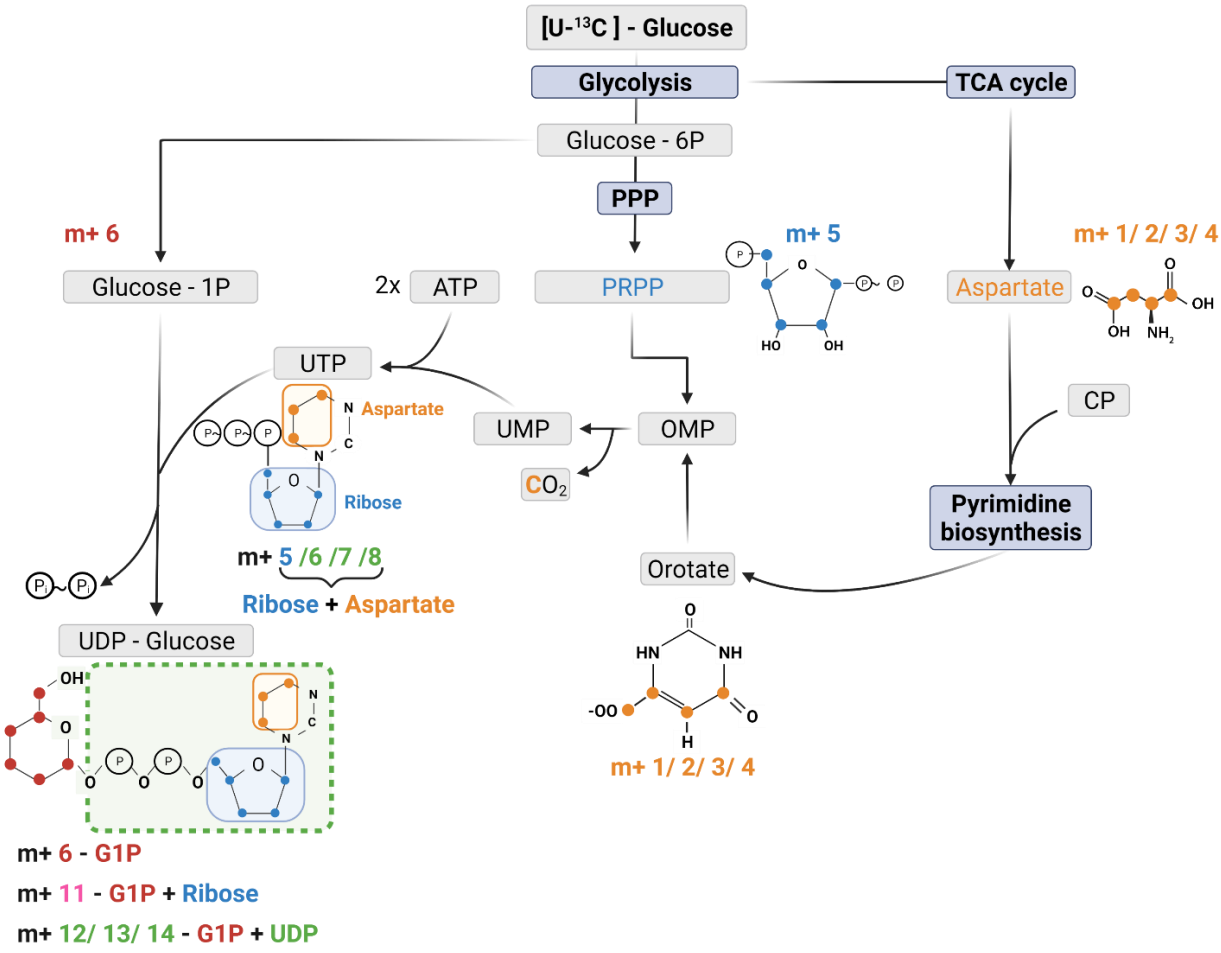

Figure 10: Schematic of UTP and UDP-glucose biosynthesis with contribution of the different precursors to tracer incorporation from $^{13}C_6$-glucose. Carbamoyl phosphate (CP); Orotidine 5'-monophosphate (OMP). Lackner et al. 2022

1.3.3.6. Biosynthesis of amino acids and adenylated ribonucleotides from [U-^{15}N] glutamine

Glutamine and glutamate are crucial hubs for the biosynthesis of further amino acids e.g. aspartate, serine and glycine. Alanine, proline, aspartate, and serine obtain nitrogen from aminotransferases using glutamate as substrate. Using [U-^{15}N] glutamine will consequently result in m+1 isotopologues in corresponding amino acids, provided they are *de novo* biosynthesized. In subsequent reactions, other amino acids like e.g., glycine and asparagine incorporate ^{15}N in their molecule structure from their labeled precursor. Specific pathway activities can be resolved in metabolites incorporating nitrogen from multiple amino acid sources like in adenylated ribonucleotides. Here, specific labeling patterns are distinctive for the incorporation of a unique amino acid. These nitrogen atoms are incorporated within the purine ring and originate from glutamine, glycine, and aspartate (Figure 11). An additional nitrogen atom is introduced by the adenylosuccinate synthetase that produces adenylosuccinate (AMPS) from inosine monophosphate (IMP) by reacting with the amino group of the aspartic acid (Engelking 2015). Depending on the amino acids involved and the velocity of nitrogen incorporation into these amino acids, labeling patterns can vary from m+1 isotopologues to m+5 isotopologues. However, it is worth mentioning, during the formation of purines, glutamine is the first amino acid to be incorporated within the purine ring, making it unlikely to produce m+1 isotopologues from other amino acids when using an [U-^{15}N] glutamine tracer.

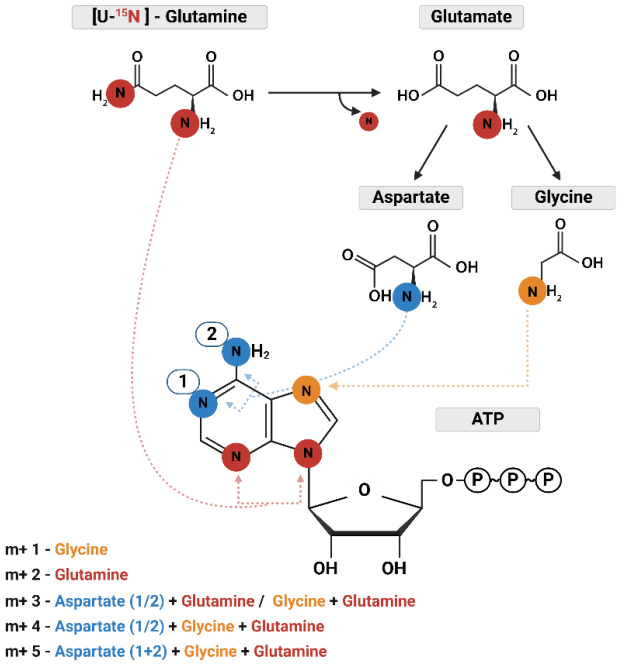

Figure 11: Schematic display of ^{15}N tracer incorporation into ATP from [U-^{15}N] glutamine. Created with BioRender.com

1.3.4 Steady state vs. dynamic labeling

Knowledge about labeling patterns provides a crucial insight into involved pathways and enzymatic activities. However, the metabolic state of an organism can have a substantial influence on these labeling pattern, as nutrient utilization varies over the cell cycle (Ahn et al. 2017). During metabolic steady state, however, uptake, excretion, and utilization of macromolecules are constant and do not significantly change over time (Leighty and Antoniewicz 2011; Wahl et al. 2008). For adherent cells, this metabolic steady state is typically reached during their exponential growth phase and referred to as pseudo-metabolic steady state. Here, corresponding metabolic rates are stable as long as the medium is not deprived of any substrates (Ahn and Antoniewicz 2011; Buescher et al. 2015). Employment of stable isotope tracers at the metabolic steady state, will lead to a constant increase of tracer incorporation into downstream intermediates until they reach isotopic steady state. At this point, the tracer incorporation into corresponding intermediates does not change over time. The major benefits of metabolites being at isotopic steady state is that labeling patterns are independent of corresponding metabolite levels and labeling patterns can be used for the calculation of further metabolic parameters. At isotopic steady state, nutrient contributions or fractional contribution (FC) from the tracer substrate in the formation of an intermediate can be calculated based on the enrichment of the intermediate, thus providing additional insights into contributing pathways (Buescher et al. 2015). This is particularly helpful when an intermediate is produced by only a limited number of nutrients e.g. within the TCA cycle. Here, harnessing multiple labeled substrates (e.g., [U-^{13}C] glucose or glutamine, respectively) allows the calculation of each corresponding FC and finally determination of the major contributing pathway (i.e. glycolysis or glutaminolysis). Aside from fractional contribution, isotopic steady state allows for the investigation of pathway activities, in a relative and a qualitative manner (Buescher et al. 2015). The ratio of specific isotopologues in intermediates of converging pathways can provide insights into corresponding pathway activities (Comte et al. 1997; Panchal et al. 2000). Qualitative assessment only considers isotopologues produced from specific pathways as it is the case for example in ribonucleotides, where the m+5 isotopologues originates from PRPP synthase activity when [U-^{13}C] glucose is employed. It is noteworthy, that turnover rates and pool sizes can significantly affect the time required to reach steady state and need to be considered when interpreting labeling patterns. While upon incubation with [U-^{13}C] glucose, glycolytic intermediates reach isotopic steady state within minutes, TCA cycle intermediates need hours (Lorkiewicz et al. 2019). The isotopic steady state might even be further delayed due to contributions from multiple pathways or even unlabeled sources. In turn, isotopic steady state is not always in scope for all intermediates within an experimental setting. The condition of isotopic non-steady state is referred to dynamic labeling and provides valuable insights into pathway activities. However, the interpretation of

dynamic labeling data is challenging. In contrast to isotopic steady state, labeling patterns are dependent on metabolite concentrations, pool sizes and labeling of metabolites located upstream of respective intermediates (Buescher et al. 2015). For the distinction of isotopic steady state from dynamic labeling, plotting of the fractional labeling over a time course is crucial (Lorkiewicz et al. 2019).

1.3.5 Non-targeted SIRM

Although targeted SIRM approaches allow for visual inspection, manual curation of peak areas as well as correction for isotope impurities and natural abundance, they require some knowledge about pathways and involved metabolites beforehand. This, however, leaves a large fraction of data unexplored which limits interpretation of metabolic effects including the generation of pathway models desired for more advanced metabolic flux analysis. In this regard, non-targeted tracer fate detection has emerged as a powerful tool that allows a system wide analysis of pathway activities and exploration of metabolic networks not anticipated by targeted SIRM (Creek et al. 2012; Hiller et al. 2010). Various software tools have been developed to enable detection and quantification of isotopologues in an untargeted fashion in stable isotope labeled datasets derived from high-resolution LC/MS experiments (Bueschl et al. 2017; Chokkathukalam et al. 2013; Hoffmann et al. 2018; Huang et al. 2014; Wang et al. 2022). It is worth mentioning that all of these tools require basic programming skills, where on the other hand a more user-friendly version of X^{13}CMS has been introduced with a browser based graphical user interface (Baumeister et al. 2018). Moreover, X^{13}CMS (Huang et al. 2014) extends the feature detection capabilities of XCMS, which is widely applied in label-free non-targeted metabolomics (Smith et al. 2006) to applications using isotopic labeled substrates. XCMS takes part in this routine by peak detection and retention time alignment. X^{13}CMS uses those detected features to iteratively check for enriched features by comparison against unlabeled reference samples and the introduced mass shift from the corresponding stable isotope. Subsequent comparison of two biological conditions (e.g. control vs. treatment) allows statistical evaluation of label incorporation and labeling patterns. Other XCMS based tools for untargeted tracer fate detection are geoRge and HiResTEC (Capellades et al. 2016; Hoffmann et al. 2018), that differ from X^{13}CMS in their isotopologue extraction procedure and further functionalities e.g. metabolite identification at MS1 level and time series evaluation. Although differences in corresponding algorithms and functionalities had already been elucidated (Capellades et al. 2016; Dange et al. 2020), enhancement of isotopic data by improved isotopologue extraction and grouping has just recently been investigated (Butin et al. 2022). Despite their differences, a shared, important feature of all tools is the selection of potential candidate structures that, once identified, can be readily implemented into targeted data analysis workflows, thus combining benefits of data curation in targeted SIRM with the

explorative characteristics of non-targeted SIRM. Such kind of data curation is expected to improve reproducibility of tracer experiments, an aspect that is equally important to well-established procedures for validation of spectral accuracy and precision of isotopic distribution (Heuillet et al. 2018; Schwaiger-Haber et al. 2019).

1.4. Sample preparation for metabolomics of mammalian cells

Conventional steady state metabolomics and stable isotope resolved metabolomics both answer important questions about metabolic activity or the metabolic state of a biological system. Nevertheless, reliable and reproducible readout of metabolic data is highly dependent on various factors during sample preparation and needs to consider the velocity of the metabolic reactions, the interference of unwanted intermediates and lastly the overall recovery of metabolites. In conventional monolayer cell culture, this procedure is comprised of multiple steps i.e. wash, detach, interrupt metabolic activity (i.e. quench), and metabolite extraction. The establishment of a reliable sample preparation workflow and the investigation of sample collection and storage procedures is a prerequisite to address issues that might compromise data interpretation from metabolomic analysis.

1.4.1 Overview of sample preparation methods

The metabolome is highly dynamic, with enzymatic reactions displaying turnover rates of just a few seconds (Sellick et al. 2009; Weibel et al. 1974). In turn, sample collection can be highly challenging and needs to be performed as quickly as possible to ensure an exact representation of the metabolic profile at a given experimental condition and time point. To avoid ongoing metabolic activity during the sampling process several approaches have been proposed to instantly interrupt metabolic activity. Early studies with yeast proposed a rapid quenching procedure with ultra-cool 60% MeOH (- 40 to - 50 °C) (Koning and van Dam 1992) and has since then led to a wide array of quenching procedures in mammalian cells (Table 2) and further optimization approaches of such (Kapoore et al. 2017; Purwaha et al. 2014; Sellick et al. 2010). Unlike yeasts or prokaryotes, mammalian cells are prone to quicker membrane disintegration due to the lack of a protective cell wall, thus leading to a loss of metabolites under harsh quenching conditions (Kapoore et al. 2017). Employment of buffering agents and salts in the extraction solvent has been shown to circumvent this issue (Kapoore et al. 2017; Purwaha et al. 2014; Sellick et al. 2010), wherein wash procedures can help to alleviate osmotic shock and maintain membrane integrity, while at the same time removing unwanted excreted intermediates (Dietmair et al. 2010; Kapoore et al. 2017). Additionally, the extraction solvent drives the selectivity of extracted compounds, where e.g. MeOH is more suitable for polar compounds and chloroform for hydrophobic compounds like unpolar lipids. It is noteworthy that sample preparation of adherent cells is particularly challenging, as cell harvest

is a time-consuming procedure. Here, trypsination has been shown to deteriorate the metabolic coverage thus pushing towards simultaneous quenching and extraction methods for the determination of intracellular metabolites (Teng et al. 2009).

Table 2: Sample preparation procedures for metabolomics in mammalian cell culture

Investigated Pathways	Wash	Quench	Extraction solvent	Reference
Glycolysis, TCA, amino acids, fatty acids	-	60% MeOH with 0.85% AMBIC	MeOH, EtOH, KOH, PCA, MeOH/$CHCl_3$	(Sellick et al. 2010)
Glycolysis, TCA	Water (37 °C)	LN_2	MeOH/$CHCl_3$	(Lorenz et al. 2011)
Untargeted	0.9% NaCl (RT)	50% MeOH (- 20 °C)	50% MeOH (-20 °C), $CHCl_3$	(Sapcariu et al. 2014; Weindl et al. 2016)
Glycolysis, TCA, PPP	0.9% NaCl (4 °C)	0.9% NaCl (4 °C)	MeOH/H_2O/$CHCl_3$	(Peterson et al. 2016)
Glycolysis, TCA, amino acids	1x PBS, 0.9% NaCl *	LN_2	ACN/IPA/H_2O (3:3:2, - 20 °C)	(Lanning et al. 2017)
Untargeted	1x PBS (37 °C)	LN_2 bath and MeOH (-20 °C)	MeOH/ACN/H_2O (- 20 °C)	(Puchalska et al. 2018)
Purines	-	MeOH/H_2O (8:2)	MeOH/H_2O (8:2)	(Nybo and Lamberts 2019)

** Cells were detached by trypsination prior wash procedure. AMBIC, ammonium bicarbonate; KOH, potassium hydroxide; PCA, perchloric acid*

1.4.2 Evaluation of the quenching efficiency

While broad metabolite and pathway coverage is useful to drive the development of hypotheses towards a scientific question, determination of metabolites and metabolite levels only yields limited information regarding the performance of a sample preparation procedure, especially considering the high turnover rates of some enzymatic reactions. Adenylated ribonucleotides are never excreted under physiological conditions and corresponding levels are constant across cells (Kapoore et al. 2017). Furthermore, turnover rates of 1-2 seconds make it an appealing parameter for the assessment of the quenching efficiency (Sellick et al. 2009). Here, the adenylated energy charge (i.e. AEC or EC, (Atkinson and Walton 1967) is a concentration independent and intrinsic ratio of AMP, ADP and ATP levels (Equation 1) that gives an insight into a cell's energy state and has been used as a quenching efficiency readout (Faijes et al. 2007; Ritter et al. 2008; Sellick et al. 2009).

Equation 1: Calculation of energy charge from levels of adenylated ribonucleotides (Atkinson D. E. & Walson G. 1967)

$$EC = \frac{ATP + \frac{1}{2}ADP}{(AMP + ADP + ATP)}$$

The energy charge corresponds to values between zero and one, wherein zero displays a fully discharged system with no measurable levels of ATP or ADP. On the contrary, an EC of one corresponds to the sole presence of ATP. In proliferating cells, the energy charge has been shown to be typically between 0.8 and 0.9 (Chapman et al. 1971), whereas under metabolic stress it can drop to less than 0.2 within one minute (Talwalkar and Lester 1973).

1.4.3 Normalization approaches in metabolomics

In quantitative metabolomics, readouts (i.e. signal intensities) are adjusted to a shared parameter that takes variations from technical/analytical (e.g. sample preparation, matrix effects) or biological (e.g. cell density, sample weight) origin into account. Normalization can be applied either pre-analytical, by adjusting for instance the sample volume based on intrinsic parameters like cell count, or post-analytical, by normalizing to parameters such as signal intensities (Wu and Li 2016).

In targeted approaches, analytical variations are compensated by the usage of an internal standard. Best practice involves spiking of the sample prior analysis with a known concentration of the stable isotope labeled version (e.g. ^{13}C, ^{15}N, D) of the analyte or compounds of its class and subsequent analysis *via* the so called isotope dilution mass spectrometry (IDMS) (Sargent et al. 2002) procedure, in which the intensity ratio of the unlabeled analyte is compared to the labeled molecule. When stable isotope labeled analytes are not available, spiking of exogenous compounds can account for corresponding variations (Silva et al. 2013; Wu and Li 2016). Furthermore, biological variations from cell culture experiments are taken into consideration by monitoring other intrinsic parameters like cell count, dry weight, protein, or DNA content (Munger et al. 2006; Muschet et al. 2016; Wu and Li 2016). It is worth mentioning that these intrinsic parameters also display certain limitations in their applications. Normalization to protein content at low cell numbers resulted in larger variations, while normalization to DNA concentration is time-consuming (Silva et al. 2013). Although methods with higher throughput have been proposed (Muschet et al. 2016).

On the contrary, absolute quantification in untargeted metabolomics is impossible due to the large fraction of unknowns within the sample excluding the possibility of performing signal correction to internal standards. Nevertheless, several normalization approaches have been proposed for relative quantification, in which the sum normalization (i.e. total ion count, TIC) is often employed (Deininger et al. 2011; Ejigu et al. 2013). More sophisticated approaches employ spiking of fully stable isotope-labeled cell extracts in order to compensate for analytical variations (Bueschl et al. 2014; Weindl et al. 2015).

Labeling patterns in targeted SIRM at isotopic steady state are independent of metabolite levels and require only correction for natural abundance. In untargeted SIRM, correction for

natural abundance is impossible due to the lack of structural information or missing compound identification. This leads to difficulties in data interpretation especially in features with only minor tracer incorporation (Llufrio et al. 2019).

1.5. Aims of this dissertation

Metabolomics has become an important tool for the assessment of drug response phenotypes and the identification of metabolic signatures associated with altered metabolism in cancer. However, conventional steady state metabolomics approaches provide a rather static picture on the metabolome thereby limiting the translation into biologically meaningful mechanisms. In this context, stable isotope-resolved metabolomics (SIRM) analysis represents a promising approach to qualitatively and quantitatively assess the activity of metabolic networks in cell culture.

The primary objective of this work was to establish an analytical platform to enable SIRM as a test system to assess membrane-associated drug targets in cancer *in vitro*. This comprised all aspects of the analytical workflow including cell line cultivation, optimization of drug dosing, cell feeding with stable labeled isotopic precursors, optimization of sample preparation and mass spectrometric analysis. As part of the workflow establishment, another goal was to set up a data analysis routine in the R software environment, enabling pre-processing, quality control, statistical analysis, and visualization of the acquired SIRM data. A further part of the work was planned to deal with the functional characterization of two breast cancer cell lines (MDA-MB-468 and MDA-MB-231) followed by optimization of experimental conditions for SIRM experiments including assessment of metabolism quenching, washing, sample storage and normalization. As a proof-of-concept application, the workflow was demonstrated in MDA-MB-468 cells by using [U-^{13}C] glucose to investigate metabolic pathway activities in the absence and presence of the selective PI3Kβ inhibitor AZD8186. An important aspect of the workflow establishment aimed at combining targeted isotopologue feature extraction with the non-targeted X^{13}CMS routine. This strategy was chosen to enable monitoring of changes related to PI3Kβ inhibition in known pathways as well as the discovery of hitherto unknown metabolic alterations.

Based on the established workflow a further aim was to investigate AZD8186-induced metabolic alterations of isotope enrichment metabolites within metabolic pathways downstream of pyruvate, using [U-^{15}N] and [U-^{13}C,^{15}N] glutamine as tracers. Finally, differences in [U-^{13}C] glucose tracer incorporation were planned to be assessed in two different PTEN-null breast cancer cell lines (HCC70 and MDA-MB-468) to demonstrate isotope-enriched features that were altered in the presence of AZD8186 both collectively and uniquely for each cell line.

2. Materials and Methods

2.1. Materials

2.1.1 Computer software

Table 3: List of software used, packages and databases

Software & packages	Vendor/developer
Gen5 (version 3.08.01)	Agilent Technologies, Waldbronn, Germany
GraphPad Prism® 5.00 (version 5.04)	GraphPad Software, San Diego, USA
Microsoft Office 2016	Microsoft, Redmond, WA, USA
Acquisition and data analysis software for mass spectrometry	Agilent Technologies, Waldbronn, Germany
Acquisition software:	
Mass Hunter Workstation Data Acquisition (QTOF 6550, version B.08.00, build 8.00.8058.3 SP1)	
Mass Hunter Workstation Data Acquisition (QQQ 6400, version B.08.00, build 8.00.80233.8 SP1 HF2)	
Mass Hunter Workstation Data Acquisition (GC-MSD, version 10.0,service release 1, build 10.0.384.1)	
Data analysis software:	
MassHunter PCDL Manager (version B.07.00, build 7024.35, service pack 2)	
MassHunter Pathway to PCDL (version B.07.00, build 19)	
MassHunter Profinder (version 10.0, build 10.0.10062.0)	
MassHunter Qualitative Analysis for QTOF (version B.07.00, Agilent Technologies)	
MassHunter Quantitative Analysis for QQQ (version B.08.00, build 8.0.598.0)	
MassHunter Quantitative Analysis for GC-MS (version 10.2, build 10.2.733.8)	
Seahorse XF analyzer	Agilent Technologies, Waldbronn, Germany
Cell Imaging (version 1.1.0.11)	
Wave (version 2.6.3.)	
Statistical analysis and visualization with R	
eulerr (version 6.1.1)	(Larsson J 2021)
fuzzyjoin (version 0.1.6)	(Robinson 2020)
RStudio (version 2021.9.0.351, Ghost Orchid)	(R Core Team 2021)
stats (version 4.0.3)	(R Core Team 2021)
tidyverse (version 1.3.1)	(Wickham et al. 2019)
X^{13}CMS (version 1.4)	(Huang et al. 2014)

2.1.2 Laboratory equipment

Table 4: List of laboratory equipment

Equipment	Vendor
CCD camera, STELLA3200	Raytest, Straubenhardt, Germany
Cell imaging reader, Cytation 1	Agilent Technologies, Waldbronn, Germany
Centrifuge:	
Eppendorf, type: 5424R	Eppendorf, Hamburg, Germany
Rotina, type: 380R	Hettich, Tuttlingen, Germany
CO_2 incubator, New Brunswick Galaxy 170S	Eppendorf, Hamburg, Germany
Freezing container, “Mr. Frosty“	Nalgene Nunc, Rochester, New York, USA
Laboratory balance, XS802S	Mettler Toledo, Gießen, Germany
Microplate reader, Enspire™ 2300	PerkinElmer, Waltham, USA
Non-CO_2 incubator, Modell B 28	Binder GmbH, Tuttlingen, Germany
Pipettes: 0.1-2.5 µl 0.5-10 µl 10-100 µl 20–200 µl 100–1000 µl 500-5000 µl Multipette® E3	Eppendorf, Hamburg, Germany
Qubit 2.0 fluorometer	Thermo Fisher Scientific GmbH, Waltham, USA
Rotational Vacuum Concentrator RVC 2-25CDplus	Martin Christ Gefriertrocknungsanlagen GmbH, Osterode, Germany
Seahorse XFe96 Analyzer	Agilent Technologies, Waldbronn, Germany
Sonication, homogenisator Sonoplus	Bandelin Elektronik, Berlin, Germany
Vortex (Reax top)	Heidolph Instruments, Schwabach, Germany
Western blot, Mini-PROTEAN® Tetra Vertical Electrophoresis & Wet Blot Cell	BIO-RAD, Hercules, CA, USA)
Mass spectrometry	Agilent Technologies, Waldbronn, Germany
GC-MS: 5975C inert XL coupled to an Agilent GC 7890A LC-MS/MS: 1200 HPLC System equipped with column oven, autosampler, degasser and binary pump Agilent 6460 triple quadrupole mass spectrometer LC-QTOF-MS (SIRM): 1290 Infinity UHPLC System equipped with column oven, autosampler, degasser and binary pump 6550 iFunnel quadrupole time of flight mass spectrometer	

2.1.3 Chemicals and reagents

Table 5: List of chemicals and reagents

Reagents	Vendor
ß-mercaptoethanol	Sigma Aldrich, München, Germany
[U-^{13}C]-glucose [99%]	EURISO-TOP GmbH, Saarbrücken, Germany
[U-^{15}N]-glutamine [98%]	EURISO-TOP GmbH, Saarbrücken, Germany
[U-^{13}C,^{15}N] glutamine [99%]	EURISO-TOP GmbH, Saarbrücken, Germany
0.1 mM HP-0321 (hexamethoxyphosphazine) dissolved in acetonitrile	Agilent Technologies, Waldbronn, Germany
2-deoxy-glucose (2-DG)	Agilent Technologies, Waldbronn, Germany
2-propanol	Carl Roth GmbH, Karlsruhe, Germany
Acrylamide/bis solution (30%)	Bio-Rad Laboratories Inc., Hercules, USA
Ammonium persulfate (APS)	Bio-Rad Laboratories Inc., Hercules, USA
AZD8186	Biomol GmbH, Hamburg, Germany
Bovine serum albumin (BSA)	Sigma Aldrich, München, Germany
Bromophenol blue	Sigma Aldrich, München, Germany
Ethanol absolute for analysis	Merck KGaA, Darmstadt, Germany
Ethylenediaminetetraacetic acid (EDTA), disodium salt dihydrate	Sigma-Aldrich, Taufkirchen, Germany
D-glucose	Carl Roth GmbH, Karlsruhe, Germany
Dimethyl sulfoxide suitable for hybridoma, sterile	Sigma-Aldrich, Taufkirchen, Germany
Dulbecco´s phosphate buffered saline (1x PBS)	Biozym Scientific GmbH, Hessisch Oldendorf, Germany
Fetal bovine serum – classic, Lot: BCBT 2317	Sigma-Aldrich, Taufkirchen, Germany
Fetal bovine serum – supreme, Lot: P190303	PAN-Biotech GmbH, Aidenbach, Germany
Gibco™ RPMI 1640 Medium, without glucose	Fisher Scientific GmbH, Schwerte, Germany
Glycine	Merck, Darmstadt, Germany
Glycerol	Merck, Darmstadt, Germany
InfinityLab Deactivator Additive	Agilent Technologies, Waldbronn, Germany
Hoechst 33342	Agilent Technologies, Waldbronn, Germany
KCl	Sigma-Aldrich, Taufkirchen, Germany
LC/MS calibration standard for ESI-TOF	Agilent Technologies, Waldbronn, Germany
LC-MS grade ammonium acetate (AmAc)	Sigma-Aldrich, Taufkirchen, Germany
L-glutamine (200 mM)	Biozym Scientific GmbH, Hessisch Oldendorf, Germany
NaCl	Sigma-Aldrich, Taufkirchen, Germany
N-Methyl-N-tert-butyldimethylsilyltrifluoracetamid (MBDSTFA)	Macherey-NageL GmbH & Co. KG, Düren, Germany
N,N-Dimethylformamid- (DMF)	Sigma-Aldrich, Taufkirchen, Germany
N,O-bis(trimethylsilyl)trifluoracetamide (BSTFA)	Sigma-Aldrich, Taufkirchen, Germany
Octylammoniumacetate (OAA)	Synthesized in-house
O-Methylhydroxylamin –hydrochlorid (MOX)	Merck KGaA, Darmstadt, Germany
Phenylmethanesulfonyl Fluoride (PMSF)	Cell Signaling Technology, Danvers, USA
Pierce™ BCA Protein Assay Kit	Thermo Fisher Scientific GmbH, Waltham, USA

Reagents	Vendor
Ponceau S solution	Sigma-Aldrich, Taufkirchen, Germany
Ultra-pure water was obtained from a Milli-Q system, referenced in this work as “water”	Merck Millipore, Burlington, USA
Pyridine	Sigma-Aldrich, Taufkirchen, Germany
Radioimmunoprecipitation Assay (RIPA) Buffer (10X)	Cell Signaling Technology, Danvers, USA
Restore™ Western Blot Stripping Buffer	Thermo Fisher Scientific GmbH, Waltham, USA
ROT/AA	Agilent Technologies, Waldbronn, Germany
Roti® Stock, Sodium Dodecyl Sulfate (SDS) (20%)	Carl Roth GmbH, Karlsruhe, Germany
RPMI 1640 without L-glutamine	Biozym Scientific GmbH, Hessisch Oldendorf, Germany
Skim milk powder	Sigma-Aldrich, Taufkirchen, Germany
Spectra™ Multicolor Broad Range Protein Ladder	Thermo Fisher Scientific GmbH, Waltham, USA
SuperSignal™ West Dura Extended Duration Substrate	Thermo Fisher Scientific GmbH, Waltham, USA
StemPro™ Accutase™ Cell Dissociation Reagent	Thermo Fisher Scientific GmbH, Waltham, USA
TEMED	Carl Roth GmbH, Karlsruhe, Germany
Tris-Base	Carl Roth GmbH, Karlsruhe, Germany
Tris-HCl	Sigma-Aldrich, Taufkirchen, Germany
Tween®-20	Merck, Darmstadt, Germany
Trypan blue solution (0.4%)	Merck KGaA, Darmstadt, Germany
Ultra LC-MS grade acetonitrile (ACN)	Carl Roth GmbH & Co KG, Karlsruhe, Germany
Ultra LC-MS grade methanol (MeOH)	Carl Roth GmbH & Co KG, Karlsruhe, Germany
XF RPMI medium, pH 7.4	Agilent Technologies, Waldbronn, Germany
XF 1.0 M glucose solution	Agilent Technologies, Waldbronn, Germany
XF 100 mM pyruvate solution	Agilent Technologies, Waldbronn, Germany
XF 200 mM glutamine solution	Agilent Technologies, Waldbronn, Germany

2.1.4 Materials for cell line cultivation and characterization

2.1.4.1. Employed tumor cell lines

Table 6: List of used tumor cell lines

Cell line	Entity	Vendor
HCC-70	Breast cancer (TNBC, PTEN-null)	ATCC, CRL-2315
MDA-MB-231*	Breast cancer (TNBC, PTEN Wild type (WT))	ATCC, HTB-26; Obtained in-house, AG Hiltrud Brauch/ Werner Schroth
MDA-MB-468*	Breast cancer (TNBC, PTEN-null)	ATCC, HTB-132; Obtained in-house, AG Hiltrud Brauch/ Werner Schroth

** STR analysis performed; HCC-70 newly obtained from vendor.*

2.1.4.2. Cell culture consumables

Table 7: List of cell culture consumables

Consumables	Vendor
1,8 ml Cryo Tube TM	Nalgene Nunc, Rochester, New York, USA
C-Chip, Neubauer Improved Disposable Counting Chamber, 50 pieces	Science Services GmbH, Munich, Germany
Cell culture flasks, Nunc™ (25 cm², 80 cm²)	VWR International GmbH, Darmstadt, Germany
Cell culture multiwell plates (6- well plates), CELLSTAR®	VWR International GmbH, Darmstadt, Germany
Cell scraper, blade width 20 mm, total length 25 cm	VWR International GmbH, Darmstadt, Germany
PowerPlex® 21 System	Promega, Madison, USA
PCR tubes, 0.2 ml	Fisher Scientific GmbH, Schwerte, Germany
Syringe filter (sterile, 0.22 µm, cellulose acetate)	VWR International GmbH, Darmstadt, Germany

2.1.5 Materials for mass spectrometry

2.1.5.1. Employed GC and HPLC columns

Table 8: List of GC and HPLC columns

Column	Dimensions	Method	Vendor
GC column			
J&W DB-5MS column	25 m, inner diameter 0.20 mm, film thickness 0.33 µm	Quantitative: TCA cycle intermediates, glucose, amino acids, and cholesterol	Agilent Technologies, Waldbronn, Germany
HPLC columns			
BioBasic™ AX Polyethyleneimine Mixed Mode column	50 mm x 2.1 mm, 5 µm particle size	Quantitative: Adenylated ribonucleotides	Thermo Fisher Scientific GmbH, Waltham, USA
Synergi™ Hydro-RP 80 Å column	150 x 2 mm, 4 µm particle size	Quantitative: Lactate and glycolytic intermediates	Phenomenex LTD, Aschaffenburg, Germany
InfinityLab Poroshell 120 HILIC-Z column	100 mm x 2.1mm, 2.7 µm particle size, peek lined	Qualitative: Metabolites from SIRM workflow	Agilent Technologies, Waldbronn, Germany
UHPLC Guard for Poroshell 120 HILIC-Z	5 mm x 2.1 mm, 2.7 µM particle size		Agilent Technologies, Waldbronn, Germany

2.1.5.2. Standard compounds and stable isotope labeled internal standards

Unless otherwise indicated, substances were LC-MS grade, dissolved in ultra-pure water and obtained from Sigma-Aldrich, Taufkirchen, Germany.

Table 9: List of standard compounds used for mass spectrometric analysis

Compound	Sum formula	Stock concentration	Vendor
Algal [U-^{13}C,^{15}N]-amino acid mixture*		10 mg/ml	Campro Scientific GmbH, Berlin, Germany
[U-^{13}C,^{15}N]-glycine (Mol% 10.8)	$^{13}C_2H_5{}^{15}NO_2$		
[U-^{13}C,^{15}N]-alanine (Mol% 14.0)	$^{13}C_3H_7{}^{15}NO_2$		
[U-^{13}C,^{15}N]-serine (Mol% 4.4)	$^{13}C_3H_7{}^{15}NO_3$		
[U-^{13}C,^{15}N]-proline (Mol% 4.7)	$^{13}C_5H_9{}^{15}NO_2$		
[U-^{13}C,^{15}N]-valine (Mol% 8.1)	$^{13}C_5H_{11}{}^{15}NO_2$		
[U-^{13}C,^{15}N]-threonine (Mol% 6.2)	$^{13}C_4H_9{}^{15}NO_3$		
[U-^{13}C,^{15}N]-cysteine (Mol% 0.4)	$^{13}C_3H_7{}^{15}NO_2S$		
[U-^{13}C,^{15}N]-isoleucine (Mol% 5.8)	$^{13}C_6H_{13}{}^{15}NO_2$		
[U-^{13}C,^{15}N]-leucine (Mol% 9.6)	$^{13}C_6H_{13}{}^{15}NO_2$		
[U-^{13}C,^{15}N]-aspartate (Mol% 10.2)	$^{13}C_4H_7{}^{15}NO_4$		

Compound	Sum formula	Stock concentration	Vendor
[U-^{13}C,^{15}N]-lysine (Mol% 3.9)	$^{13}C_6H_{14}{}^{15}N_2O_2$		
[U-^{13}C,^{15}N]-glutamate (Mol% 10.1)	$^{13}C_5H_9{}^{15}NO_4$		
[U-^{13}C,^{15}N]-methionine (Mol% 2.7)	$^{13}C_5H_{11}{}^{15}NO_2S$		
[U-^{13}C,^{15}N]-histidine (Mol% 0.9)	$^{13}C_6H_9{}^{15}N_3O_2$		
[U-^{13}C,^{15}N]-phenylalanine (Mol% 4.4)	$^{13}C_9H_{11}{}^{15}NO_2$		
[U-^{13}C,^{15}N]-arginine (Mol% 2.9)	$^{13}C_6H_{14}{}^{15}N_4O_2$		
[U-^{13}C,^{15}N]-tyrosine (Mol% 0.8)	$^{13}C_9H_{11}{}^{15}NO_3$		
Amino acid standard mixture *		2.5 µmol/ml in 0.1 N HCL	
Glycine	$C_2H_5NO_2$		*
Alanine	$C_3H_7NO_2$		*
Serine	$C_3H_7NO_3$		*
Proline	$C_5H_9NO_2$		*
Valine	$C_5H_{11}NO_2$		*
Threonine	$C_4H_9NO_3$		*
Iso-/Leucine	$C_6H_{13}NO_2$		*
Aspartate	$C_4H_7NO_4$		*
Lysine	$C_6H_{14}N_2O_2$		*
Glutamate	$C_5H_9NO_4$		*
Methionine	$C_5H_{11}NO_2S$		*
Histidine	$C_6H_9N_3O_2$		
Phenylalanine	$C_9H_{11}NO_2$		*
Arginine	$C_6H_{14}N_4O_2$		*
Tyrosine	$C_9H_{11}NO_3$		*
Cystine	$C_6H_{12}N_2O_4S_2$	1.25 µmol/ml	
Single substances			
Urea	CH_4N_2O	2 mg/ml	Serva GmbH, Heidelberg, Germany
[U-^{13}C,^{15}N]-urea	$^{13}CH_4{}^{15}N_2O$	1 mg/ml	
Pyruvate	$C_3H_4O_3$	2 mg/ml	
[U-^{13}C]-pyruvate	$^{13}C_3H_4O_3$	1 mg/ml	Euriso-TOP GmbH, Saarbrücken, Germany
Lactate	$C_3H_6O_3$	1 mg/ml	
[U-^{13}C]-lactate	$^{13}C_3H_6O_3$	1 mg/ml	
Fumarate	$C_4H_4O_4$	1 mg/ml	
[U-^{13}C]-fumarate	$^{13}C_4H_4O_4$	1 mg/ml	Euriso-TOP GmbH, Saarbrücken, Germany
Succinate	$C_4H_6O_4$	1 mg/ml	
Asparagine	$C_4H_8N_2O_3$	1 mg/ml	
[U-^{13}C]-asparagine	$^{13}C_4H_8N_2O_3$	2 mg/ml	

Compound	Sum formula	Stock concentration	Vendor
Ornithine	$C_5H_{12}N_2O_2$	1 mg/ml	
D_7-ornithine	$C_5H_5{}^2H_7N_2O_2$	1 mg/ml	CDN Isotopes, Quebec, Canada
Malate	$C_4H_6O_5$	2 mg/ml	
[U-^{13}C]-malate	$^{13}C_4H_6O_5$	1 mg/ml	Euriso-TOP GmbH, Saarbrücken, Germany
α-ketoglutarate	$C_5H_6O_5$	2 mg/ml	
[U-^{13}C]-α-ketoglutarate	$^{13}C_5H_6O_5$	1 mg/ml	Euriso-TOP GmbH, Saarbrücken, Germany
Glutamine	$C_5H_{10}N_2O_3$	2 mg/ml	
[U-^{13}C,^{15}N]-glutamine	$^{13}C_5H_{10}N_2O_3$	1 mg/ml	Euriso-TOP GmbH, Saarbrücken, Germany
2-hydroxyglutarate	$C_5H_8O_5$	1 mg/ml	
Phosphoenolpyruvate (PEP)	$C_3H_5O_6P$	1 mg/ml	
[U-^{13}C]-PEP	$^{13}C_3H_5O_6P$	10 mg/ml	In-house synthesis
Aconitate	$C_6H_6O_6$	2 mg/ml	
Glucose	$C_6H_{12}O_6$	1 mg/ml	
D_2-glucose	$C_6H_{10}{}^2H_2O_6$	2 mg/ml	
3-phosphoglycerate (3-PG)	$C_3H_7O_7P$	1 mg/ml	
[U-^{13}C]-2-phosphoglycerate ([U-^{13}C]-2-PG)	$^{13}C_3H_7O_7P$	10 mg/ml	In-house synthesis
Citrate	$C_6H_8O_7$	4 mg/ml	
D_4-citrate	$C_6H_4{}^2H_4O_7$	2 mg/ml	
Isocitrate	$C_6H_8O_7$	2 mg/ml	
Tryptophan	$C_{11}H_{12}N_2O_2$	1 mg/ml	
D_5-trypthophan	$C_{11}H_7{}^2H_5N_2O_2$	2 mg/ml	Euriso-TOP GmbH, Saarbrücken, Germany
Ribose 5-phosphate	$C_5H_{11}O_8P$	1 mg/ml	
D-Ribulose 5-phosphate	$C_5H_{11}O_8P$	1 mg/ml	
D-fructose 6-phosphate (F6P)	$C_6H_{13}O_9P$	1 mg/ml	
Glucose 1-phosphate (G1P)	$C_6H_{13}O_9P$	1 mg/ml	
[U-^{13}C]-G1P	$^{13}C_6H_{13}O_9P$	1 mg/ml	Omicron Biochemicals, Inc., South Bend, USA
Glucose 6-phosphate (G6P)	$C_6H_{13}O_9P$	1 mg/ml	
[U-^{13}C]-G6P	$^{13}C_6H_{13}O_9P$	1.33 mg/ml	In-house synthesis
6-Phosphogluconic acid (6-PG)	$C_6H_{13}O_{10}P$	1 mg/ml	
[U-^{13}C]-6-PG	$^{13}C_6H_{13}O_{10}P$	5 mg/ml	In-house synthesis
Sedoheptulose 7-phosphate (Sed 7P)	$C_7H_{15}O_{10}P$	1 mg/ml	Glycoteam GmbH, Hamburg, Germany
Fructose-1,6-BP (F16BP)	$C_6H_{14}O_{12}P_2$	1 mg/ml	
[U-^{13}C]-F16BP	$^{13}C_6H_{14}O_{12}P_2$	1 mg/ml	Omicron Biochemicals, Inc., South Bend, USA
Adenosine monophosphate (AMP)	$C_{10}H_{14}N_5O_7P$	1 mg/ml	
[U-^{13}C,^{15}N]-AMP	$^{13}C_{10}H_{14}{}^{15}N_5O_7P$	1 mg/	
Adenosine diphosphate (ADP)	$C_{10}H_{15}N_5O_{10}P_2$	1 mg/ml	

Compound	Sum formula	Stock concentration	Vendor
Adenosine triphosphate (ATP)	$C_{10}H_{16}N_5O_{13}P_3$	1 mg/ml	
[U-^{13}C]-ATP	$^{13}C_{10}H_{16}{}^{15}N_5O_{13}P_3$	100 mM in 5 mM TRIS Buffer pH 7	
Pyroglutamic acid	$C_5H_7NO_3$	2 mg/ml	
3-hydroxy-3-methylglutarate (3H3MG)	$C_6H_{10}O_5$	2 mg/ml	
N-acetyl- aspartate (NAA)	$C_6H_9NO_5$	2 mg/ml	
Glutathione (GSH)	$C_{10}H_{17}N_3O_6S$	2 mg/ml	
N-acetylneuraminate (NANA)	$C_{11}H_{19}NO_9$	2 mg/ml	
Uridine diphosphate (UDP)	$C_9H_{14}N_2O_{12}P_2$	2 mg/ml	
Uridine triphosphate (UTP)	$C_9H_{14}N_2O_{12}P_2$	2 mg/ml	
UDP-glucose (UDP-Gluc)	$C_{15}H_{24}N_2O_{17}P_2$	2 mg/ml	
Uridine diphosphate-N-acetylglucosamine (UDP-GlcNAc)	$C_{17}H_{27}N_3O_{17}P_2$	2 mg/ml	
Oxidized glutathione (GSSG)	$C_{20}H_{32}N_6O_{12}S_2$	2 mg/ml	
CMP-N-acetylneuraminic acid (CMP-NANA)	$C_{20}H_{31}N_4O_{16}P$	2 mg/ml	Merck KGaA, Darmstadt, Germany

**Concentration of amino acids corresponded to 2.5 µmol/ml except for cystine which was 1.25 µmol/ml*

2.1.6 Buffers and solutions

2.1.6.1. SDS-PAGE and Western blot

Table 10: List of buffers and solutions used for SDS-PAGE and Western blot

Buffer and solutions	Components	Composition
APS (10%)	Ammonium persulfate	1g
	Water	10 ml
Laemmli loading buffer (5x), pH 6.8	Tris-HCl (0.5 M, pH 6.8)	306 mM
	Glycerol	25 % (v/v)
	SDS	10% (v/v)
	Bromophenol blue	0.1%
	ß-mercaptoethanol	25 % (v/v)
PMSF protease inhibitor (200 mM)	PMSF	34.84 mg
	2-propanol	1 ml
Protein extraction buffer	1x RIPA buffer	1 ml
	PMSF (200mM)	50 µl
	Water	Ad 10 ml
SDS-PAGE running buffer (10x), pH 8.3	Tris-Base	150 g
	Glycine	720 g
	SDS (20%)	250 m
	Water	Ad 5000 ml
SDS-PAGE running buffer (1x), pH 8.3	SDS-PAGE running buffer (10x)	500 ml
	Water	Ad 5000 ml
TBS (10x), pH 7.4	Tris-Base	150 g
	NaCl	400 g
	KCl	10 g
	Water	Ad 5000 ml
TBS-T wash buffer (1x)	TBS (10x)	500 ml
	Tween 20 (50% v/v)	10 ml
	Water	Ad 5000 ml
Transfer buffer	Tris-Base	29 g
	Glycine	14.6 g
	SDS (20%)	9.25 ml
	Water	Ad 4000 ml
	Ethanol	Ad 5000 ml
Tris-HCl (1.5 M, pH 8.8)	Tris-Base	90.75 g
	Water	Ad 500 ml
		Adjust pH with HCl to 8.8
Tris-Base (0.5 M, pH 6.8)	Tris-Base	30 g
	Water	Ad 500 ml
		Adjust pH with HCl to 6.8
WB blocking buffer 1	5% (w/v) skim milk powder in TBS-T	
WB blocking buffer 2	5% (w/v) BSA in TBS-T	

2.1.6.2. LC-MS/MS and LC-HRMS

Table 11: List of eluents and solutions used for LC-MS/MS and LC-HRMS analysis

Eluents & solutions	Components	Composition
	Cell extraction buffer	
MeOH:water (8:2, v/v)	Methanol	18 ml
	Water	2 ml
	SIRM experiments (LC-HRMS)	
100 mM AmAc (pH 7.0)	Ammonium acetate	925 mg
	Water	120 ml
Eluent A zHILIC	100 mM AmAc	50 ml
	Deactivator additive	0.5 ml
	Water	450 ml
Eluent B zHILIC	100 mM AmAc	50 ml
	Deactivator additive	0.5 ml
	ACN	450 ml
Calibration mix QTOF	HP-0321	5 µl
	Calibration standard for ESI-TOF	10 ml
	Acetonitrile	85.5 ml
	Water	4.5 ml
	Sugar phosphates and lactate (LC-MS/MS)	
Eluent A	ACN	125 ml
	Water	875 ml
	OAA	750 mg
Eluent B	ACN	500 ml
	Water	500 ml
	OAA	750 mg
	Adenylated ribonucleotides (LC-MS/MS)	
Eluent A (pH 6.0)	Water	350 ml
	ACN	150 ml
	Ammonium acetate	385 mg
Eluent B (pH 10.5)	Water	350 ml
	ACN	150 ml
	Ammonium acetate	38.5 mg
50 mM EDTA (pH 10.5)	EDTA	1861 mg
	Water	100 ml

2.1.7 Further materials

Table 12: List of general consumables

Consumables	Vendor
Miscellaneous material	
0.8 ml vial, borosilicate glass, amber	CS - Chromatographie Service GmbH, Langerwehe, Germany
Axygen® 96-well Clear V-Bottom well plate	Corning Inc., Corning, USA
Combitips advanced® Eppendorf Biopur®, sterile: 0.5, 1 ml, 2.5 ml, 5 ml, 10 ml	Eppendorf, Hamburg, Germany
Dry ice pellets (particle size 3mm)	Kraiss & Friz, Stuttgart, Germany
Polypropylene tube 0.5, 1.5, and 2mL	Eppendorf, Hamburg, Germany
Qubit 1X dsDNA HS Assay Kit	Thermo Fisher Scientific GmbH, Waltham, USA
Seahorse	
Seahorse XF Glycolytic Rate Assay Kit	Agilent Technologies, Waldbronn, Germany
Seahorse XFe96 FluxPak	
Western blot	
Amersham Protran 0,45 µm Nitrocellulose Membran	GE Healthcare, München, Germany
Gel-blotting paper	Schleicher & Schuell, Dassel, Germany

2.2. Methods

2.2.1 Basic cell culture handling

2.2.1.1. Cell line cultivation

The adherent breast cancer cell lines (Table 6) were cultivated in RPMI-1640 (Biozym) supplemented with 10% FBS and 2 mM L-glutamine at 37 °C and 5% CO_2 atmosphere in cell culture incubators. Unless otherwise stated, this prepared medium is further referenced as cultivation medium. Passaging was done according to manufacturer's specifications in a sub cultivation ratio of 1:3 to 1:4, two times per week. In more detail, cells were first washed with 1x PBS and subsequently trypsinated. Detached cells were centrifuged for 5 minutes at 1400 rpm (Rotina, type: 380R, Table 4) and resuspended in fresh cultivation medium according to the desired sub cultivation ratio. The cell lines were regularly tested for mycoplasma and authenticated by short tandem repeat (STR) profile analysis with PowerPlex® 21 System. The cells were cultivated for less than 3 months, or 26 passages, respectively.

2.2.1.2. Cell line preservation

To ensure genetic stability, early passages (p5 through p10) of respective cell lines were cryopreserved once they showed healthy morphology and stable proliferation rates. To this end, the cell counts as well as the cell viability was assessed using trypan blue exclusion test after trypsination. Afterwards, cells were resuspended in freezing medium (95% FBS v/v, 5% DMSO v/v) at a concentration of 1 to $2*10^6$ cells/ml, transferred into cryovials, and placed in a freezing container overnight to ensure a steady cooling rate of 1 °C/min at -80 °C. Next morning cryovials were removed from the container and stored under nitrogen.

2.2.1.3. Cell line initiation

Cryopreserved cells were thawed in a prewarmed water bath set to 37 °C. The defrozen cell suspension was then quickly transferred into 9 ml warmed cultivation medium and centrifuged. After centrifugation at 1400 rpm for 5 minutes (Rotina, type: 380R), cells were initiated in T25 cultivation flasks for the first passage and cultivated as described.

2.2.2 Optimization of sample preparation

2.2.2.1. Quenching of metabolism

For the optimization of the quenching procedure, cells were plated in 6-well plates at a concentration of $7.5*10^5$ cells/well and incubated for 24 hours. On the next day, the medium was completely removed, and the metabolic activity was immediately quenched using two different approaches. The first approach was performed by submersing the culture plate in a liquid nitrogen bath for 30 seconds. After that, plates were removed from the liquid nitrogen bath and placed on dry ice, followed by the addition of 600 µl ultra-cool 80% MeOH (- 80 °C) to the wells. Cells were scraped off and incubated on dry ice for 15 minutes. The second quench approach was based on a one-step quench and extraction procedure. After medium removal, cultivation plates were placed on dry ice and 600 µl of ultra-cool 80% MeOH (- 80 °C) was directly added to the wells. Consecutively, cells were scrapped off and incubated on dry ice for 15 minutes. Cell lysis was achieved by repeated aspiration and dispensing in the well (2–3 times using 1.000 µl pipette tip), followed by transfer to polypropylene tubes (Eppendorf), and three freeze-thaw cycles on dry ice and iced-water. Subsequently, extracts from both approaches were transferred to Eppendorf tubes and shortly vortexed. 10 µl of corresponding cell homogenates were collected in separate aliquots for DNA quantification. Cell suspensions were centrifuged at 4°C for 5 min at 15.000 rpm (Centrifuge type: 5424R, Eppendorf, Germany). Supernatants were transferred to new tubes and stored at – 80 °C until analysis by mass spectrometry.

2.2.2.2. Storage condition and stability

The assessment of the storage conditions was performed for samples worked up with the one-step quench and extraction procedure. Here, samples were collected after the cell cultivation and extraction procedure as described in 2.2.2.1 to investigate three storage conditions: (i) control (i.e. stored at - 80 °C in extraction solvent for one day), (ii) MeOH extract (lq) (i.e. samples were stored in extraction solvent at - 80 °C for three weeks) and (iii) dried extract (i.e. extraction solvent was evaporated in a rotational vacuum concentrator overnight and stored for three weeks at - 80 °C).

2.2.2.3. Washing procedure

The optimization of the washing procedure followed the cultivation conditions from the metabolic quenching optimization (2.2.2.1) with minor modifications. Briefly, prior to quenching, the medium was completely removed by aspiration and either 1 ml of prechilled or warmed 1x PBS (i.e. 4 °C, 37 °C, respectively) was added to the wells. The plates were briefly rocked, the

wash solvent aspirated followed by quenching and extraction with ultra-cool MeOH (- 80 °C) and further processed as previously reported.

2.2.2.4. Optimized procedure

The protocol for optimized sample work up for metabolomic analysis was performed as follows. Cells were cultivated as indicated in 2.2.2.1 for 24 h. Upon removal of cultivation medium by aspiration, cells were quickly washed by the addition of 1 ml pre-chilled (i.e. 6 °C) 1x PBS to each well. Plates were quickly transferred onto dry ice and further worked up according to the one-step quench and extraction procedure. To this end, 600 µl of ultra-cool (i.e. -80 °C) 80% MeOH was added directly to the wells. Cells were scrapped off the wells and left on dry ice for 15 minutes. Subsequent steps were performed as described in 2.2.2.1.

2.2.2.5. Assessment of the sample preparation workflow

In the case of the quench and the wash procedure, the levels of adenylated ribonucleotides as well as the calculated energy charge (Equation 1) were used to estimate the performance of the proposed workflow. Levels of TCA cycle intermediates were additionally used to assess the effect of the wash procedure.

2.2.2.6. Normalization strategies for metabolomic data

Normalization based on dsDNA concentration of the cell homogenate

The DNA concentration of the cell homogenate was determined using the Qubit 2 fluorometer and the high sensitivity assay kit (Table 12). To this end, the working solution was prepared by diluting the Qubit™ reagent 1:200 with the Qubit™ buffer. Calibration standards were prepared by adding 10 µl of the standards from the kit to 190 µl of the working solution in PCR tubes. Samples were prepared from 5 µl cell homogenate and 195 µl working solution mixed in PCR tubes. Standards and samples were briefly vortexed and incubated for 2 minutes at room temperatures. DNA concentration of the samples was estimated from the two-point calibration.

Normalization based on cell count using live cell imaging

The cell count was determined with the Cytation 1 Cell Imaging Reader controlled by the Gen5 software prior to any work up procedures. The instrument was brought to 37 °C and a gas controller maintained the atmosphere at 5% CO_2 within the chamber. Plates were subsequently transferred from the incubator to the instrument and visualized using a 4x objective in bright field mode. Images were acquired using an image matrix of 12 x 15 and exposure settings set to LED, 5; Integration time, 35; Gain, 0. For normalization purposes the imaging and cell count procedure was adjusted to allow for quicker image acquisitions. Here, the focus plane was preselected for each well to ensure sharp, high contrast images. Acquired images were automatically background adjusted by a rolling ball filter with the threshold set to 9000 for the cell count. Touching objects were split and only objects with a size between 17 to 35 µm were included in the cell count. Primary edge objects were also excluded from the cell count. The total cell count per well was given by summing the cell count for each captured image. The selected image matrix produced a well coverage of at least 50% and allowed imaging of a 6-well plate in roughly 15 minutes.

2.2.3 Cell line characterization upon PI3Kβ inhibition

2.2.3.1. Preparation of AZD8186 stock solution

AZD8186 was prepared at a stock concentration of 2 mM in DMSO and subsequently sterile filtered through a 0.22 µm cellulose acetate filter. The inhibitor was stored under nitrogen until use.

2.2.3.2. Protein expression analysis with Western blot

MDA-MB-468 as well as MDA-MB-231 cells were seeded in 6-well plates at a concentration of $3*10^5$ cells/well and left to adhere overnight. Next morning the cultivation medium was replaced with cultivation medium containing AZD8186 in a concentration range between 3 µM and 0.01 µM and treated for 24h. Prior to protein extraction medium was removed and cells were washed with 1x PBS. Subsequently, cells were placed on ice and lysed in protein extraction buffer (Table 10). Cell lysates were sonicated three times for 30 seconds in an ice-water bath and centrifuged at 4 °C for 15 minutes at 13.000 rpm (Eppendorf, type: 5424R). Protein concentrations from lysates were determined using the Pierce™ BCA assay following manufacturer's instructions and measuring the absorbance at 562 nm with a microplate reader. The presence of specific proteins as well as the assessment of the phosphorylation status at $pAKT_{Ser}$ and $pAKT_{Thr}$ was done by separation of total protein on a SDS-polyacrylamide gel (SDS-PAGE) and subsequent immunoblotting with respective antibodies. Polyacrylamide gels were prepared according to Table 13.

Table 13: List of composition details for SDS polyacrylamide (PAA) gels with 1 mm thickness

Components	Stacking gel (5% PAA) [ml]	Resolving gel (10% PAA) [ml]
Water	6.1	9.95
Acrylamide/bis solution (30%)	1.35	8.3
1.5 M Tris-HCl, pH 8.0	-	6.22
0.5 M Tris-HCl, pH 6.8	2.5	-
10% SDS	0.1	0.25
10% APS	0.1	0.25
TEMED	0.01	0.025

Prior gel loading, 10 µg of protein samples were mixed with loading buffer (Table 10, final concentration 2x) and denatured at 95 °C for 5 minutes in a water bath. Samples were then loaded onto the gel along with the protein ladder as mass reference. Gels were mounted into the gel holder cassettes and placed into the buffer tank filled with 1x running buffer. For more consistent sample entry into the resolving gel, electrophoresis was initially performed at 90 V for 10 minutes and later increased to 160 V for 60 minutes. After the electrophoresis, gels were transferred onto 0.45 µm nitro cellulose membranes and blotted for 90 minutes at 40 mA/gel. Successful protein transfer onto membranes was assessed by incubation with Ponceau S solution for 5 minutes. After destaining with wash buffer, membranes were blocked for 1 hour with either blocking buffer 1 or blocking buffer 2 depending on the specifications of the primary antibody (Table 14).

Table 14: List of antibodies and dilutions for Immunoblotting

Antibody	Dilution	Isotype	Vendor
HRP-linked Antibody Anti-rabbit IgG	1:3000 in blocking buffer 1	Goat IgG (secondary Ab)	Cell Signaling Technology, Danvers, USA
PTEN	1:1000 in blocking buffer 2	Rabbit mAb	
PI3 Kinase p110β	1:1000 in blocking buffer 2	Rabbit mAb	
Phospho-AKT$_{Thr308}$ XP®	1:1000 in blocking buffer 1	Rabbit mAb	
Phospho-AKT$_{Ser473}$ XP®	1:1000 in blocking buffer 2	Rabbit mAb	
GAPDH XP®	1:1000 in blocking buffer 1	Rabbit mAb	

Afterwards the primary antibody was added to the blocking buffer according to the desired dilution and incubated overnight at 4 °C. On the next day, membranes were washed three times with washing buffer for 10 minutes, before 1 hour incubation with anti-Rabbit HRP-linked secondary antibody. Unbound secondary antibody was removed by washing with wash buffer

for 10 minutes each (three times). At last, chemiluminescence of the HRP-activity was visualized by a CCD camera using SuperSignal™ West Dura Extended Duration Substrate.

2.2.3.3. Seahorse XF - Glycolytic rate assay

Extracellular flux analysis was performed with the Agilent Seahorse XFe96 Analyzer using the glycolytic rate assay kit. Glycolytic rate upon PI3Kβ inhibition was determined following procedures according to manufacturer's instructions (User Guide Kit 103344-100). In further detail, two days before metabolic flux analysis was carried out, cells were plated at a concentration of 1.5 *10^4 cells/well into provided cell culture microplates in cultivation medium. On the next morning, medium was replaced with fresh cultivation medium supplemented with different concentrations of AZD8186 (0.1 µM, 0.5 µM, 1 µM, 3 µM, n =3) and incubated for 24 hours. Sensor cartridges were hydrated for 16 hours prior to the beginning of the experiment in a CO_2- free incubator at 37 °C. On the day of the experiment, the cultivation medium was removed and the cells were quickly washed with 1x PBS. Cells were then cultivated with the RPMI assay medium containing 1 mM pyruvate, 2 mM glutamine, 10 mM glucose, and the inhibitor at 37 °C in the non-CO_2 incubator for one hour. In the meantime, the required assay compounds (i.e. ROT/AA, 2-DG, and Hoechst 3342) were prepared and loaded into the injection ports at indicated concentrations (Table 15).

Table 15: Compound concentrations for Seahorse XF glycolytic rate assay

Compound	10x concentration in port	Final well concentration
Port A: ROT/AA	5 mM	0.5 mM
Port B: 2-DG	500 mM	50 mM
Port C: Hoechst 33342	20 µM	2 µM

Right before the start of the assay, the medium was renewed with fresh medium and the plate was placed inside the Seahorse flux analyzer. After a 15 minute equilibration duration, the assay was started, and data was collected every 6 to 7 minutes for approximately 1 hour. Sequential injection of the mitochondrial inhibitor Rot/AA at first and the glycolytic inhibitor 2-DG allowed the calculation of the glycolytic capacity. At the end of the assay, the nuclei dye Hoechst 3342 was injected, and cells were counted using the Cell Imaging software and Cytation 1. Normalization from cell count and calculation of assay parameters (i.e. OCR, ECAR, mitoOCR/glycoPER (basal) were automatically performed by the Wave software and visualized in Excel.

2.2.3.4. Cell growth assay

Cells were harvested from cultivation flasks and plated in a 6-well plate at a concentration of $5*10^5$ cells/well and left to adhere for 16 hours in cultivation medium at 37 °C, 5% CO_2. Meanwhile, the vehicle was prepared as DMSO 0.05% (v/v), and the inhibitor was diluted to 500 µM with serum free RPMI supplemented with 2 mM L-glutamine. On the next morning, the cultivation medium was replaced by serum free RPMI supplemented with 2 mM l-glutamine. After 2 hour serum starvation, medium was replaced with AZD8186 (0.5 µM) or vehicle containing serum free medium. The plate was then transferred to the cell imaging reader set to 37 °C and 5% CO_2 and cultivated for 72 hours. Images were acquired every 12 hours using the kinetic mode function with the same exposure settings as described in 2.2.2.6. The originally selected image matrix of 12 x 15 was kept, where additionally the image tile overlap for the column and rows was set to -600 µm. Further minor adjustments of acquisition and imaging parameters followed specifications described elsewhere (Nybo and Lamberts 2019). In more detail, images were captured using the autofocus function of the instrument, selecting the cell's focal plane. From this focal plane another set of images was acquired with an offset of 200 µm from the original plane producing high contrast images of cells. Resulting offset images were background adjusted by a rolling ball filter with options set to dark background and a rolling ball diameter of 50 µm. No image smoothing was applied and priority was set to fine results. The cell count of these preprocessed images was then determined using a threshold of 13000 on dark background where touching objects were split and holes in masks were filled. Only objects with a size between 12 to 50 µm were counted, while edge objects were also excluded. The total cell counts per well resulted from summing the cell counts for each captured image. Fully imaging of a 6-well plate took roughly 30 minutes.

2.2.4 Stable isotopic labeling experiments

2.2.4.1. Preparation of stock solutions for labeling experiments

Stock concentrations of labeled and unlabeled substrates for tracing experiments were prepared in glucose- or glutamine-free RPMI-1640 medium at concentrations of 887.5 mM for glucose and 200 mM for glutamine, respectively (Table 16). To avoid contaminations, dissolved compounds were sterile filtered through a 0.22 µm cellulose acetate filter. To monitor carbon flux from glycolytic breakdown, [U-^{13}C] labeled glucose was employed. ^{13}C incorporation *via* glutamine anaplerosis into the TCA cycle was followed by the double labeled [U-^{13}C, ^{15}N] glutamine. Glutamine derived nitrogen was monitored using [U-^{15}N] glutamine. AZD8186 was prepared as described in 2.2.3.1 and used at a concentration of 0.5 µM for tracing experiments.

Table 16: List of tracer substrates, corresponding stock and concentrations used in tracer experiments

Compound	Medium	Stock concentration [mM]	Final concentration per well [mM]	Investigated label
[U-^{13}C]-glucose [99%]	RPMI-1640 (Gibco™)	887.5	11.1	^{13}C
Unlabeled glucose	RPMI-1640 (Gibco™)	887.5	11.1	-
[U-^{15}N]-glutamine [98%]	RPMI-1640 (Biozym)	200	2	^{15}N
[U-^{13}C,^{15}N] glutamine [99%]	RPMI-1640 (Biozym)	200	2	^{13}C
Unlabeled glutamine	RPMI-1640 (Biozym)	200	2	-

2.2.4.2. Performed stable isotope labeling experiments

An overview of all performed tracer experiments and corresponding result sections are displayed in Table 17.

Table 17: List of tracer experiments performed during this work

#	Tracer substrate	Cell lines	Time points	Chapter
1	[U-^{13}C] glucose	MDA-MB-468	1, 3, 6 & 24h	3.3
2	[U-^{13}C] glucose	MDA-MB-468	0.5, 1, 1.5, 2 & 3h	3.3.3
3	[U-^{13}C] glucose	MDA-MB-468, HCC70	0,25, 1, 3, 6 & 24h	3.5
4	[U-^{13}C,^{15}N] glutamine	MDA-MB-468	1, 3, 6 & 24h	3.4
5	[U-^{15}N] glutamine	MDA-MB-468	1, 3, 6 & 24h	3.4

2.2.4.3. General procedure

MDA-MB-468 cells were seeded at a concentration of $7.5*10^5$ cells/well in 6-well plates and left to adhere overnight in cultivation medium. After 16 h, the medium was replaced with fresh RPMI-1640 cultivation medium without FBS. After 2 h of serum starvation, medium was exchanged to tracer enriched RPMI-1640 (Table 16), supplemented with 0.5 µM AZD8186 or vehicle, respectively.

After indicated sampling times (Table 17), plates were imaged for normalization purposes and subsequently worked up according to the optimized quench and extraction protocol (2.2.2.4). Parallel cultures that were treated identically except that the medium contained naturally labeled glucose or glutamine, respectively, were used as unlabeled reference and sampled after the last time point of the performed tracing experiment.

2.2.4.4. Inter-day reproducibility

For the evaluation of inter-day assay performance during the robustness assessment (3.3.3), the 1h and 3h sampling time points (referenced as “Day 1”, #1 [U-^{13}C] glucose experiment) were compared against corresponding sampling times of an independent labeling experiment that was performed on another day (referenced as “Day 2” ”, #2 [U-^{13}C] glucose experiment) using the same cultivation and treatment conditions.

2.2.4.5. Cell line comparison between MDA-MB-468 and HCC70

For the comparison of tracer incorporation from [U-^{13}C] glucose in two PTEN-null cell lines (i.e. MDA-MB-468 and HCC70), cultivation conditions were adapted and a pretreatment phase was introduced (#3 [U-^{13}C] glucose experiment). Here, cells were plated at $5.0*10^5$ cells/well and left to adhere overnight for a period of 16 h. On the next morning, the medium was replaced with fresh cultivation medium RPMI-1640 (Biozym) supplemented with 0.5 µM AZD8186, respectively, vehicle and incubated for 24 hours. After serum starvation for 2 hours, the medium was exchanged on the next day for tracer containing RPMI-1640 (Gibco) supplemented with respective inhibitor or vehicle. After 6 and 24 h, plates were imaged and subsequently worked up following the optimized quench and extraction protocol.

2.2.5 Targeted metabolomics

LC-MS/MS analysis was performed on an Agilent 6460 triple quadrupole mass spectrometer coupled to an Agilent 1290 HPLC system according to (Hofmann et al. 2008). GC-MS analysis was performed on a 5975C inert XL MSD coupled to an Agilent GC 7890A using a J&W DB-5MS column (25 m, inner diameter 0.20 mm, film thickness 0.33 µm) following procedures as described by (Hofmann et al. 2008) for TCA cycle and amino acid intermediates, respectively cholesterol (Maier et al. 2009). Quantification of glucose by GC-MS was done according to procedures by (Küry and Keller 1991).

2.2.5.1. Quantification of adenylated ribonucleotides by LC-MS/MS

Preparation and processing of samples and standards for LC-MS/MS analysis were performed on ice. Specification regarding internal standard, calibration range, and QC concentrations are summarized in Table 22. For the calibration curve (nine calibrators per compound), a mix of corresponding reference compounds (Table 9) was prepared in 50 mM EDTA. Calibrators were subsequently diluted to their corresponding concentration and a mix of stable isotope labeled compounds were prepared at indicated concentration.

Table 18: Specifications for the quantification of adenylated ribonucleotides by LC-MS/MS

Analyte	Range [pmol / sample]	Internal standard	IS [pmol / 10 µl]	QC low [pmol / sample]	QC mid. [pmol / sample]	QC high [pmol / sample]
AMP	10 - 2000	[U-^{13}C,^{15}N]-AMP	500	50	250	1000
ADP	10 - 2000	[U-^{13}C]-ADP	500	50	250	1000
ATP	10 - 2000	[U-^{13}C]-ATP	500	50	250	1000

For the quantitation of adenylated ribonucleotides 140 µl of water was mixed with 10 µl internal standard (IS) and 10 µl calibrator solution, respectively 25 µl cell extract and briefly vortexed. Samples and standards were subsequently centrifuged (Eppendorf) for 10 minutes at 15000 rpm, 4 °C. Lastly, 90 µl were transferred to a 96-well plate (Axygen®) and transferred to the autosampler.

Measurement was performed in positive ESI mode. Electrospray jetstream conditions were as follows: Capillary voltage 3500 V, nozzle voltage 1000 V, drying gas flow 10 L/min nitrogen, drying gas temperature 270°C, nebulizer pressure 40 psi, sheath gas temperature 350°C, sheath gas flow 11 L/min. HPLC separation was achieved on a BioBasic AX column (5 µm, 2.1x50 mm) using 10 mM ammonium acetate in water:ACN (7:3, v:v) as Eluent A and 1 mM ammonium acetate in water:ACN (7:3, v:v) as Eluent B (Table 11) as mobile phases at a flow

rate of 0.15 mL/min with. Samples were kept at 6 °C and injection volume corresponded to 5 µl. Gradient runs were programmed as follows: 0 % B from 0 min to 1 min, linear increase to 35 % B after 2.5 minutes. The flow rate was increased to 0.25 ml/min and the gradient was held from 2.51 to 5 minutes. From 5.01 to 7 minutes increase to 65% B and maintaining gradient until 10 minutes. From 10 to 10.5 minutes linear increase to 100% B and holding until 13 minutes, then equilibration to 100% A after 13.1 minutes for 6.4 minutes. The mass spectrometer was operated in the MRM mode (Table 19).

Table 19: MRM settings for adenylated ribonucleotides

Compound	Precursor ion	Product ion	Dwell time	Fragmentor voltage [V]	Collision energy [V]
[U-^{13}C]-ATP	518	141	70	127	38
ATP	508	136	80	127	38
ADP	428	136	80	113	22
[U-^{13}C,^{15}N]-AMP	363	146	70	98	14
AMP	348.1	136	80	98	14

2.2.5.2. Quantification of sugar phosphates by LC-MS/MS

Preparations and processing of samples and standards were performed on ice. Specification regarding internal standard, calibration range, and QC concentrations are summarized in Table 20. For the calibration curve (nine calibrators per compound), a mix of corresponding reference compounds (Table 9) was prepared in water. Calibrators were subsequently diluted to their corresponding concentration and a mix of stable isotope labeled compounds was prepared at the indicated concentration.

Table 20: Specifications for the quantification of sugar phosphates by LC-MS/MS

Analyte	Range [pmol / sample]	Internal standard	IS [pmol / 10 µl]	QC low [pmol / sample]	QC mid. [pmol / sample]	QC high [pmol / sample]
Glycolytic intermediate method						
Ribulose-5-phosphate	5 - 5000	[U-^{13}C]-G6P	500	25	100	3750
Ribose-5-phosphate	5 - 5000	[U-^{13}C]-G6P	500	25	100	3750
G6P	5 - 5000	[U-^{13}C]-G6P	500	25	100	3750
G1P	5 - 5000	[U-^{13}C]-G1P	500	25	100	3750
Sed 7P	5 - 5000	[U-^{13}C]-G6P	500	25	100	3750
6PG	5 - 5000	[U-^{13}C]-6PG	500	25	100	3750

Analyte	Range [pmol / sample]	Internal standard	IS [pmol / 10 µl]	QC low [pmol / sample]	QC mid. [pmol / sample]	QC high [pmol / sample]
3-PG	5 - 5000	[U-^{13}C]-2-PG	500	25	100	3750
F1,6-BP	5 - 5000	[U-^{13}C]-F1,6-BP	500	25	100	3750
PEP	5 - 5000	[U-^{13}C]-PEP	500	25	100	3750

For the quantitation of sugar phosphates 20 µl of methanol was mixed with 10 µl internal standard (IS) and 5 µl calibrator solution, respectively 25 µl cell extract and briefly vortexed. Subsequently, 40 µl of water was added to the tubes and vortexed again. Samples and standards were then centrifuged (Eppendorf) for 10 minutes at 15000 rpm, 4 °C. Lastly, the supernatant was transferred to a 96-well plate (Axygen®) and placed in the autosampler.

Measurement was performed in negative ESI mode. Electrospray jetstream conditions were as follows: Capillary voltage 3500 V, nozzle voltage 1000 V, drying gas flow 10 L/min nitrogen, drying gas temperature 325°C, nebulizer pressure 50 psi, sheath gas temperature 350°C, sheath gas flow 11 L/min. HPLC separation was achieved on a Synergi™ Hydro-RP 80 Å column (150 x 2 mm, 4 µm particle size) using 4 mM OAA in water:ACN (7:1, v:v) as Eluent A and 4 mM OAA in water:ACN (1:1, v:v) as Eluent B (Table 11) at a flow rate of 0.25 mL/min with. Samples were kept at 6 °C and injection volume corresponded to 5 µl. Gradient runs were programmed as follows: 2% B from 0 min to 5 min and subsequent linear increase to 20 % B from 5 to 17 minutes. From 17 to 18 minutes increase to 35% B and maintaining gradient until 18.5 minutes. From 18.5 to 22 minutes linear increase to 60% B and holding until 23 minutes. From 23 to 24 minutes, further increase to 90% B and keeping the gradient until 25 minutes, then equilibration to 2% B after 25.1 minutes for 6.5 minutes. The mass spectrometer was operated in MRM mode (Table 21).

Table 21: MRM settings for sugar phosphates

Compound	Precursor ion	Product ion	Dwell time	Fragmentor voltage [V]	Collision energy [V]
Time segment: 4-15 minutes					
Rib-5P	229	97	50	80	10
G1P	259	241	50	90	6
G6P	259	241	50	90	10
Sed7P	289	97	50	90	10
[U-^{13}C]-G1P	265	247	50	90	6
[U-^{13}C]-G6P	265	97	50	90	10
Time segment: 15-26 minutes					
PEP	167	79	50	70	8

Compound	Precursor ion	Product ion	Dwell time	Fragmentor voltage [V]	Collision energy [V]
3-PG	185	97	50	130	8
6-PG	275	97	50	80	8
F1,6-BP	339	97	50	100	12
[U-^{13}C]-PEP	170	79	50	70	8
[U-^{13}C]-2-PG	188	78.9	50	81	8
[U-^{13}C]-6-PG	281.1	97	50	80	8
[U-^{13}C]-F1,6-BP	345	97	50	100	12

2.2.5.3. Quantification of lactate by LC-MS/MS

Samples and standards were processed at room temperature. Specification regarding internal standard, calibration range, and QC concentrations are summarized in Table 22. For the calibration curve (nine calibrators per compound), a mix of corresponding reference compounds (Table 9) was prepared in ultra-pure water. Calibrators were subsequently diluted to their corresponding concentration and the internal standard was prepared at the indicated concentration.

Table 22: Specifications for the quantification of lactate by LC-MS/MS

Analyte	Range [pmol / sample]	Internal standard	IS [pmol / 10 µl]	QC low [pmol / sample]	QC mid. [pmol / sample]	QC high [pmol/ sample]
Lactate	25 - 5000	[U-^{13}C]-Lactate	2000	50	500	2500

For the determination of intracellular lactate levels, 40 µl of cell extract was spiked with 10 µl of internal standard mix and evaporated under N_2-flow. Samples were subsequently reconstituted in 100 µl Eluent A (4 mM OAA in water:ACN (7:1, v:v) ,Table 11). 10 µl of calibrator solution was mixed with 10 µl internal standard and 80 µl of Eluent A. Samples and calibrators were briefly vortexed and centrifuged for 10 minutes at 3500 rpm (Centrifuge type: 5424R, Eppendorf, Germany). 76 µl of supernatant were transferred to a 96-well plate (Axygen®). For the quantification of extracellular lactate from the cultivation medium, medium aliquots obtained prior quenching were diluted 1:20 with water. Afterwards, 10 µl of diluted medium was transferred to the 96-well plate (Axygen®) and 40 µl of methanol and 10 µl of internal standard was added to the samples. The plate was briefly vortexed and spun down in a centrifuge (Rotina, type: 380R).

Measurement was performed in ESI negative mode. Electrospray jetstream conditions were as follows: Capillary voltage 3500 V, nozzle voltage 1000 V, drying gas flow 10 L/min nitrogen,

drying gas temperature 325°C, nebulizer pressure 50 psi, sheath gas temperature 350°C, sheath gas flow 11 L/min. HPLC separation was achieved on a Synergi™ Hydro-RP 80 Å column (150 x 2 mm, 4 µm particle size) using Eluent A (Table 11) and 4 mM OAA in water:ACN (1:1, v:v) as Eluent B (Table 11) as mobile phases at a flow rate of 0.3 mL/min with. Samples were kept at 6 °C and injection volume corresponded to 5 µl. Gradient runs were programmed as follows: 0% B from 0 min to 2.5 min and subsequent linear increase to 20 % B from 2.5 to 5 minutes. From 5 to 6 minutes increase to 90% B. Equilibration from 6 to 6.2 minutes to 0% B and maintaining the gradient until 8.3 minutes before the next injection. The mass spectrometer was operated in MRM mode (Table 23).

Table 23: MRM settings for lactate

Compound	Precursor ion	Product ion	Dwell time	Fragmentor voltage	Collision Energy
Time segment: 1.5-4 minutes					
Lactate	89	43	200	56	8
[U-^{13}C]-Lactate	92	45	200	56	8

2.2.5.4. Quantification of organic acids by GC-MS

Samples and standards were processed at room temperature. Specification regarding internal standard, calibration range, and SIM masses are summarized in Table 24. For the calibration curve (nine calibrators per compound), a mix of corresponding reference compounds (Table 9) for organic acids was prepared in ultra-pure water for TCA cycle. Calibrators were subsequently diluted to their corresponding concentration and a mix of internal standards was prepared at the indicated concentration.

Table 24: Specifications for the quantification of organic acids with GC-MS

Analyte	Range [pmol / sample]	Internal standard	IS [pmol / 10 µl]	SIM mass analyte [m/z]	SIM mass IS [m/z]	Derivate
Pyruvate	2.5 - 500	[U-^{13}C]-pyruvate	500	174.1	177.1	MOX-TBDMS
Fumarate	2 - 200	[U-^{13}C]-fumarate	200	287.1	291.1	TBDMS
α-ketoglutarate	2 - 200	1,2,3,4-$^{13}C_4$-α-ketoglutarate	250	346.2	350.2	MOX-TBDMS
Malate	5 - 375	[U-^{13}C]-malate	500	419.3	423.3	TBDMS
Citrate	5 -500	D_4-citrate	250	591.3	595.3	TBDMS
3-hydroxy butyrate	1 - 200	D_4-3-hydroxy butyrate	200	275.1	279.1	MOX-TBDMS

For the quantitation of intracellular organic acids 50 µl ethanol (p.a.) was mixed with 10 µl internal standard (IS) along with 40 µl cell extract or 10 µl calibrator solution in borosilicate vials (CS) and evaporated under N_2-flow and 40 °C. Derivatization to methyloximes was performed with 25 µl O-methylhydroxyamine hydrochloride in pyridine at a concentration of 10 mg/ml at 60 °C for 1 hour. Reaction with 40 µl MBDSTFA at 60 °C for 15 minutes formed the tert-butyldimethylsilyl derivative. The injection volume was 1.2 µl and the GC temperature parameters are summarized in Table 25.

Table 25: Parameters for GC-MS analysis of organic acids

Time segment	Rate [°C/min]	Temperature [°C]	Hold time [min]
1	-	100	1.5
2	10	270	0
3	20	300	3
		Runtime	23

2.2.5.5. Quantification of amino acids by GC-MS

Specifications regarding internal standard, calibration range, and SIM masses are summarized in Table 26. For the calibration curve (nine calibrators per compound), a mix of corresponding reference compounds (Table 9) for the analysis of amino acids was prepared in ultra-pure water. Calibrators were subsequently diluted to their corresponding concentration. Concentration of the labeled amino acids in the algal [U-^{13}C,^{15}N]-amino acid stock solution was calculated from the Mol% of the corresponding amino acid mixture (Table 9). The internal standard for labeled amino acids was subsequently prepared at the indicated concentration.

Table 26: Specifications for the quantification of amino acids with GC-MS

Analyte	Range [pmol / sample]	Internal standard	IS [pmol / 10 µl]	SIM mass analyte [m/z]	SIM mass IS [m/z]	Derivate
Alanine	5 - 2000	[U-^{13}C-^{15}N]-alanine	2307	232	235	TBDMS
Glycine	5 - 2000	[U-^{13}C-^{15}N]-glycine	1780	246	249	TBDMS
Urea	20 - 8000	[U-^{13}C]-urea	4000	231	234	TBDMS
Valine	5 - 2000	[U-^{13}C-^{15}N]-valine	1335	288	294	TBDMS
Leucine	5 - 2000	[U-^{13}C-^{15}N]-leucine	1582	274	281	TBDMS
Isoleucine	5 - 2000	[U-^{13}C-^{15}N]-isoleucine	956	274	281	TBDMS
Proline	5 - 2000	[U-^{13}C-^{15}N]-proline	774	286	292	TBDMS

Analyte	Range [pmol / sample]	Internal standard	IS [pmol / 10 µl]	SIM mass analyte [m/z]	SIM mass IS [m/z]	Derivate
Asparagine	2.5 - 1000	[U-^{13}C]-asparagine	500	285	289	TBDMS
Methionine	5 - 2000	[U-^{13}C-^{15}N]-methionine	445	320	326	TBDMS
Serine	5 - 2000	[U-^{13}C-^{15}N]-serine	725	390	394	TBDMS
Threonine	5 - 2000	[U-^{13}C-^{15}N]-threonine	1022	404	409	TBDMS
Phenylalanine	5 - 2000	[U-^{13}C-^{15}N]-phenylalanine	725	336	346	TBDMS
Aspartate	5 - 2000	[U-^{13}C-^{15}N]-aspartate	1681	418	423	TBDMS
Cysteine	5 - 2000	[U-^{13}C-^{15}N]-cysteine	66	406	410	TBDMS
Glutamate	5 - 2000	[U-^{13}C-^{15}N]-glutamate	1664	432	438	TBDMS
Ornithine	2.5 - 1000	D_7-ornithine	500	474	481	TBDMS
Lysine	5 - 2000	[U-^{13}C-^{15}N]-lysine	643	431	439	TBDMS
Glutamine	10 - 4000	[U-^{13}C-^{15}N]-glutamine	2000	431	438	TBDMS
Arginine	5 - 2000	[U-^{13}C-^{15}N]-arginine	478	442	451	TBDMS
Tyrosine	5 - 2000	[U-^{13}C-^{15}N]-tyrosine	132	466	476	TBDMS
Tryptophane	2.5 - 1000	D_5-tryptophane	1000	244	249	TBDMS

Extracellular concentrations of amino acids were determined by diluting the cultivation medium aliquots 1:10 with water. 10 µl of diluted medium samples or 10 µl calibrator solution were mixed with 50 µl ethanol (p.a.) and spiked with 10 µl internal standard in borosilicate vials and evaporated under N_2-flow at 40 °C. Addition of 20 µl DMF and 10 µl MBDSTFA formed the tert-butyldimethylsilyl derivative after 30 minutes at 75 °C. The injection volume was 1.2 µl and the GC temperature parameters are summarized within Table 27.

Table 27: Parameters for GC-MS analysis of amino acids

Time segment	Rate [°C/min]	Temperature [°C]	Hold time [min]
1	-	90	1.5
2	10	200	11
3	3	240	13.3
4	15	300	4
5		300	10
		Runtime	40

2.2.5.6. Quantification of intra and extracellular glucose by GC-MS

Specifications regarding internal standard, calibration range, and SIM masses are summarized in Table 28. For the calibration curve (nine calibrators per compound), a stock solution of glucose (Table 9) was prepared in ultra-pure water. Calibrators were subsequently diluted to their corresponding concentration and the internal standard was prepared at the indicated concentration.

Table 28: Specifications for the quantification of glucose with GC-MS

Analyte	Range [pmol / sample]	Internal standard	IS [pmol / 10 µl]	SIM mass analyte [m/z]	SIM mass IS [m/z]	Derivate
Glucose	2.5 – 200 ng	D_2-glucose	200 ng	319.1	321.1	MOX-TMS

Intracellular glucose levels were determined by combining 10 µl of internal standard, 50 µl of ethanol (p.a.) along with 10 µl cell extract or 10 µl of calibrator solution into borosilicate vials. For extracellular glucose concentrations, cultivation medium was diluted 1:200 and 5 µl of diluted medium aliquots were mixed with the internal standard and ethanol. The mixtures were briefly vortexed and evaporated under N_2-flow at 40 °C. Derivatization to methyloximes was performed with 10 µl O-methylhydroxyamine hydrochloride in pyridine at a concentration of 10 mg/ml at 60 °C for 30 minutes. Subsequent addition of 40 µl BSTFA formed the Trimethylsilyl-O-methyloxime derivative at room temperature. The injection volume was 1.2 µl and the GC temperature parameters are summarized within Table 29.

Table 29: Parameters for GC-MS analysis of glucose

Time segment	Rate [°C/min]	Temperature [°C]	Hold time [min]
1	-	100	1.5
2	15	180	5.33
3	30	300	6
		Runtime	12.83

2.2.5.7. Quantification of cholesterol by GC-MS

Specification regarding internal standard, calibration range, and SIM masses are summarized in Table 30. For the calibration curve (nine calibrators per compound), a mix of corresponding reference compounds (Table 9) for the quantification of cholesterol from cell extract was prepared in hexane. Calibrators were subsequently diluted to their corresponding concentration and a mix of internal standards was prepared at the indicated concentration.

Table 30: Specifications for the quantification of cholesterol with GC-MS

Analyte	Range [pmol / sample]	Internal standard	IS [pmol / 10 µl]	SIM mass analyte [m/z]	SIM mass IS [m/z]	Derivative
Cholesterol	1000 - 50000	D_5-cholesterol	12500	443.4	448.4	TBDMS
Lathosterol	6.25 - 500	D_7-lathosterol	250	443.4	450.4	TBDMS
Lanosterol	6.25 - 500	D_7-lathosterol	250	393.4	450.4	TBDMS

For the quantification of intracellular cholesterol, lathosterol and lanosterol levels, cell pellets were obtained after extraction and centrifugation from the proposed one-step quench and extraction workflow (2.2.2.4). Cell pellets were spiked with 10 µl of internal standard and subsequently extracted with 500 µl hexane:2-propanol (3:2, v/v) by sonication for 10 minutes. Meanwhile, 10 µl of calibrators were spiked with 10 µl internal standard and subsequently evaporated under N_2-flow at 40 °C and reconstituted in 500 µl hexane in 2-propanol (3:2, v/v). Cell extracts and standards were centrifuged for 10 minutes (Eppendorf, type: 5424R). 400 µl of the supernatant was transferred to a new reaction tube and evaporated under N_2-flow at 40 °C. Samples were saponified with 500 µl 1 M NaOH in 90% Ethanol at 70 °C for 1 hour. After saponification and sample cool down, 250 µl of water and 3 ml of hexane were added to the samples and mixed. Following a centrifugation step at 3000 rpm (Rotina, type: 380R) the organic phase was transferred to a new reaction tube and evaporated to a volume of roughly 1 ml before being transferred and further dried in borosilicate vials. Here, derivatization was achieved by the addition of 20 µl MBDSTFA and 20 µl DMF for 30 minutes at room temperature. For the quantification of cholesterol, samples were diluted 1:10 using 4 µl of sample and 18 µl of DMF and MBDSTFA, respectively. The injection volume was 1.2 µl and the GC temperature parameters are summarized in Table 31.

Table 31: Parameters for GC-MS analysis of cholesterol

Time segment	Rate [°C/min]	Temperature [°C]	Hold time [min]
1	-	150	1
2	30	260	5
3	30	300	20
		Runtime	31

2.2.5.8. Data analysis

For the quantification of metabolite levels from cell extracts, cultivation medium, and cell pellets raw data files were processed with the MassHunter Quantitative Analysis software. Regression curves were established from a dilution series of corresponding calibrators in relation to the

internal standard added at a fixed concentration. 1/x weighted standard curves were calculated based on the peak-area ratio of the analyte to the internal standard against the amount of the analyte. Metabolite levels from unknown samples were subsequently calculated based on these calibration curves. Quality controls ensured accuracy and precision for the analytical run and were prepared in the same way as the calibrators.

2.2.6 Stable isotope resolved metabolomics

Cell extracts from tracing experiments were investigated in a targeted and non-targeted manner using high-resolution LC-MS. 90 µl of cell extract was transferred into 96-well plates (Axygen®), evaporated under N_2-flow at 40 °C, and reconstituted in 45 µl ACN/water (8:2, v/v). Samples were analyzed on an Agilent Infinity 1290 UHPLC coupled to a 6550 iFunnel quadrupole time-of-flight mass spectrometer from Agilent Technologies equipped with a Dual Agilent Jet Stream electrospray source. Electrospray parameters were as follows: gas and sheath gas temperature, 200°C and 300°C; drying gas and sheath gas flow, 11 L/min and 12 L/min; nebulizer pressure, 40 psi; capillary and nozzle voltage, 3000 V and 0 V; fragmentor and octopole radio frequency peak voltage, 125 V and 750 V. The QTOF was operated in the extended dynamic range mode (~ 2GHz) and low mass range (up to 1650 m/z). Measurements were performed in ESI negative mode. Cell, quadrupole, optics and funnel settings were set to the default lipid settings as described by the manufacturer. Fragment spectra were acquired from the unlabeled, pooled cell extracts from the #1 [U-^{13}C] glucose experiment by auto MS/MS as described by Leuthold et al. (Leuthold et al. 2017). Briefly, fragment spectra were collected at a rate of 3 spectra/s for MS1 and MS/MS acquisitions, respectively. A maximum of 3 precursors per cycle that exceeded an absolute threshold of 200 counts triggered MS/MS spectra acquisition. Collision energy (V) was selected based on a function of m/z following Equation 2. The quadrupole band pass for precursor isolation was set to narrow (~1.3 Da).

Equation 2: Calculation of the collision energy as function of m/z

$$\left(3.5 * \frac{\left(\frac{m}{z}\right)}{100}\right) + 7$$

Chromatographic separation of cell extracts was performed using the zwitterionic InfinityLab Poroshell 120 HILIC-Z column with an UHPLC Guard and Eluent A (10 mM AmAc in water, pH 7 with 5 µM InfinityLab Deactivator Additive) and Eluent B (10 mM AmAc in ACN:water (9:1, v:v), pH 7 with 5 µM InfinityLab Deactivator Additive, Table 11). The autosampler was operated at 6 °C, the column oven at 35 °C, and the injection volume was 2 µl. The column was operated at a flowrate of 0.25 mL/min and 35 °C. After the sample injection, the column was kept for 2 min at 90% B followed by gradient elution from 2-12 min (90% to 60% B).

Subsequently, the column was maintained at 60% B for 3 minutes. The column returned to the initial condition from 15-16 min and re-equilibrated for 8 minutes at 90% B before injection of the next sample. Needle wash with 80% ACN in water (8:2, v:v) was applied between injections. The total run time was 24 minutes per sample.

2.2.6.1. Targeted stable isotope resolved metabolomics data analysis

Establishment of the targeted SIRM data preprocessing workflow was based on the VistaFlux Software package (Agilent Technologies, Germany), comprised of MassHunter PCDL Manager (version B.07.00, build 7024.35, service pack 2), MassHunter Pathway to PCDL (version B.07.00, build 19), MassHunter Profinder (version 10.0, build 10.0.10062.0), and Omix Premium (version 1.9.30). In a first step, a reference library (.cdb) of metabolites from central carbon and amino acid metabolism, as well as the adenylate ribonucleotide biosynthesis was generated using MassHunter Pathway to PCDL. Corresponding standards of these metabolites were purchased and prepared as stocks (Table 9). These compounds were diluted 1:1000 with ACN/water (8:2, v/v) for LC-QTOF-MS analysis and investigated for their specific retention times after chromatographic separation as described (2.2.6). Resulting retention times were added to the reference library using MassHunter PCDL Manager (Lackner et al. 2022).

Acquired data from the tracer experiments were preprocessed with MassHunter Profinder using the “Batch Isotopologue Extraction” workflow and the established reference library. The default negative ion species was set to -H, charge state to 1, and the isotope purity was adjusted according to the employed tracer substrate (Table 5). In addition, the extracted ion chromatogram (EIC) was smoothed prior integration using Gaussian smoothing with a function width of 9 points and Gaussian width of 5.000 points. The peak core area was selected as ion abundance criterion and set to 20% of peak height. The mass window corresponded to 15 ppm + 2 mDa, while the retention time window was 0.2 minutes. For isotopologue ion thresholds the anchor ion height was set to ≥ 250 counts and the sum of ion heights to ≥ 1000 counts. The correlation coefficient of the coelution threshold corresponded to ≥ 0.50. After curation (i.e. manual reintegration of falsely integrated peaks) of EICs, results were exported as “Detailed csv” and subsequently imported into R studio (R version 4.0.3) for visualization and statistical analysis. The imported data was processed using the tidyverse package (Wickham et al. 2019), while diagrams and other graphics were generated from the ggplot2 and eulerr package, respectively (Wickham 2016; Larsson J 2021). The total fractional labeling was calculated within R following the equation:

Equation 3: Equation for the calculation of fractional labeling. F_l, fractional labeling in [%]; N, Number of possible isotopic substituents; i, isotopologue, M_i, normalized fractional abundance of corresponding isotopologue in [%]

$$F_l = \frac{1}{N} \times \sum_{i=1}^{N} i \times M_i$$

For statistical analysis, the incorporation of tracer into isotopologues and total fractional labeling between control and treatment was tested followed by correction for multiple testing *via* the Benjamini-Hochberg procedure (Benjamini and Hochberg 1995).

2.2.6.2. Untargeted stable isotope resolved metabolomics data analysis with X^{13}CMS

Untargeted analysis of the ^{13}C tracer from [U-^{13}C] glucose, the ^{13}C, and ^{15}N tracer from [U- ^{13}C, ^{15}N] glutamine (i.e. #1 and #4 experiments in Table 17), was done using the X^{13}CMS approach as previously described (Huang et al. 2014; Llufrio et al. 2019) with method details summarized in Table 32 and using labeled and unlabeled samples from the 24h time point. In short, raw data files (.d) were firstly transformed into .mzXML files by msConvert selecting vendor specific peak picking (Adusumilli and Mallick 2017; Chambers et al. 2012). Converted files from unlabeled and labeled samples were subsequently processed by R studio based XCMS (XCMS version 3.12.0, (Benton et al. 2010; Smith et al. 2006; Tautenhahn et al. 2008). Here peaks were selected using the “centWave” method and corrected for their retention times employing the “obiwarp”-method and saved as the “xcmsSet” object. This object contained grouped and retention-time aligned features of both, unlabeled and labeled samples (Huang et al. 2014). The unlabeled reference samples were required to identify the base peak (lowest m/z of a pair of isotopologues) of labeled features. From the xcmsSet object, X^{13}CMS extracted significantly labeled features (Welch’s t-test comparing relative intensities of unlabeled vs. labeled samples for each isotopologue) in control and treatment (getIsolabelReport), where the tolerance parameters, i.e. mass error (ppm), noise cutoff, and retention time window, had to be fulfilled (Table 32). Significantly labeled features were investigated for a different labeling upon exposure to AZD8186 patterns (getIsoDiffReport) and filtered for their significance between control and treatment after Welch’s t-test (filterIsoDiffReport).

Table 32: Parameter non-targeted SIRM

XCMS parameters		
centWave	ppm	10
	Peakwith	c(10,60)
Obiwarp	Profstep	0.9
	bw	5
	mzwid	0.015
Minidiffreport	varEq	FALSE

XCMS parameters		
	intChoice	intb
X^{13}CMS parameters		
getIsolabelReport	RTwindow	10
	ppm	15
	noiseCutoff	100'000
	intChoice	intb
	alpha	0.05
getIsoDiffReport	varEq	FALSE
	singleSample	FALSE
filterIsoDiffReport	alpha	0.05

2.2.6.3. Metabolite identification from unlabeled samples

For metabolite identification, the final list of filtered features only from the #1 [U-^{13}C] glucose tracer experiment (Table 17) was investigated for corresponding fragment spectra from the auto MS/MS analysis of unlabeled samples with Mass Hunter Qualitative Analysis (Version B.07.00, Agilent Technologies). Spectral information (accurate mass and fragment ions) of these unlabeled MS/MS data was compared against spectral information from the METLIN Metabolite PCDL (Version B.07.00, Agilent Technologies). Identified compounds from database search were then confirmed after spectral comparison of respective pure substances in order to achieve MSI level 1 annotation (Salek et al. 2013; Sumner et al. 2007). Newly identified and confirmed metabolites complemented the established targeted SIRM workflow by adding sum formula and retention time information to the reference library.

2.2.6.4. Untargeted data analysis of unlabeled samples with XCMS functions integrated within X^{13}CMS and with Mass Hunter Profinder

Unlabeled features from the #1 [U-^{13}C] glucose tracer (Table 17) experiment were extracted from the "xcmsSet" object after the X^{13}CMS workflow using the "Minidiffreport()" command. Here, the baseline corrected integrated peak intensities were exported and further processed in R studio. Features were firstly filtered according to a CV cutoff of 20% between technical replicates (n = 3) and subsequently sum normalized (peak area of each feature divided by the sum of peak areas of all features in one sample). Data was then log2-transformed and treatment effects between vehicle and AZD8186 treated samples were statistically evaluated using a Welch's t-test with correction for multiple testing (Benjamini and Hochberg 1995). Finally, only features with an adjusted p-value of < 0.05 and a FC < 0.8 or FC > 1.2 of the mean area between treatment and vehicle were retained for comparison of the different non targeted workflows. Additionally, the same samples, were preprocessed with MassHunter Profinder Software (version B.08.00, Agilent Technologies) using the unlabeled raw data files

(.d) similarly as described (Neef et al. 2020). In brief, features were obtained using “Batch recursive feature extraction” with an intensity threshold of 1000 counts and deprotonated molecular ions (H-) as adducts. In further detail, RT tolerance was set to +/- 0.3 min, and a mass tolerance of +/- 15 ppm +2 mDa for the binning and alignment of features. The EIC range corresponded to +/- 35 ppm and peak integration was performed with the Agile 2 algorithm. Peak spectra with a saturation above 30% were excluded from analysis. After curation of EICs, integrated peak areas were exported as comma separated values (.csv) and further processed using R studio. In a first step, features were filtered with a CV value < 20% between the technical triplicates and subsequent sum normalized and log2-transformed. Statistical testing was done with a Welch’s t-test comparing vehicle and AZD8186 treated cells followed by correction for multiple with Benjamini-Hochberg procedure. At last, features were filtered according to an adjusted p-value of < 0.05 and FC < 0.8 or FC > 1.2 of the mean area between treatment and vehicle.

2.2.6.5. Comparison label-free untargeted metabolomics with untargeted stable isotope labeling for [U-^{13}C] glucose tracer experiment

Resulting features that were obtained after statistical filtering from untargeted analysis of unlabeled samples with XCMS and Profinder (i.e. 2.2.6.4) and those obtained from the X^{13}CMS workflow (i.e. 2.2.6.2 from the #1 [U-^{13}C] glucose experiment) were imported and processed with R studio. Overlaps were determined by aligning respective features by mass and retention time with a mass window of m/z +/- 0.1 and retention time window +/- 5 seconds. Additionally, insignificantly altered features (p-value >0.05) from the unlabeled samples after the XCMS workflow were also overlapped against the features obtained after the X^{13}CMS workflow with identical alignment parameters for mass and retention time tolerance.

2.2.6.6. Comparison of untargeted stable isotope resolved metabolomics of features from [U-^{13}C,^{15}N] glutamine with [U-^{13}C] glucose tracer

Features obtained from the X^{13}CMS workflow (filterIsoDiffReport) for all three tracer atoms (i.e. ^{13}C from #1 [U-^{13}C] glucose, ^{13}C and ^{15}N from #4 [U-^{13}C, ^{15}N] glutamine tracer experiment) were imported and processed with R studio. Overlaps were determined by aligning respective features by mass and retention time with a mass window of m/z +/- 0.5 and retention time window +/- 15 seconds using the fuzzyjoin package in R (Robinson 2020). For metabolite identification, the final list of filtered features for both SIRM experiments (i.e. #1 [U-^{13}C] glucose and #4 [U-^{13}C, ^{15}N] glutamine tracer) experiments was investigated for corresponding fragment spectra from the auto MS/MS analysis of unlabeled samples with Mass Hunter Qualitative Analysis (Version B.07.00, Agilent Technologies). Spectral information (accurate mass and

fragment ions) of these unlabeled MS/MS data was compared against spectral information from the METLIN Metabolite PCDL (Version B.07.00, Agilent Technologies).

2.2.6.7. Cell line comparison of MDA-MB-468 and HCC70 using targeted and untargeted stable isotope resolved metabolomics with [U-^{13}C] glucose tracer

Raw data files from both cell lines were processed as indicated above (2.2.6.2) with X^{13}CMS where resulting features after statistical evaluation (filterIsoDiffReport) were aligned according to mass and retention time with a mass tolerance of m/z +/- 0.5 and retention time window +/- 15 seconds with the fuzzyjoin package in R (Robinson 2020). 22 features could not unambiguously be attributed to a single feature from the opposite cell line due to multiple feature candidates for corresponding alignment parameters. The resulting list of 184 features was thereby reduced to 162 unique features (Figure 39).

Targeted analysis of overlapping features and 6-PG were performed as described (2.2.6.1) for the 24h sampling time point. The incorporation difference (i.e. delta incorporation) of overlapping features between cell lines was calculated based on the difference in average label incorporation from three technical replicates using the following equation:

Equation 4: Calculation of the delta incorporation based on the average label incorporation in the MDA-MB-468 and the HCC70 cell lines

$$Delta\ incorporation\ [\%] = Average\ label\ incorporation\ (HCC70 - (MDA - MB - 468))$$

For statistical analysis, the incorporation of tracer into isotopologues between the HCC70 and the MDA-MB-468 cell line was tested followed by correction for multiple testing *via* the Benjamini-Hochberg procedure (Benjamini and Hochberg 1995).

For metabolite identification, the final list of cell line specific unique features was investigated for corresponding fragment spectra from the auto MS/MS analysis of unlabeled samples with Mass Hunter Qualitative Analysis (Version B.07.00, Agilent Technologies) as previously described 2.2.6.3. Features that could not be identified by this approach, were additionally investigated by SIRIUS4 (Dührkop et al. 2019). To this end, fragment spectra of cell line specific unique features from the auto MS/MS analysis of unlabeled samples were exported as .mgf files from Mass Hunter Qualitative Analysis (Version B.07.00, Agilent Technologies). Corresponding files were then imported into SIRIUS4 and analyzed as previously reported (Dührkop et al. 2019) using parameters detailed in Table 33. Identified compounds were then confirmed after spectral comparison of respective pure substances in order to achieve MSI level 1 annotation (Salek et al. 2013; Sumner et al. 2007).

Table 33: Computational parameters for feature identification with SIRIUS4

SIRIUS Molecular Formula Identification & CSI:Finger ID – Structure Elucidation	
Instrument	QTOF
MS/MS Isotope Scorer	Score
MS2 Mass Dev (ppm)	15
Candidates	10
Candidates per Ion	1
Databases	HMBD & PubChem
Possible Ionizations & Fallback Adducts	$[M - H]^-$

.

3. Results

3.1. Establishment of a sampling and processing workflow

For the investigation of metabolic changes in cell culture a suitable sample preparation protocol needs to address several issues. Rapid inactivation of metabolic activity by quenching ensures the closest possible representation of the metabolite profile after sampling. Analyzing intracellular metabolites requires a wash step prior cell harvest to reduce interferences arising from intermediates present in or excreted to the cultivation medium. Furthermore, knowledge on the storage stability of extracted metabolites enables flexible analysis of samples throughout a defined period. Lastly, a systematic assessment of different pre-analytical normalization procedures is pivotal to assess potential bias resulting from different sample amounts and corresponding effects on metabolite concentration. To this end, the sample preparation workflow was assessed and optimized in MDA-MB-468 cells with respect to (i) metabolism quenching, (ii) storage condition and stability, (iii) wash procedures, and (iiii) preanalytical normalization methods. The optimization efficacy of these parameters was evaluated by targeted metabolomics, considering quantitative data of adenylated ribonucleotides, intermediates of glycolysis, pentose phosphate pathway, and TCA cycle.

3.1.1 Optimization of sample preparation

3.1.1.1. Quenching of metabolism

Quenching of metabolism was investigated comparing liquid nitrogen quench and subsequent extraction with 80% MeOH (- 80 °C) or simultaneous quench and extraction of metabolites with ultra-cool 80% MeOH (- 80 °C). One-step quench and extraction of metabolites from cultured cells with ultra-cool MeOH resulted in higher levels of adenylated ribonucleotides (sum AMP, ADP, and ATP) and a significantly higher energy charge compared to the liquid nitrogen quench (Figure 12 A). The levels of ADP and AMP were comparable across both quench approaches (i.e. range between 5 to 10 pmol/ng $_{(DNA)}$) and not significantly changed ($p > 0.5$). In contrast, the levels of ATP were 2.3 fold higher when the one-step quench was performed, which in turn resulted in a significantly ($p < 0.05$) elevated energy charge of 0.86. Based on these findings, the single quench and extraction procedure with ultra-cool MeOH was selected as method of choice to efficiently interrupt metabolic activity and was employed for further optimization of the sample preparation.

3.1.1.2. Storage condition and stability

For the examination of the effect of sample storage on adenylated ribonucleotide levels and energy charge, control samples stored for one day at – 80 °C (2.2.2.2) were compared to those

stored at -80 °C for three weeks (Figure 12 B). Stored samples were further investigated for the effect of solvent evaporation to dryness compared to keeping them in the original extraction solvent (i.e. 80% MeOH). ATP levels dropped by approximately one third when metabolite extracts were stored under dry conditions, while AMP and ADP levels remained at comparable levels for all three approaches (0.72 to 0.95 and 4.15 to 4.54 pmol/$ng_{(DNA)}$, respectively). Nevertheless, under both storage conditions, the change in metabolite levels (i.e. AMP, ADP, and ATP) was insignificant compared to the control samples. Interestingly, samples stored in extraction solvent did not suffer from diminished recovery of adenylated ribonucleotides but rather displayed increased ATP levels leading to a higher energy charge of 0.97. The energy charge remained largely unaffected by the storage indicated by an energy charge of > 0.95 across all storage conditions.

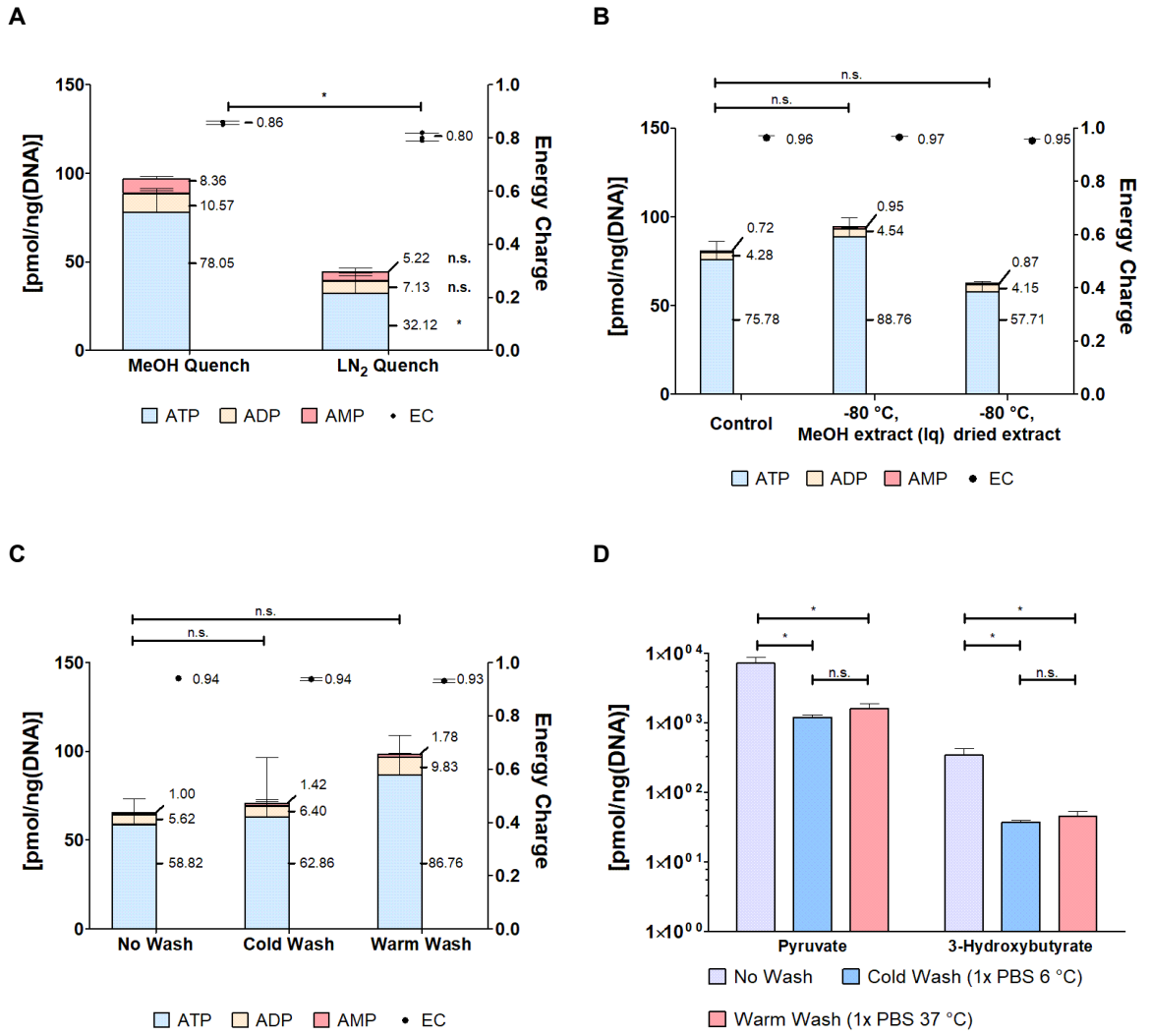

Figure 12: Optimization of quench and sample processing regarding cellular energy charge (EC) and adenylated ribonucleotide concentrations. The MDA-MB-468 cell line was cultivated for 24h and subjected to the indicated conditions during sample preparation (n=3). (A) Comparison of quenching with liquid nitrogen *vs.* one-step quenching and extraction with ultra-cool 80% MeOH (-80 °C). (B) Influences of storage conditions for different sample processing routines after MeOH quench. Sample storage was assessed either under dry conditions (i.e., evaporated extraction solvent = "dried extract") or in extraction solvent (i.e. "lq" = 80% MeOH), for three weeks at –80 °C. (C, D) Investigation of different washing procedures prior to applying metabolite quenching and extraction on ribonucleotide levels, EC, pyruvate and 3-hydroxybutyrate. * $p < 0.05$ (Welch's t-test)

3.1.1.3. Washing procedure

With respect to the assessment of metabolite removal during washing, cells that were washed with warm PBS displayed higher levels of ribonucleotides while showing an energy charge of 0.93 (Figure 12 C). Interestingly, cold wash resulted in similar ribonucleotide levels, as well as a similar energy charge compared to no washing. The washing efficiency was further evaluated based on the excreted intermediates pyruvate and 3-hydroxybutyrate which are present in cultivation medium (Figure 12 D). Regardless of the employed washing procedure, both metabolites were significantly removed ($p < 0.05$) indicated by a tenfold reduction in metabolite levels compared to if no washing was applied. Similarly, to the adenylated ribonucleotides, washing with warm PBS led to elevated levels of pyruvate and 3-hydroxybutyrate.

3.1.2 Normalization of quantitative metabolomics

Pre-analytical normalization to DNA concentration is commonly applied in cell culture metabolomics, however, this approach requires additional steps of DNA isolation and analysis (Silva et al. 2013). Normalization to cell count by live cell imaging is a convenient alternative, as the cell count can be readily determined under cultivation conditions in a non-invasive manner, thus allowing higher sample throughput (Nybo and Lamberts 2019). To analyze whether normalization to DNA content is comparable to normalization *via* cell count by live cell imaging, cells were cultivated for 24h and images were acquired and compared with DNA levels determined after lysis and extraction from the same wells. Cell count and DNA content strongly correlated with a coefficient of determination of $R^2 > 0.97$ (Figure 13 A). Next, the performance of the two normalization routines was assessed with respect to the repeatability of measurements of metabolite levels from glycolysis, TCA cycle, and adenylated ribonucleotides (n=3 technical replicates, Figure 13 B). DNA normalization showed a significantly ($p < 0.001$) higher variability (mean CV 22%) compared to normalization based on cell count (mean CV 6%). This is also reflected in a higher variability for most of the metabolites (e.g., G6P, 3PG, and ATP) with CV values > 20% (DNA normalization). On the contrary, the cell counts normalized data typically displayed a CV of less than 10% for most of the metabolites (Appendix 1).

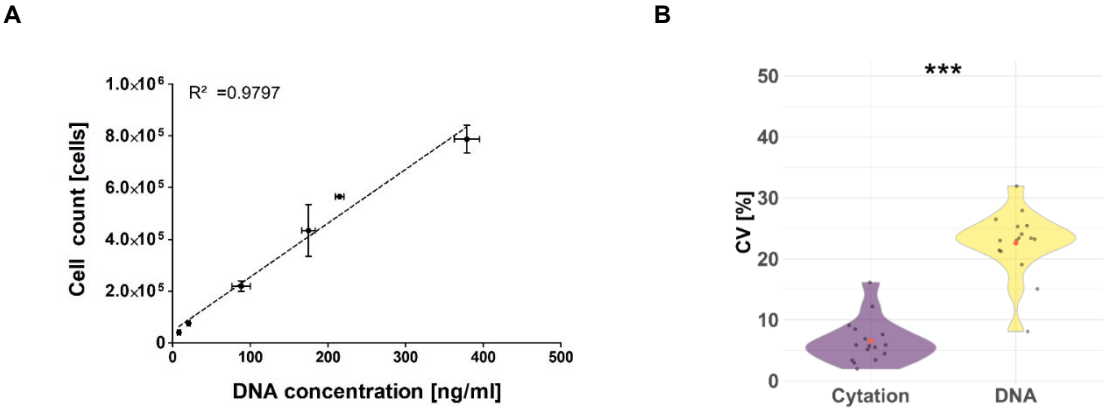

Figure 13: Examination of different normalization strategies for quantitative metabolomics. MDA-MB-468 cells were cultivated for 24h prior image acquisition and metabolite extraction (A) Linear regression for DNA concentration vs. cell count obtained from MDA-MB-468 cells and corresponding cell homogenates, respectively. (B) Distribution of CV values from three technical replicates for the two normalization approaches. Mean levels and standard deviations were determined for different intermediates (i.e. G1P, G6P, F16BP, 3PG, PEP, 6PG, Pentose5P, Sed7P, pyruvate, citrate, a-ketoglutarate, fumarate, malate, 3-hydroxybutyrate, ADP and ATP, Appendix 1). *** $p < 0.001$ (two-tailed Welch's t-test)

Taken together, the optimized sample preparation workflow for the metabolomics analysis of adherent mammalian cancer cells was found to benefit from a washing step with cold (i.e. 4 °C) 1x PBS and a subsequent simultaneous quenching and extraction with ultra-cool (i.e. – 80 °C) 80% MeOH on dry ice (Figure 14). Furthermore, worked up samples could be stored at -80 °C in its' corresponding extraction solvent (i.e. 80% MeOH) for at least three weeks without noticeable degradation in adenylated ribonucleotide levels. Cell-count normalized data was found to be more robust compared to DNA concentration normalized data and was therefore used as the normalization procedure of choice for subsequent metabolomics experiments.

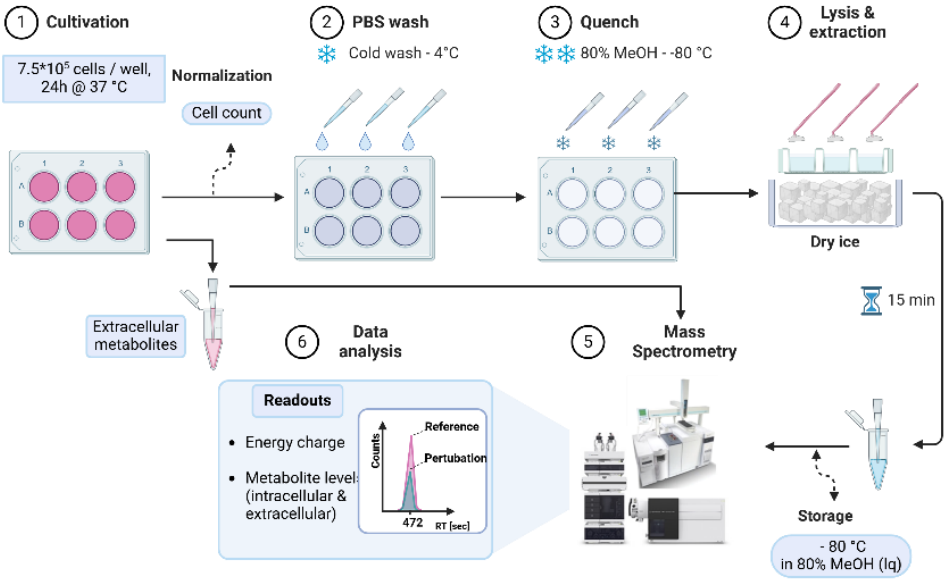

Figure 14: Optimized sample preparation protocol for metabolomics analysis used for further establishment of the SIRM platform (**3.3**). After cell cultivation (1), extracellular metabolites were quickly removed by washing with cold PBS (2). A one-step quench and extraction procedure ensured interruption of any metabolic activity (3) and cell detachment by scraping followed by lysis and metabolite extraction on dry ice (4). Data acquisition on mass spectrometers (i.e. GC-MS, TQ-MS) (5) allowed determination of metabolite levels from adenylated ribonucleotides, glycolytic, and TCA cycle intermediates (6). For quantitative analysis, metabolite levels were normalized to cell count by live cell imaging. Created with BioRender.com

3.2. Functional assessment and validation of breast cancer cell lines upon PI3Kβ inhibition

The two TNBC cell lines (i.e. PTEN WT MDA-MB-231 and PTEN-null MDA-MB-468) were characterized with respect to inhibition of PI3Kβ by AZD8186 (Hancox et al 2015) and corresponding effects on AKT signaling pathways, cell metabolism and cell growth. These investigations allowed to (1) ensure cell line integrity (i.e. PTEN protein expression for PTEN WT and confirmation of PTEN absence in PTEN-null cell line, (2) enable drug dose finding with respect to (i) modulation of the pAKT signaling pathway (i.e. phosphorylation at $pAKT_{Thr308}$ and $pAKT_{Ser473}$) and (ii) metabolic phenotype (i.e. steady state metabolomics and refined dose finding with real time metabolic flux analysis and steady state metabolomics) and (3) confirm impaired cell growth at refined drug dose. Altogether, these functional assessments and comprehensive cell line characterization were an important pre-requisite for the establishment of the SIRM workflow *in vitro* (3.3).

3.2.1 Effects of PI3Kβ inhibition on AKT signaling pathway

Concentration dependent effects (in the range 0.01 – 3 µM) of AZD8186 on MDA-MB-231 and MDA-MB-468 cells were investigated by immunoblotting (Figure 15). As expected, PTEN was only detectable in the MDA-MB-231 but not in the PTEN-null cell line. Furthermore, both cell lines showed expression of PI3Kβ, thereby indicating the presence of the inhibitor's drug target. Expression levels of PI3Kβ were not altered upon exposure to different concentrations of the inhibitor AZD8186 (0.01- 3 µM). Moreover, the Threonine phosphorylation site was not detectable in the MDA-MB-231 cell line while for the PTEN-null cell line, a concentration dependent decrease in the phosphorylation was noticeable upon inhibition of PI3Kβ. At a concentration of 3 µM, pAKT phosphorylation was not detectable anymore, especially the $pAKT_{Ser473}$ displayed either a higher sensitivity over the entire concentration range or had lower expression levels compared to $pAKT_{Thr308}$ in the MDA-MB-468 cell line. Expression of $pAKT_{Ser473}$ in the MDA-MB-231 cell line was lower compared to the MDA-MB-468 cell line regardless of the presence of the inhibitor.

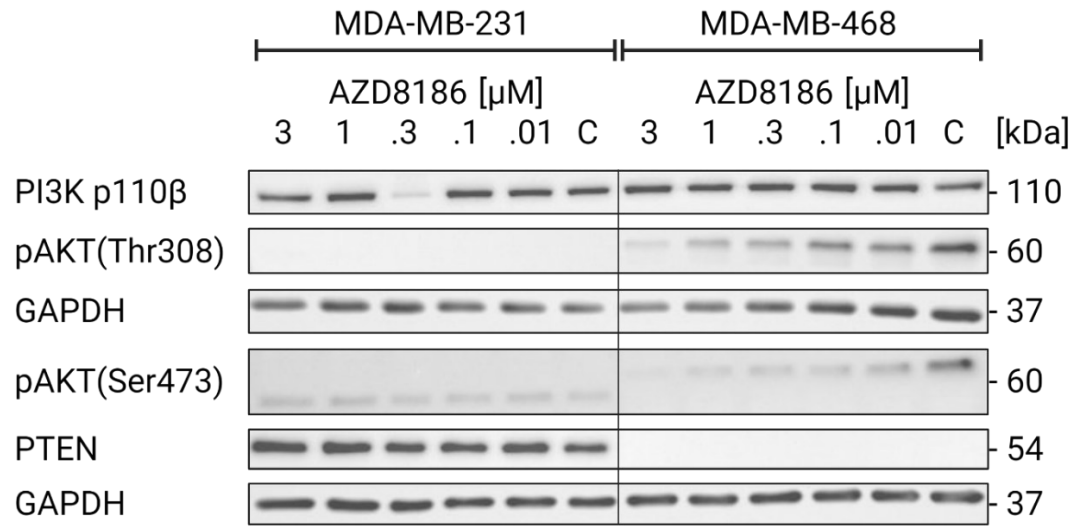

Figure 15: Assessment of protein expression within PI3K/AKT signaling pathways in the TNBC cell lines MDA-MB-231 and MDA-MB-468 upon exposure to the indicated concentration of AZD8186. Cells were seeded at $1*10^6$ cells/well and treated for 24h with the inhibitor. Protein extracts were analyzed by western blotting for the expression of PTEN, PI3K p110β, $pAKT_{Thr308}$ and $pAKT_{Ser473}$. Expression of GAPDH was used as loading control. (C; Vehicle control)

3.2.2 Effect of PI3Kβ inhibition on the metabolic phenotype

Exposure to AZD8186 was assessed at the metabolite level. To this end, metabolites within pathways relevant to cancer metabolism (i.e. glycolysis, TCA cycle, amino acid biosynthesis, and ribonucleotide *de novo* synthesis) were analyzed by targeted (i.e. GC-MS and TQ-MS, 2.2.5). Aside from estimating drug responses from intracellular metabolite levels, extracellular metabolic rates (i.e., metabolite uptake and excretion) were assessed to ensure that tracer substrates (glucose and glutamine) are taken up by the cells as important prerequisite for the establishment of a SIRM platform. Moreover, additional knowledge about cell line's metabolite consumption and excretion profile can be helpful in the interpretation of SIRM data at a larger stage. In addition, real time metabolic flux analysis (i.e., Seahorse Flux analysis, 2.2.3.3) was carried out to investigate the effect of PI3Kβ inhibition on mitochondrial respiration and glycolysis for refined dose finding.

3.2.2.1. Effect of AZD8186 within cancer relevant pathways

Cells were cultivated for 24h with 3 µM AZD8186 and worked up according to the optimized sample preparation protocol (3.1). Exposure to AZD8186 lead to a significant decrease of glycolytic (e.g., G6P, F16BP, 3PG, etc.) and TCA cycle intermediates (e.g., citrate, α-ketoglutarate, fumarate, and malate) while adenylated ribonucleotides were not significantly altered (Figure 16 A). Likewise lactate and pyruvate as the final product of the glycolysis were found reduced upon PI3Kβ inhibition. The observed intracellular depletion of lactate aligns well with a threefold compromised excretion rate of lactic acid (Figure 16 B). Furthermore, no

additional fueling of the TCA cycle by increased glutamine uptake was observable. Interestingly, the metabolic rates of aspartate and alanine remained unchanged by the presence of the inhibitor. In addition, there was no significant change in the uptake rate of glucose in treated cells, which aligns well with the findings from intracellular levels of glucose (Figure 16 A).

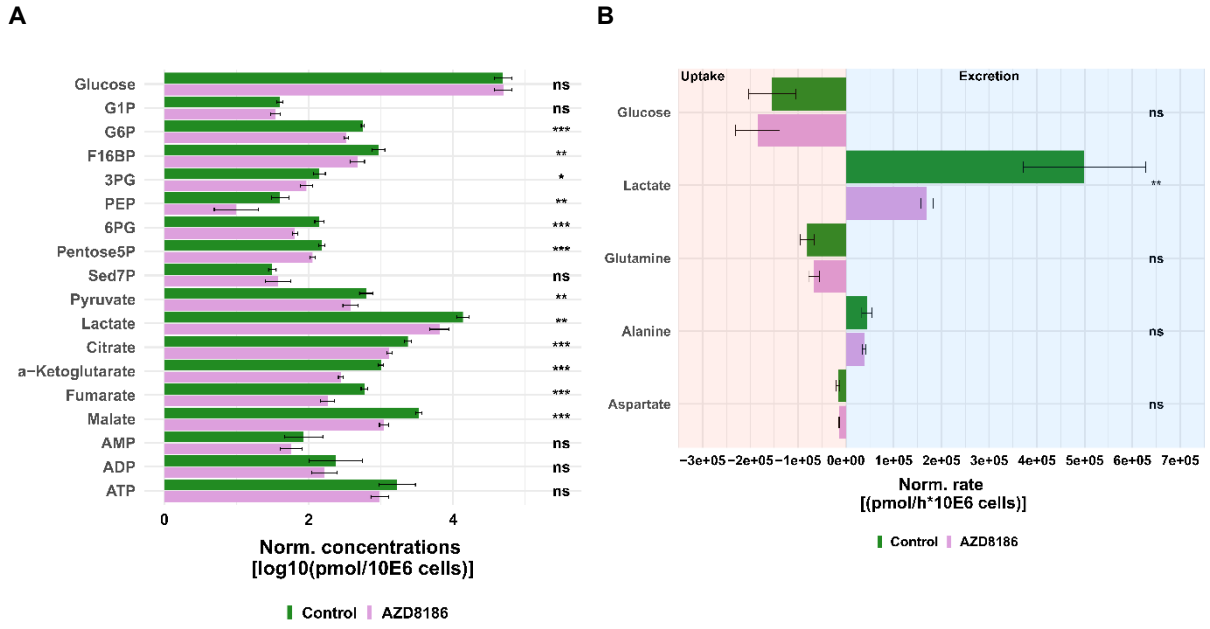

Figure 16: Steady state quantitative metabolomics in cell extracts and corresponding cultivation medium obtained after 24h incubation of MDA-MB-468 cells treated with 3 µM AZD8186. (A) Intracellular levels of glycolytic, TCA cycle intermediates and adenylated ribonucleotides. (B) Metabolic rates of respective intermediates determined from cultivation medium aliquots. Bar charts ± standard deviation (n=6 technical replicates) showing mean levels of corresponding intermediates. * p< 0.05; ** p< 0.01 (adjusted p-value; Welch's t-test)

Regarding metabolic uptake and secretion rates irrespective of PI3Kβ inhibition, glucose and glutamine both displayed the highest uptake rate (- 1 to ~- 1.5*10^5 pmol/h*10^6 cells) of all investigated extracellular metabolites underlining their suitability as tracer substrate for the establishment of the SIRM platform (Figure 16 B). As expected, lactate was excreted at the highest rate (5*10^5 pmol/h*10^6 cells), while the excretion rate of alanine corresponded to only 0.5 *10^5 pmol/h*10^6 cells. Although there was only minor aspartate uptake noticeable (0.25 *10^5 pmol/h*10^6 cells), the contribution of unlabeled aspartate during tracing experiments needs to be considered when interpreting labeling data at a later stage.

3.2.2.2. Optimization of AZD8186 concentration with real time metabolic phenotyping using Seahorse XF analyzer and steady state metabolomics

The effect of different AZD8186 concentrations regarding real time measurement of glycolysis was assessed. This allowed an insight into dose-dependent effects of PI3Kβ inhibition on the two major energy producing pathways (i.e. glycolysis and OXPHOS), thereby enabling a refined treatment dose to be employed for the establishment of the SIRM workflow (3.3). To

this end, the PTEN WT MDA-MB-231 and the PTEN-null MDA-MB-468 cell line were treated with different concentrations of AZD8186 (i.e. range from 0.1 µM to 3 µM, Figure 17). Inhibition with AZD8186 led to a concentration dependent decrease of basal glycolysis as well as OXPHOS activity (i.e. prior addition of Rot/AA) indicated by ECAR and OCR in the PTEN-null cell line (Figure 17 A, B). Already at the lowest employed concentration (i.e. 0.1 µM) a drop in ECAR from 1.3 to ~ 1 and in OCR from 5.8 to 5 compared to the vehicle was noticeable. On the contrary, the PTEN WT cell line displayed only at the two highest concentrations (i.e. 1 and 3 µM) a noticeable decrease in the ECAR compared to the vehicle, while in general the OCR remained largely unaffected (Figure 17 A, B). Exposure to 0.5 µM AZD8186 did not lead to noticeable differences in glycolytic or OXPHOS activity in the PTEN WT MDA-MB-231 cell line. Interestingly, the vehicle treated controls of both cell lines showed metabolically different phenotypes (Figure 17 C). The PTEN-null cell line had a higher OXPHOS activity (higher basal OCR) while the PTEN WT cell line showed an increased glycolytic activity (higher basal ECAR). Moreover, the relationship between OXPHOS and glycolytic activity, as seen as the mitoOCR/glycoPER ratio (Figure 17 D), indicated a concentration dependent shift from glycolysis towards higher OXPHOS activity (increasing mitoOCR/glycoPER), which was significantly elevated at an inhibitor concentration of 3 µM for the PTEN negative cell line. This tendency was also noticeable for the PTEN WT cell line at concentrations > 1 µM, although it remained insignificant over the entire concentration range.

A

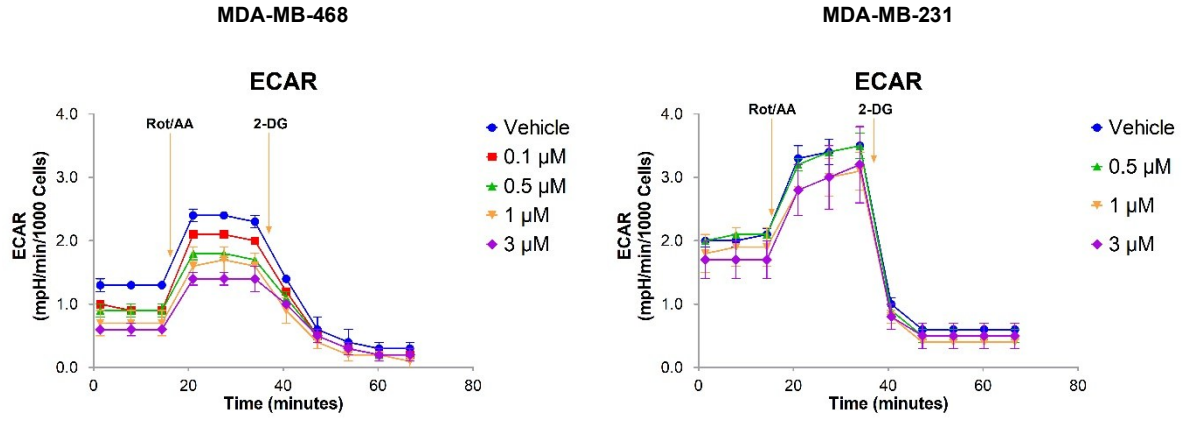

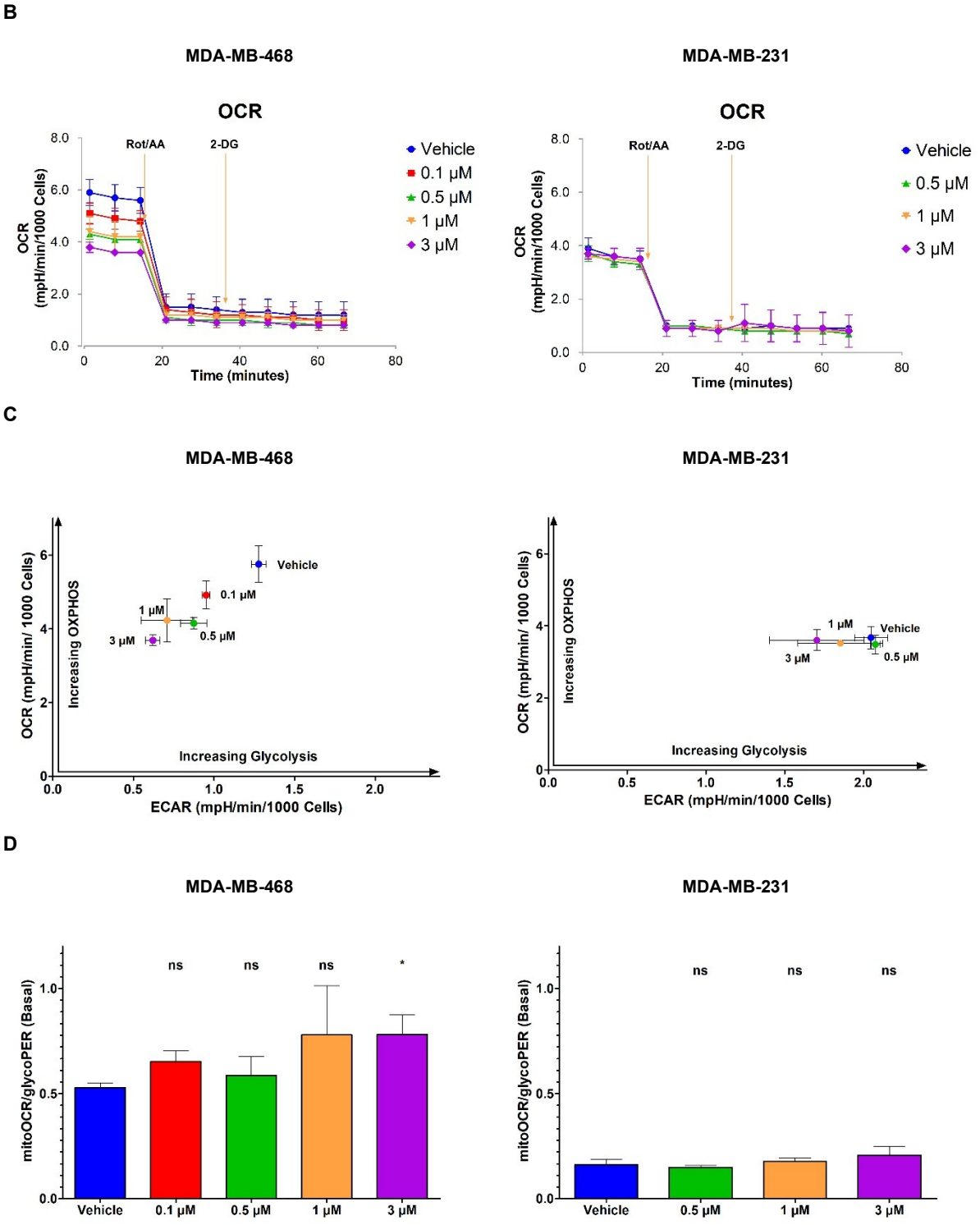

Figure 17: Extracellular flux analysis using Seahorse XF Glycolytic Rate assay. (A) Extracellular consumption rate (ECAR) and (B) Oxygen Consumption rate (OCR) of MDA-MB-468 and MDA-MB-231 treated with indicated concentrations of AZD8186. (C) Basal metabolic profile obtained from the mean of OCR and ECAR values measured after 1, 8 and 14 minutes into the assay. (D) OXPHOS vs. glycolytic activity indicated by basal mitoOCR/glycoPER ratio. Assay data from the 0.1 µM concentration used in the MDA-MB-231 cell line were not interpretable as data normalization could not be performed and are therefore not displayed. Data points and bar charts ± standard deviation (n=3 technical replicates) * $p < 0.05$ (two-tailed Welch's t-test)

The observations from the real time glycolytic analysis were reassessed with quantitative metabolomic analysis of metabolites related to OXPHOS (i.e. TCA cycle intermediates pyruvate, citrate, a-ketoglutarate, fumarate and malate) and ECAR (i.e. excretion rate of lactic

acid) for the MDA-MB-468 cell line at AZD8186 concentrations ranging from 0.5 - 3 µM. As depicted in Figure 18, intracellular levels of TCA cycle intermediates, as well as excretion rates were significantly reduced at all investigated concentrations.

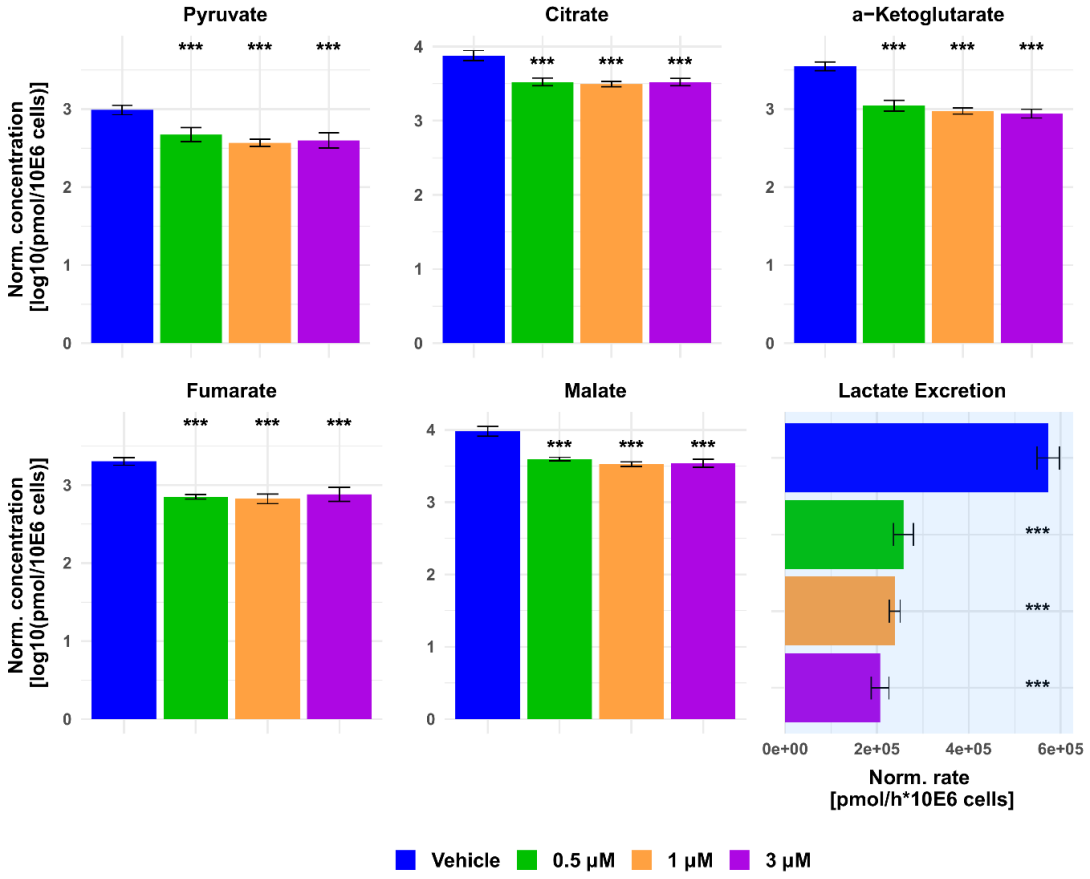

Figure 18: Quantitative metabolomics of cell extracts from MDA-MB-468 cells and corresponding cultivation medium after incubation with AZD8186 at the indicated concentrations for 24h. Intracellular levels of TCA cycle intermediates and excretion rate of lactate. Bar charts ± standard deviation (n=6 technical replicates) showing mean levels of corresponding intermediates. * p< 0.05; ** p< 0.01, *** p< 0.001 (adjusted p-value; Welch's t-test)

In conclusion, AZD8186 concentration exceeding 1 µM demonstrated disturbed glycolytic activity even in the PTEN WT cell line. Applying a lower concentration (i.e. 0.5 µM) of the inhibitor did not show an impaired glycolytic activity in the MDA-MB-231 cell line, whilst glycolytic and TCA cycle activity was still significantly affected in the PTEN-null cell line determined by real time metabolic phenotyping and steady state metabolomics. Consequently, 0.5 µM represented the lowest concentration that displayed inhibitory activity on glycolysis and TCA cycle metabolism while at the same time no metabolic impairments as seen in the PTEN WT cell line at higher concentrations (i.e. > 1 µM), were detectable.

3.2.3 Effect of PI3Kβ inhibition on cell growth

The PTEN-null cell line was examined with respect to effects of the refined AZD8186 concentration (i.e. 0.5 µM) on cell growth for a treatment duration of up to 72h. To this end, the

cell count was determined after 0h, 24h, 48h and 72h (Figure 19). At the beginning of the time series (i.e. 0h), cell count was not significantly different between the vehicle and the treatment condition. However, already after 24h, the cell count was significantly lower in AZD8186 treated cells. Over the course of this experiment (i.e. 48h and 72h), cells continued to grow significantly slower displayed by the diminished cell count in the treatment condition. After 72h the cell count in the vehicle treated cells corresponded to ~4.3*10^5 cells compared to 3.7*10^5 cells in AZD8186 treated cells. In conclusion, employment of the refined 0.5 µM AZD8186 concentration did not only lead to diminished glycolytic and TCA cycle activity (3.2.2), but also significantly reduced proliferation in the PTEN-null cell line for an extended duration of three days.

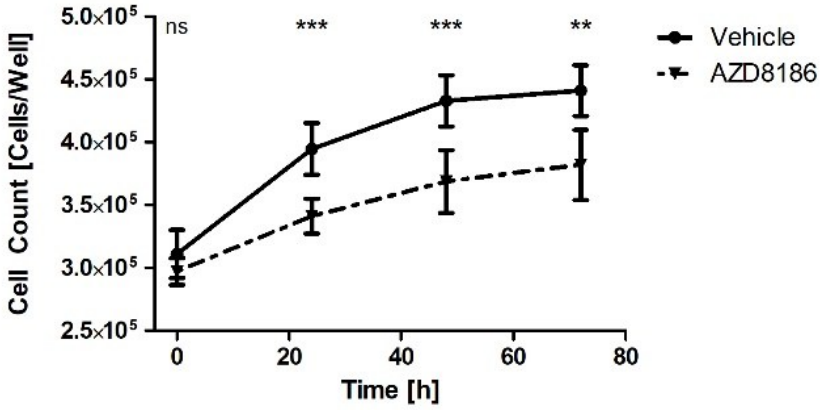

Figure 19: Proliferation assay of MDA-MB-468 over a period of 72h treated with 0.5 µM AZD8186. Data points ± standard deviation (n=3 technical replicates) * p< 0.05; ** p< 0.01, *** p< 0.001 (two-tailed Welch's t-test)

3.3. Application of the optimized sample preparation protocol to stable isotope tracing experiments

Based on the established sample preparation protocol (3.1) and optimized dosing AZD8186 (3.2.2.2), a SIRM workflow from cell culture to data analysis and visualization in R was developed. To assess drug-induced metabolic changes upon PI3Kβ inhibition the workflow was applied to MDA-MB-468 cells treated with the selective inhibitor AZD8186 or vehicle following the fate of labeled glucose and glutamine (3.4) into glucose and glutamine derived intermediates (Figure 20). Cell extracts from time series experiments were measured by high-resolution LC-mass spectrometry and acquired data were processed using two different approaches. The first approach was based on an established targeted library of preselected intermediates from the central carbon metabolism, amino acid metabolism and ribonucleotide biosynthesis while the second approach harnessed the untargeted data analysis capabilities of the R based package X^{13}CMS (Huang et al. 2014). Resulting candidate structures from untargeted analysis were confirmed by matching retention time and fragment spectra of corresponding reference compounds. These newly identified metabolites complemented the existing targeted library. Further characterization of the SIRM workflow was done based on (i) comparison of untargeted SIRM to tools commonly used for label-free non-targeted metabolomics (Profinder´s batch recursive feature extraction and XCMS), (ii) robustness evaluation in regards to label-incorporation for intra-day and inter-day experiments using the complemented targeted library and (iiii) detailed assessment of drug-induced alterations in pathway activities and intermediates from the complemented targeted library.

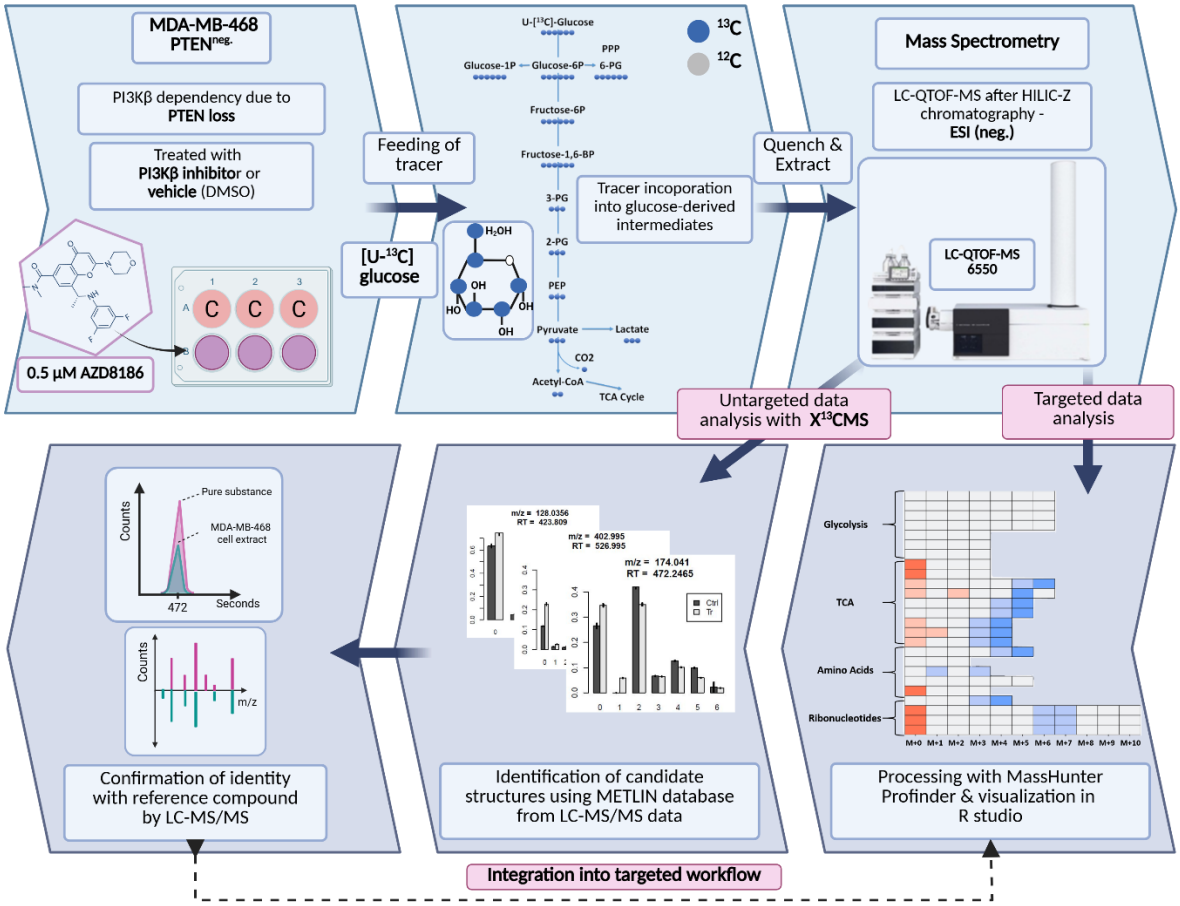

Figure 20: Schematic of the SIRM workflow for tracer experiments exemplary shown for [U-^{13}C] glucose. Cells were cultivated in glucose (or glutamine) tracer containing RPMI medium supplemented with 0.5 µM AZD8186 or vehicle. Cells were harvested after multiple time points according to the optimized quench and extraction protocol. Cell extracts were measured with LC-QTOF-MS and the obtained data analyzed in a targeted as well as untargeted manner. Targeted data analysis was performed with the MassHunter Profinder software environment and harnessed a metabolite library with corresponding sum formulas, masses, and retention times. Untargeted analysis with X^{13}CMS (Huang et al. 2014) produced a list of differentially labeled metabolites between drug treated and control conditions. Fragment spectra from unlabeled cell extracts allowed the assignment of potential candidate structures from the X^{13}CMS feature list. Metabolite identity was confirmed by the corresponding pure substance, its retention time, and fragment spectra. Finally, the identified metabolites were integrated into the targeted SIRM workflow. Adapted from Lackner et al. 2022

3.3.1 Untargeted data analysis with X^{13}CMS of the #1 [U-^{13}C] glucose tracer experiment

Features with differential labeling patterns between controls and AZD8186 treated cells were detected with X^{13}CMS using a multi-step process (Figure 21 A). In the first step, a base peak list used for the identification of labeled features is extracted from the unlabeled reference samples with the miniDiffReport() function within the X^{13}CMS package. Here, 12.391 unique features with corresponding *m/z* values and retentions times were identified (Lackner et al. 2022). From that, 416 unique ^{13}C-enriched isotopologue groups reported as 360 and 310 compounds identified in control and AZD treated cells, respectively (Lackner et al. 2022). Of these, the majority (254, 61%) was found in both conditions, while 106 (25%) features were solely detectable in the control cells and 56 (13%) in the AZD8186 treated cells (Figure 21 B). After comparison between the two conditions with IsoDiffReport, 286 features displayed

significant changes in their labeling pattern upon PI3Kβ inhibition compared to control (Lackner et al. 2022). Of these, 106 (38%) and 56 (20%) features were solely found in the control and treatment condition, respectively, while the common pool of features was reduced to 124 (42%) features (Figure 21 C).

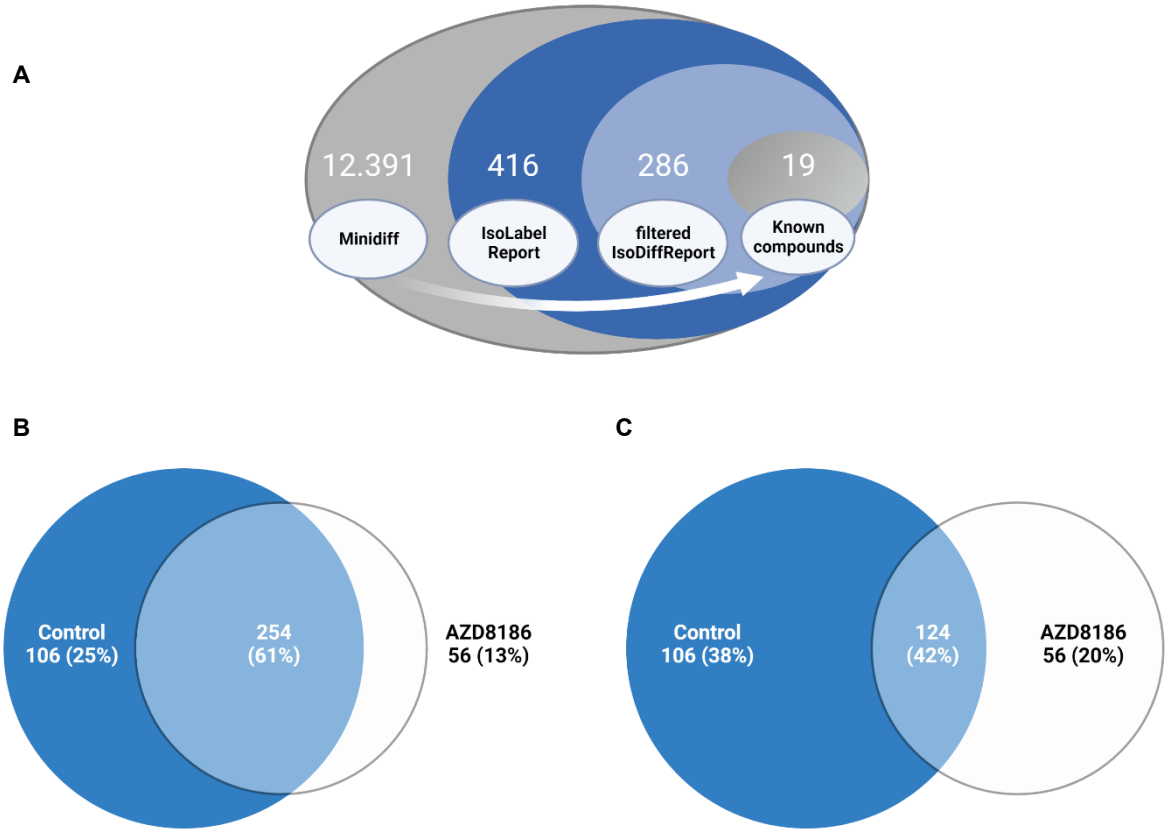

Figure 21: Differential labeling analysis of MDA-MB-468 cells treated for 24h with vehicle or 0.5 µM AZD8186. A: Schematic display of the feature filtering procedure with the number of features obtained in the different processing steps. B: Euler diagram of total labeled isotopologue groups in vehicle and AZD8186 treated cells (IsoLabelReport). C: Euler diagram of differentially labeled isotopologue groups between vehicle and AZD8186 treated cells (filterIsoDiffReport). Adapted from Lackner et al. 2022

Metabolite identification

From the significantly altered features determined by the untargeted data analysis filtering procedure (Figure 21 A), 19 could be attributed to known compounds from the established targeted library (i.e. TCA cycle, glycolysis, and ribonucleotide biosynthesis). Further 11 metabolites were identified from their respective fragment spectra with corresponding pure reference compounds. These identified metabolites were associated with the ribonucleotide biosynthesis (UDP, UTP), the mevalonate pathway (3-hydroxy-3-methyl glutaric acid, 3H3MG), amino acid (NAA, pyroglutamic acid) and glutathione (GSH, GSSG) metabolism, as well as the hexosamine pathway (UDP-GlcNAc, UDP-glucose, CMP-NANA, NANA) and were added to the preexisting library (Appendix 2). Thus, metabolites identified by the untargeted

X^{13}CMS analysis allowed the extension to assess AZD8186 treatment effects within pyrimidine biosynthesis, mevalonate and hexosamine pathways.

3.3.2 Comparison of label-free untargeted metabolomics with untargeted stable isotope labeling

To evaluate the overlap and differences between the untargeted SIRM approach and conventional label-free non-targeted metabolomics, the 286 features obtained from untargeted isotope labeling were compared with the unlabeled features from the miniDiffReport() and after MassHunter Profinder preprocessing of unlabeled samples. To this end, the miniDiffReport() function within the X^{13}CMS package extracted 12.391 features from the unlabeled samples (Lackner et al. 2022). After CV filtering (CV < 20% of three technical replicates), as well as p-value and fold change filtering (adjusted p-value <0.05, FC < 0.8 or, FC > 1.2), 322 features were significantly altered by the inhibitor (Lackner et al. 2022). Preprocessing of unlabeled samples with MassHunter Profinder resulted in 490 features. After CV and p-value/fold change filtering similar to above (CV < 20%, adjusted p-value < 0.05, FC < 0.8 or, FC > 1.2), 20 features remained (Lackner et al. 2022). Comparison of the feature recovery by the respective workflows displayed an overlap of 10 features for all three approaches (Figure 22 A). The processed miniDiffReport shared 16 features with labeled X^{13}CMS workflow, whereof six features were exclusively recovered by both workflows, while the Profinder workflow shared 11 features with the X^{13}CMS workflow with only one feature solely recovered by both workflows. Interestingly, label-free analysis with Profinder workflow only recovered features that were also covered by the XCMS workflow and/or the X^{13}CMS workflow.

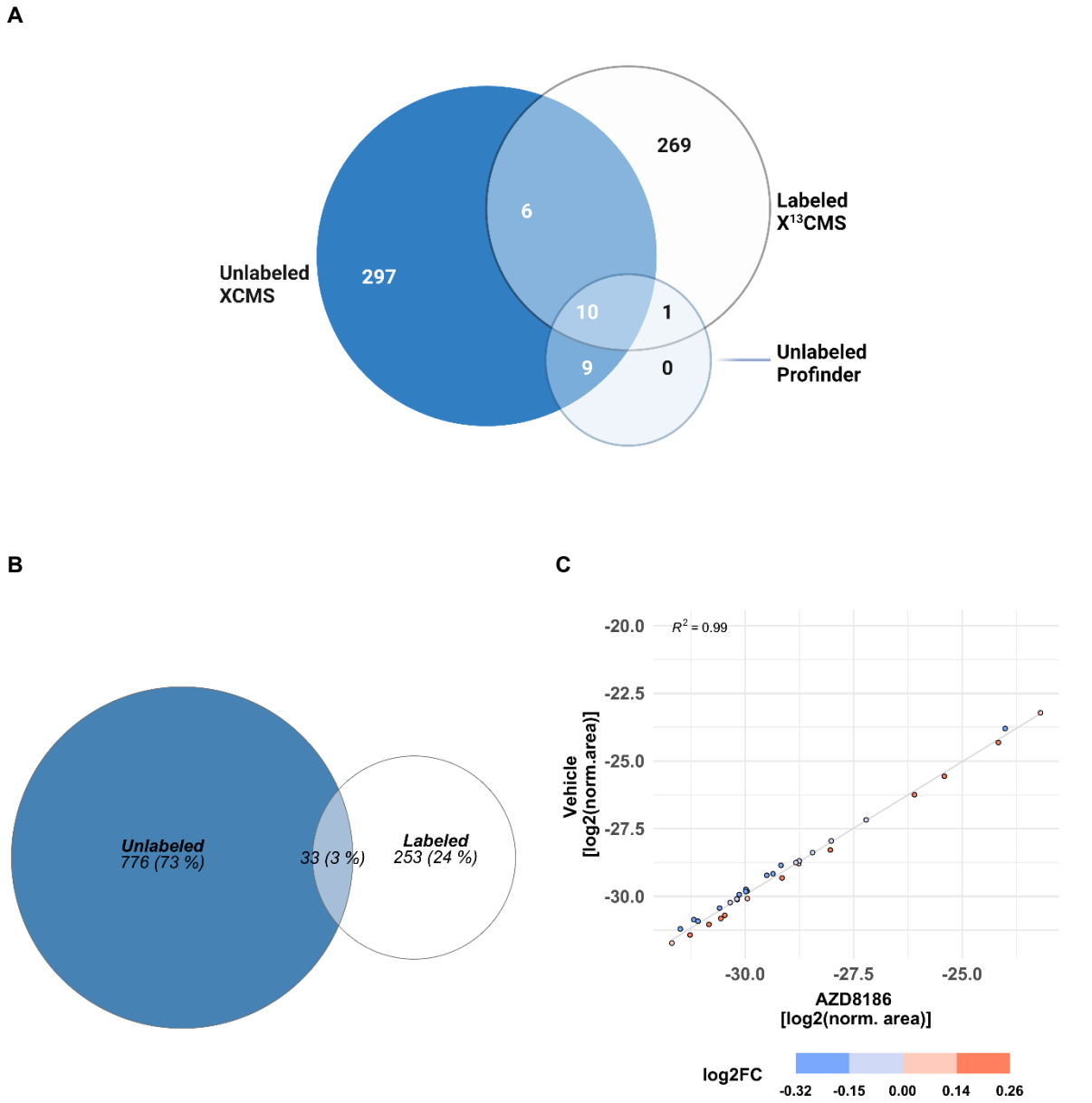

Figure 22: A: Comparison of significantly altered features related to AZD8186 treatment identified by untargeted SIRM ("Labeled $X^{13}CMS$") compared to results obtained upon data pre-processing with vendor-dependent Profinder and XCMS (i.e. miniDiffReport export) in unlabeled samples followed by statistical testing. (n = 3 technical replicates, unlabeled and labeled samples after 24h cultivation with 0.5 µM AZD8186. FC < 0.8, FC > 1.2, Welch's t-test, and BH-adjusted p_{adj} < 0.05). Adapted from Lackner et al. 2022. B: Determination of overlapped features from insignificant features of the Minidiffreport (i.e. Minidiffreport export, n = 3, FC > 0.8, FC < 1.2, Welch's t-test, and BH-adjusted p_{adj} > 0.05) and the 286 features obtained after $X^{13}CMS$ workflow. C: Display of the log2 normalized area (vehicle vs. AZD8186) from the resulting 33 overlapped features

The potential complementary role of the SIRM workflow was also assessed by comparing the 286 unique features from the $X^{13}CMS$ workflow from Figure 22 A, with the insignificantly changed features from the label free samples obtained from the Minidiffreport. This comparison showed how SIRM can detect drug-induced metabolic changes that would have otherwise been overlooked by conventional label-free metabolomic. To this end, features from the Minidiffreport were processed similarly with a CV filter of < 20% between the technical replicates and log2 normalized. After statistical testing and correction for multiple testing, only

features with an adjusted p-value of $p > 0.05$ and a fold change (normalized area of treatment vs. control) of $0.8 < FC < 1.2$ were retained. After these processing steps, the normalized area of 809 features was found to be insignificantly altered between the vehicle and treatment condition (Figure 22 B). Comparing these features with the 286 features extracted after the X^{13}CMS workflow yielded an overlap of 33 features from which three could be structurally identified as pyruvate, malate, and glutamate. Although X^{13}CMS revealed significantly altered labeling patterns for these 33 features, the normalized area of these 33 features correlated well between the two treatment conditions (R^2 of > 0.99) (Figure 22 C) indicating only a minor influence of the inhibitor on the presence of the feature. Taken together, these findings illustrate the importance of the complementary role of the untargeted SIRM approach, where features would have been overlooked by conventional label-free untargeted metabolomics, although significant drug-induced changes on the metabolic pathway activity were apparent.

3.3.3 Robustness evaluation of SIRM workflow

The performance of the entire SIRM workflow was evaluated by comparison of the isotopologue distributions of 35 metabolites from the targeted library (Lackner et al. 2022, Appendix 2) utilizing the processing pipeline from MassHunter Profinder (Lackner et al. 2022). Intra-day reproducibility was evaluated by technical replicates based on all 1585 isotopologues of the 35 metabolites comprising both, untreated and treated conditions as well as all sampling times (Figure 23 A, Lackner et al. 2022)

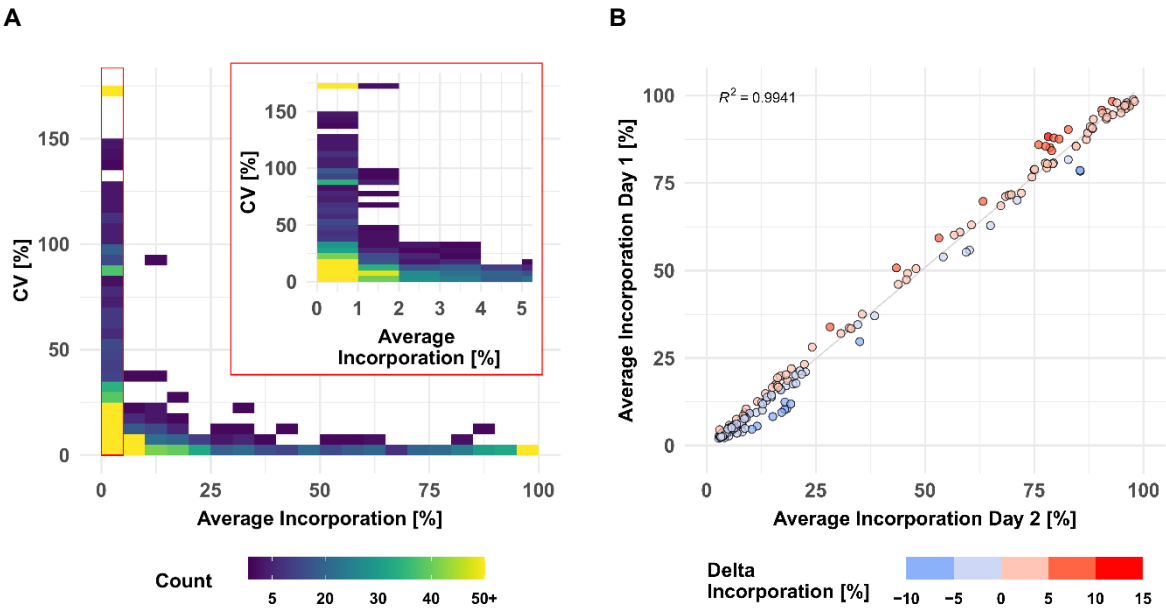

Figure 23: SIRM robustness evaluation after targeted workflow based on metabolites from extended targeted library. A: CV of technical replicates against average incorporation as density plot (Day 1 data set, samplings 1, 3, 6, and 24h, n = 3, 1585 isotopologues, binwidth = 5%). B: Day-to-day reproducibility of SIRM experiments indicated as average tracer incorporation on Day 1 vs. Day 2 (tracer incorporation >2% and <100%). Tracer incorporation after 3h cultivation with [U-^{13}C] glucose and 0.5 µM AZD8186. Adapted from Lackner et al. 2022

Tracer incorporation was highly reproducible for technical replicates with an average incorporation between 40 and 100% and a CV value of <5%. Only eight isotopologues out of 269 in this range had a CV value above 10%. The CV value increased with lower label incorporation. From 220 isotopologues in the range from 10 to 35% label incorporation, only three isotopologues displayed CV values above 25% while 26 isotopologues had a CV value between 10 to 25%. The remaining 191 isotopologues had a CV below 10% indicated by the high isotopologue count in this range. Only with tracer incorporations of less than 10% the data became more variable, and especially incorporations of less than 2% became highly imprecise. Here, 228 out of 762 isotopologues had a CV between 25 to 150% where further 81 isotopologues displayed a CV value of more than 150%. Although the variability with low levels of label incorporation (0-2%) increased, 453 from the 762 isotopologues still displayed high reproducibility with a CV value below 25% from which 223 even had a CV value below 10%.

Inter-day repeatability of the SIRM workflow was evaluated with an independent tracer experiment performed on a different day and the tracer incorporation dynamic into 33 out of 35 metabolites from the targeted library of both experiments was compared for 3h and 1h time points (Lackner et al. 2022). As described above, low levels of tracer incorporation (< 2%) can lead to higher variations of the respective data, while the presence of an m+0 isotopologue at a fractional labeling of 100% is indicative of an unlabeled molecule. Therefore, isotopologues with less than 2% or 100% incorporation were excluded from the correlation analysis. Overall, only 6 metabolites differed by more than 6% of the average incorporation between day one and day two at an incubation time of 3h, yielding a strong correlation (R^2 > 0.99) of the tracer incorporation dynamic on different days (Figure 23 B, Lackner et al. 2022). This positive association was confirmed by correlation analysis of isotopologues from the 1h time point resulting in a R^2 >0.99 (Appendix 3, Lackner et al. 2022).

3.3.4 Integrated targeted SIRM workflow upon PI3Kβ inhibition – [U-^{13}C] glucose

Next, the tracer incorporation in treated and untreated MDA-MB-468 cells was examined for the 35 metabolites to investigate the impact of AZD8186 (Figure 24). Here, illustrating these metabolites in time resolved heat maps over the course of the experiment allowed a first assessment and perception of alterations in corresponding labeling patterns, where a final interpretation of labeling patterns will be done for exemplary metabolites.

3.3.4.1. PI3Kβ inhibition affects glycolysis

Incorporation of ^{13}C tracer from glucose into glycolytic intermediates occurs within minutes. Consequently, the respective metabolites from G6P to PEP reach isotopic steady state with near complete labeling already at the first time point (1h) making it impossible to assess drug induced changes of the glycolytic flux with these metabolites (Appendix 4 A & B). This in turn results in no observable differences in labeling patterns after the 3h time point (Figure 24). Nevertheless, the labeling pattern of pyruvate with diminished fractional enrichment of the m+3 isotopologue (Appendix 5 A) and corresponding increased proportion of the unlabeled m+0 isotopologue points to reduced glycolytic ^{13}C-flux upon treatment noticeable starting after 3h (Figure 24). Lactate, as further end product of glycolysis, displayed a similar isotope pattern, thereby indicating a potential beneficial effect of PI3Kβ inhibition on aerobic glycolysis. Irrespective of pharmacological effects, the occurrence of only m+6 labeling in the hexose-6-phospate (i.e., F6B and F16BP) pool indicates low basal level of fructose bisphosphatase activity (Jang et al. 2018; Lorkiewicz et al. 2019) in MDA-MB-468 cells. This is further supported by only trace quantities of m+3 labeling detected in metabolites along upper glycolysis (e.g. G6P, Appendix 5 B). Interestingly, G1P, formed from G6P by phosphoglucomutase shows the most pronounced effect at 1h (Figure 24). A strong decrease

of the m+6 isotopologue accompanied by elevated m+0 indicates reduced substrate availability for glycogen or other downstream biosynthetic reactions (e.g. UDP-glucose production).

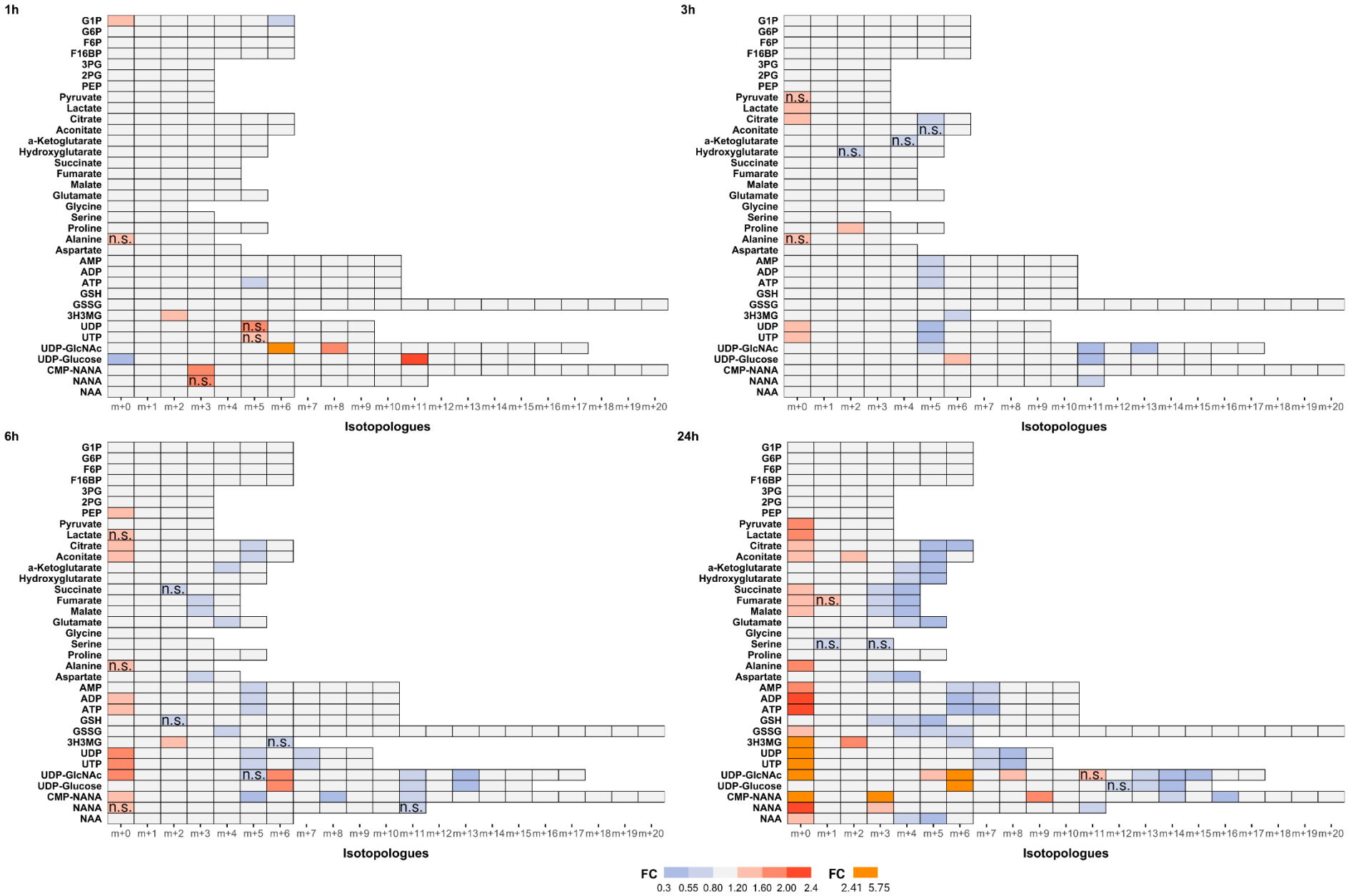
1h
3h
6h
24h
G1P
G6P
F6P
F16BP
3PG
2PG
PEP
Pyruvate
Lactate
Citrate
Aconitate
a-Ketoglutarate
Hydroxyglutarate
Succinate
Fumarate
Malate
Glutamate
Glycine
Serine
Proline
Alanine
Aspartate
AMP
ADP
ATP
GSH
GSSG
3H3MG
UDP
UTP
UDP-GlcNAc
UDP-Glucose
CMP-NANA
NANA
NAA
n.s.
m+0 m+1 m+2 m+3 m+4 m+5 m+6 m+7 m+8 m+9 m+10 m+11 m+12 m+13 m+14 m+15 m+16 m+17 m+18 m+19 m+20
Isotopologues
FC
0.3 0.55 0.80 1.20 1.60 2.00 2.4
FC
2.41 5.75

Figure 24: Impact of AZD8186 treatment on ^{13}C tracer incorporation into different metabolic pathways at indicated time points. MDA-MB-468 cells were cultivated in RPMI with [U-^{13}C] glucose and treated with 0.5 µM AZD8186 or vehicle. Fold changes (AZD8186 vs. vehicle) of the individual isotopologues were calculated from the average labeling fraction of three technical replicates per condition and are represented by the indicated color code and isotopologues colored when FC <0.8 and >1.2 and tracer incorporation >3%. G1P, glucose-1 phosphate, G6P, glucose-6 phosphate, F16BP, fructose-1,6,-bisphosphate, 3PG, 3-Phosphoglycerate, 2PG, 2-Phosphoglycerate, PEP, Phosphoenolpyruvate, 3H3MG, 3-hydroxy-3-methylglutarate; AMP/ADP/ATP, adenosine mono/di/triphosphate, GSH, glutathione; GSSG, oxidized glutathione; UDP/UTP, uridine di/triphosphate; UDP-GlcNAc, uridine diphosphate N-acetylglucosamine; NANA, N-acetylneuraminate, CMP-NANA, CMP-N-acetylneuraminate, NAA, N-acetylaspartate. Glutamine was disregarded due to minor ^{13}C incorporation after 24h. Adapted from Lackner et al. 2022

3.3.4.2. Alterations within TCA cycle upon PI3Kβ inhibition

Opposed to glycolytic intermediates, incorporation of tracer into TCA cycle intermediates takes longer and relevant treatment effects (i.e. FC < 0.8 or FC > 1.2) became apparent after 3h (Figure 24). Here, the reduced ^{13}C-flux into pyruvate upon PI3Kβ inhibition carried over into TCA cycle metabolites displayed by diminished tracer incorporation (FC < 0.8) in isotopologues generated after multiple rounds of TCA (>m+2) and elevated presence of the unlabeled m+0 isotopologues (FC > 1.2). In more detail, pyruvate is produced from PEP and can either enter the TCA cycle after oxidative decarboxylation to acetyl-CoA *via* pyruvate dehydrogenase (PDH) or as oxaloacetate *via* pyruvate carboxylase (PC) which is referred to as pyruvate anaplerosis (Figure 7 A and D). Here, the route of pyruvate entry into mitochondrial metabolism can be deduced from the m+2 vs. m+3 isotopologue profiles of citrate.

Citrate showed high relative proportion (>45%) of the m+2 isotopologues at early labeling times (i.e. 1h, Figure 25 A), both in controls and treated cells suggesting conversion to acetyl-CoA *via* pyruvate dehydrogenase (PDH) as the predominant route of carbon feeding into the cycle and subsequent citrate synthase activity. Entry of $^{13}C_3$-pyruvate as oxaloacetate *via* pyruvate carboxylase plays only a minor role as evidenced by a low proportion of the m+3 isotopologue in citrate and other TCA cycle intermediates. The reduced fractional enrichment of these isotopologues upon treatment at later times (i.e. 3h, 6h, Figure 25 B, C) points to compromised carbon feeding *via* PDH. In line with these findings, Lynch et al. demonstrated upregulation of the pyruvate dehydrogenase kinase (PDHK4) and increased PDH phosphorylation in HCC70 cells upon PI3Kβ inhibition, indicative of reduced carbon flux (Lynch et al. 2017). Aside from the PC activity, the occurrence of higher isotopologues (i.e. m+3, m+4, m+5) also displayed the transition from first round of TCA cycle into second or multiple rounds of TCA cycle and became more apparent over the course of the experiment (Figure 7 B, C). After 24h the m+5 and m+6 isotopologue occurred at a significantly higher proportion compared to the treated cells, emphasizing the impaired tracer incorporation from PDH activity upon exposure to AZD8186 (Figure 25 D). Interestingly, at this point the formation of the m+1 and m+3 isotopologue of citric acid was higher in treated cells, supporting reduced carbon flux from glycolysis as larger pool size of unlabeled acetyl-CoA in treated cells could produce these labeling patterns. At the same time the m+2 citrate pool size is also higher in treated cells,

which can lose one of the labeled carbons during the TCA cycle eventually ending up as an m+1 isotopologue. The m+3 isotopologue on the other hand is then produced i.a. from the combination of the m+1 citrate and fully labeled acetyl-CoA.

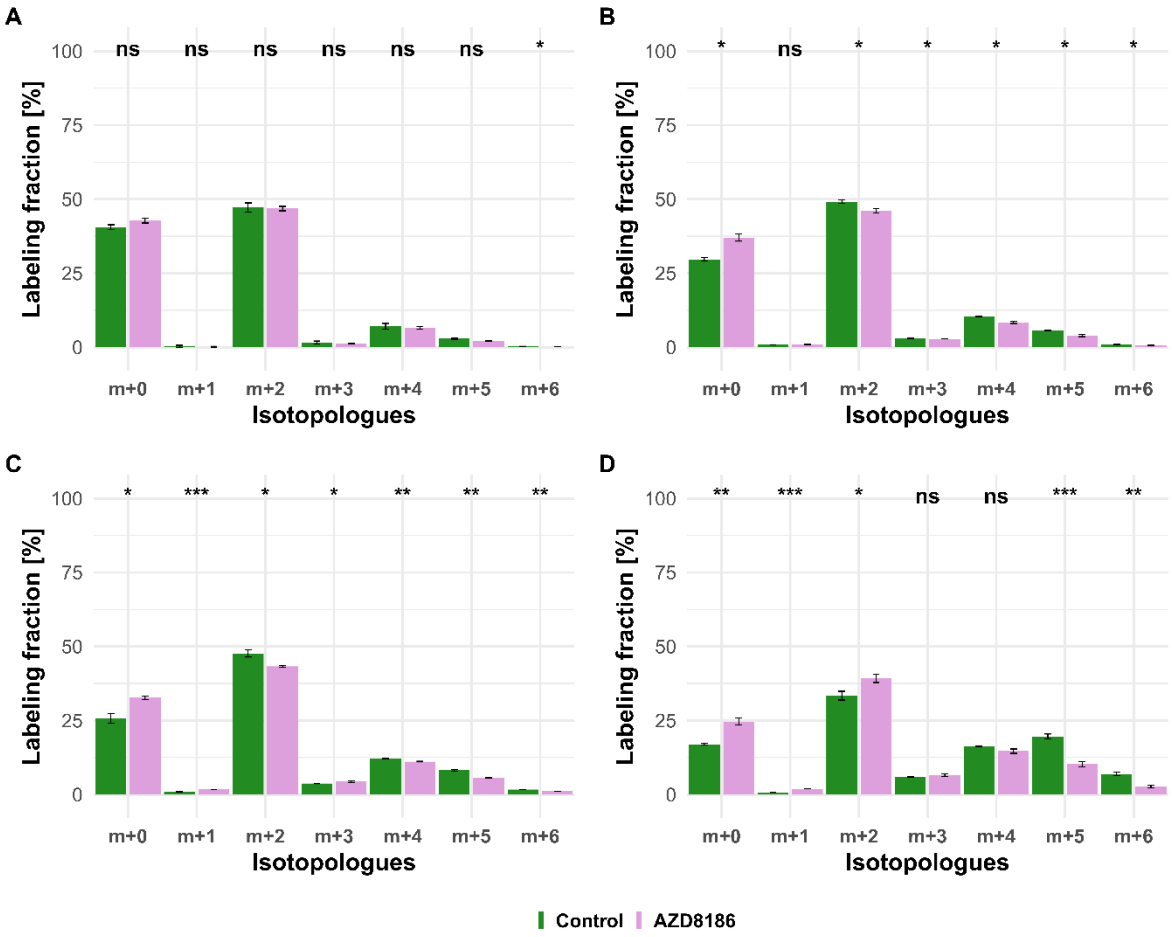

Figure 25: MDA-MB-468 cells were cultivated in RPMI with [U-^{13}C] glucose and treated with 0.5 µM AZD8186 (purple) or vehicle (green). Bar charts ± standard deviation (n=3 technical replicates) showing the fractional enrichment of ^{13}C into citrate at 1h (A), 3h (B), 6h (C) and 24h (D) sampling times. * p< 0.05; ** p< 0.01 (adjusted p-value; Welch's t-test)

As indicated above, m+3 isotopologues can also be produced *via* multiple rounds of TCA cycle and therefore leading to false assumptions about pyruvate carboxylase activity. To this end, the m+3 isotopologues of aspartate, malate and fumarate were compared against the m+3 isotopologue of succinate. Here, the m+3 isotopologue pattern of corresponding intermediates were distinguishable from succinate, on the one hand confirming PC activity, while reduced incorporation into m+3 also pointed towards diminished PC activity upon PI3Kβ inhibition after 24h (Figure 26 A, B). The m+3 and m+4 isotopologue patterns of α-ketoglutarate did not match (i.e. label incorporation) with the m+3 isotopologue of aspartate, malate (Appendix 6) and fumarate, indicating no fumarate reductase activity within this cell line (Figure 26 C) (Buescher et al. 2015).

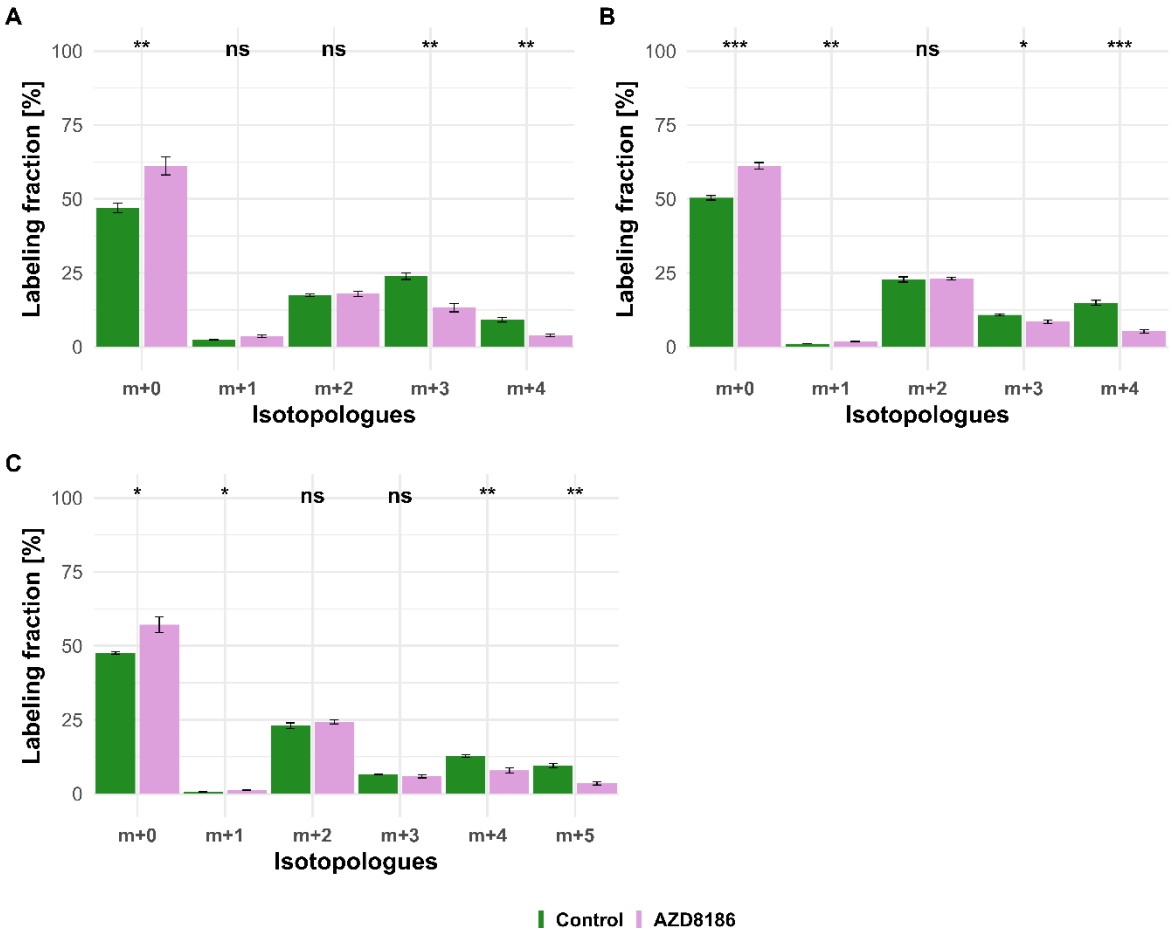

Figure 26: MDA-MB-468 cells were cultivated in RPMI with [U-^{13}C] glucose and treated with 0.5 µM AZD8186 (purple) or vehicle (green). Bar charts ± standard deviation (n=3 technical replicates) showing the fractional enrichment of ^{13}C at 24h into (A) fumarate, (B) succinate, and (C) α-ketoglutarate. * p< 0.05; ** p< 0.01 (adjusted p-value; Welch's t-test)

3.3.4.3. Tracing of glucose derived carbons in the biosynthesis of amino acids

The biosynthesis of alanine is directly linked to the glycolysis as it is biosynthesized *via* alanine aminotransferase (ALT1/2) using carbon from pyruvate and nitrogen from glutamate (Choi and Coloff 2019). Consequentially, diminished labeling in alanine originated from reduced ^{13}C incorporation into pyruvate and was observable after 1h. Over the course of the experiment, carbon feeding into alanine remained reduced as indicated by the elevated presence of the unlabeled m+0 isotopologue (FC >1.2, Figure 24) and was significantly lower after 24h compared to the vehicle treated control. Glutamate on the other hand, can either be synthesized from glutamine *via* glutaminolysis and the glutaminase enzyme in a deamination reaction or from the TCA cycle intermediate α-ketoglutarate *via* reductive amination from branched-chain amino acids using branched-chain amino transferases (BCAT1/2) (Figure 8, Choi and Coloff 2019). In this regard, glutamate displayed similar labeling patterns at 24h (Figure 27 A, B) compared with α-ketoglutarate, suggesting branched chain amino acid transferase activity. Furthermore, the reduced carbon flux from the TCA cycle carried over into

the biosynthesis of glutamate, where the m+4 isotopologue showed diminished levels in treated cells after 6 and 24h (FC <0.8, Figure 24). While reduced tracer incorporation was observable for these intermediates, the comparable labeling patterns point towards unaffected branched chain amino acid transferase activity upon exposure to AZD8186 (Figure 27 A, B). On the other hand, glutamine can be *de novo* synthesized from glutamate *via* the enzyme glutamine synthetase, although minor tracer incorporation (i.e. <1.3%) was only observable for the m+2 isotopologue (Figure 27 C). Moreover, tracer incorporation was not significantly different between the treatment conditions, pointing towards unaffected glutamine synthetase activity.

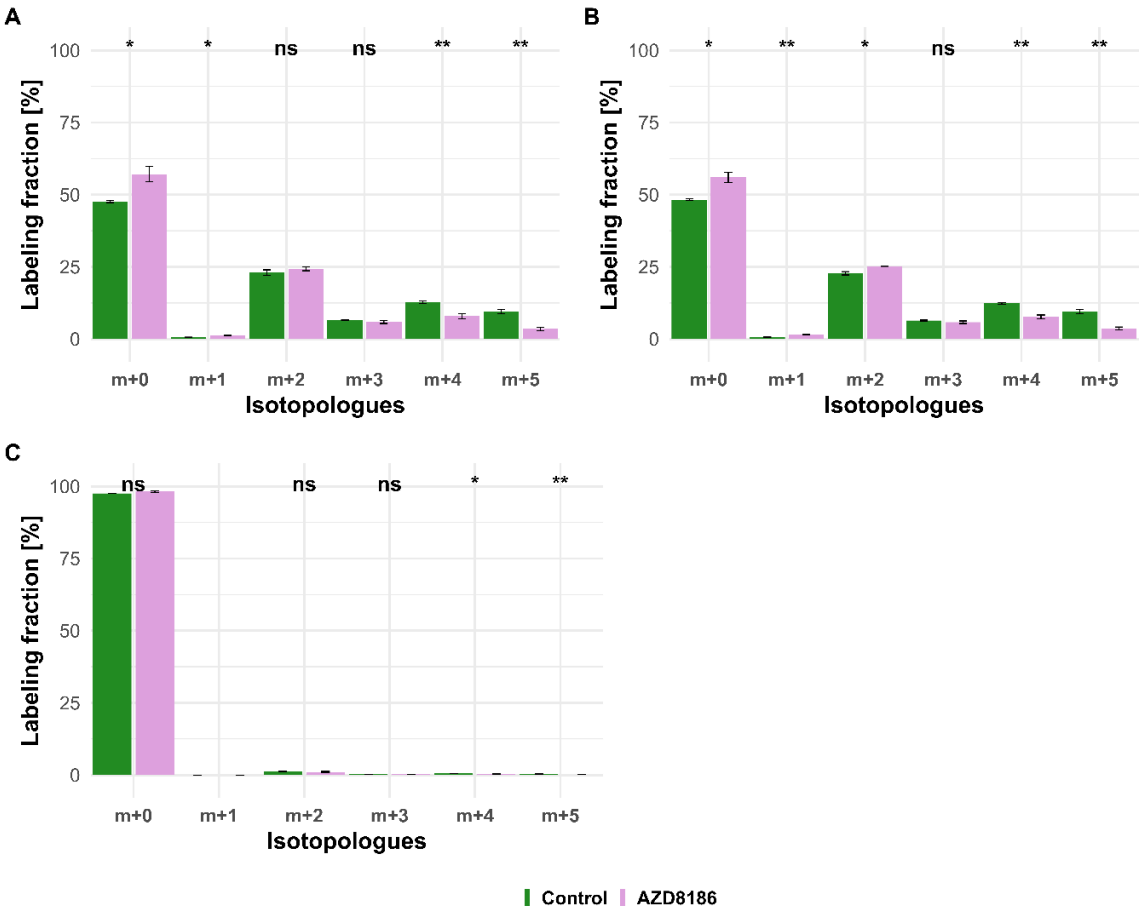

Figure 27: MDA-MB-468 cells were cultivated in RPMI with [U-^{13}C] glucose and treated with 0.5 µM AZD8186 (purple) or vehicle (green). Bar charts ± standard deviation (n=3 technical replicates) showing the fractional enrichment of ^{13}C at 24h into (A) α-ketoglutarate, (B) glutamate, and (C) glutamine. * p< 0.05; ** p< 0.01 (adjusted p-value; Welch's t-test)

As described earlier (3.3.4.1), drug related effects were not efficiently resolved in glycolytic intermediates, consequentially tracer incorporation into serine only showed relevant effects for the m+3 isotopologue after 24h (Figure 24, FC < 0.8), despite this effect was shown not to be statistically significant (Appendix 5 C). This observation is further supported by the biosynthesis of glycine from serine *via* hydroxymethyltransferases (Jain et al. 2012). Here, no

significantly diminished labeling of m+2 isotopologue within glycine were observable upon PI3Kβ inhibition over the entire course of the experiment (Figure 24 & Figure 28 A). This observation may be indicative of unaffected hydroxymethyltransferase activity. On the contrary, aspartate displayed diminished tracer incorporation due to reduced tracer incorporation within the TCA cycle (Figure 28 B). Here, glutamate donates only nitrogen (Figure 8) *via* aminotransferases to the aspartate structure (similar to serine), remaining carbons derive from the oxaloacetate which is a direct successor of the TCA cycle intermediate malate (Figure 7). Hence, reduced label incorporation in aspartate were directly related to diminished labeling of the TCA cycle intermediates (Figure 24 & Figure 28 B). Depleted levels of fractional labeling of aspartate indicated reduced biosynthesis of aspartate which affects *de novo* biosynthesis of purine and pyrimidines. Here, aspartate acts as an essential building block for purines donating nitrogen and for pyrimidines carbons (Figure 10).

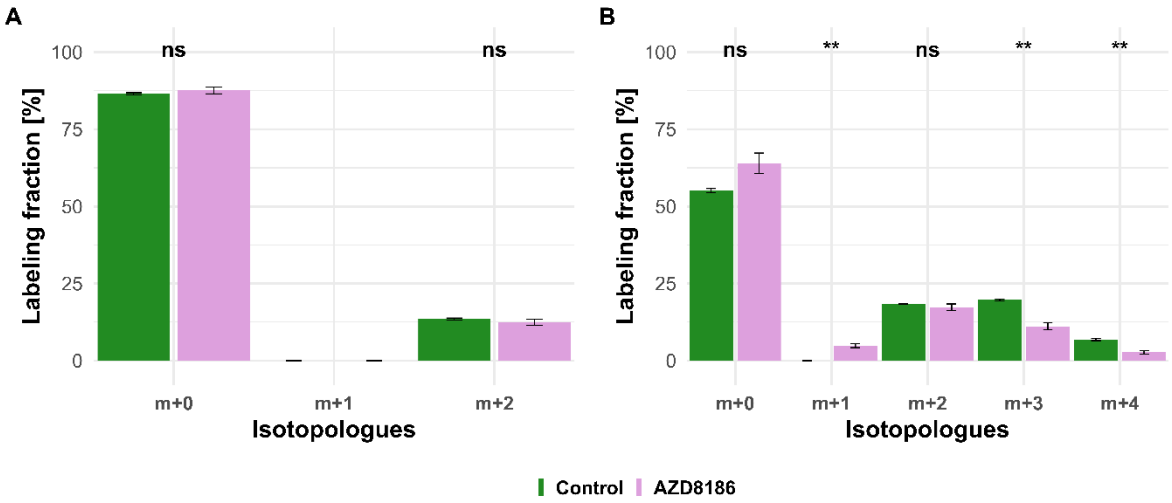

Figure 28: MDA-MB-468 cells were cultivated in RPMI with [U-^{13}C] glucose and treated with 0.5 µM AZD8186 (purple) or vehicle (green). Bar charts ± standard deviation (n=3 technical replicates) showing the fractional enrichment of ^{13}C at 24h into (A) glycine and (B) aspartate. * p< 0.05; ** p< 0.01 (adjusted p-value; Welch's t-test)

3.3.4.4. AZD8186 reduces tracer incorporation into ribonucleotides and intermediates of the hexosamine pathway

One of the most prominent effects of AZD8186 treatment was reduced tracer incorporation into adenylated purines (i.e. AMP, ADP and ATP) and uracil nucleotides (i.e. UDP and UTP) as demonstrated by fractional depletion of m+6/m+7 or m+7/m+8 isotopologues and a >2-fold higher presence of the m+0 isotopologues after 24h (Figure 24). In accordance, the depleted labeling of these isotopologues in uracil nucleotides (i.e. m+6 / m+7 or m+7 / m+8) and indirectly in adenylated ribonucleotides was caused by decreased biosynthetic production of aspartate. Likewise, at earlier time points (i.e. 3h and 6h), the most prominent fractional enrichment of the m+5 isotopologues, attributable to $^{13}C_5$ ribose, was significantly reduced by

treatment FC < 0.8 (Figure 24). For both metabolite classes this implied reduced incorporation of glucose carbon into nucleobases and ribose subunits. This emphasizes the importance of the pentose phosphate pathway in MDA-MB-468 cells and suggests its inhibition as one potential mode of action of the PI3Kβ inhibitor. Interestingly, although diminished labeling for these intermediates was observable at 3h and later time points, incorporation of tracer occurred quicker in treated cells within the first hour indicated by the elevated presence of the m+5 isotopologue in uracil nucleotides (Figure 24). Adenylated ribonucleotides on the other hand did not display such behavior, where the m+5 isotopologue for ATP was already reduced after 1h (FC < 0.8).

As expected from metabolic alterations observed within glycolysis and nucleotide biosynthesis, downstream metabolites including the nucleotide sugars UDP-glucose and UDP-GlcNAc showed corresponding changes. Both metabolites contain moieties from glycolytic intermediates (G1P in UDP-glucose, G6P in UDP-GlcNAc) and pyrimidine nucleotides and carbon contribution from TCA cycle *via* aspartate (Figure 10).

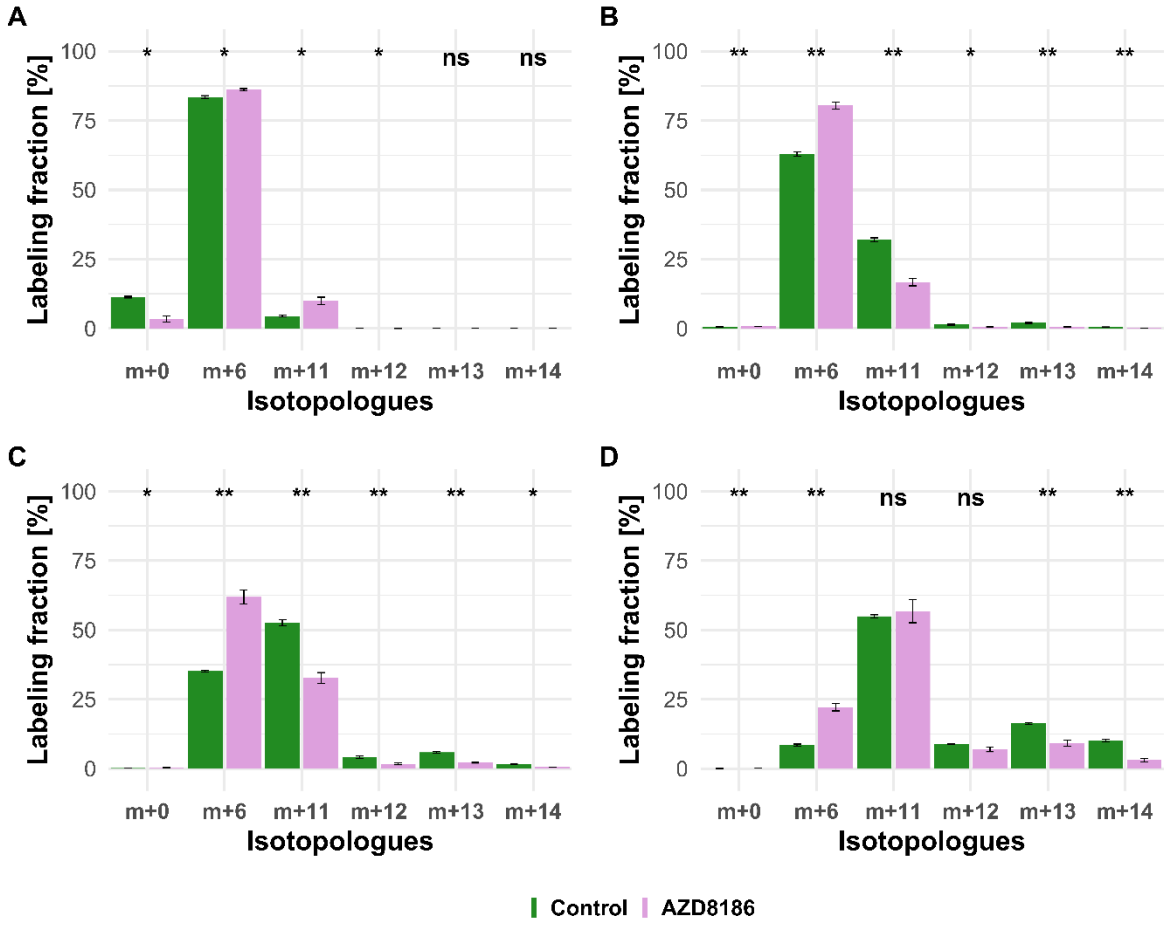

Figure 29: Time course of ^{13}C tracer incorporation in UDP-glucose. MDA-MB-468 cells were cultivated in RPMI with [U-^{13}C] glucose and treated with 0.5 µM AZD8186 (purple) or vehicle (green). Bar charts ± standard deviation (n=3 technical replicates) showing the fractional enrichment of ^{13}C into UDP-glucose at 1h (A), 3h (B), 6h (C) and 24h (D) sampling times. * p< 0.05; ** p< 0.01 (adjusted p-value; Welch's t-test)

Elevated tracer incorporation (FC > 1.6) into isotopologues (i.e. m+6 and m+8 for UDP-GlcNAc and m+11 for UDP-glucose) cross-validated findings made earlier for the pyrimidine nucleotides for the 1h time point (Figure 24). After 24h, drug-induced alterations in these pathways were observable as elevated tracer levels in the isotopologues m+5, 6, 8 and 11 for UDP-GlcNAc (Figure 24) and m+6 for UDP-glucose (Figure 24 and Figure 29). Despite an increased label incorporation into these isotopologues, UDP-GlcNAc and UDP-glucose both displayed diminished labeling in isotopologues generated by multiple pathway contributions (>m+11) indicating the reduced glycolytic ^{13}C-flux in the presence of PI3Kβ inhibition (Figure 24 and Figure 29).

3.3.4.5. PI3Kβ inhibition reduces tracer incorporation into mevalonate pathway

3H3MG, a metabolite of the mevalonate pathway, connects the central carbon metabolism with the fatty acid and cholesterol metabolism and gives an insight into metabolic changes upon PI3Kβ inhibition in this pathway (Caspi et al. 2014; Trefely et al. 2016). Here, incorporation of label occurred *via* the precursor acetyl-CoA in pairs of two and resulted in labeling patterns m+2, m+4, m+6. After 24h the incorporation of the m+6 isotopologue was significantly reduced in treated cells (Figure 24 D), while additionally the incorporation of tracer overall was depleted as indicated by the elevated presence of the m+0 isotopologue in the treated cells (Figure 24 and Figure 30 A). These findings align well with steady state quantitative data of cholesterol pathway intermediates (i.e. lathosterol and lanosterol), where the ratio of these intermediates vs. cholesterol levels was significantly reduced in treated cells (Figure 30 B), thus confirming reduced biosynthetic activity found by the SIRM approach.

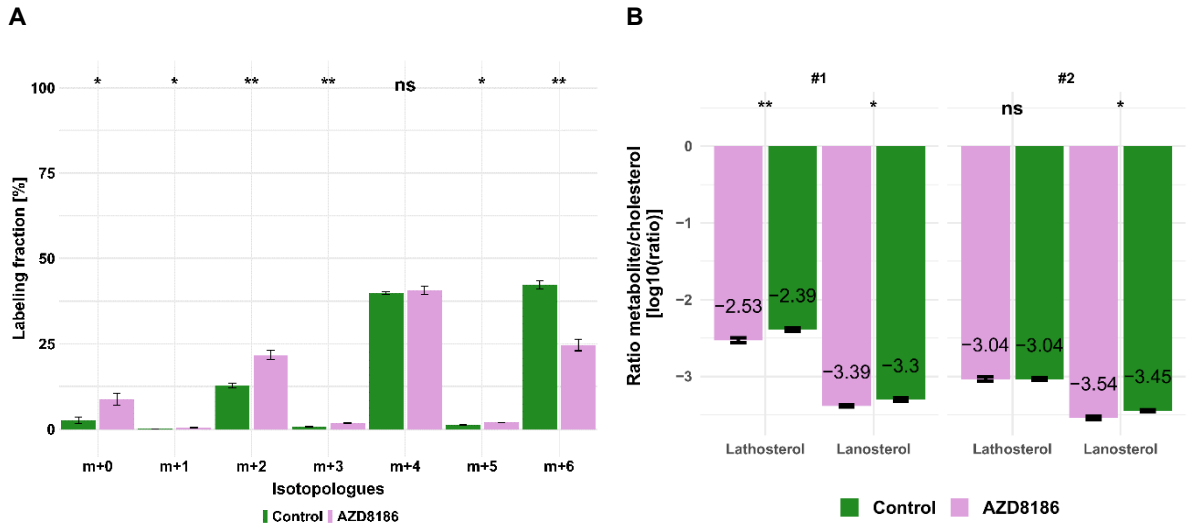

Figure 30: MDA-MB-468 cells were cultivated in RPMI with [U-^{13}C] glucose or unlabeled glucose, respectively and treated with 0.5 µM AZD8186 (purple) or vehicle (green). A: Bar chart ± standard deviation (n=3 technical replicates) showing the fractional enrichment of ^{13}C into 3H3MG at 24h. B: Bar chart ± standard deviation (n=3 technical replicates) showing the ratio of lathosterol and lanosterol levels vs. cholesterol levels obtained from steady state metabolomics of unlabeled samples after 24h incubation with AZD8186 from two independently performed experiments (#1, #2). * p< 0.05; ** p< 0.01 (adjusted p-value; Welch's t-test)

3.4. Established Stable Isotope Resolved Metabolomics workflow using ^{13}C and ^{15}N labeled glutamine

3.4.1 Integrated targeted SIRM workflow upon PI3Kβ inhibition – [U-^{15}N] and [U-^{13}C,^{15}N] glutamine tracer

Aside from fueling the TCA cycle *via* carbons from glucose breakdown or fatty acid oxidation, glutamine can also act as an important carbon donor *via* glutaminolysis for the TCA cycle and as a nitrogen source for the biosynthesis of e.g. amino acids (Figure 8 and Figure 11). Here, labeled glutamine can be used to monitor glutamine derived carbon and nitrogen contribution due to glutaminolytic activity thus allowing for the elucidation of further associated pathways. It is worth mentioning, that the MassHunter Profinder software, used for data pre-processing, only allowed for the analysis of one labeled atom at a time. In turn, double labeled [U-^{13}C,^{15}N] glutamine was used for the investigation of carbon contribution from glutamine to the TCA cycle, while intermediates simultaneously incorporating nitrogen and carbons from glutamine (e.g. amino acids, ribonucleotides) were disregarded for data analysis and interpretation. For these disregarded compounds, [U-^{15}N] glutamine allowed monitoring of nitrogen contributions from glutamine. Incorporation of corresponding glutamine tracers was followed in previously described intermediates (Figure 24, Appendix 2).

3.4.1.1. [U-^{15}N] glutamine

Employment of the [U-^{15}N] glutamine tracer allowed monitoring of the ^{15}N atom into amino acids, adenylated ribonucleotides, metabolites of the hexosamine pathway, as well as amino acid derivatives (i.e. pyroglutamic acid), glutathione, and oxidized glutathione (i.e. GSH and GSSG) from the targeted list of metabolites (Appendix 2). The heatmaps displaying ^{15}N atom incorporation for different time points (Figure 31) enable a comprehensive evaluation of drug-induced changes in corresponding metabolites and the associated pathways within the glutamine metabolism.

Incorporation of ^{15}N from glutamine into the amino acids aspartate, and alanine was unaffected by the presence of the inhibitor as indicated by the FC between 0.8 and 1.2 after 24h (Figure 31). However, label incorporation for aspartate was significantly elevated after 6h (Figure 31). Moreover, tracer incorporation into the m+1 isotopologue of proline was significantly elevated at all time points (Appendix 7), although at 1h and 24h no relevant effects between the control and the treatment condition were observable (i.e. FC > 0.8 and FC <1.2, Figure 31). In accordance with findings from the [U-^{13}C] glucose tracer experiment (Figure 24), the most prominent treatment effects were indicated by differences in the tracer incorporation into intermediates of the hexosamine pathway already after 1h (i.e. UDP-GlcNAc and CMP-NANA) and ribonucleotides after 3h (e.g. UDP and UTP). Here, the depleted fractional labeling was noticeable as the highly elevated presence of the m+0 (FC > 2.4) isotopologue and reduced labeling (FC < 0.8) of higher isotopologues (>m+2) (Figure 31) throughout the time course of this experiment (i.e. 3h, 6h, and 24h). Additional effects in the presence of the inhibitor were observed for intermediates of the glutathione metabolism. Here, the m+2 isotopologue GSSG was significantly reduced after 24h.

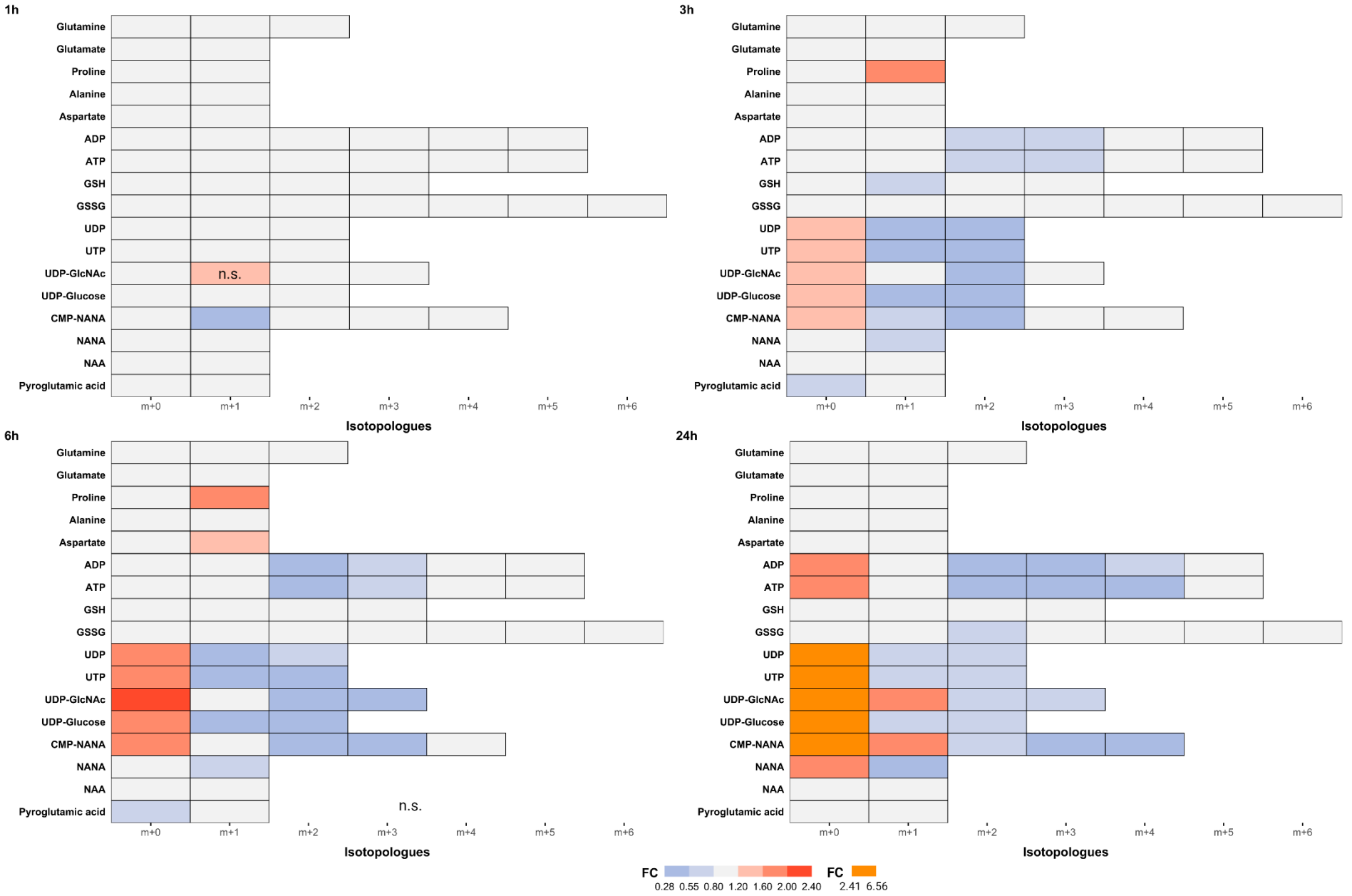
1h
3h
6h
24h
Glutamine
Glutamate
Proline
Alanine
Aspartate
ADP
ATP
GSH
GSSG
UDP
UTP
UDP-GlcNAc
UDP-Glucose
CMP-NANA
NANA
NAA
Pyroglutamic acid
n.s.
m+0
m+1
m+2
m+3
m+4
m+5
m+6
Isotopologues
FC
0.28 0.55 0.80 1.20 1.60 2.00 2.40
FC
2.41 6.56

Figure 31: Impact of AZD8186 treatment on ^{15}N tracer incorporation into different metabolic pathways. MDA-MB-468 cells were cultivated in RPMI with [U-^{15}N] glutamine and treated with 0.5 µM AZD8186 or vehicle for 24h. Fold changes (AZD8186 vs. vehicle) of the individual isotopologues were calculated from the average labeling fraction of three technical replicates per condition and are represented by the indicated color code. Only effects are displayed in the heat map that exhibit a FC <0.8 and >1.2 and tracer incorporation > 3%. Serine and glycine were disregarded due to low or no tracer incorporation after 24h

In further detail, the precursor was quickly taken up as indicated by > 95% fractional labeling of glutamine after 1 hour (Figure 32 A). Additionally, no significant effects in the presence of AZD8186 were noticeable at any time point (Figure 32 A), aligning well to the unaltered level of the glutamine pool as assessed by quantitative metabolomics (Figure 16 B). Interestingly, minor tracer incorporation (< 2%) into m+1 isotopologue of glutamine, is suggestive of low glutamine synthetase activity similarly as observed for the [U-^{13}C] glucose tracer experiments (Figure 27 C). Notably, incorporation into m+1 isotopologue was significantly lower in treated cells, pointing towards alterations related to PI3Kβ inhibition (Figure 32 B).

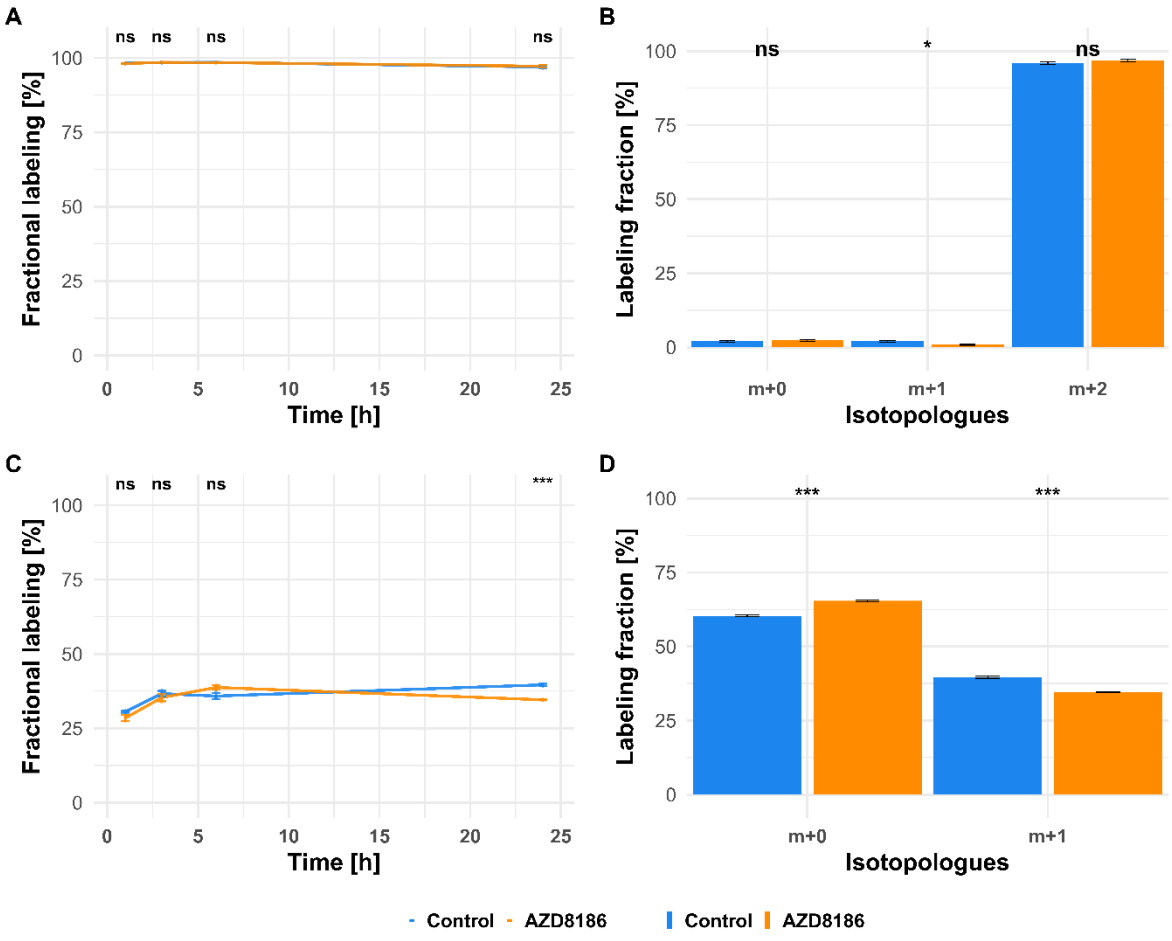

Figure 32: Line charts ± standard deviation (n=3 technical replicates) displaying fractional labeling over 24h hours for (A) glutamine and (C) glutamate using [U-^{15}N] glutamine tracer. Bar charts ± standard deviation (n=3 technical replicates) showing the fractional enrichment of ^{15}N at 24h into (B) glutamine and (D) glutamate. * p< 0.05; ** p< 0.01; *** p< 0.001 (adjusted p-value; Welch's t-test)

Despite the almost sole presence of labeled glutamine, fractional labeling of glutamate did not exceed 40%, suggesting nitrogen contributions from other sources or even direct uptake of

glutamate from the medium (Figure 32 C). Although isotopic steady state was reached for both conditions after 6h, AZD8186 treated cells displayed a decline in fractional labeling after 24h, pointing towards drug-induced alterations in substrate fluxes, whereas vehicle treated cells remained in isotopic steady state. Consequently, glutamate displayed significantly elevated levels of the m+0 isotopologue and diminished labeling fraction of the m+1 isotopologue after 24h in treated cells (Figure 32 D).

3.4.1.2. [U-^{13}C,^{15}N] glutamine

The ^{13}C atoms from the double labeled [U-^{13}C, ^{15}N] glutamine tracer were followed to investigate shuttling of glutamine derived carbon into the TCA cycle. Here, α-ketoglutarate is directly produced from glutamate *via* glutamate dehydrogenase or transaminases connecting glutaminolysis with the TCA cycle (Choi and Coloff 2019). Although α-ketoglutarate initially (i.e. 3h and 6h sampling times) displayed elevated label incorporation in treated cells (significant after 3h), after 24h this effect inverted and treated cells demonstrated significant lower tracer incorporation (Figure 33 A). A similar significant reduction in tracer incorporation in the presence of AZD8186 was observed for glutamate using the ^{15}N tracer, supporting these findings (Figure 32 C). Furthermore, the total fractional labeling for α-ketoglutarate was between 48 to 50% after 24h in both conditions, hinting at other routes of carbon contributions. Here, tracing of ^{13}C glucose already demonstrated carbon contributions originating from glycolytic breakdown, although only accounting for 30% in untreated cells after 24h (Appendix 8). Aside from the overall labeling of α-ketoglutarate, labeling patterns of malate revealed predominantly oxidative metabolism (i.e. forward TCA cycle) indicated by the m+4 isotopologue after 1h (Figure 33 B). Reductive carboxylation was weakly active, as seen by the presence (< 4%) of the m+3 isotopologue in this intermediate. In both cases no significant drug-induced alteration was noticeable. This was further supported by the assessment of the m+4 and m+5 isotopologues in citrate, which can be used to infer oxidative and reductive carboxylation activity, respectively. Likewise, no significant effects related to PI3Kβ inhibition were noticeable for these isotopologues throughout the experiment (Appendix 9). It should be noted that pyruvate and lactate also displayed low levels of tracer incorporation as m+3 isotopologue (< 3%) after 24h (Appendix 10), thus, the likelihood of producing m+5 isotopologues in citrate from labeled acetyl-CoA and m+3 labeled oxaloacetate (from m+3 malate) was increased and pharmacological effects in citrate could not be clearly attributed. Nevertheless, unchanged reductive carboxylation was also confirmed by steady state metabolomics. Here, the ratio of intracellular levels of α-ketoglutarate to citrate was used as a measure of reductive carboxylation activity (Fendt et al. 2013) and displayed no significant alteration regardless of the employed AZD8186 concentration, even though a tendency towards reduced reductive carboxylation was noticeable (Figure 33 C).

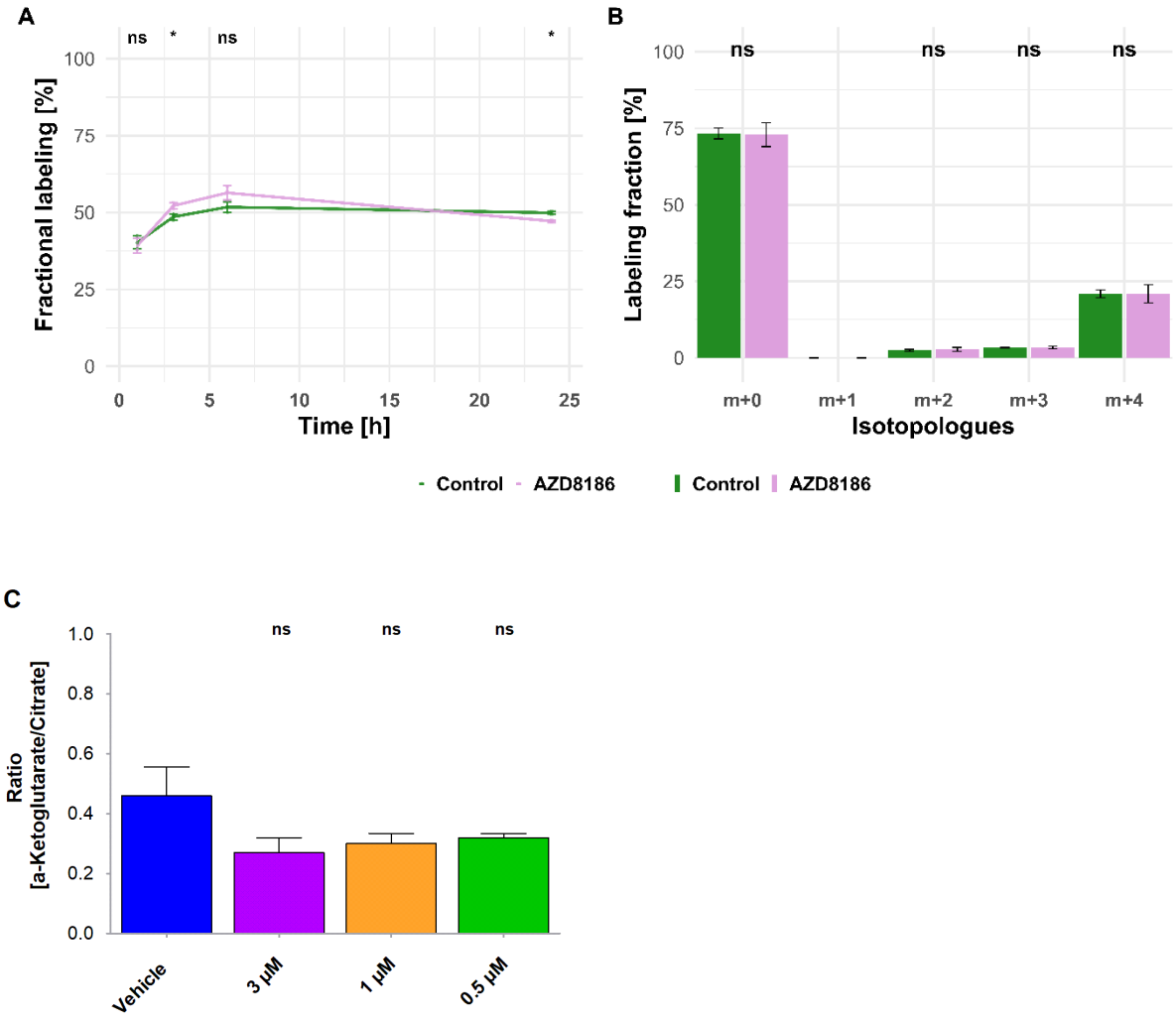

Figure 33: A: Line chart ± standard deviation (n=3 technical replicates) displaying fractional labeling over 24h hours from [U-^{13}C,^{15}N] glutamine into α-ketoglutarate. * p< 0.05; ** p< 0.01; *** p< 0.001 (adjusted p-value; Welch's t-test). B: Bar charts ± standard deviation (n=3 technical replicates) showing the fractional enrichment of ^{13}C into malate at 1h sampling time. Reductive carboxylation and oxidative metabolism in malate indicated as m+3 and m+4 isotopologues, respectively. * p< 0.05; ** p< 0.01; *** p< 0.001 (adjusted p-value; Welch's t-test). C: Ratio of a-ketoglutarate to citrate levels obtained from steady state metabolomic analysis of unlabeled samples incubated for 24h with AZD8186 at various concentrations (n =3, two-tailed Welch's t-test)

Drug-induced alterations in glutaminolytic activity from AZD8186 on other intermediates of the TCA cycle or glycolysis were small (Appendix 11). As exemplified for α-ketoglutarate (Figure 33 A), incorporation of ^{13}C into TCA cycle intermediates was observable over the course of the experiment (fractional labeling >45%) while changes in labeling patterns were not relevant for most intermediates (FC > 0.8 and FC < 1.2, respectively (Appendix 11). Only malate and fumarate showed reduced tracer incorporation into the m+3 isotopologue after 24h (FC < 0.8, Appendix 11), although with a low incorporation of <6% (Figure 34 A,B). Additionally, the poor tracer incorporation into pyruvate due to minor malic enzyme activity and the subsequent conversion to lactate also showed no relevant difference in the labeling patterns after 24h (FC > 0.8 and FC < 1.2, respectively). As a consequence, tracer incorporation into glycolytic intermediates from a potential gluconeogenic activity was negligible.

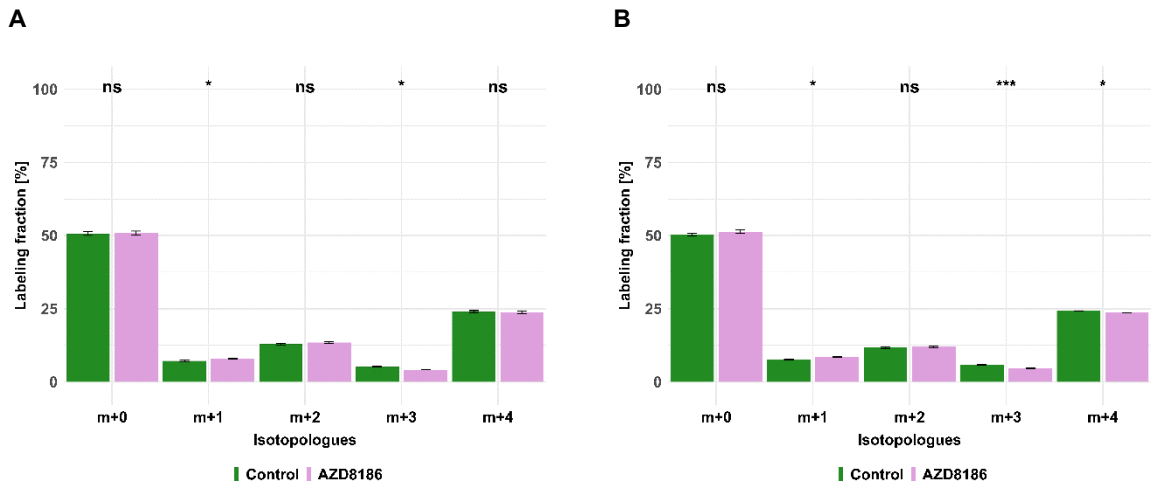

Figure 34: MDA-MB-468 cells were cultivated in RPMI with [U-^{13}C, ^{15}N] glutamine and treated with 0.5 µM AZD8186 (purple) or vehicle (green). Bar charts ± standard deviation (n=3 technical replicates) showing the fractional enrichment of ^{13}C into (A) fumarate and malate (B) at 24h sampling time. * p< 0.05; ** p< 0.01; *** p< 0.001 (adjusted p-value; Welch's t-test)

3.4.2 Comparison of untargeted SIRM using [U-^{13}C] glucose and [U-^{13}C,^{15}N] glutamine

As demonstrated in 3.3.1 untargeted analysis of the [U-^{13}C] glucose SIRM data allowed the unbiased extraction of isotopic data to gain information on pathways affected by AZD8186 (beyond pre-defined pathways). It was therefore expected that applying the untargeted data analysis workflow to assess tracer incorporation from [U-^{13}C,^{15}N] glutamine will further expand the insight into additional pathway changes related to PI3K-inhibition. To this end, untargeted data analysis of the labeling experiment with [U-^{13}C,^{15}N] glutamine was performed and compared with data from the untargeted data analysis of the [U-^{13}C] glucose experiment. Furthermore, the limitations of targeted analysis described earlier with MassHunter Profinder due to the double labeled glutamine (3.4) were overcome by the untargeted approach, as the extraction algorithm is capable to detect isotopic enrichment from different types of tracer by comparing the labeled sample with the unlabeled sample.

Cell extracts from tracer experiments harnessing either [U-^{13}C] glucose (3.3) or the [U-^{13}C,^{15}N] glutamine as tracer substrates were investigated in an untargeted manner using X^{13}CMS and aligned according to the corresponding retention times and masses for extracted features. While for [U-^{13}C] glucose 286 features showed a significantly altered labeling pattern upon PI3Kβ inhibition and compared to controls (3.3.1), the non-targeted analysis of ^{13}C and ^{15}N incorporation from glutamine resulted in 413 (Figure 35 A) and 293 features (Figure 35 B), respectively.

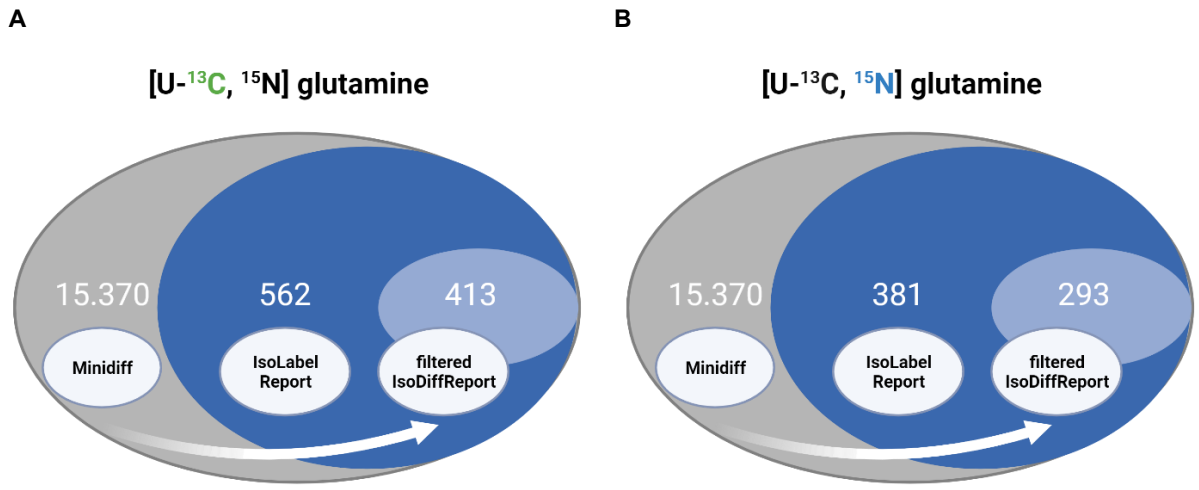

Figure 35: Differential labeling analysis of MDA-MB-468 cells cultivated with [U-^{13}C, ^{15}N] glutamine and treated for 24h with vehicle or 0.5 µM AZD8186. A: Schematic display of the feature filtering procedure with the number of features obtained in the different processing steps for ^{13}C glutamine. B: Schematic display of the feature filtering procedure with the number of features obtained in the different processing steps for ^{15}N glutamine

A comparison of the significantly altered features from the different labeling experiments revealed 71 unique features (12.2%) derived from the ^{13}C glucose tracer, whilst 125 (21.5%) and 55 features (9.5%) could solely be attributed to the ^{13}C glutamine and ^{15}N glutamine tracer, respectively (Figure 36). In turn, features with ^{13}C or ^{15}N label incorporation from glutamine shared the largest group of overlapping features (22.2%). Furthermore, 103 features (17.7%) were jointly recovered by the ^{13}C glucose and ^{13}C glutamine analysis. ^{15}N glutamine and ^{13}C glucose analysis commonly retrieved 58 features (10%). Interestingly, comparing the identified features from all three tracers resulted in an overlap of 40 features (6.9%) from which ten features could be attributed to known compounds from the hexosamine pathway, the pyrimidine and purine ribonucleotide biosynthesis, the TCA cycle, as well as glutathione and amino acid metabolism (e.g., UDP-GlcNAc, UTP, and 2-HG) (Figure 36). 2-HG was falsely recovered by the ^{15}N glutamine tracer, although the molecule does not contain nitrogen. Manual revision subsequently revealed, a false labeling pattern with the presence of an m+4 isotopologue with an extremely low abundance (Appendix 12). As expected, no other molecules from the TCA cycle were identified among the commonly shared 40 features. Furthermore, despite the false retrieval of 2-HG, the remaining intermediates recovered by all thee tracer types displayed significant alterations of their labeling pattern as demonstrated in Figure 24 for the glucose tracer and Figure 31 for the glutamine tracer, hence indicating major metabolic disturbances from alternating pathway routes caused by the presence of the inhibitor.

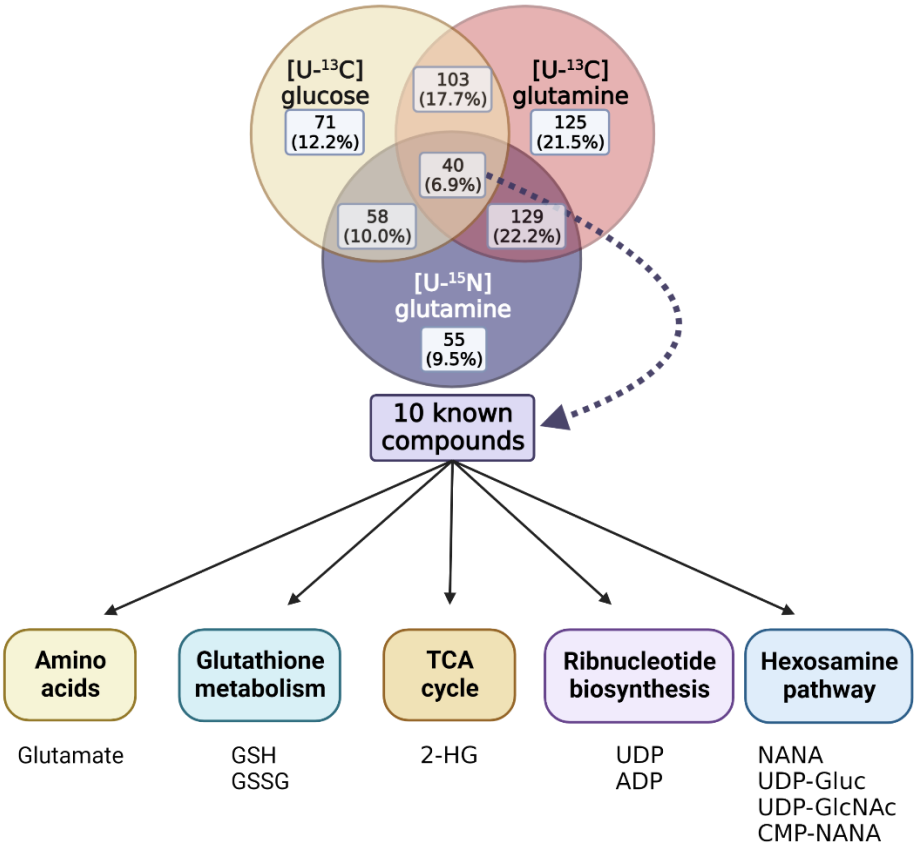

Figure 36: Venn diagram of significantly changed features (as obtained with filterIsoDiffReport) after untargeted analysis with X^{13}CMS employing [U-^{13}C] glucose and [U-^{13}C, ^{15}N] glutamine as tracer substrates. MDA-MB-468 cell were cultivated either in [U-^{13}C] glucose or [U-^{13}C,^{15}N] glutamine enriched RPMI medium and treated for 24h with 0.5 µM AZD8186. Due to overlaps in mass and retention time alignment, 13 features were disregarded from the comparison of ^{13}C with ^{15}N labeled glutamine, 19 features for the comparison of ^{13}C glucose with ^{13}C glutamine, and nine features for the comparison of ^{13}C glucose with ^{15}N glutamine

In addition to the ten structurally identified compounds from the commonly shared feature pool, untargeted data analysis yielded a list of unique features according to the tracer substrate used. Further investigation of the 71 unique features extracted from [U-^{13}C] glucose tracer experiment revealed structural identification of 12 known compounds (e.g. PEP, pyruvate, malate, and glutamine). Six of these compounds were associated with the TCA cycle, while three of the remaining compounds each belonged to the glycolysis and amino acids metabolism, respectively. With regards to the glutamine tracers, 55 features were uniquely found using the ^{15}N tracer, while 125 features were found for the ^{13}C glutamine tracer. The identification of the unique features from the glutamine tracer resulted in the annotation of the two adenylated ribonucleotides AMP (for ^{13}C glutamine) and ATP (for ^{15}N glutamine), respectively, could be annotated (Appendix 13).

In conclusion, untargeted data analysis of the two isotopes (i.e., ^{13}C and ^{15}N) of the double labeled [U-^{13}C,^{15}N] glutamine confirmed findings made for the targeted analysis of the ^{15}N and ^{13}C isotopes of glutamine in 3.4.1, where drug-induced impairment of the ribonucleotide

biosynthesis and the hexosamine pathway showed the most prominent effect (Figure 31 and Figure 36). Furthermore, the number of unique features retrieved for the corresponding isotope of glutamine (i.e., 125 features for the ^{13}C and 55 features for ^{15}N) demonstrated that the employment of differently labeled tracer substrates can lead to a substantial gain of potentially new molecules and pathways, albeit the feature annotation was low and did not reveal novel intermediates or pathways associated with PI3Kβ inhibition.

3.5. Characterization of metabolic differences between MDA-MB-468 and HCC70 cell lines using untargeted and integrated targeted SIRM

Metabolic heterogeneity in TNBC subtypes is a well-known phenomenon (Lanning et al. 2017) which might become even more pronounced under the influence of an external stimulus like drug treatment. Therefore, it was assumed that a comprehensive metabolic characterization of the effects of PI3Kβ inhibition in different TNBC cell lines may uncover metabolic changes in the presence of AZD8186 both collectively and uniquely for each cell line. As demonstrated in this work (3.3 and 3.4), targeted and untargeted SIRM enabled monitoring of AZD8186 mediated changes in metabolic pathway activities within the MDA-MB-468 cell line. In addition, work by Lynch et al. demonstrated metabolic changes in the PTEN-null cell line HCC70 (e.g., reduced levels of glycolytic intermediates and deoxyribonucleotide triphosphates). Nevertheless, a comprehensive comparison of metabolic differences related to PI3Kβ inhibition between the MDA-MB-468 and the HCC70 cell lines by SIRM has not been carried out. As outlined in the following chapters, untargeted and targeted SIRM was performed for these two cell lines using [U-^{13}C] glucose as tracer substrate. In contrast to all previous labeling experiments, an additional 24h pretreatment phase with AZD8186 prior to the addition of tracer substrate was carried out. The experimental conditions were adapted to allow for sampling at early time points (i.e., 15 minutes), which should enable assessment of drug-related effects in metabolic pathways with high glucose turnover rates (e.g., glycolysis and PPP).

3.5.1 Global ^{13}C tracer incorporation in HCC70 and MDA-MB-468 cell lines upon exposure to AZD8186

Untargeted differential tracing of label incorporation in response to PI3Kβ inhibition for each cell line was done *via* the X^{13}CMS routine as described in 3.3.1. As shown in Figure 37, the base peak list obtained by the miniDiffReport() function resulted in 9.104 and 8.487 features in the MDA-MB-468 and HCC70 cell line, respectively. From these features, 740 were significantly labeled (IsoLabelReport) in the MDA-MB-468 and 508 in the HCC70 cell line. Employment of the filterIsoDiffReport() function resulted in 521 features in the MDA-MB-468 and 417 features in the HCC70 cell line with significantly altered labeling pattern between control and the treatment condition. (Figure 37).

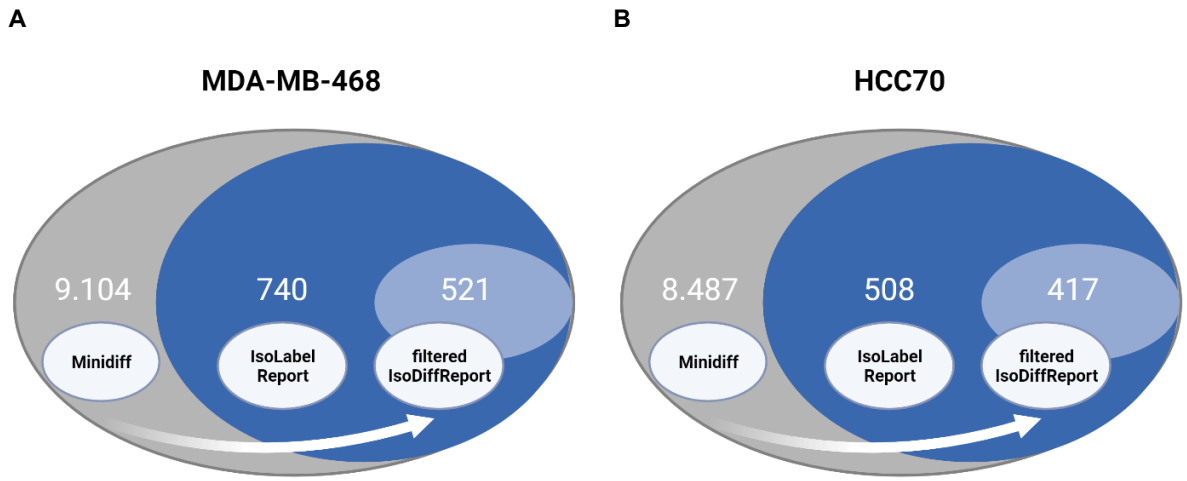

Figure 37: Differential labeling analysis of MDA-MB-468 and HCC70 cells cultivated with [U- ^{13}C] glucose and treated for 24h with vehicle or 0.5 µM AZD8186. A: MDA-MB-468. B: HCC70

Interestingly, the number of significant features was 1.8-fold higher compared to the number of filtered features (i.e. 286) of the experiment with [U-^{13}C] glucose carried out in the MDA-MB-468 cell line without a pretreatment phase (3.3.1). Regarding the feature distribution between the different groups (i.e., control, treatment and those found in both conditions in MDA-MB-468 cells), 176 features could be detected in both conditions, while 183 were uniquely recovered in the vehicle and 162 features were only retrievable in the AZD8186 condition (Figure 38 A). While this allocation was evenly distributed across the three groups (i.e. between 31 and 35%) for the MDA-MB-468 cell line, the significantly changed features in the HCC70 cell line were unevenly distributed. Here, the largest fraction of significant features was found in the vehicle condition with 49% or 204 features, respectively (Figure 38 B). This accounts for a 1.4-fold increase in the number of features compared to the vehicle treated MDA-MB-468 cells (i.e. 35%). Furthermore, 66 (16%) features were uniquely found in the presence of AZD8186 in HCC70 cells, thereby displaying the largest differences in significantly altered features under drug exposure (i.e. 66 vs. 162) between the two cell lines. Nevertheless, 147 features (35%) were recovered from both conditions in HCC70 cells which corresponds to a similar proportion (34%) as found in the MDA-MB468.

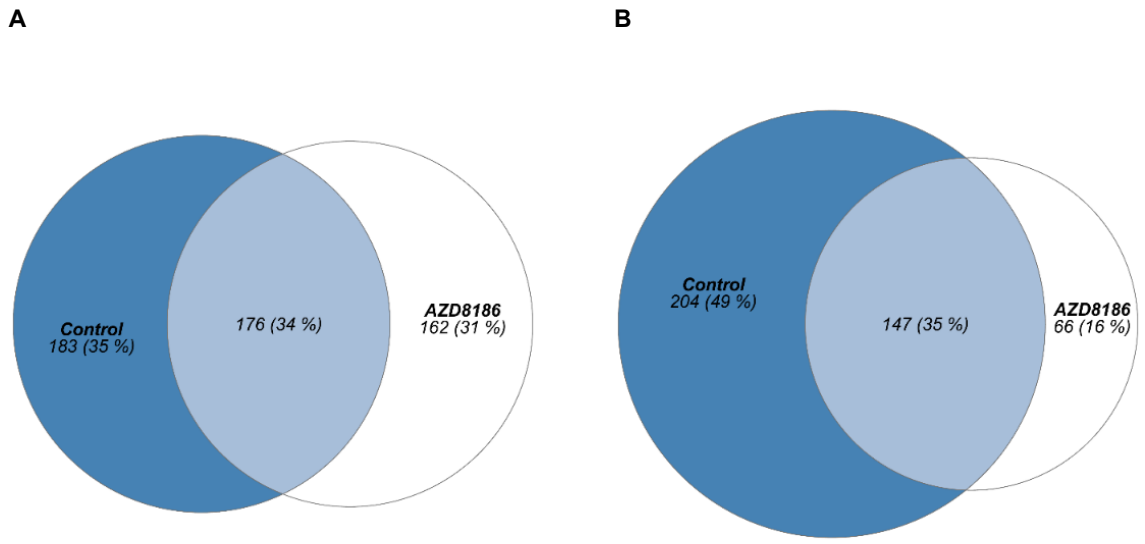

Figure 38: Differential labeling analysis of MDA-MB-468 and HCC70 cell line cultivated in [U-^{13}C] glucose enriched RPMI and treated with vehicle or 0.5 µM AZD8186 for 24h. Euler diagram of differentially labeled isotopologue groups between vehicle and AZD8186 treated cells (filterIsoDiffReport) for (A) MDA-MB-468 and (B) HCC70

3.5.2 Characterization of common and cell line specific features altered by AZD8186

Features with significantly altered labeling patterns after inhibition with AZD8186 (filterIsoDiffReport) for the two cell lines were aligned according to their mass and retention time. Out of the 521 extracted features in the MDA-MB-468 cell line and the 417 features from the HCC70 cell line, 162 features (21.8%) were shared between both cell lines (Figure 39). Notably, the majority of the features were specific to the corresponding cell line (i.e., 46.0% and 32.2%, respectively), indicating cell-line specific metabolic alterations related to inhibition of PI3Kβ. Features that were commonly altered in both cell lines were subsequently assessed by targeted isotopologue feature extraction to examine cell-line specific metabolic characteristics in the absence and presence of AZD8186 (3.5.3) The cell line specific features were subsequently structurally annotated (3.5.4) to identify metabolites within additional metabolic pathways that are affected for each cell line in the presence of the PI3Kβ inhibitor.

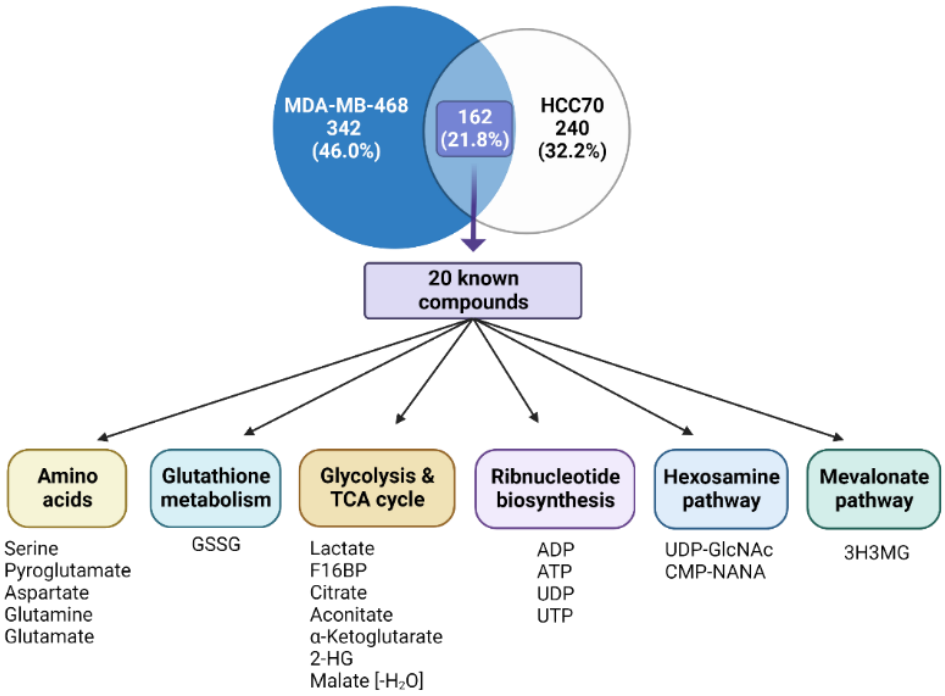

Figure 39: Significantly altered features upon exposure to 0.5 µM AZD8186 obtained after untargeted X^{13}CMS analysis of PTEN-null MDA-MB-468 and HCC70 cell lines incubated with [U-^{13}C] glucose enriched RPMI at 24h sampling point. Euler diagram displaying feature distribution across both cell lines

3.5.3 Integrated targeted SIRM analysis to elucidate metabolic differences in presence and absence of PI3Kβ inhibition for overlapping features

The characterization and identification of overlapping features allows to identify metabolic pathway changes related to drug treatment that are altered in common for both cell lines. To this end, the 162 overlapping features were structurally annotated based on mass and retention times from compounds provided in the targeted list (Appendix 2) thereby identifying 20 metabolites covering different pathways including hexosamine pathway, TCA cycle, and ribonucleotides (Figure 39). Notably, the identified intermediates confirmed metabolic pathway changes in the MDA-MB-468 cell line as seen in previous experiments (Figure 24). In addition, AZD8186 exhibited similar effects on central pathways in the HCC70 cell line related to the mode of action (Appendix 14).

While untargeted SIRM can help to identify metabolic changes within unexpected pathways based on differences in label incorporation between two biological conditions, the targeted SIRM workflow allows for manual curation of data thereby allowing a more accurate quantitation of tracer incorporation (Lackner et al. 2022). To this end, an integrated targeted analysis of corresponding features was performed comparing the metabolic differences in tracer incorporation within pre-defined pathways between the two cell lines in i) the absence (vehicle treated control) and ii) the presence of PI3Kβ inhibition (AZD8186) (Figure 40).

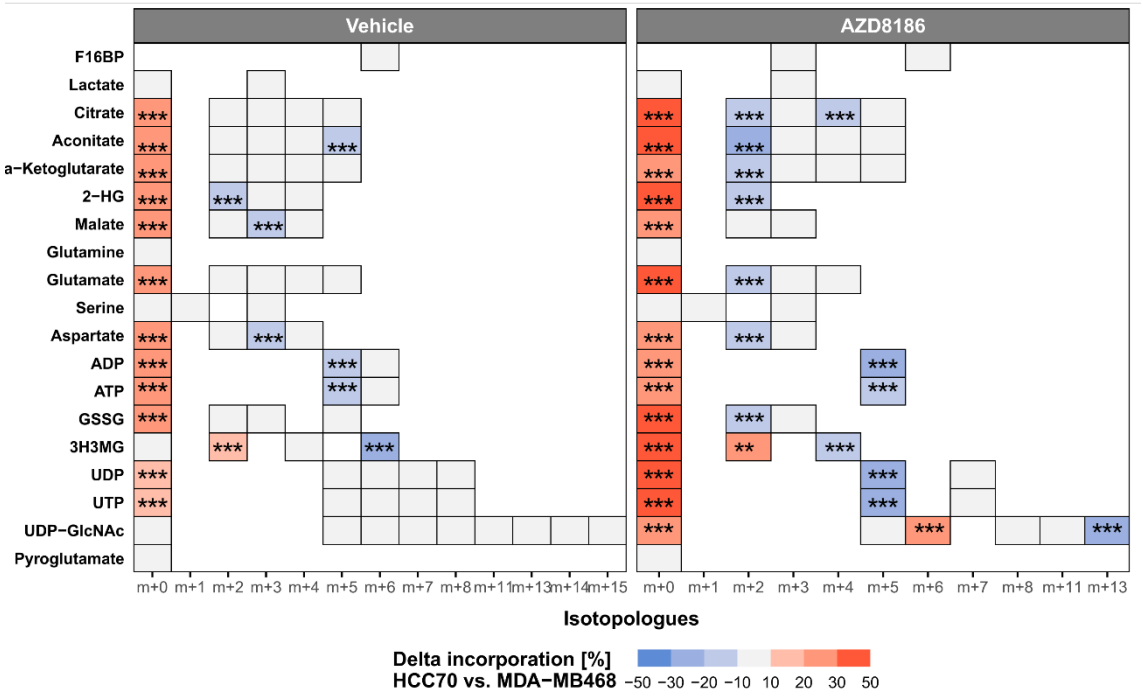

Figure 40: Impact of AZD8186 treatment on ^{13}C tracer incorporation into overlapping compounds after targeted SIRM analysis. MDA-MB-468 and HCC70 cells were cultivated in RPMI enriched [U-^{13}C] glucose and treated with 0.5 µM AZD8186 or vehicle for 24h. Difference in ^{13}C tracer incorporation was calculated *via* delta incorporation (2.2.6.7, Equation 4) of individual isotopologues and was calculated from the difference in average label incorporation (HCC70 vs. MDA-MB-468) from three technical replicates after targeted analysis with MassHunter Profinder. Statistical testing was performed comparing the fractional enrichment of corresponding metabolites between the MDA-MB-468 and HCC70 cell lines across three technical replicates. ** p< 0.01, *** p< 0.001 (adjusted p-value; Welch's t-test). Targeted analysis of CMP-NANA was disregarded as isotopologue ion thresholds were not reached. Label incorporation into Pyroglutamate was < 3%

Both cell lines already differed in the control condition, with the HCC70 cell line displaying diminished tracer incorporation after 24h indicated by a delta incorporation of > 20% for the m+0 isotopologue in 12 overlapping compounds (e.g. citrate, aconitate, α-ketoglutarate). TCA cycle intermediates as well as aspartate and the adenylated ribonucleotides further demonstrated reduced labeling (delta incorporation -10 to -30%) of higher isotopologues (> m+2) in the vehicle treated condition, pointing to slower tracer incorporation in the HCC70 cell line. Interestingly, fractional labeling of the m+3 isotopologue in aspartate and malate was reduced after 24h suggesting reduced pyruvate anaplerotic activity *via* the enzyme pyruvate carboxylase. Likewise, tracer incorporation in the m+5 isotopologue of the adenylated ribonucleotide was diminished, suggesting reduced ^{13}C flux from the PPP into the biosynthesis of corresponding ribonucleotides in HCC70 cells. Labeling of UDP-GlcNAc did not demonstrate major alterations in labeling as delta incorporation of every isotopologue was between -10 and 10%. These labeling differences became more apparent when cells were treated with AZD8186. Delta incorporation for the m+0 isotopologue was >20% for all compounds except pyroglutamate, serine, glutamine, and lactate. This indicates further drug-induced depletion of tracer incorporation into the HCC70 cell line. This is particularly true for TCA cycle intermediates, noticeable by a diminished delta incorporation (< -10%) of the m+2

isotopologue, pointing to diminished PDH activity in the HCC70 cell line. Furthermore, highly reduced PPP flux was observable in the HCC70 in the presence of AZD8186 where all overlapping ribonucleotides indicated a delta incorporation of < -20% (ATP < -10%) into the m+5 isotopologue. UDP-GlcNAc, indistinguishable in the vehicle treated condition, now displayed alterations in tracer incorporation upon AZD8186 exposure. Here, elevated delta incorporation into m+6 isotopologue (>20%) and reduced incorporation into the m+13 isotopologue (<-20%) were noticeable. Interestingly, F16BP, lactate, glutamine, serine, and pyroglutamate displayed similar labeling patterns in the two cell lines regardless of the treatment conditions indicated by a delta incorporation between -10 to 10%. Overall, the tracer incorporation appeared to occur slower for most of the intermediates in the HCC70 cell line regardless of the pathway. However, it is worth mentioning that the cell number of HCC70 was significantly lower after 24h, which could be an explanation for the observed slower tracer incorporation (Appendix 15).

One of the most prominent distinctions between the two cell lines was the diminished labeling of the m+5 isotopologue in the corresponding ribonucleotides in HCC70 cells. Here, labeling of the ribose moiety originates from PRPP (Figure 9), an intermediate produced from ribose-5-phosphate. As labeling of these compounds was not determinable due to detection limitations, tracer incorporation into 6-PG as surrogate intermediate for PPP activity was further elucidated by targeted SIRM analysis. 6-PG produces ribulose-5-phosphate *via* the enzyme 6-phosphogluconate dehydrogenase, which is then converted to ribose-5-phosphate.

Tracer incorporation into 6-PG was considerably different between the two cell lines, as indicated by the corresponding labeling patterns (Figure 41). After 15 minutes, the MDA-MB-468 cell line showed a labeling fraction of ~81% in the vehicle and ~75% in the treatment condition for the m+6 isotopologue, compared to 12.5% and 12.6% for the m+5 isotopologue, respectively (Figure 41 A). In contrast, in the HCC70 cell line the m+6 isotopologue displayed a fractional labeling of 48% for the vehicle and ~47% for the AZD8186 treated cells, compared to ~31% and 33.4% for the m+5 isotopologue, respectively (Figure 41 B). Furthermore, the m+0 isotopologue was considerably higher in the HCC70 (>14%) compared to the MDA-MB-468 cell line (< 6%) after 15 min for both conditions, pointing towards slower labeling of 6-PG in the HCC70 cell line. Both cell lines demonstrated low tracer incorporation (< 4%) of the m+2, m+3, and m+4 isotopologues in 6-PG. After 1h, label incorporation had slightly increased for the m+5 and m+6 isotopologues in both cell lines in (Figure 41 C, D), while the m+0 isotopologue decreased and was <2% for the MDA-MB-468 and < 7% for the HCC70 cell line with not significant differences between the treatment conditions. At 24h, the labeling pattern was similar to the labeling pattern of the 1h time point regardless of the cell line (Appendix 16). In the MDA-MB-468 cell line, the labeling fraction for the m+6 isotopologue had further

increased to 88% in the vehicle and to 82.5% in the treatment condition, compared to 10.4% and 13.1% for the for the m+5 isotopologue, respectively, respectively (Appendix 16 A). Both isotopologues were significantly different between the two treatment conditions. In contrast, the HCC70 cell line showed almost equal labeling fractions for the m+5 and m+6 isotopologues after 24h with no significant differences between AZD8186 treated and untreated cells (Appendix 16 B). The m+6 isotopologue displayed a fractional labeling of 50.3% for the vehicle and 47% for the AZD8186 treated cells, compared to 47.5 and 51% for the m+5 isotopologue, respectively.

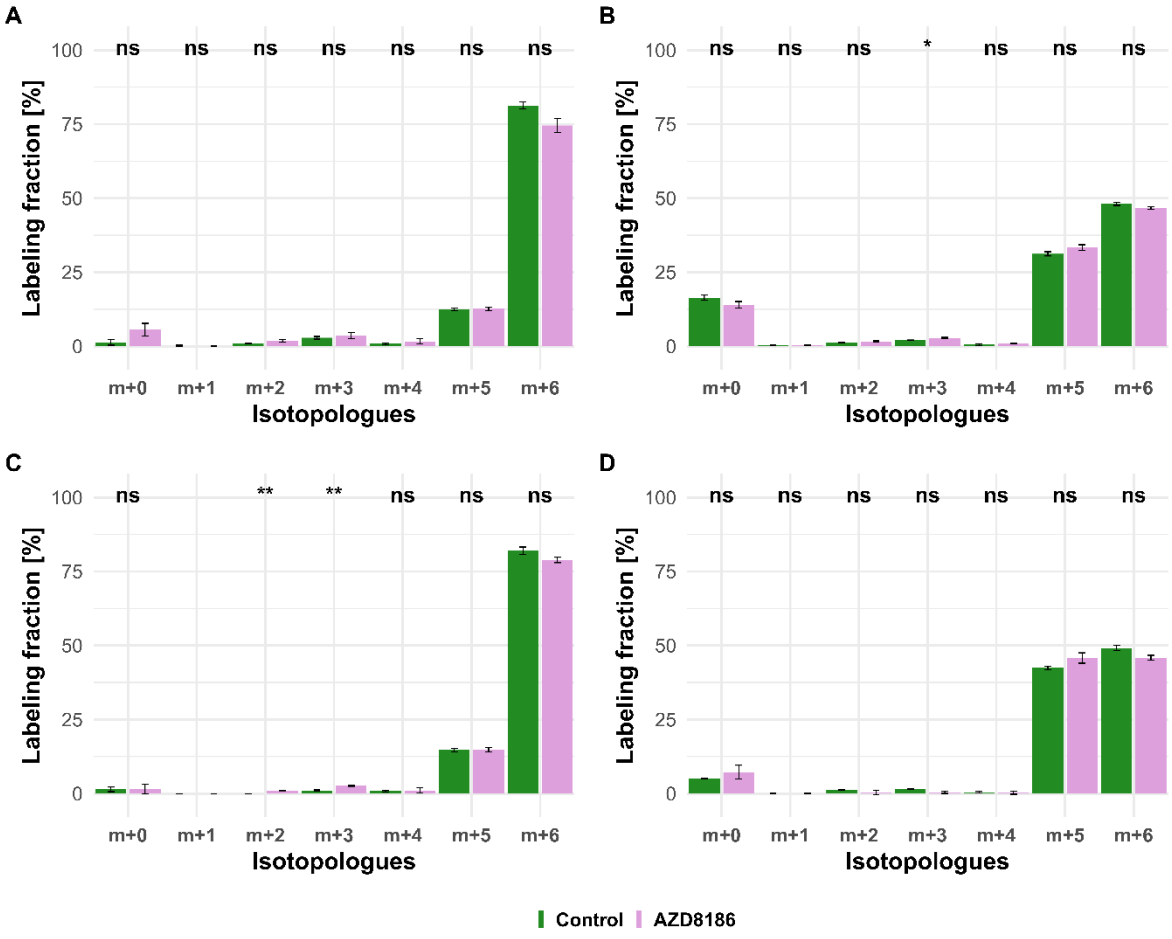

Figure 41: Time course of ^{13}C tracer incorporation of 6-PG for the MDA-MB-468 and HCC70 cell line. MDA-MB-468 and HCC70 cells were cultivated in RPMI with [U-^{13}C] glucose and treated with 0.5 µM AZD8186 (purple) or vehicle (green). Bar charts ± standard deviation (n=3 technical replicates) showing the fractional enrichment of ^{13}C into 6-PG after 15 minutes for (A) MDA-MB-468 and (B) HCC70, and after 1h for (C) MDA-MB-468 and (D) HCC70. * p< 0.05; ** p< 0.01 (adjusted p-value; Welch's t-test)

3.5.4 Identification of cell line specific features that are altered upon inhibition with AZD8186

An assessment of metabolic changes upon inhibition of PI3Kβ based on overlapping features (see 3.5.3) can reveal insights into the activities of metabolic pathways that are altered in common across different cancer cell lines. Annotation of metabolic features that are uniquely altered for each cell line can offer valuable information on cell line specific drug responses and potentially reveal previously undetected metabolic changes. This could contribute to new therapeutic approaches for PI3Kβ deficient cancer cells.

To this end, the unique isotope-enriched features, that were significantly altered between control and treatment (i.e. AZD8186) for each cell line (i.e. MDA-MB-468 with 342 and 240 features for the HCC70 cell line, Figure 39) were investigated for fragment spectra which were compared with MS/MS spectra of previously identified compounds (Appendix 2) or further elucidated based on MS/MS spectra database (Dührkop et al. 2019). Overall, 26 features for the MDA-MB-468 and 20 features for the HCC70 cell line could be attributed to different metabolites (Appendix 17).

Several features that were significantly affected in only one cell line, are related to pathways or metabolites known to be changed by AZD8186 treatment (e.g., glycolysis, TCA cycle, amino acid and glutathione metabolism (Figure 39). For the MDA-MB-468 cell line seven unique compounds were associated with these pathways (i.e., proline, succinate, malate, tyrosine, NAA, G6P, GSH). Annotation of features from the HCC70 cell line resulted in the identification of five intermediates from the glycolysis, TCA cycle, and hexosamine pathway (i.e., 2-PG, G6P, fumarate, NANA, and UDP-glucose).

Furthermore, metabolites and pathways that had not previously been identified as being altered by AZD8186 treatment were annotated for the two cell lines. For the MDA-MB-468 cell line 13 features were linked to the biosynthesis of lipids belonging either to the group of phospholipids (i.e. phosphatidylethanolamine (PE) and phosphatidylinositol (PI)), fatty acids (i.e., 2-hexyldecanoic acid, stearic acid) or sterols (i.e., cholesterol sulfate). Six features belonged to the group of benzenesulfonic acids, amino acids, sugar phosphates, or hexoses (e.g., 4-dodecylbenzenesulfonic acid, N-acetyl glutamic acid, and galactose). Annotation of features from the HCC70 cell line revealed similarities in the affected pathways, where three compounds were linked to lipid synthesis (i.e., stearic acid, glycerophosphoglycerole, and PI(18:1(9Z)/0:0)). Seven compounds were found to be associated with the PPP, the amino acid and hexose metabolism, and UDP-sugars (e.g., ribulose 1,5-diphosphate, galactose, and UDP-glucuronic acid). The remaining identified features (e.g., arabitol, 2-methyl-4-phenyl thiazole, and mannitol 1-phosphate,) were compounds from exogenous sources, or do not

incorporate any ^{13}C into their structure (i.e., pyrophosphate), thus pointing towards incorrect feature annotation. It is noteworthy that G6P, galactose, and stearic acid were found in the pool of unique features in both cell lines. However, an overlap could not be established due to missed retention time alignment.

In conclusion, the metabolic characterization of the MDA-MB-468 and HCC70 TNBC cell lines based on untargeted and targeted SIRM allowed to gain a deeper understanding of the similarities in AZD8186-induced alterations in metabolic pathways. Of the ~900 significantly altered features (i.e. 504 features in the MDA-MB-468 and 402 features in the HCC70 cell line), more than 20% were found in both cell lines, demonstrating that similar drug-induced changes in metabolic pathways occur in both cell lines. In addition, the metabolic characterization allowed the investigation of cell line specific differences in substrate fluxes, as exemplified for 6-PG as part of the PPP, as well as the discovery of cell line specific compounds that were significantly altered by the presence of AZD8186. Although some of these metabolites were cell line specific and not previously known to be affected by AZD8186 treatment, they indicated similar changes in metabolic pathways of the two cell lines in response to AZD8186.

4. Discussion

Stable isotope resolved metabolomics has become an important approach to investigate metabolic changes related to cancer and drug response (Bruntz et al. 2017; Choudhury et al. 2020; Faubert et al. 2021; Lane et al. 2019; Winnike et al. 2018). These changes can be explored by following the flux of stable isotopes from labeled precursors (e.g. [U-^{13}C] glucose and [U-^{15}N] glutamine) through cellular metabolic networks by using targeted and untargeted metabolomics.

Typically, the analysis of isotopic tracer enrichment is carried out in a targeted manner, which requires knowledge on the metabolic pathways beforehand. In contrast, profiling of metabolome-wide labeling in a non-targeted manner (Bueschl et al. 2017; Baumeister et al. 2018; Capellades et al. 2016; Dudek et al. 2020; Hoffmann et al. 2018; Huang et al. 2014; Kiefer et al. 2015; Llufrio et al. 2019; Puchalska et al. 2018; Weindl et al. 2016) holds great potential to detect pathway activity in unexpected parts of metabolism. The objective of this work was to establish stable isotope-resolved metabolomics as a test system for the characterization of metabolic alterations in cancer upon drug treatment. In a proof-of-concept application, the platform was applied to assess cancer metabolic network activities *in vitro* and to enable the characterization of drug induced alteration in the absence and presence of the selective PI3Kβ inhibitor AZD8186 in PTEN-WT and PTEN-null TNBC cell lines.

Several important aspects were addressed during the development of the SIRM platform. One goal was to establish and optimize the sample preparation workflow, which involved evaluation of metabolism quenching, sample storage and stability, as well as cell washing and pre-analytical normalization. Furthermore, the two TNBC cell lines (i.e. PTEN-null MDA-MB-468 and PTEN-WT MDA-MB-231) were functionally characterized, which included the determination of the PTEN status and dosage optimization of the PI3Kβ inhibitor AZD8186. These steps were important prerequisites to study the effects of PI3Kβ inhibition on metabolic pathways with the SIRM platform.

In the proof-of-concept application, the SIRM platform was applied using [U-^{13}C] glucose as a tracer. Here, the combination of targeted isotopologue feature extraction with a non-targeted routine based on X^{13}CMS allowed for the identification of isotope-enriched features that significantly differed between control and treatment conditions. Additionally, the established platform was harnessed to study lower parts of the central metabolism downstream of pyruvate using [U-^{13}C,^{15}N] glutamine, as well as [U-^{15}N] glutamine. Lastly, untargeted differential tracing was employed to study AZD8186 induced alterations in enrichment of labeled isotopes between the HCC70 and the MDA-MB-468 cell line. This revealed isotope-enriched features

that were significantly altered by the presence of the inhibitor, both shared and unique to each cell line.

4.1. Establishment of a sampling and processing workflow

4.1.1 Optimization of sample preparation

As some metabolites (e.g. ATP and glucose 6-phosphate) have turnover rates of a few seconds (Weibel et al. 1974), the result of a metabolomic analysis can be significantly affected by the sample preparation process. Therefore, the sample preparation needs to be performed as quickly as possible in order to accurately capture the state of a sample's metabolite profile at the time of collection. Furthermore, metabolites that are present in high amounts in the medium can complicate result interpretation when the focus is on analyzing intracellular metabolites. Here, the concentration of intracellular metabolites may be masked by higher abundant metabolites present extracellularly. Thus, several sample preparation procedures using different quench procedures, extraction solvents or wash steps for the removal of extracellular metabolites have been proposed (Bi et al. 2013; Dietmair et al. 2012; Ivanisevic et al. 2013; Kapoore et al. 2015, 2017; Lanning et al. 2017; Lorenz et al. 2011; Peterson et al. 2016; Sapcariu et al. 2014; Sellick et al. 2009; Sellick et al. 2010; Tang et al. 2013; Tang et al. 2016; Teng et al. 2009).

One major goal of this thesis was to develop a suitable and optimized workflow for conducting SIRM experiments. This involved addressing metabolism quenching, removal of extracellular metabolites present in the medium through a wash step and assessing the stability of cell extracts. The performance of the sample preparation workflow was evaluated based on the adenylated ribonucleotide levels and the adenylated energy charge (AEC). The use of the adenylated energy charge or the determination of ATP levels has been applied in various metabolomic studies to evaluate the efficiency of sample preparation workflows (Fu et al. 2019; Kapoore et al. 2017; Meyer et al. 2013; Sellick et al. 2010; Sellick et al. 2009; Zhang and Vertes 2015). Additionally, the effectiveness of the wash procedure was assessed using pyruvate and 3-hydroxybutyrate, which are intermediates present both intracellularly and excreted into the medium.

4.1.1.1. Quenching of metabolism

Albeit this work demonstrated that quenching and extraction with 80% ultra-cool methanol was superior compared to quenching with liquid nitrogen, successful metabolic arrest and better coverage using liquid nitrogen had been demonstrated previously for ribonucleotides (Lorenz et al. 2011; Kapoore et al. 2017). For example, Kapoore et al. reported higher ATP levels in LN_2 quenched samples compared to MeOH quenched samples, however no evaluation based

on the adenylated energy charge was performed by the authors. Furthermore, it was shown that reduced ATP levels in MeOH quenched samples were shown to be a result of leakage due to disrupted cell membrane upon extraction with unbuffered methanol. Additionally, an important characteristic of the established sample preparation procedure in this work is that quenching and extraction occurs simultaneously in a single well. Consequently, metabolite leakage is a desirable effect of using unbuffered methanol and circumvents the use of harsher and time consuming cell lysis procedures like an ultrasonic bath (Ivanisevic et al. 2013). Moreover, the authors point out that there are some difficulties in handling LN_2 (i.e. loss of sample and safety issues). Due to these issues, quenching was performed very carefully and thus was overall a slower procedure compared to the one-step quenching and extraction procedure with 80% MeOH. As turnover rates of 1.5 seconds for ATP have been described (Weibel et al. 1974), the observed low levels of ribonucleotides in this work are likely due to the slower quenching process associated with the LN_2 quenching method.

4.1.1.2. Wash procedure

The washing procedure is an important part of the sample preparation workflow, ensuring accurate quantification of intracellular metabolites while minimizing interference from residual medium attached to the cells. In this work a single PBS wash at two temperatures (i.e. 37 °C and 4 °C) was compared and demonstrated no significant differences with respect to the EC and extent of metabolite removal. The slightly higher, although not statistically significant, levels of intracellular pyruvate and 3-hydroxybutyrate upon warm wash (Figure 12 D) may be due to higher leakage with cold PBS. Another explanation might be that the warm wash introduces metabolic changes arising from ongoing metabolic activity leading to higher levels of ATP, ADP and AMP as observed in tendency in this work. Consequently, ATP-dependent metabolic reactions necessary for the biosynthesis of pyruvate and 3-hydroxybutyrate (i.e. glycolysis and TCA cycle) can continue for an extended period, explaining the slightly higher metabolite concentrations (Figure 12 C). It has been established by Kapoore et al. that a single wash step with ice-cold PBS does not causes a significant loss of metabolite levels, enabling an efficient removal of extracellular intermediates while simultaneously slowing down enzymatic reactions early in the sampling process (Kapoore et al. 2017). These observations from literature are in line with the findings from this work demonstrating no significant effect of the PBS washing buffer with respect to the analysis of intracellular metabolites.

4.1.1.3. Storage condition and stability

Additionally, the stability of the sample extracts when stored in the extraction solvent compared to storage of the sample after drying was investigated. Although both storage conditions did not significantly alter the ribonucleotide levels, analysis of the extract after drying and

resuspension in solvent prior to LC-MS analysis displayed lower ATP levels compared to the control condition, while the samples stored in extraction solvent showed higher concentrations than the control samples. The reduced levels in the dried extracts can potentially be a result of degradation during the drying process in the rotational vacuum concentrator, which operates at room temperature. Although ATP is not stable at room temperature (Chen and Xia 2021), the concentration of ADP and AMP does not increase in a similar manner to the decrease of ATP which points towards potential adsorption effects on the plastic surfaces (Verbeke et al. 2020) of these ribonucleotides, thus influencing the recovery of metabolites upon reconstitution of cell extracts, leading to diminished concentrations of the adenylated ribonucleotides. Since enzymatic activity is rapidly disrupted upon addition of 80%MeOH, there is no further *de novo* biosynthesis of ribonucleotides possible that could explain the increase in ribonucleotide levels. However, samples are only centrifuged and aliquoted into new plastic tubes prior freezing, which does not guarantee cell-free samples. Consequently, the slight increase in ribonucleotide levels can also be a result from longer extraction periods of residual cells in the centrifuged aliquots.

4.1.2 Normalization of quantitative metabolomics

Besides optimizing the sample preparation procedure, two different normalization procedures were assessed, as proper normalization is required to compensate for biological variations and to obtain accurate quantitative data. Commonly employed normalization approaches in cell culture based metabolomics include normalization to the DNA concentration, the protein content of a sample and the cell count (Wu and Li 2016). An appropriate approach for cell counting is automated live cell imaging that has been successfully employed for quantitative metabolomics (Nybo and Lamberts 2019) and bypasses time-consuming harvesting steps (i.e. trypsination) typically required prior cell counting of adherent cells (Silva et al. 2013; Wu and Li 2016).

Results obtained in this work displayed a strong correlation between normalization to DNA concentration and cell count and aligns well with findings made by Silva et al. (Silva et al. 2013). Here, the authors showed a strong correlation ($R^2 > 0.98$) between DNA concentration and cell counts for four different adherent cell lines (i.e. OVCAR-4, OVCAR-8, MDA-MB-435, and U251). A notable finding of this thesis was that normalization *via in situ* imaging was shown to be more robust compared to DNA content (Figure 13). While images were acquired directly in the cell culture dish, determining DNA concentration requires an additional sample aliquot obtained from the homogenate. This collection step reduces sample throughput and simultaneously may compromise reproducibility. For example, this could be due to the high vapor pressure of the extraction solvent (i.e. 80% methanol) in combination with the small sample volume required for the quantification (i.e. 10 µl), that potentially introduced pipetting

errors. Furthermore, the high organic proportion of the extraction solvent (i.e. 80%) might limit the extraction of the DNA from the homogenate. In this regard, a beneficial effect of using additional work up procedures (column based DNA extraction methods (Tolosa et al. 2007)) with respect to variability remains to be investigated.

4.2. Functional assessment and validation of breast cancer cell lines upon PI3Kβ inhibition

Concentration-dependent effects of the PI3Kβ isoform selective inhibitor AZD8186 on the MDA-MB-468 cell line were characterized by immune blotting and extracellular flux analysis and compared to the PTEN wildtype cell line MDA-MB-231. The determination of the optimal dose for the MDA-MB-468 cell line was further supported by quantification of intracellular intermediates and determination of extracellular rates. This characterization was necessary to provide the experimental basis for conducting time and cost-expensive SIRM studies.

The initial assessment of the effect of PI3Kβ inhibition on pAKT signaling showed, diminished phosphorylation of pAKT(Ser_{473}) caused by exposure to AZD8186 (Figure 15), thereby confirming the findings of Hancox et al (Hancox et al. 2015), who conducted similar experiments with the MDA-MB-468 cell line. Regarding effects on metabolism, the observations in the MDA-MB-468 cell line at 3 µM (Figure 16 A) are in accordance with the results of Lynch et al. (Lynch et al. 2017) who demonstrated decreased levels of glycolytic intermediates, and deoxyribonucleotide triphosphates (dNTPs) in the PTEN-null LNCAP prostate and HCC70 TNBC cell lines upon exposure to AZD8186 (0.25 µM). Limited availability of dNTPs has been associated with reduced proliferation and survival of tumor cells due to DNA damage (Juvekar et al. 2016) and has also been observed in other *in vitro* and *in vivo* studies employing AZD8186 (Hancox et al. 2015; Lynch et al. 2017; Maynard et al. 2016).

Further assessment of the MDA-MB-468 metabolic profile by real-time metabolic phenotyping displayed similarities to other PTEN-null cell lines (i.e. HCC70 and LNCAP cell lines), in which a concentration dependent reduction in glycolytic activity, indicated by ECAR and OCR, was observed (Lynch et al. 2017). It is noteworthy that reduced levels of TCA cycle intermediates, as determined by quantitative metabolomics, first described in this work for AZD8186 treatment (Figure 18) are in accordance with the observed reduction in OCR. This also holds true for the significantly reduced lactate excretion rate (Figure 18) that aligns well with the concentration dependent decrease in ECAR. Interestingly, the use of concentrations exceeding 1 µM also caused disturbances in the PTEN wildtype cell line (MDA-MB-231), suggesting off-target effects (Hancox et al. 2015). Although selectivity of AZD8186 for the PI3Kβ isoform over other PI3K isoforms exists, diminished phosphorylation of pAKT has been described at higher concentrations for AZD8186 supporting the observed reduction in ECAR and OCR for the

MDA-MB-231 PTEN wildtype cell line (Hancox et al. 2015). To ensure that inhibition of the PI3Kβ was not masked by off-target effects, a concentration of 0.5 µM AZD8186 was chosen for SIRM experiments. This concentration showed significant effects on cell proliferation (Figure 19), potentially due to DNA damage caused by the impaired biosynthesis of dNTPs (Juvekar et al. 2016).

It is worth mentioning that, when administered to humans, AZD8186 treatment was generally well tolerated although clinical development was discontinued. Maximum plasma concentrations reached about 1 µM after administering a dose of 60 mg AZD8186 twice a day for 5 days (Choudhury et al. 2022; Hansen et al. 2017; Owusu-Brackett et al. 2020; Vanhaesebroeck et al. 2021).

4.3. Application of the established Stable Isotope resolved metabolomics workflow

An integral part of this work involved the establishment of a stable isotope resolved metabolomics workflow, which was based on optimizing the sample preparation protocol (3.1). This optimization, along with the functional characterization of the TNBC cell line (3.2) served as an important pre-requisite. This SIRM workflow was employed to assess metabolic pathway alterations and drug induced changes in stable isotope incorporation upon pharmacological intervention with AZD8186. This section provides the discussion on all aspects of the SIRM workflow covered in this thesis including (i) extending pathway coverage by harnessing the untargeted data analysis capabilities of X^{13}CMS (Huang et al. 2014; Llufrio et al. 2019), (ii) detection of additional isotope-enriched features relevant to drug responses compared to steady state label-free untargeted metabolomics, (iii) evaluation of the workflow robustness based on intra-day and inter-day repeatability, (iv) monitoring drug induced changes in pathway activities using stable isotope labeled glucose and glutamine (v) in a targeted and untargeted manner, and lastly (vi) cell line specific metabolic differences upon PI3Kβ inhibition for distinct TNBC cell lines (MDA-MB-468 and HCC70, respectively).

4.3.1 Untargeted data analysis with X^{13}CMS using [U-^{13}C] glucose as a tracer

Using the X^{13}CMS workflow as a discovery and filtering tool for non-targeted identification of isotope-enriched metabolites produced candidate features that were assessed for structural assignment. Currently, besides 19 metabolites that could be attributed to pre-defined pathways, 11 additional compounds were identified with high confidence (Metabolomics Standard Initiative (MSI) level 1) (Salek et al. 2013) and integrated into the targeted feature extraction workflow for manual curation of the data thus increasing the accuracy of isotopologue quantitation. Most important, the knowledge of sum formulas of the newly

identified metabolites enables the correction for natural isotopic abundance (Heinrich et al. 2018; Nilsson 2020) thus overcoming a current limitation of the X^{13}CMS workflow (Llufrio et al. 2019). Albeit beyond the scope of this work, annotation of additional features can be achieved by retrospective examination of high-resolution QTOF-MS data for a continuous integration of novel identified metabolites into the targeted data analysis workflow. Likewise, the available LC/MS data can be used for the extraction of isotopic data by other tools than X^{13}CMS in order to expand the list of potential markers of drug response that, after their identification, can be implemented in the targeted data analysis routine. These tools may comprise geoRge (Capellades et al. 2016) or novel approaches that perform parameter optimization throughout the data processing workflow (Butin et al. 2022), thereby maximizing the yield of valuable isotopic data.

In this work, integration of the 11 newly identified metabolites into the existing targeted workflow resulted in an expansion of pathway coverage. Notably, all these metabolites have been associated with cancer metabolism and therapy, e.g. pyrimidine metabolism (Wang et al. 2021), the hexosamine pathway (Ferrer et al. 2016; Lam et al. 2021), glutathione (Kennedy et al. 2020), sialic acids (Pearce and Läubli 2016) and UDP-glucose (Wang et al. 2019). More specifically, they all belong to key metabolic processes (i.e. glucose metabolism, biosynthesis of macromolecules, and maintenance of redox balance) that are activated downstream of the PI3K/AKT signaling network (Hoxhaj and Manning 2020). Another interesting observation was made for 3H3MG that was found among the newly identified metabolites (3.3.1). 3H3MG belongs to the mevalonate pathway and is produced from (S)-3-hydroxy-3-methylglutaryl-CoA (HMG-CoA) (Fu et al. 2006; Hoffmann et al. 2019). Lynch et al. reported decreased HMG-CoA levels for PTEN negative cells upon exposure to AZD8186 and reported expression of genes encoding lanosterol synthase and genes for the biosynthesis of lathosterol (Lynch et al. 2017). The decreased carbon flux into 3H3MG, demonstrated by the applied SIRM workflow, supports these findings. In contrast to Lynch et al., it was possible to quantify the cholesterol precursors lanosterol and lathosterol in this work, and thus to confirm a reduced cholesterol biosynthesis by a significant decrease of the metabolite ratios lanosterol:cholesterol and lathosterol:cholesterol (Figure 30 B).

4.3.2 Comparison of label-free untargeted metabolomics with untargeted stable isotope labeling

The complementary nature of significantly changed features found by the X^{13}CMS routine compared to statistically altered features revealed upon data pre-processing in unlabeled samples with XCMS is in accordance with the literature (Huang et al. 2014). This complementarity was further confirmed by results obtained with vendor-specific Profinder pre-processing whose outcome reflected the 95% (19 out of 20) of significantly altered features

retrieved by XCMS. As previously shown (Huang et al. 2014) this comparison demonstrates that different biological information can be obtained from the datasets. For the insignificantly changed features of the label-free samples obtained from the Minidiffreport (Figure 22 B & C), a larger overlap with features from the SIRM workflow was observed (i.e. 33 features). These 33 features would have been missed by conventional label-free untargeted metabolomics due to their p-value or FC, and underline the complementary information provided by the SIRM workflow.

While the labeling approach provides results as a function of alterations in tracer incorporation, untargeted analysis in unlabeled samples discovers metabolites whose levels significantly change upon drug treatment. It must be noted that comparison between labeled and unlabeled untargeted metabolomics as done here and previously by (Huang et al. 2014), allows for the detection of significantly altered features obtained after data preprocessing with different workflows in labeled and unlabeled replicate samples from the very same cell culture experiment (i.e., similar to a “paired” experiment).

4.3.3 Robustness evaluation of SIRM workflow

Quality control and method validation is still a challenge in conventional LC-MS non-targeted metabolomics (Begou et al. 2018). In this regard, the use of tracer technology can be beneficial as this work demonstrates by the high repeatability for technical replicates (intra-day) and between independent experiments (inter-day). While careful visual inspection and curation of peak area integration during targeted data pre-processing is a factor that contributes to high precision within batches, internal normalization of mass isotopomer distribution vectors have a positive effect as well. Thus, the obtained results underline the robust and repeatable sample preparation and analysis between different batches (inter-day) which may minimize the need for inter-batch corrections in large-scale studies. Altogether, this work shows that targeted SIRM in cell culture provides a highly reproducible readout that makes a valuable contribution to the already established validation schemes for tracer experiments (Heuillet et al. 2018; Schwaiger-Haber et al. 2019).

4.3.4 Integrated targeted SIRM workflow upon PI3Kβ inhibition – [U-^{13}C] glucose

The results obtained with SIRM when treating the TNBC cells with AZD8186 (i.e. reduced carbon flux through glycolysis and *de novo* purine nucleotide synthesis) are in line with data obtained by real-time metabolic flux analysis and quantitative metabolomics (i.e. diminished levels of glycolytic intermediates, adenylated ribonucleotides, and a reduced lactate excretion rate, 3.2) and previous observations made by others (Lynch et al. 2017). A decreased glycolytic rate as well as markedly decreased levels of dNTPs were observed in HCC70 and LNCAP cells upon PI3Kβ inhibition by Lynch et al. as previously discussed (4.2). In addition, the

presented SIRM experiments uncovered that AZD8186 lowers carbon incorporation into purine and pyrimidine ribonucleotides, indicating that depletion of the dNTP pool results from reduced biosynthesis and was also observed for other PI3K inhibitors in breast cancer cells (i.e., HCC1937) (Juvekar et al. 2016). Another notable observation was a significantly reduced incorporation of glucose-derived carbon into intracellular lactate, which has not been demonstrated before for this isoform-specific inhibitor. Altogether, these metabolic changes suggest that PI3Kβ inhibition has a beneficial effect by reducing the anaerobic conversion from glucose to lactate. Given that Lynch et al. observed a decrease in the extracellular acidification in the presence of the same AZD8186 concentration (i.e. 0.5 µM), it can be assumed that the reduced intracellular lactate production is a significant contributor to a de-acidification of the extracellular space by reduced lactate secretion. Further, while Lynch et al. deduced a potentially reduced carbon flux into the TCA cycle from bioenergetic measurements (i.e. *via* reduced oxygen consumption) and an increased PDHK4 expression, the results of this work show that carbon flow into these metabolites is indeed compromised. This in turn supports a potential impact of the inhibitor on mitochondrial metabolism. Here, novel protocols to determine compartment-specific metabolic fluxes (Nonnenmacher et al. 2019) either alone or complemented by data on mitochondrial oxygen consumption (Jones et al. 2021) will be a powerful combination to broaden the understanding of how mitochondrial metabolism is affected upon PI3Kβ inhibition. The observations of a reduced glycolytic rate confirm that PI3K/AKT signaling is a key regulator of important cellular processes including glucose homeostasis (Schultze et al. 2012). Therefore, targeting PI3K/AKT pathways may have consequences on whole body energy metabolism including the treatment of complex metabolic disease. For example, altering PI3K/AKT signaling in pancreatic β-cells is considered as emerging therapeutic strategy for type 1 diabetes (Camaya et al. 2022). Experiments using transgenic murine models have provided evidence that PI3K/AKT signaling is a critical determinant of β-cell mass and function whose impairment is supposed to be an early feature of pathogenesis in type 1 and type 2 diabetes (Chen et al. 2017). With respect to PI3Kβ, a potential mechanism of the regulation of insulin secretion has been described. As kinase inhibition affects the differentiation of human stem cells into beta cells, thereby suggesting a role for PI3Kβ in embryonic development of the pancreas (Mao et al. 2017). Isoform-specific targeting may therefore be an attractive strategy in the clinic to develop inhibitors with optimal therapeutic index to control altered blood glucose homeostasis, which can be a potential side effect due to the complex involvement of PI3K isoforms in insulin action (Molinaro et al. 2019).

Stable isotope tracing is a powerful method for interrogating metabolic enzyme activities. Using [U-^{13}C] glucose as tracer, the route of pyruvate entry into mitochondrial metabolism can be deduced from the m+2 vs. m+3 isotopologue profiles of citrate and other TCA cycle intermediates (Buescher et al. 2015; Ma et al. 2019). Irrespective of AZD8186 exposure, MDA-

MB-468 cells showed a high PDH activity signature as indicated by the more pronounced basal m+2 isotopologues compared to m+3. The reduced incorporation into m+2 citrate upon treatment is in line with previously reported inhibition of PDH activity as evidenced by increased PDH phosphorylation (Lynch et al. 2017).

It must be emphasized that interpretation of the TCA cycle isotopologue profiles was carried out in the dynamic labeling phase which limits interpretation to the assessment of relative flux differences in metabolic pathways. The quantitative contribution of ^{13}C glucose to TCA intermediates pool sizes would either require enrichment to isotopic steady state (Buescher et al. 2015; Lorkiewicz et al. 2019) or analysis by non-stationary metabolic flux analysis (Jazmin and Young 2013). This is an often overlooked aspect and should be carefully considered when information about metabolite pool sizes is inferred from dynamic labeling data. Non-steady state labeling was also observed in larger composite molecules like UDP GlcNAc and UDP-glucose where the reduced carbon flux through glycolysis and TCA cycle was reflected in structural subunits (i.e. ribose, aspartate) that represent contributions of these pathways (Moseley et al. 2011; Nakajima et al. 2013). As an example, this work demonstrated different pathway contributions in the presence of AZD8186 for UDP-glucose (Figure 29). Here reduced incorporation into higher isotopologues (≥ m+11) mirrors the reduced carbon incorporation into metabolites of glycolysis, TCA cycle and pyrimidine biosynthesis. Altogether, these observations provide a first hypothesis for a more refined investigation of these branching pathways and their potential contribution to the mode of action of AZD8186.

4.3.5 Integrated targeted SIRM workflow upon PI3Kβ inhibition – [U-^{15}N] and [U-^{13}C,^{15}N] glutamine tracer

Aside from glucose, glutamine is also an important substrate that can act as a nitrogen source for the biosynthesis of e.g. amino acids and ribonucleotides and as a carbon donor *via* glutaminolysis for the TCA cycle and (Figure 8 and Figure 11). Therefore, investigation of nitrogen and carbon flux was expected to further elucidate potential drug induced changes upon AZD8186 inhibition in corresponding metabolic pathways.

The SIRM experiments using [U-^{15}N] glutamine demonstrated diminished nitrogen incorporation into purine and pyrimidine ribonucleotides upon AZD8186 treatment, pointing towards the described impaired biosynthesis of ribonucleotides (4.3.4). However, the biosynthesis of ribose *via* glycolysis appears to be the limiting factor as ^{15}N label incorporation from glutamine was unaffected by the presence of the inhibitor (Figure 32 B). Additionally, aspartate and glycine, key contributors of nitrogen to purine and pyrimidine structures, were not influenced by AZD8186, further supporting this hypothesis (Figure 31). Consequently, diminished ^{15}N labeling of ribonucleotides and composite molecules like UDP-GlcNAc and

CMP-NANA were potentially a result of impaired glycolytic activity and thus compromised supply of essential precursor molecules, such as ribose.

Monitoring of the ^{13}C flux from [U-^{13}C,^{15}N] glutamine into the TCA cycle allowed to investigate glutaminolytic activity in the MDA-MB-468 cell line. Although no relevant drug induced changes (aside from minor label incorporation into malate and fumarate, Figure 34 A,B) in pathway activities were observed after 24h (Appendix 11), further comprehensive information about metabolic activities was collected for the MDA-MB-468 cell line. For instance, tracing of [U-^{13}C] glucose resulted in a total ^{13}C labeling of 30%, while [U- ^{13}C, ^{15}N] glutamine yielded a ^{13}C fractional labeling of 50% after 24h. If the fractional contribution is calculated according to Buescher et al. 2015, 20% of the carbon atoms originate from other sources, with acetate possibly playing a role as shown by Kamphorst et al. (Kamphorst et al. 2014). Furthermore, other unlabeled carbon sources, e.g. glutamate, can also be freely taken up from the culture media and thus be directly involved in the biosynthesis of α-ketoglutarate.

Another interesting observation was made from monitoring ^{13}C flux from labeled glutamine and the labeling patterns of α-ketoglutarate, malate, and citrate, which indicated a predominantly oxidative decarboxylation of the TCA cycle with only minor reductive carboxylation activity under the normoxic cultivation conditions. Although no significant changes were observed for the AZD8186 treated cells, investigation of reductive carboxylation and oxidative decarboxylation has been demonstrated for other cancer cell lines (e.g. SF188) using these metabolites (i.e., malate and citrate), and corresponding isotopologues respectively (Jang et al. 2018; Wise et al. 2011). Moreover, under hypoxic conditions, reductive carboxylation activity was shown to be increased for the MDA-MB-468 cell line (Kamphorst et al. 2014). Therefore, subsequent SIRM experiments using hypoxic conditions may provide valuable insights into alterations of metabolic pathway activities upon AZD8186 treatment.

At last, the comparison of the untargeted SIRM analysis from the glutamine tracing experiment (i.e, [U-^{13}C,^{15}N] glutamine) with the previously obtained data from the [U-^{13}C] glucose labeling experiment (3.3.1) was expected to add complementary information on metabolic changes upon treatment with AZD8186 beyond the preselected targeted list. This was done to gain a better insight into commonly affected pathways and to collect information about drug induced alterations in metabolic pathways that were only detectable with one of the tracer substrates (i.e. [U-^{13}C] glucose or [U-^{13}C,^{15}N] glutamine).

A feature overlap with the untargeted SIRM data of the [U-^{13}C] glucose experiment was to a certain extend likely, since major drug induced disturbances within e.g. the ribonucleotide biosynthesis and hexosamine pathway were shown in this thesis for both tracers (Figure 24 and Figure 31). The resulting overlap of ~7% (i.e. 40 features) for the combination of the

untargeted data from the three tracers (i.e., ^{13}C from glucose, ^{13}C and ^{15}N from glutamine) was therefore expected. While structural identification linked 10 of these features belonging to the e.g. amino acid metabolism, ribonucleotide biosynthesis, and hexosamine pathway, and these were discussed in this thesis previously (4.3.4 and 4.3.5), the remaining features could indicate other metabolic pathways not yet associated with AZD8186 treatment, but which could be investigated using either tracer substrate.

While these overlapping metabolites display commonly affected pathways, the features uniquely found for the corresponding tracer may provide additional information of drug induced alterations specifically occurring for catabolic pathways of glutamine and glucose, respectively. Of the unique features for the [U-^{13}C] glucose tracer (i.e., 71 features, Figure 36), 12 could be identified, 11 of which belonged to the central carbon metabolism (e.g. pyruvate, lactate, and aconitate) and one was the amino acid glutamine (Appendix 13).

Regarding the unique features incorporating ^{13}C (125 features) or ^{15}N (55 features) from [U-$^{13}C^{15}N$] glutamine (Figure 36), only AMP or ATP, respectively, could be identified (Appendix 13) and have been shown to be significantly affected by the presence of the inhibitor using [U-^{13}C] glucose (Figure 24). Although the robustness of this SIRM workflow has been demonstrated within this work, preanalytical (i.e. quenching and metabolite extraction) and postanalytical steps, especially in the case of two individually performed experiments, can have a crucial effect on the collected data, thus also explaining the variation in the presented data and the absence of certain features (Gertsman and Barshop 2018).

Furthermore, it is apparent that only a minor fraction of features could be identified for the commonly shared features (i.e. 10 out of 40 features) as well as for the unique features (e.g. 12 out of 71 for the ^{13}C glucose tracer), underlining the difficulties associated with feature annotation in untargeted metabolomics (Schrimpe-Rutledge et al. 2016). In turn, it was not possible to detect novel metabolites or pathways associated with PI3Kβ inhibition in general or specific to a certain tracer substrate. Nevertheless, comparing these data and extracting the corresponding unique features showed that there are specific features that depend on the tracer employed. Consequently, data mining of fragment spectra with other tools (e.g., SIRIUS, MetFrag, or MS-Finder (Dührkop et al. 2019; Tsugawa et al. 2016; Wolf et al. 2010)) might significantly improve pathway coverage providing a better insight into drug induced changes.

4.3.6 Characterization of metabolic differences between the cell lines MDA-MB-468 and HCC70

The established SIRM platform was employed to assess AZD8186-induced alterations and the cell line specific differences in ^{13}C isotope enrichment between the two PTEN-null TNBC cell lines HCC70 and MDA-MB-468, using [U-^{13}C] glucose as a tracer substrate. This allowed for

the investigation of metabolic changes upon PI3Kβ inhibition that were either global, cell line specific, or common to both cell lines. In contrast to the experimental conditions of the initial tracing experiments with [U-^{13}C] glucose (3.3), a preincubation period with AZD8186 for 24h without the tracer substrate was applied for both cell lines. This allowed for monitoring of drug related changes in tracer incorporations in pathways with high turnover rates (e.g. glycolysis, pentose phosphate pathway). Additionally, with sampling after 15 minutes a more comprehensive illustration of label incorporation into glycolytic metabolites was envisioned, as these intermediates typically reach isotopic-steady state a few minutes after the addition of tracer (Jang et al. 2018).

4.3.6.1. Global ^{13}C tracer incorporation into MDA-MB-468 and HCC70 upon exposure to AZD8186

Comparison of the global ^{13}C incorporation in the MDA-MB-468 and HCC70 cell lines provided a first insight into differences and potential similarities in the metabolic phenotype. Interestingly, the MDA-MB-468 cell line displayed a 1.8-fold increase in features (286 vs. 521 features) when compared to the previously performed SIRM experiment using [U-^{13}C] glucose (3.3.1). Especially in the treated condition a ~3-fold increase in features was observed (162 compared to 56 features) suggesting the activation or shift in compensating metabolic pathways, resulting in the labeling of features not typically produced under vehicle-treated conditions or under the previous employed experimental conditions (i.e. preincubation and 24h treatment duration).

Furthermore, the cell line comparison revealed notable differences in both the number and distribution of features with significantly altered labeling patterns between control and AZD8186 treatment (Figure 38). The HCC70 cell line showed fewer features (i.e., 417 vs. 521) compared with the MDA-MB-468 cell line. Interestingly, 49% of these features were found in the control condition for the HCC70 cell line, compared to only 35% for the MDA-MB-468 cell line. This could indicate a different baseline metabolic activity in the vehicle treated condition potentially due to slower tracer uptake by the HCC70 cell line. Furthermore, only 16% (i.e. 66 features) of significantly altered features in the HCC70 cell line were found in the treatment condition indicating a distinct metabolic response to AZD8186 treatment compared to the MDA-MB-468 cell line, where 31% (i.e. 162 features) were altered under treatment. This difference may either be a result of the slower uptake, or it could also reflect drug-induced diminished tracer uptake or even interruption or downregulation of metabolic pathways upon PI3Kβ inhibition in the HCC70 cell line.

The comparison of the global ^{13}C incorporation provided a basis for further data interpretation and assessment of metabolic changes that were different for the two cell lines (4.3.6.2) as well

as the cell line specific responses based on unique features that were identified in the presence of AZD8186 (4.3.6.3). To this end, the two datasets after untargeted SIRM data analysis were combined, aligning features from both cell lines (i.e. 521 for the MDA-MB-468 and 417 for the HCC70 cell line) according to their mass and retention time.

This alignment resulted in a high number of identical features ~22% (i.e. 162 features) affected in both cell lines (Figure 39). Among these, 20 features were identified and shown in this work to be affected by PI3Kβ inhibition for the MDA-MB-468 cell line using the [U-^{13}C] glucose tracer (Figure 24). The targeted isotopologue extraction demonstrated similar drug induced changes (e.g. diminished labeling of glycolytic and TCA cycle intermediates, ribonucleotides) in the HCC70 cell line for these intermediates upon treatment with AZD8186 (Appendix 14). The large part of overlapping features align well with findings by Roig et al. 2017 who performed untargeted metabolomics and investigated the metabolic profile of breast cancer cell lines with and without BRCA1 gene mutations (i.e., HCC70, MDA-MB-468, MCF-7, MDA-MB-231, and MDA-MB-436). Here, HCC70 and MDA-MB-468 segregated into the same cluster (along with MDA-MB-436) based on their metabolic profile upon unsupervised principal component analysis.

4.3.6.2. Integrated targeted SIRM analysis to elucidate metabolic differences upon PI3Kβ inhibition in commonly altered features

Although the same pathways and metabolites were affected by the inhibitor, the label incorporation differed notably within the control condition as well as in the AZD8186 treated condition after 24h (Figure 40). Lanning et al. 2017 also observed differences between the cell lines used (i.e., HCC70, MDA-MB-468) in the corresponding basal and maximal metabolic profiles obtained from Seahorse extracellular flux analysis. While the MDA-MB-468 cell line predominantly uses oxidative over glycolytic metabolism, the HCC70 relies on both pathways similarly. Faster labeling of TCA cycle intermediates and subsequent metabolites (e.g. ribonucleotides), as presented in this work (Figure 40), could result from this predominantly oxidative metabolism in MDA-MB-468. Interestingly, the authors also determined metabolic flexibility (i.e. compensational capabilities if one pathway is disturbed), with the MDA-MB-468 being more flexible. Consequently, the larger delta incorporation seen under the AZD8186 treated condition (Figure 40) can be a result of this flexibility, where potentially diminished glycolytic activity caused by AZD8186 leads to an increased oxidative metabolism (*via* TCA cycle) compared to the HCC70 cell lines.

Notably, the cell count was significantly lower in the HCC70 cell line after 24h with the tracer (Appendix 15), although both cell lines were initially seeded at identical concentrations (i.e., $5*10^5$ cells/well). As the tracer uptake rate is dependent on the growth rate (Antoniewicz 2018),

the significantly lower cell count after 24h could indicate a slower growth rate, and thus also explain the slower tracer incorporation in the HCC70 cell line and the diminished labeling of subsequent metabolites. Moreover, although glucose transporters (e.g., GLUT1) have been shown to be overexpressed in TNBC (Oh et al. 2017; Shi et al. 2020), different expression levels or activities might also explain differences in tracer incorporation observed between the two cell lines. Furthermore, while slower tracer incorporation for the HCC70 cell line was observed, the metabolic activity (e.g. tracer uptake) could still be similar due to larger metabolite pool sizes that require more time to be labeled (Buescher et al. 2015; Jang et al. 2018). However, this remains to be investigated for example by targeted quantitative metabolomics or even ^{13}C metabolic flux analysis to quantify intracellular fluxes (Antoniewicz 2018; Buescher et al. 2015).

Another interesting observation was related to the ribonucleotides. For these metabolites, the label incorporation of the m+5 isotopologue (i.e., ribose moiety obtained from PRPP after PPP, 1.3.3.4), was one of the most prominent differences between the two cell lines. It was therefore of interest to investigate cell line dependent differences using targeted isotopologue feature extraction of 6-PG as a surrogate metabolite of the PPP. While the larger labeling fraction of the m+0 isotopologue after 15 minutes in the HCC70 cell line indicated slower incorporation, the labeling pattern differed significantly for both cell lines throughout the experiment (Figure 41). The oxidative branch of the PPP is considered irreversible (Perl et al. 2011), the resulting m+5 isotopologue of 6-PG therefore cannot result from reductive carboxylation activity of the 6-phosphogluconate dehydrogenase. However, the ribose moiety can reenter the glycolysis *via* F6P after multiple steps and conversions within the non-oxidative branch of the PPP (e.g. xylulose-5-phosphate → F6P, sedoheptulose-7-phosphate → F6P) (Patra and Hay 2014; Shestov et al. 2016). G6P is subsequently produced from F6P via the enzyme glucose-6-phosphate isomerase (Achari et al. 1981) and can then reenter the PPP via 6-PG. These metabolic reactions may be the explanation for the presence of the m+5 isotopologue in both cell lines. However, the difference in the labeling fraction between the two cell lines may suggest cell line dependent differences in enzymatic activity. Moreover, both cell lines showed higher labeling fractions of the m+5 isotopologue after 24h suggesting an increase in non-oxidative PPP activity as a compensatory mechanism in order to maintain energetic demands and avoid further depletion of ribonucleotide levels. In this context positionally labeled glucose (i.e. [$^{13}C_2$-1,2] glucose) could contribute to a better understanding of oxidative and non-oxidative PPP activity of both cell lines in future studies (Miccheli et al. 2006).

4.3.6.3. Identification of cell line specific features

Besides the commonly changed features and metabolites, the alignment of the two datasets after untargeted SIRM data analysis also produced a list of significantly altered features that

were unique to the corresponding cell line (i.e., 342 features in MDA-MB-468 and 240 features in HCC70). Identification of these features aimed to expand the metabolites affected by AZD8186 to investigate cell line specific responses upon PI3Kβ inhibition. and potentially get a deeper understanding of the drugs mode of action.

To this end, the unique features specific to each cell line were investigated for their fragment spectra and compared with MS/MS spectra and retention times of previously identified compounds (Appendix 2) or annotated using the SIRIUS workflow (Dührkop et al. 2019). This approach has identified some metabolites that have already been shown to be affected by AZD8186 treatment and are associated with the central carbon, amino acid and UDP-sugar metabolism (Appendix 17, 3.3.4 and 3.5.3).

Interestingly, metabolites related to the lipid metabolism were identified at MSI level of at least 2 which had not previously been associated with AZD8186 treatment. While 3H3MG, a metabolite of the mevalonate pathway, a key pathway for lipid biosynthesis, has been shown to be significantly affected by PI3Kβ inhibition (Lackner et al. 2022), the identification of these hitherto unknown metabolites of the lipid metabolism further supports the drug-induced effect on lipid homeostasis. This also suggests a broader effect of PI3Kβ inhibition beyond the down-regulation of the cholesterol metabolism as shown upon AZD8186 treatment by Lynch et al. (Lynch et al. 2017). Specifically, 13 compounds were associated with lipid biosynthesis (i.e. phospholipids and fatty acids) and were identified exclusively in the MDA-MB-468 cell line. This is also true for the HCC70 cell line, although only three metabolites (i.e., stearic acid, glycerophosphoglycerole, and PI(18:1(9Z)/0:0) could be associated with the lipid metabolism. Although these metabolites were cell line specific, the pathway involved suggests a consistent drug response and a similar impact of PI3Kβ inhibition on cellular metabolism, regardless of the cell line.

The use of SIRIUS (Dührkop et al. 2019) increased the identification rate, especially compared to the sole use of the METLIN Metabolite PCDL as previously described for the glutamine tracer (^{13}C and ^{15}N, 4.3.5). This allowed to further link metabolites of the lipid metabolism to AZD8186 treatment beyond the mevalonate pathway. However, the low or potential misidentifications (i.e., metabolites from exogenous sources that did not incorporate ^{13}C) highlights one of the bottlenecks in the untargeted metabolomics workflows (Gertsman and Barshop 2018). In this experimental setting, 26 out of 342 features were identified in the MDA-MB-468 cell line and 20 out of 240 features in the HCC70 cell line. These results are consistent with other metabolomics studies reporting identification rates of about 10% (Gauglitz et al. 2022; Stancliffe et al. 2022). While approaches such as improving chromatography conditions (Anderson et al. 2021) or using a pseudo-MS/MS reference library from a metadata-annotated source (Gauglitz et al. 2022) have been proposed to enhance compound identification, this

challenge persists in untargeted metabolomics. Lastly, confirming these hitherto unknown features beyond MSI level 2 (Salek et al. 2013; Sumner et al. 2007) was not within the scope of this work. Nonetheless, the annotation of additional features has the potential to further expand the established targeted list, thus identifying cell line-specific responses to AZD8186 inhibition that may reflect distinct metabolic characteristics and could contribute to a better understanding of the metabolic response of PI3Kβ inhibition across different TNBC cell lines.

4.4. Conclusion and future directions

4.4.1 Conclusion

This work demonstrated the successful establishment of a targeted and non-targeted SIRM workflow including its' application in assessing metabolic pathway activities related to drug-induced alterations upon PI3Kβ inhibition with AZD8186. Several key aspects of the experimental set up and conduction of SIRM experiments were addressed, contributing to the platform's successful establishment.

First, the protocol was robust with respect to metabolic quenching as shown by a high energy charge (>0.9). Moreover, the protocol ensured efficient removal of secreted metabolites through washing and maintained stable sample extracts. Normalization based on live cell imaging was found to be superior to DNA concentration-based normalization for quantitative metabolomics, thus enabling a rapid pre-analytical adjustment of solvent ratios for metabolite extraction without the need for additional DNA preparation steps. With respect to assay performance, the entire workflow was validated and demonstrated high reproducibility for technical replicates and between experiments.

Real-time flux analysis and quantitative label-free metabolomics enabled determination of appropriate dosing of AZD8186. These prerequisites were successfully accomplished, providing the necessary framework for the envisioned SIRM platform.

In the proof-of-concept application using [U-^{13}C] glucose, specific inhibition of the PI3Kβ isoform in the PTEN-deficient breast cancer cell line MDA-MB-468 confirmed significant alterations in central metabolism while additional changes in pyrimidine biosynthesis and the hexosamine pathway were identified. Discovery of additional metabolites, that were found changed as a function of drug response, were in turn revealed by applying X^{13}CMS routine for global tracking of isotopic labels in untargeted metabolomics. This kind of unbiased data analysis strategy demonstrates how specific changes in drug-induced pathways activities can be uncovered without preliminary assumptions. This may lead to new hypotheses about potentially targetable pathways while paving the way for novel treatment concepts in cancer precision medicine.

Using tracer substrates beyond [U-^{13}C] glucose such as labeled glutamine [U-^{13}C and U-^{13}C,^{15}N] allowed to investigate metabolic fluxes in lower parts of the central metabolism (e.g. hexosamine pathway and pyrimidine *de novo* biosynthesis) thereby demonstrating broad application of the established workflow to monitor isotopic enrichment from various tracer substrates. Finally, assessment differences and similarities in isotopic enrichment between two cancer cell lines showed cell-line specific metabolic responses that provide a starting point for further elucidation of uncharacterized pathways associated with metabolic flexibility and drug response.

4.4.2 Future directions

An important aspect of the newly established workflow is its general applicability. Albeit it was set up in 2D cell culture (Figure 14), it can be easily adapted to monitor the metabolic fate of isotopic tracers in other *in vitro* systems, including patient-derived 3D models (Fan et al. 2018) or to probe tumor (Faubert et al. 2021) or cell metabolism (Fernández-García et al. 2020) *in vivo*. Notably, a recent comparison using metabolic flux analysis demonstrated that glucose metabolism in 3D spheroids differs significantly from 2D cultures (Tidwell et al. 2022), hence emphasizing the need to make use of 3D models for investigating cancer metabolism and drug response in cell culture. In this regard, *in vivo* profiling of tumor metabolic routes in the appropriate tissue environment will be key for interrogating drug action in human cancers (Lane et al. 2016) and identifying relevant alterations that contribute to cancer onset and progression (Grima-Reyes et al. 2021). While the adaptability to different biological systems is one aspect of this workflow, usage of different tracers can also be readily implemented to gain complementary information (e.g. on pyrimidine biosynthesis with [U-^{15}N] glutamine (Jang et al. 2018) or to consider other pathways (e.g. pentose phosphate pathway with [1,2-^{13}C]glucose) that are relevant for cancer metabolic reprogramming (Cossu et al. 2020; Wang et al. 2016). Lastly, the implementation of novel isotope tracing metabolomics technologies that can increase the coverage of isotope label detection (Wang et al. 2022), enable the assessment of metabolism in cell subpopulations (Roci et al. 2016), spatially resolve tracer incorporation and fluxes in tumor tissues (Schwaiger-Haber et al. 2023), or large-scale profiling *via* “deep labeling” (Grankvist et al. 2020) can further support the discovery of previously unknown markers of cancer and drug response.

Regarding PI3Kβ inhibition, employment of other PTEN-null cell-line models (e.g. LNCaP or PC-3) might help uncover further drug-induced effects on metabolic pathways, potentially leading to novel metabolic signatures for diagnostic, prognostic or treatment response monitoring markers. Additionally, studying PIK3β inhibition using SIRM in further PTEN-null *in vitro* or *in vivo* models (e.g. mouse tumor xenografts, organoids), may enhance understanding of drug responses considering cell-cell interaction and the tumor microenvironment and

potentially prevent clinical trial failures like those with AZD8186 (Choudhury et al. 2022; Hansen et al. 2017; Owusu-Brackett et al. 2020). Furthermore, using positionally labeled tracers (like [1,2-^{13}C] glucose) can provide a deeper understanding of specific fluxes, such as the pentose phosphate pathway or ribonucleotide biosynthesis, in therapeutic intervention (Jang et al. 2018). This approach can offer novel mechanistic insights into the drug mode of action and resistance mechanisms in cancer cell metabolism. Finally, combining quantitative metabolomics with stable isotope labeling data can establish the framework for quantitative metabolic flux analysis (Antoniewicz 2018). This will allow quantitative determination of changes in substrate fluxes upon PI3Kβ inhibition, providing further insights into drug-induced metabolic changes by AZD8186.

Lastly, increased metabolic coverage of less polar compounds can be achieved by combined approaches using both RP and HILIC columns, and for other compound classes by additional measurement in positive mode, which could be easily integrated into the existing workflow (Contrepois et al. 2015; Leuthold et al. 2017).

This work underlines the potential of the SIRM platform as an important tool for advancing cancer cell metabolomics. Combining targeted and untargeted SIRM can complement conventional label-free metabolomics, by identifying altered metabolic pathway activities that may be missed by label-free metabolomics approaches, providing novel insights into cancer metabolism. Overall, this work established a SIRM platform that allowed for the investigation of changes in metabolic pathway activities that is neither limited to the PI3K signaling pathway nor specifically to PIK3β inhibition in TNBC cell lines. This platform has the potential to further drive the exploration of cancer cell metabolism contributing significantly to cancer research and potentially supporting the development of new treatment strategies for patients.

5. Appendix

Appendix 1: Calculated CV values after normalization against DNA concentration or cell count. Mean levels and standard deviations of corresponding metabolites were determined from three technical replicates

Metabolite	Normalization by cell count – CV in [%]	Normalization by DNA concentration – CV in [%]
Sed7P	3.41	21.40
G6P	2.93	25.30
G1P	4.47	27.93
Pentose5P	8.47	31.93
6PG	9.11	21.22
3PG	3.37	26.48
PEP	6.90	25.45
F16BP	1.94	24.06
Pyruvate	7.60	23.01
Hydroxybutyrate	12.19	15.07
Fumarate	5.16	23.00
a-Ketoglutarate	5.86	23.40
Malate	5.89	23.23
Citrate	5.51	23.38
ADP	16.14	8.09
ATP	5.70	19.05

Appendix 2: Targeted library comprising annotated metabolites from selected pathways and newly identified metabolites from the X^{13}CMS workflow. [a]Metabolites detected in cell extracts after pre-processing with reference library established from pre-defined pathways. [b]Newly identified metabolites after X^{13}CMS based filtering for differential labeling patterns that were added to the reference library. [c]disregarded for inter-day reproducibility assessment as metabolite was not detectable in day 2 experiment. [d]metabolite not considered for robustness evaluation and proof of concept assessment due to low (<2%) fractional enrichment of label incorporation. Adapted from Lackner et al. 2022

Data analysis workflow	Compound	Neutral mass	Formula	RT [min]	Intra day	Inter day
Targeted[a]	Glycine	75.032	$C_2H_5NO_2$	5.177	x	c
	Pyruvate	88.016	$C_3H_4O_3$	1.752	x	x
	L-alanine	89.048	$C_3H_7NO_2$	4.633	x	x
	Lactate	90.032	$C_3H_6O_3$	2.563	x	x
	L-serine	105.043	$C_3H_7NO_3$	5.254	x	x
	L-proline	115.063	$C_5H_9NO_2$	3.411	x	x
	Fumarate	116.011	$C_4H_4O_4$	7.859	x	x
	Succinate	118.027	$C_4H_6O_4$	7.216	x	x
	L-aspartate	133.038	$C_4H_7NO_4$	6.934	x	x
	Malate	134.022	$C_4H_6O_5$	7.539	x	x
	a-ketoglutarate	146.022	$C_5H_6O_5$	6.731	x	x
	L-glutamine	146.069	$C_5H_{10}N_2O_3$	5.318	d	d
	L-glutamate	147.053	$C_5H_9NO_4$	7.057	x	x
	2-hydroxyglutarate	148.037	$C_5H_8O_5$	7.417	x	x
	Phosphoenolpyruvate (PEP)	167.982	$C_3H_5O_6P$	9.516	x	x
	Aconitate	174.016	$C_6H_6O_6$	7.024	x	x
	D-3-phosphoglycerate (3-PG)	185.993	$C_3H_7O_7P$	9.005	x	x
	D-2-phosphoglycerate (2-PG)	185.993	$C_3H_7O_7P$	8.818	x	x
	Citrate	192.027	$C_6H_8O_7$	9.155	x	x
	D-fructose 6-phosphate (F6P)	260.030	$C_6H_{13}O_9P$	8.121	x	x

Data analysis workflow	Compound	Neutral mass	Formula	RT [min]	Intra day	Inter day
	Glucose 1-phosphate (G1P)	260.030	$C_6H_{13}O_9P$	8.194	x	x
	D-glucose 6-phosphate (G6P)	260.030	$C_6H_{13}O_9P$	8.651	x	x
	Fructose-1,6-BP (F16BP)	339.996	$C_6H_{14}O_{12}P_2$	10.709	x	x
	Adenosine monophosphate (AMP)	347.063	$C_{10}H_{14}N_5O_7P$	7.107	x	c
	Adenosine diphosphate (ADP)	427.029	$C_{10}H_{15}N_5O_{10}P_2$	8.346	x	x
	Adenosine triphosphate (ATP)	506.996	$C_{10}H_{16}N_5O_{13}P_3$	8.956	x	x
Untargeted[b]	Pyroglutamic acid	129.043	$C_5H_7NO_3$	3.420	d	d
	3-hydroxy-3-methylglutarate (3H3MG)	162.053	$C_6H_{10}O_5$	6.572	x	x
	N-acetyl-L-aspartate (NAA)	175.048	$C_6H_9NO_5$	7.346	x	x
	Glutathione (GSH)	307.084	$C_{10}H_{17}N_3O_6S$	6.989	x	x
	N-acetylneuraminate (NANA)	309.106	$C_{11}H_{19}NO_9$	5.530	x	x
	Uridine diphosphate (UDP)	404.002	$C_9H_{14}N_2O_{12}P_2$	8.248	x	x
	Uridine triphosphate (UTP)	483.969	$C_9H_{15}N_2O_{15}P_3$	8.869	x	x
	UDP-glucose	566.055	$C_{15}H_{24}N_2O_{17}P_2$	7.179	x	x
	Uridine diphosphate-N-acetylglucosamine (UDP-GlcNAc)	607.082	$C_{17}H_{27}N_3O_{17}P_2$	7.028	x	x
	Oxidized glutathione (GSSG)	612.152	$C_{20}H_{32}N_6O_{12}S_2$	10.398	x	x
	CMP-N-acetylneuraminic acid (CMP-NANA)	614.147	$C_{20}H_{31}N_4O_{16}P$	7.875	x	x

Appendix 3: Day-to-day reproducibility of SIRM experiments indicated as average tracer incorporation on Day 1 vs. Day 2 (tracer incorporation >2% and <100%). Tracer incorporation after 1h cultivation with [U-^{13}C] glucose and 0.5 µM AZD8186

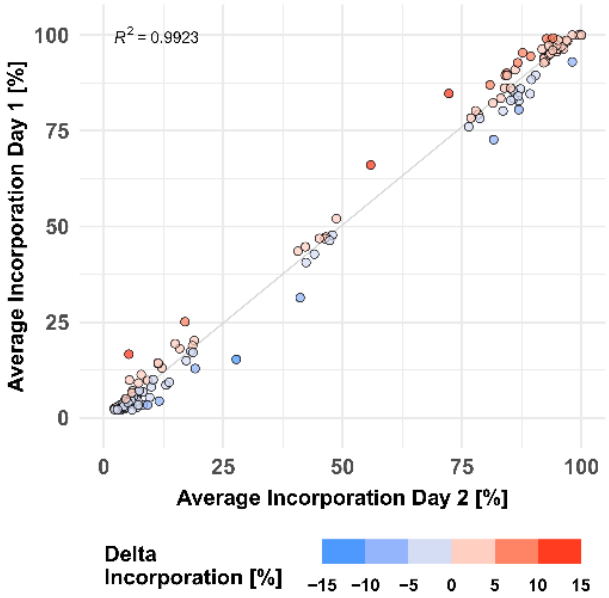

Appendix 4: MDA-MB-468 cells were cultivated in RPMI with [U-^{13}C] glucose and treated with 0.5 µM AZD8186 (purple) or vehicle (green). Bar charts ± standard deviation (n=3 technical replicates) showing the fractional enrichment of ^{13}C into G6P (A) and PEP (B) at 1h (A). * p< 0.05; (adjusted p-value; Welch's t-test)

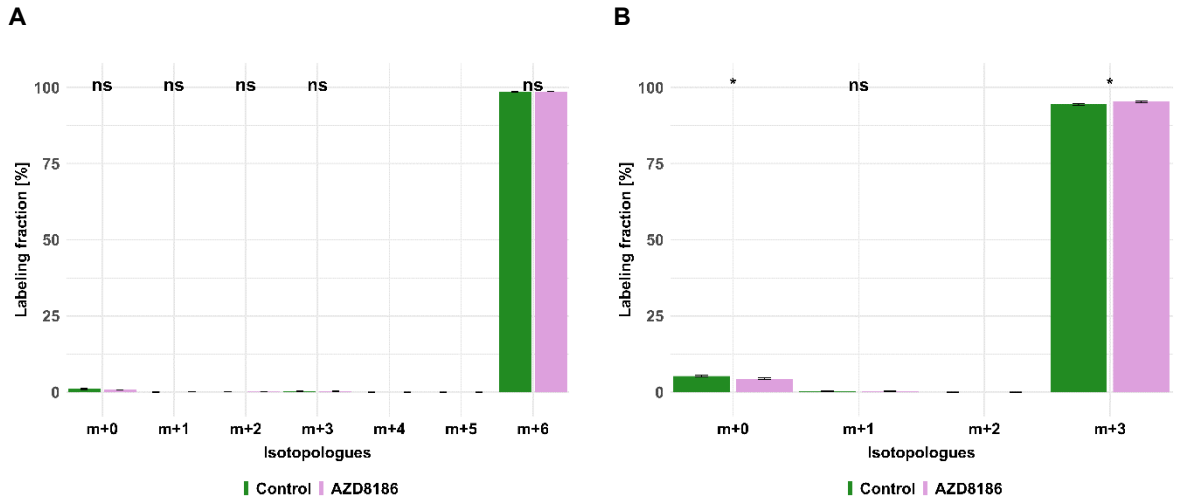

Appendix 5: MDA-MB-468 cells were cultivated in RPMI with [U-^{13}C] glucose and treated with 0.5 µM AZD8186 (purple) or vehicle (green). Bar charts ± standard deviation (n=3 technical replicates) showing the fractional enrichment of ^{13}C into pyruvate at 3h (A), G6P at 24h (B), serine at 24h (C). ns p> 0.05 (adjusted p-value; Welch's t-test)

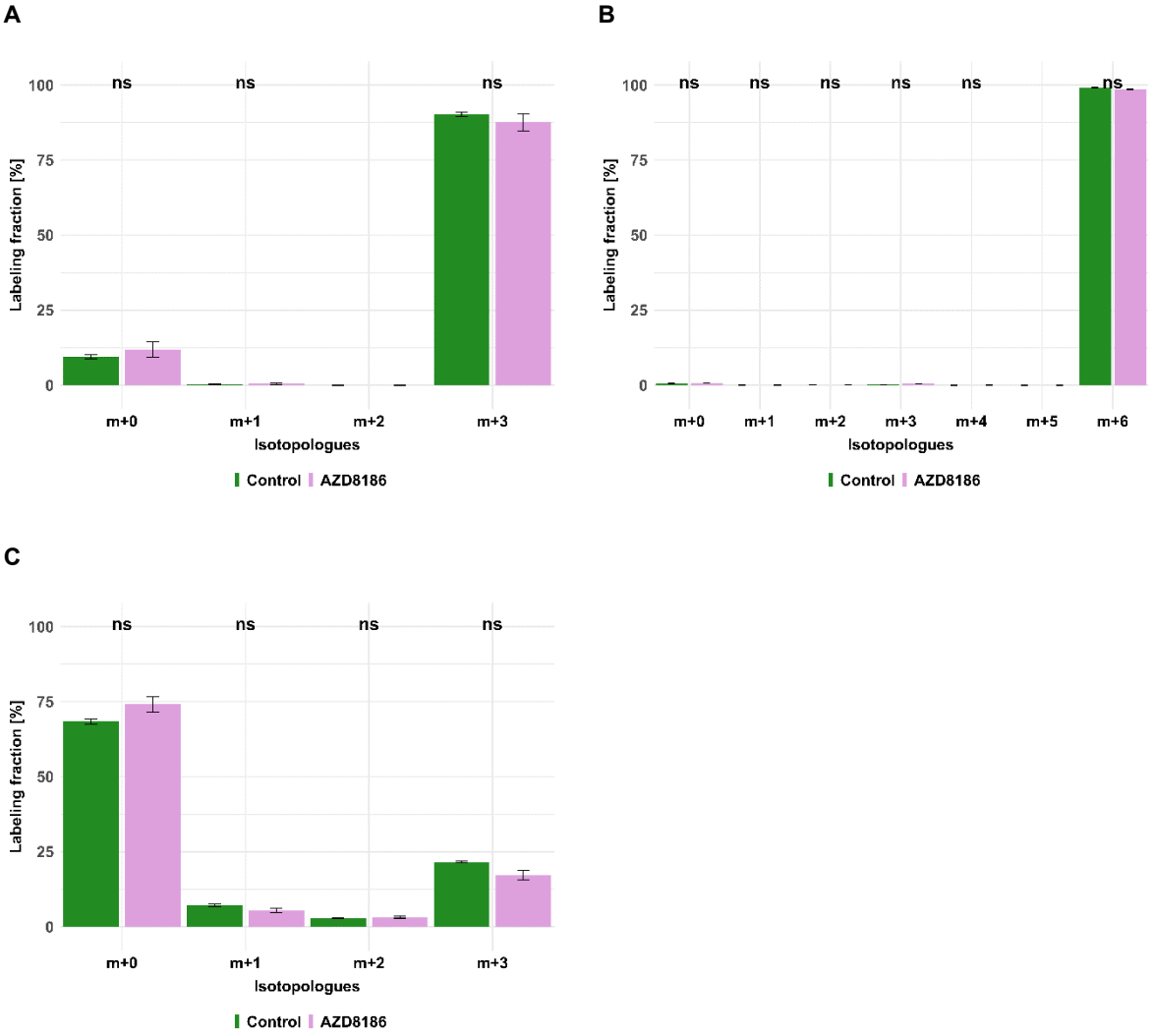

Appendix 6: MDA-MB-468 cells were cultivated in RPMI with [U-^{13}C] glucose and treated with 0.5 µM AZD8186 (purple) or vehicle (green). Bar charts ± standard deviation (n=3 technical replicates) showing the fractional enrichment of ^{13}C into aspartate (A) and malate (B) at 24h. * p< 0.05; ** p< 0.01 (adjusted p-value; Welch's t-test)

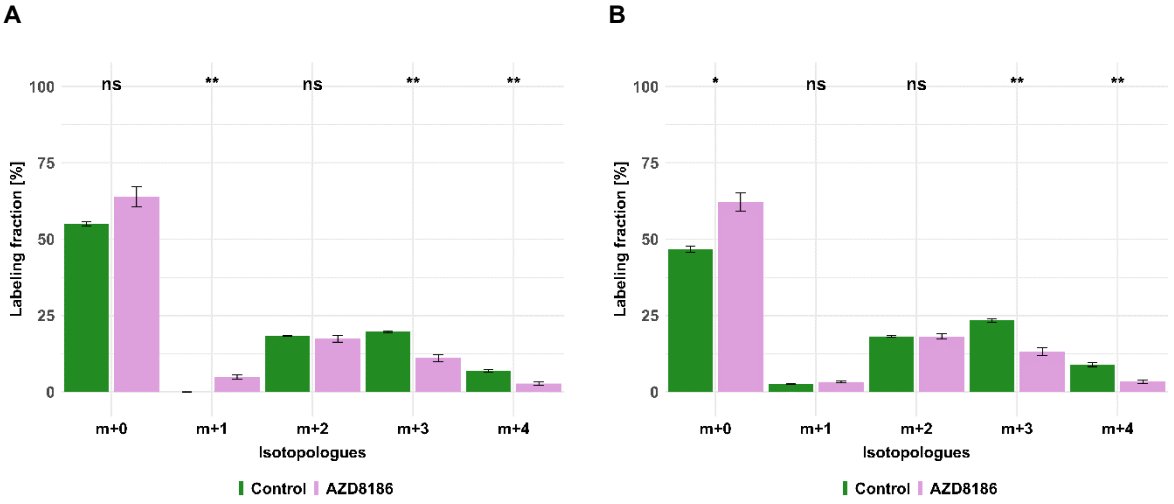

Appendix 7: MDA-MB-468 cells were cultivated in RPMI with [U-^{15}N] glutamine and treated with 0.5 µM AZD8186 (orange) or vehicle (blue). Bar charts ± standard deviation (n=3 technical replicates) showing the fractional enrichment of ^{15}N into proline over the course of 24h. * p< 0.05; ** p< 0.01; *** p< 0.001 (adjusted p-value; Welch's t-test)

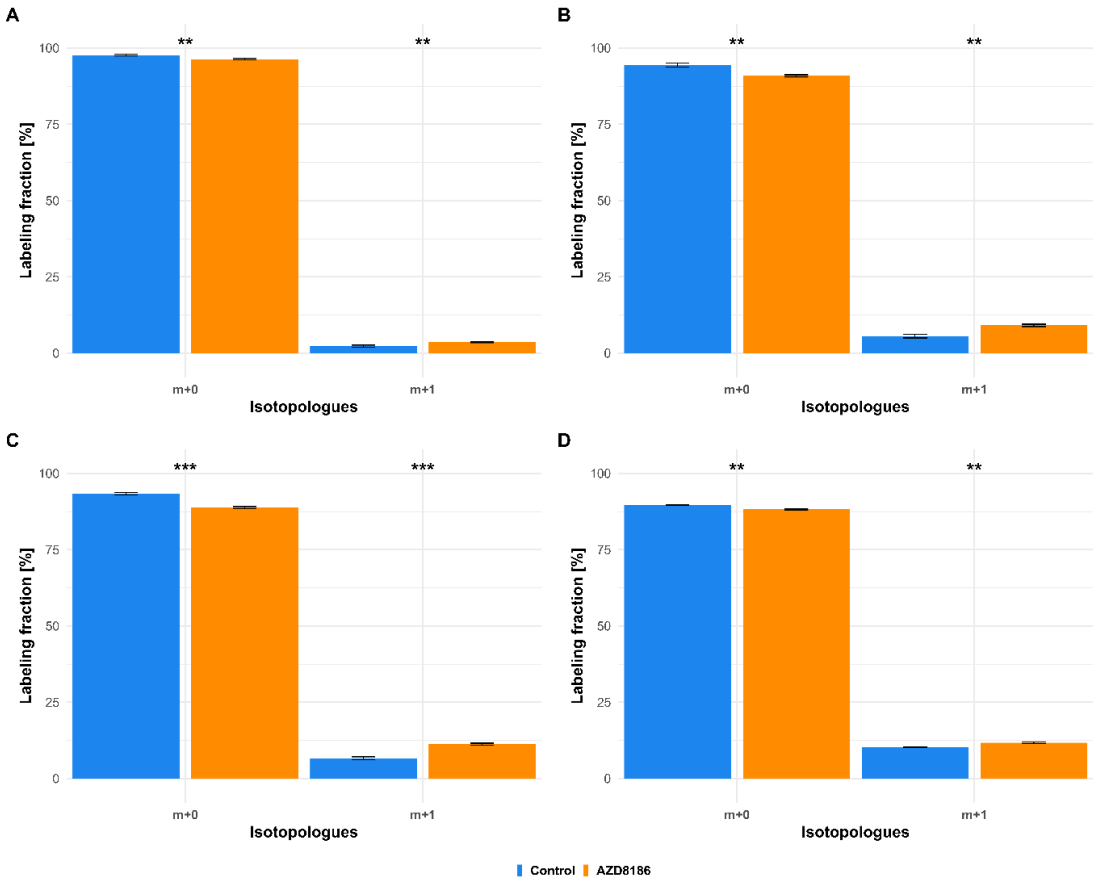

Appendix 8: Line charts ± standard deviation (n=3 technical replicates) displaying fractional labeling over 24h hours for α-ketoglutarate using [U-^{13}C] glucose tracer. * p< 0.05; ** p< 0.01 (adjusted p-value; Welch's t-test)

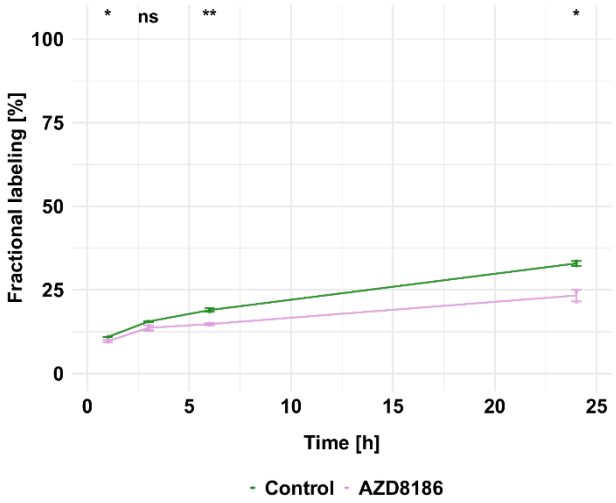

Appendix 9: MDA-MB-468 cells were cultivated in RPMI with [U-^{13}C, ^{15}N] glutamine and treated with 0.5 µM AZD8186 (purple) or vehicle (green). Bar charts ± standard deviation (n=3 technical replicates) showing the fractional enrichment of ^{13}C into citrate over the course of 24h. Fractional enrichment after A: 1h, B: 3h, C: 6h, and D: 24h. * p< 0.05; ** p< 0.01 (adjusted p-value; Welch's t-test). Label incorporation into citrate from [U-^{13}C, ^{15}N] glutamine over the course of 24h

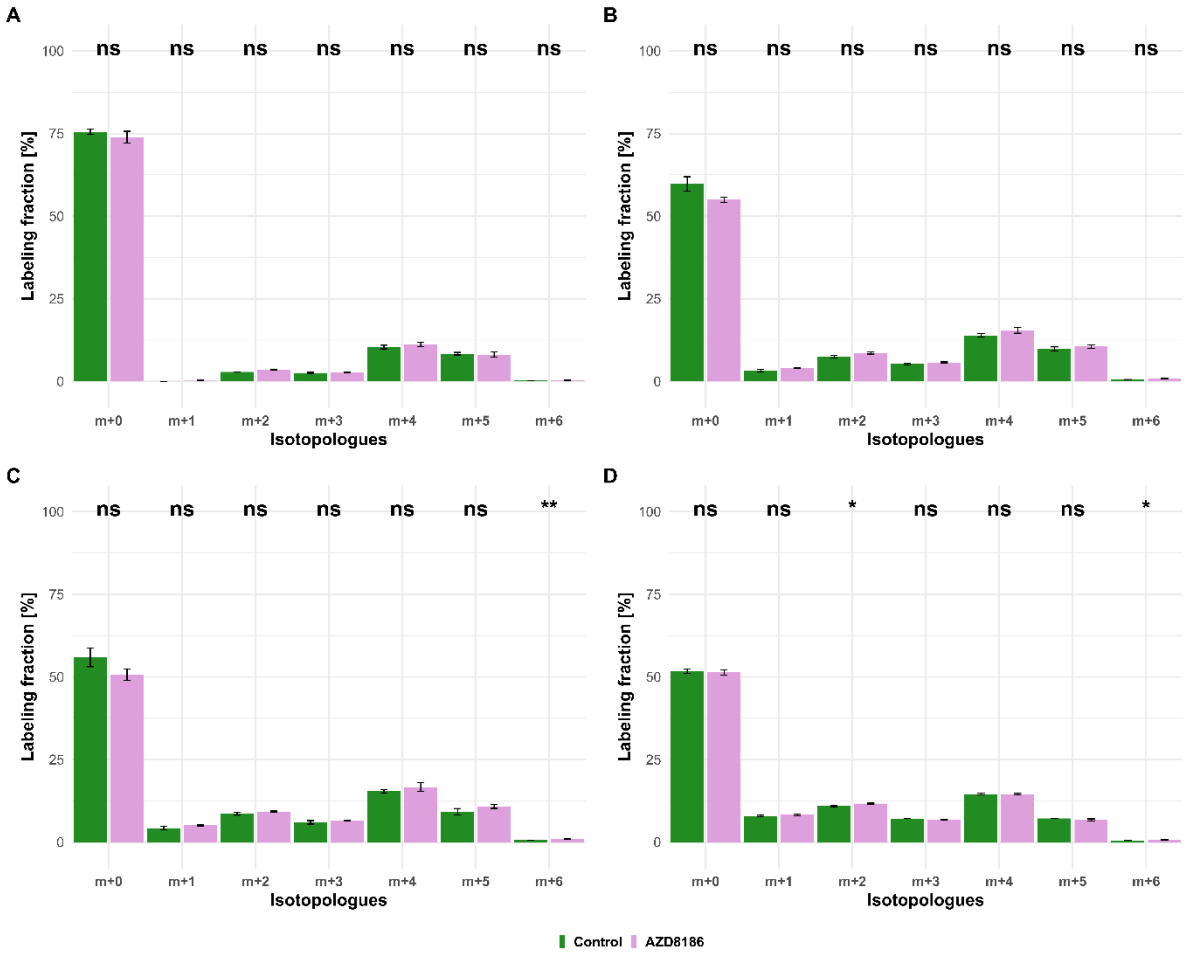

Appendix 10: MDA-MB-468 cells were cultivated in RPMI with [U-^{13}C, ^{15}N] glutamine and treated with 0.5 µM AZD8186 (purple) or vehicle (green). Bar charts ± standard deviation (n=3 technical replicates) showing the fractional enrichment of ^{13}C into (A) pyruvate and lactate (B) at 24h sampling time. * p< 0.05; ** p< 0.01 (adjusted p-value; Welch's t-test)

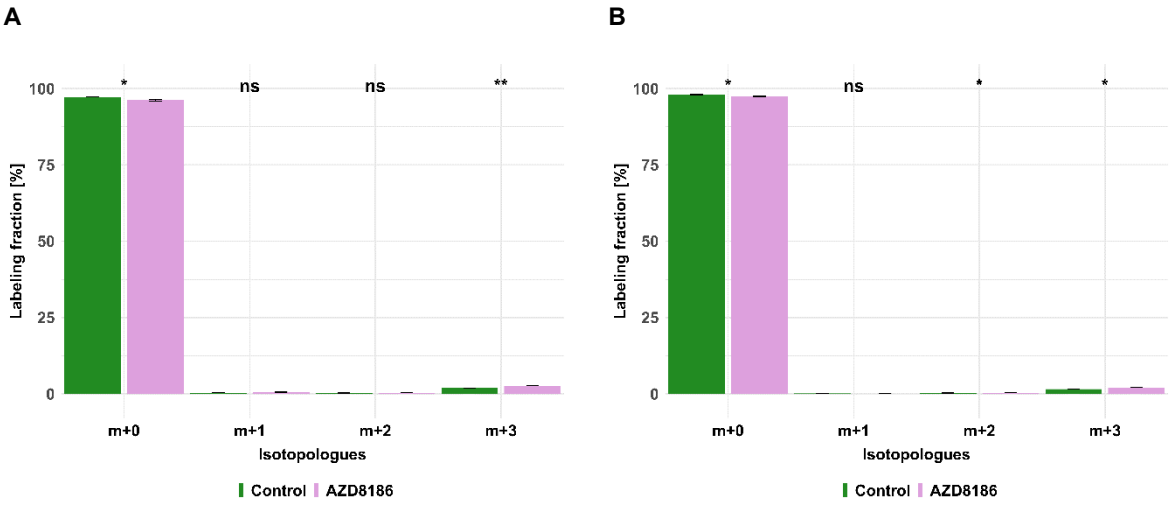

Appendix 11: Impact of AZD8186 treatment on ^{13}C tracer incorporation into different metabolic pathways. MDA-MB-468 cells were cultivated in RPMI with [U-^{13}C,^{15}N] glutamine and treated with 0.5 µM AZD8186 or vehicle for 24h. Fold changes (AZD8186 vs. vehicle) of the individual isotopologues were calculated from the average labeling fraction of three technical replicates per condition and are represented by the indicated color code. Only effects are displayed in the heat map that exhibit a FC <0.8 and >1.2 and tracer incorporation > 3%

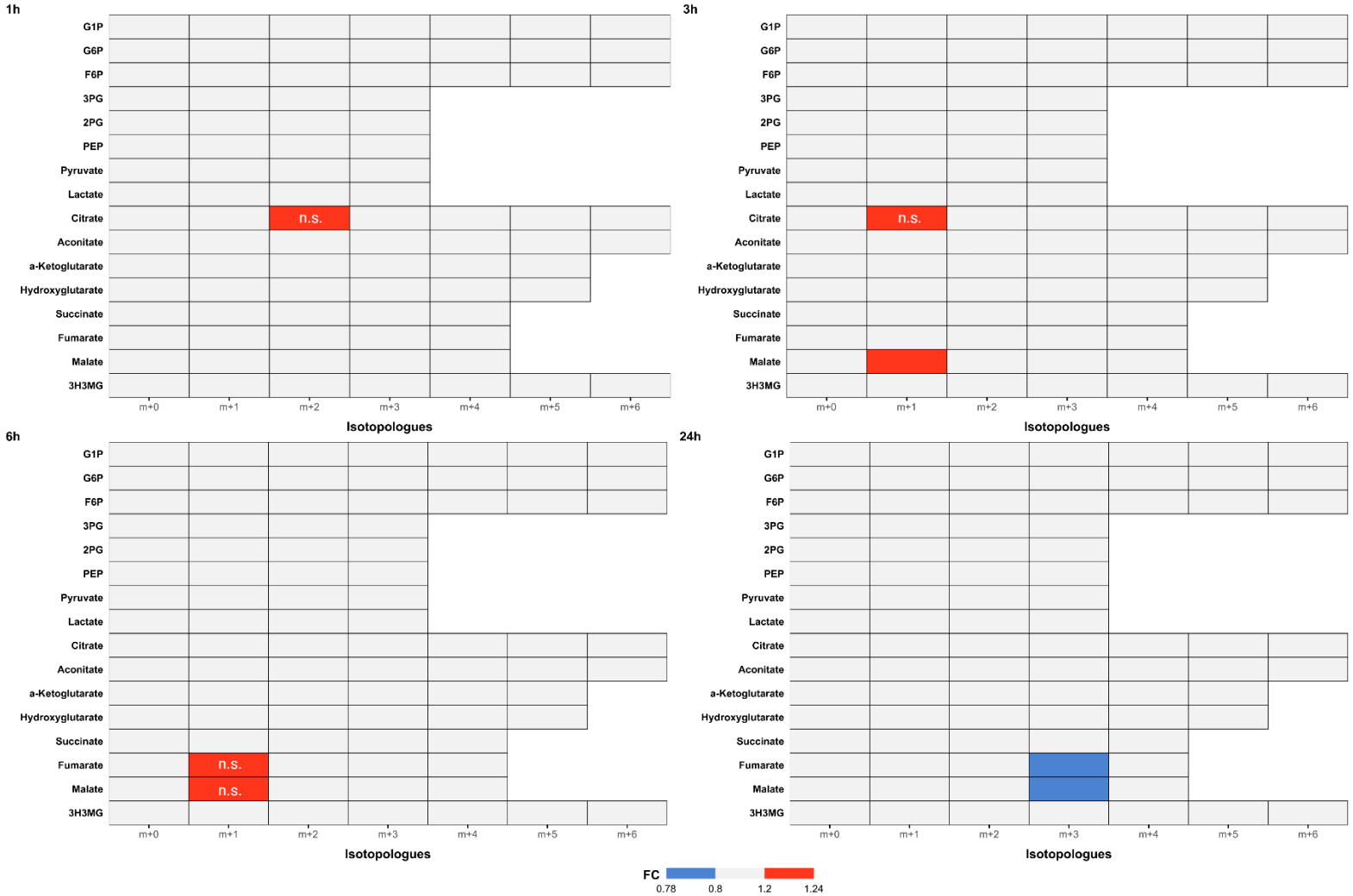

Appendix 12: MDA-MB-468 cells were cultivated in RPMI with [U-^{13}C, ^{15}N] glutamine and treated with vehicle (Ctrl) and 0.5 µM AZD8186 (Tr). Bar charts ± standard deviation (n=3 technical replicates) showing the fractional enrichment of ^{15}N into 2-hydroxyglutarate

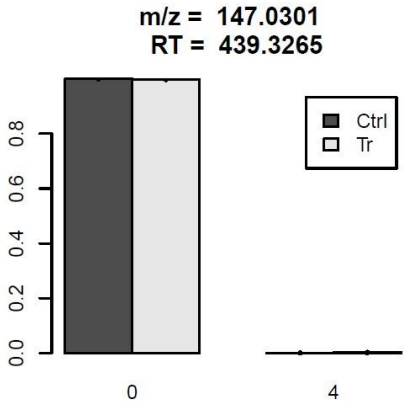

Appendix 13: Table of unique features obtained from significantly altered features after untargeted analysis of ^{13}C and ^{15}N incorporation via X^{13}CMS routine. MDA-MB-468 cells were treated with 0.5 µM AZD8186 and incubated with either [U-^{13}C] glucose, or [U-^{13}C,^{15}N] glutamine enriched RPMI for 24h

	ID	m/z	RT [min]
		[U-^{13}C] glucose	
Pyruvate	7	87.00913935	1.763
Lactate	11	89.02494079	2.592
Serine	17	104.035631	5.259
Malate [-H_2O Fragment]	25	115.0038758	7.513
Malate	44	133.0146427	7.533
Glutamine	53	145.0625085	5.309
PEP	69	166.9754788	9.540
Aconitate	74	173.009316	6.980
NAA	78	174.0410729	7.337
3-PG	86	184.9860131	8.949
Citrate	102	191.0209557	8.886
F16BP	233	338.9893635	10.718
		[U-^{13}C] glutamine	
AMP	286	346.056046	7.084
		[U-^{15}N] glutamine	
ATP	251	505.989849	8.939

Appendix 14: Impact of AZD8186 treatment on ^{13}C tracer incorporation into overlapped compounds after targeted SIRM analysis at 24h for the HCC70 cell line. MDA-MB-468 and HCC70 cells were cultivated in RPMI enriched [U-^{13}C] glucose and treated with 0.5 µM AZD8186 or vehicle for 24h. Fold changes (AZD8186 vs. vehicle) of the individual isotopologues were calculated from the average labeling fraction of three technical replicates per condition and are represented by the indicated color code and isotopologues colored when FC <0.8 and >1.2. F16BP, fructose-1,6,-bisphosphate, 3H3MG, 3-hydroxy-3-methylglutarate; ADP/ATP, adenosine di/triphosphate; GSSG, oxidized glutathione; UDP/UTP, uridine di/triphosphate; UDP-GlcNAc, uridine diphosphate N-acetylglucosamine; pyroglutamate not shown as overall ^{13}C incorporation was below 2% after 24h

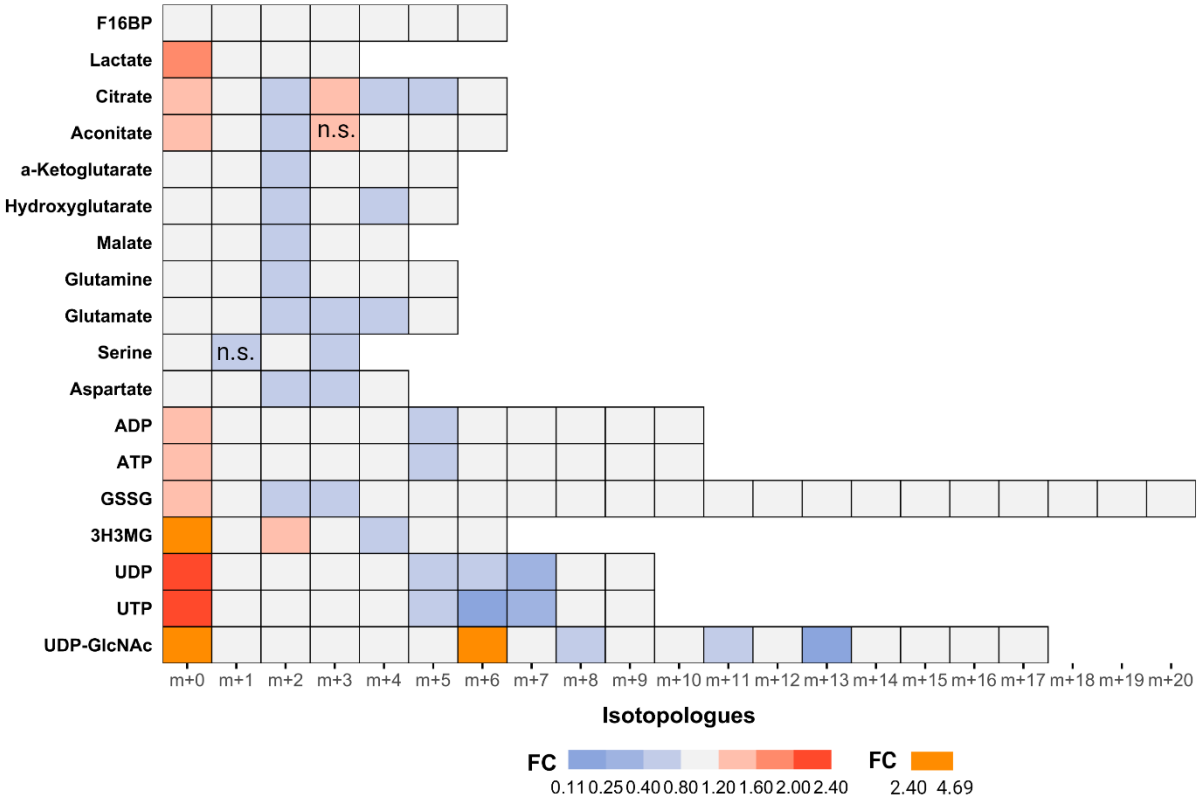

Appendix 15: Cell count after 24h for the MDA-MB-468 and HCC70 cell lines. MDA-MB-468 and HCC70 cells were cultivated in RPMI enriched [U-^{13}C] glucose and treated with 0.5 µM AZD8186 or vehicle for 24h. ** p< 0.01; *** p< 0.001 (Welch's t-test)

Perturbation	Cell Line	Mean [cells]	Standard dev.	p.value
Vehicle	HCC70	113401	1130.52	0.00175; **
	MDA-MB-468	365943	15326.05	
AZD8186	HCC70	111640	11454.26	0.00030; ***
	MDA-MB-468	327888	17338.21	

Appendix 16: ^{13}C tracer incorporation of 6-PG for the MDA-MB-468 and HCC70 cell line. MDA-MB-468 and HCC70 cells were cultivated in RPMI with [U-^{13}C] glucose and treated with 0.5 µM AZD8186 (purple) or vehicle (green). Bar charts ± standard deviation (n=3 technical replicates) showing the fractional enrichment of ^{13}C into 6-PG after 24h for (A) MDA-MB-468 and (B) HCC70. * p< 0.05; ** p< 0.01 (adjusted p-value; Welch's t-test)

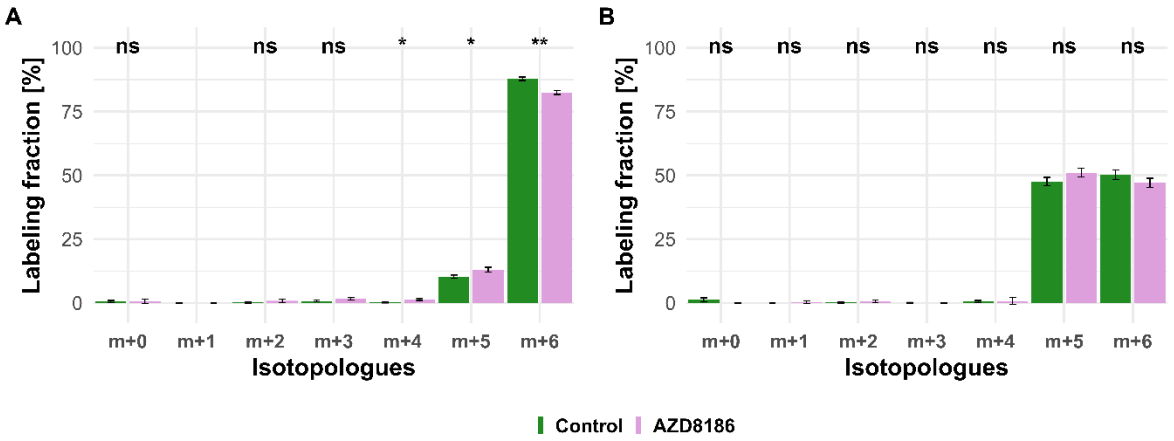

Appendix 17: Table of known (MSI level 1), putatively annotated compounds (MSI level 2), or characterized compound classes (MSI level 3) according to the four levels of metabolite identification proposed by MSI (Sumner et al. 2007). Compounds from unique features obtained after comparison of the MDA-MB-468 with HCC70 cell line at 24h sampling point. MS/MS spectra were exported from MassHunter Qualitative Analysis (version B.07.00) as .mgf files and analyzed with SIRIUS (Dührkop et al. 2019)

m/z	RT [s]	ID	Cell line	Metabolite	MSI level
114.0561	202.973	20	MDA-MB-468	Proline	1
117.0194	473.9945	22	MDA-MB-468	Succinate	1
133.0147	496.7615	34	MDA-MB-468	Malate	1
174.041	472.2465	71	MDA-MB-468	NAA	1
179.0565	187.8045	78	MDA-MB-468	Galactose	2
180.0667	193.0205	79	MDA-MB-468	Tyrosine	1
188.0568	474.49	87	MDA-MB-468	N-acetyl glutamic acid	2
218.104	177.587	135	MDA-MB-468	D/L-pantothenic acid	2
221.0605	493.700	141	MDA-MB-468	Cystathione	2
229.0121	483.694	150	MDA-MB-468	D-arabinose 5-phosphate	2
255.2327	59.3755	176	MDA-MB-468	2-hexyldecanoic acid	2
259.0226	571.1705	182	MDA-MB-468	G6P	1
283.2641	55.3	210	MDA-MB-468	Stearic acid	2
306.0779	428.443	233	MDA-MB-468	GSH	1
325.1836	55.67	248	MDA-MB-468	4-dodecylbenzenesulfonic acid	2
465.3033	54.18	342	MDA-MB-468	Cholesterol sulfate	2
571.2876	98.947	382	MDA-MB-468	LysoPI (16:0/0:0)	2
722.5112	61.635	421	MDA-MB-468	PE 20:4	3
740.5218	62.3565	426	MDA-MB-468	PE (18:2/18:1)	2
742.5368	62.382	428	MDA-MB-468	PE (18:1/18:1)	2
747.5159	59.5965	433	MDA-MB-468	PE (18:1/16:0)	2
833.5165	66.103	455	MDA-MB-468	PI 34:2	2
857.5166	65.3515	460	MDA-MB-468	PI 20:4/16:0	3
859.5293	65.5985	462	MDA-MB-468	PI 20:3/16:0	3

m/z	RT [s]	ID	Cell line	Metabolite	MSI level
861.5478	65.844	463	MDA-MB-468	PI 18:1/18:1	3
883.5325	64.803	472	MDA-MB-468	PI 20:4/18:1	3
111.0088	576.3605	20	HCC70	2-furoic acid	3
115.0037	515.6085	28	HCC70	Fumarate	1
116.0352	216.48	30	HCC70	Acetylglycine	2
151.0608	139.3425	51	HCC70	Arabitol	2
154.0623	322.3635	53	HCC70	Histidin	2
156.0277	313.529	54	HCC70	2-methyl-4-phenyl thiazole	3
168.9906	532.906	62	HCC70	Glyceraldehyde 3 phosphate	2
176.9358	469.941	71	HCC70	Pyrophosphate	2
179.0556	145.479	73	HCC70	Galactose	2
184.9862	557.788	76	HCC70	Glycerate 2-phosphate	1
245.0432	304.205	145	HCC70	Glycerophosphoglycerole	3
259.0226	550.412	155	HCC70	G6P	1
261.038	495.076	157	HCC70	Mannitol 1-phosphate	2
283.2635	57.297	183	HCC70	Stearic acid	2
308.0988	340.2885	205	HCC70	NANA	1
308.9778	558.017	206	HCC70	Ribulose 1,5-diphosphate	3
535.0367	449.576	331	HCC70	UDP-D-xylose	2
565.0475	446.9205	345	HCC70	UDP-glucose	1
579.0266	532.5165	353	HCC70	UDP-glucuronic acid	2
597.3023	94.281	358	HCC70	PI(18:1(9Z)/0:0)	2

6. References

Achari, A.; Marshall, S. E.; Muirhead, H.; Palmieri, R. H.; Noltmann, E. A. (1981): Glucose-6-phosphate isomerase. In *Philosophical transactions of the Royal Society of London. Series B, Biological sciences* 293 (1063), pp. 145–157. DOI: 10.1098/rstb.1981.0068.

Adusumilli, Ravali; Mallick, Parag (2017): Data Conversion with ProteoWizard msConvert. In *Methods in molecular biology (Clifton, N.J.)* 1550, pp. 339–368. DOI: 10.1007/978-1-4939-6747-6_23.

Agin, A.; Heintz, D.; Ruhland, E.; La Chao de Barca, J. M.; Zumsteg, J.; Moal, V. et al. (2016): Metabolomics – an overview. From basic principles to potential biomarkers (part 1). In *Médecine Nucléaire* 40 (1), pp. 4–10. DOI: 10.1016/j.mednuc.2015.12.006.

Ahmad, Tariq; Kelly, Jacob P.; McGarrah, Robert W.; Hellkamp, Anne S.; Fiuzat, Mona; Testani, Jeffrey M. et al. (2016): Prognostic Implications of Long-Chain Acylcarnitines in Heart Failure and Reversibility With Mechanical Circulatory Support. In *Journal of the American College of Cardiology* 67 (3), pp. 291–299. DOI: 10.1016/j.jacc.2015.10.079.

Ahn, Eunyong; Kumar, Praveen; Mukha, Dzmitry; Tzur, Amit; Shlomi, Tomer (2017): Temporal fluxomics reveals oscillations in TCA cycle flux throughout the mammalian cell cycle. In *Molecular systems biology* 13 (11), p. 953. DOI: 10.15252/msb.20177763.

Ahn, Woo Suk; Antoniewicz, Maciek R. (2011): Metabolic flux analysis of CHO cells at growth and non-growth phases using isotopic tracers and mass spectrometry. In *Metabolic engineering* 13 (5), pp. 598–609. DOI: 10.1016/j.ymben.2011.07.002.

Alpert, A. J. (1990): Hydrophilic-interaction chromatography for the separation of peptides, nucleic acids and other polar compounds. In *Journal of chromatography* 499, pp. 177–196. DOI: 10.1016/S0021-9673(00)96972-3.

Anderson, Brady G.; Raskind, Alexander; Habra, Hani; Kennedy, Robert T.; Evans, Charles R. (2021): Modifying Chromatography Conditions for Improved Unknown Feature Identification in Untargeted Metabolomics. In *Analytical chemistry* 93 (48), pp. 15840–15849. DOI: 10.1021/acs.analchem.1c02149.

Antoniewicz, Maciek R. (2018): A guide to 13C metabolic flux analysis for the cancer biologist. In *Experimental & molecular medicine* 50 (4), pp. 1–13. DOI: 10.1038/s12276-018-0060-y.

Atkinson, D. E.; Walton, G. M. (1967): Adenosine triphosphate conservation in metabolic regulation. Rat liver citrate cleavage enzyme. In *The Journal of biological chemistry* 242 (13), pp. 3239–3241.

Barlaam, Bernard; Cosulich, Sabina; Degorce, Sébastien; Fitzek, Martina; Green, Stephen; Hancox, Urs et al. (2015): Discovery of (R)-8-(1-(3,5-difluorophenylamino)ethyl)-N,N-dimethyl-2-morpholino-4-oxo-4H-chromene-6-carboxamide (AZD8186): a potent and selective inhibitor of PI3Kβ and PI3Kδ for the treatment of PTEN-deficient cancers. In *Journal of medicinal chemistry* 58 (2), pp. 943–962. DOI: 10.1021/jm501629p.

Baugh, Evan H.; Ke, Hua; Levine, Arnold J.; Bonneau, Richard A.; Chan, Chang S. (2018): Why are there hotspot mutations in the TP53 gene in human cancers? In *Cell death and differentiation* 25 (1), pp. 154–160. DOI: 10.1038/cdd.2017.180.

Baumeister, Tim U. H.; Ueberschaar, Nico; Schmidt-Heck, Wolfgang; Mohr, J. Frieder; Deicke, Michael; Wichard, Thomas et al. (2018): DeltaMS: a tool to track isotopologues in GC- and LC-MS data. In *Metabolomics : Official journal of the Metabolomic Society* 14 (4), p. 41. DOI: 10.1007/s11306-018-1336-x.

Bayley, Jean-Pierre; Devilee, Peter (2010): Warburg tumours and the mechanisms of mitochondrial tumour suppressor genes. Barking up the right tree? In *Current opinion in genetics & development* 20 (3), pp. 324–329. DOI: 10.1016/j.gde.2010.02.008.

Baysal, B. E.; Ferrell, R. E.; Willett-Brozick, J. E.; Lawrence, E. C.; Myssiorek, D.; Bosch, A. et al. (2000): Mutations in SDHD, a mitochondrial complex II gene, in hereditary paraganglioma. In *Science (New York, N.Y.)* 287 (5454), pp. 848–851. DOI: 10.1126/science.287.5454.848.

Begou, Olga; Gika, Helen G.; Theodoridis, Georgios A.; Wilson, Ian D. (2018): Quality Control and Validation Issues in LC-MS Metabolomics. In *Methods in molecular biology (Clifton, N.J.)* 1738, pp. 15–26. DOI: 10.1007/978-1-4939-7643-0_2.

Benjamini, Yoav; Hochberg, Yosef (1995): Controlling the False Discovery Rate: A Practical and Powerful Approach to Multiple Testing. In *Journal of the Royal Statistical Society: Series B (Methodological)* 57 (1), pp. 289–300. DOI: 10.1111/j.2517-6161.1995.tb02031.x.

Benton, H. Paul; Want, Elizabeth J.; Ebbels, Timothy M. D. (2010): Correction of mass calibration gaps in liquid chromatography-mass spectrometry metabolomics data. In *Bioinformatics (Oxford, England)* 26 (19), pp. 2488–2489. DOI: 10.1093/bioinformatics/btq441.

Bi, Huichang; Krausz, Kristopher W.; Manna, Soumen K.; Li, Fei; Johnson, Caroline H.; Gonzalez, Frank J. (2013): Optimization of harvesting, extraction, and analytical protocols for UPLC-ESI-MS-based metabolomic analysis of adherent mammalian cancer cells. In *Analytical and bioanalytical chemistry* 405 (15), pp. 5279–5289. DOI: 10.1007/s00216-013-6927-9.

Bruntz, Ronald C.; Lane, Andrew N.; Higashi, Richard M.; Fan, Teresa W-M (2017): Exploring cancer metabolism using stable isotope-resolved metabolomics (SIRM). In *The Journal of biological chemistry* 292 (28), pp. 11601–11609. DOI: 10.1074/jbc.R117.776054.

Buescher, Joerg M.; Antoniewicz, Maciek R.; Boros, Laszlo G.; Burgess, Shawn C.; Brunengraber, Henri; Clish, Clary B. et al. (2015): A roadmap for interpreting (13)C metabolite labeling patterns from cells. In *Current opinion in biotechnology* 34, pp. 189–201. DOI: 10.1016/j.copbio.2015.02.003.

Bueschl, Christoph; Kluger, Bernhard; Lemmens, Marc; Adam, Gerhard; Wiesenberger, Gerlinde; Maschietto, Valentina et al. (2014): A novel stable isotope labelling assisted workflow for improved untargeted LC-HRMS based metabolomics research. In *Metabolomics* 10 (4), pp. 754–769. DOI: 10.1007/s11306-013-0611-0.

Bueschl, Christoph; Kluger, Bernhard; Neumann, Nora K. N.; Doppler, Maria; Maschietto, Valentina; Thallinger, Gerhard G. et al. (2017): MetExtract II: A Software Suite for Stable Isotope-Assisted Untargeted Metabolomics. In *Analytical chemistry* 89 (17), pp. 9518–9526. DOI: 10.1021/acs.analchem.7b02518.

Buszewski, Bogusław; Noga, Sylwia (2012): Hydrophilic interaction liquid chromatography (HILIC)--a powerful separation technique. In *Analytical and bioanalytical chemistry* 402 (1), pp. 231–247. DOI: 10.1007/s00216-011-5308-5.

Butin, Noémie; Bergès, Cécilia; Portais, Jean-Charles; Bellvert, Floriant (2022): An optimization method for untargeted MS-based isotopic tracing investigations of metabolism. In *Metabolomics : Official journal of the Metabolomic Society* 18 (7), p. 41. DOI: 10.1007/s11306-022-01897-5.

Camaya, Inah; Donnelly, Sheila; O'Brien, Bronwyn (2022): Targeting the PI3K/Akt signaling pathway in pancreatic β-cells to enhance their survival and function: An emerging therapeutic strategy for type 1 diabetes. In *Journal of diabetes* 14 (4), pp. 247–260. DOI: 10.1111/1753-0407.13252.

Cantley, Lewis C. (2002): The phosphoinositide 3-kinase pathway. In *Science (New York, N.Y.)* 296 (5573), pp. 1655–1657. DOI: 10.1126/science.296.5573.1655.

Capellades, Jordi; Navarro, Miriam; Samino, Sara; Garcia-Ramirez, Marta; Hernandez, Cristina; Simo, Rafael et al. (2016): geoRge: A Computational Tool To Detect the Presence of Stable Isotope Labeling in LC/MS-Based Untargeted Metabolomics. In *Analytical chemistry* 88 (1), pp. 621–628. DOI: 10.1021/acs.analchem.5b03628.

Carracedo, Arkaitz; Cantley, Lewis C.; Pandolfi, Pier Paolo (2013): Cancer metabolism: fatty acid oxidation in the limelight. In *Nature reviews. Cancer* 13 (4), pp. 227–232. DOI: 10.1038/nrc3483.

Caspi, Ron; Altman, Tomer; Billington, Richard; Dreher, Kate; Foerster, Hartmut; Fulcher, Carol A. et al. (2014): The MetaCyc database of metabolic pathways and enzymes and the BioCyc collection of Pathway/Genome Databases. In *Nucleic acids research* 42 (Database issue), D459-71. DOI: 10.1093/nar/gkt1103.

Chalhoub, Nader; Baker, Suzanne J. (2009): PTEN and the PI3-kinase pathway in cancer. In *Annual review of pathology* 4, pp. 127–150. DOI: 10.1146/annurev.pathol.4.110807.092311.

Chambers, Matthew C.; Maclean, Brendan; Burke, Robert; Amodei, Dario; Ruderman, Daniel L.; Neumann, Steffen et al. (2012): A cross-platform toolkit for mass spectrometry and proteomics. In *Nature biotechnology* 30 (10), pp. 918–920. DOI: 10.1038/nbt.2377.

Chapman, A. G.; Fall, L.; Atkinson, D. E. (1971): Adenylate energy charge in Escherichia coli during growth and starvation. In *Journal of bacteriology* 108 (3), pp. 1072–1086. DOI: 10.1128/jb.108.3.1072-1086.1971.

Chen, Chunguang; Cohrs, Christian M.; Stertmann, Julia; Bozsak, Robert; Speier, Stephan (2017): Human beta cell mass and function in diabetes: Recent advances in knowledge and technologies to understand disease pathogenesis. In *Molecular metabolism* 6 (9), pp. 943–957. DOI: 10.1016/j.molmet.2017.06.019.

Chen, Yiwen; Xia, Shudong (2021): Determination of the stability of plasma ATP in vitro. In *American journal of blood research* 11 (1), pp. 96–99.

Choi, Bo-Hyun; Coloff, Jonathan L. (2019): The Diverse Functions of Non-Essential Amino Acids in Cancer. In *Cancers* 11 (5). DOI: 10.3390/cancers11050675.

Chokkathukalam, Achuthanunni; Jankevics, Andris; Creek, Darren J.; Achcar, Fiona; Barrett, Michael P.; Breitling, Rainer (2013): mzMatch-ISO: an R tool for the annotation and relative quantification of isotope-labelled mass spectrometry data. In *Bioinformatics (Oxford, England)* 29 (2), pp. 281–283. DOI: 10.1093/bioinformatics/bts674.

Choudhury, Atish D.; Higano, Celestia S.; Bono, Johann S. de; Cook, Natalie; Rathkopf, Dana E.; Wisinski, Kari B. et al. (2022): A Phase I Study Investigating AZD8186, a Potent and Selective Inhibitor of PI3Kβ/δ, in Patients with Advanced Solid Tumors. In *Clinical cancer research : an official journal of the American Association for Cancer Research* 28 (11), pp. 2257–2269. DOI: 10.1158/1078-0432.CCR-21-3087.

Choudhury, Feroza K.; Hackman, G. Lavender; Lodi, Alessia; Tiziani, Stefano (2020): Stable Isotope Tracing Metabolomics to Investigate the Metabolic Activity of Bioactive Compounds for Cancer Prevention and Treatment. In *Cancers* 12 (8). DOI: 10.3390/cancers12082147.

Cocco, Stefania; Piezzo, Michela; Calabrese, Alessandra; Cianniello, Daniela; Caputo, Roberta; Di Lauro, Vincenzo et al. (2020): Biomarkers in Triple-Negative Breast Cancer:

State-of-the-Art and Future Perspectives. In *International journal of molecular sciences* 21 (13). DOI: 10.3390/ijms21134579.

Coller, Hilary A. (2014): Is cancer a metabolic disease? In *The American journal of pathology* 184 (1), pp. 4–17. DOI: 10.1016/j.ajpath.2013.07.035.

Collins, Rebecca R. J.; Patel, Khushbu; Putnam, William C.; Kapur, Payal; Rakheja, Dinesh (2017): Oncometabolites. A New Paradigm for Oncology, Metabolism, and the Clinical Laboratory. In *Clinical chemistry* 63 (12), pp. 1812–1820. DOI: 10.1373/clinchem.2016.267666.

Comte, B.; Vincent, G.; Bouchard, B.; Des Rosiers, C. (1997): Probing the origin of acetyl-CoA and oxaloacetate entering the citric acid cycle from the 13C labeling of citrate released by perfused rat hearts. In *Journal of Biological Chemistry* 272 (42), pp. 26117–26124. DOI: 10.1074/jbc.272.42.26117.

Contrepois, Kévin; Jiang, Lihua; Snyder, Michael (2015): Optimized Analytical Procedures for the Untargeted Metabolomic Profiling of Human Urine and Plasma by Combining Hydrophilic Interaction (HILIC) and Reverse-Phase Liquid Chromatography (RPLC)-Mass Spectrometry. In *Molecular & cellular proteomics : MCP* 14 (6), pp. 1684–1695. DOI: 10.1074/mcp.M114.046508.

Cortes, Miriam; García-Cañaveras, Juan Carlos; Pareja, Eugenia; Lahoz, Agustín (2017): Liver Transplantation Biomarkers in the Metabolomics Era. In Vinood B. Patel, Victor R. Preedy (Eds.): Biomarkers in Liver Disease. Dordrecht: Springer Netherlands (Biomarkers in Disease: Methods, Discoveries and Applications), pp. 99–128.

Cossu, Vanessa; Bonanomi, Marcella; Baucknehtt, Matteo; Ravera, Silvia; Righi, Nicole; Miceli, Alberto et al. (2020): Two high-rate pentose-phosphate pathways in cancer cells. In *Scientific reports* 10 (1), p. 22111. DOI: 10.1038/s41598-020-79185-2.

Creek, Darren J.; Chokkathukalam, Achuthanunni; Jankevics, Andris; Burgess, Karl E. V.; Breitling, Rainer; Barrett, Michael P. (2012): Stable isotope-assisted metabolomics for network-wide metabolic pathway elucidation. In *Analytical chemistry* 84 (20), pp. 8442–8447. DOI: 10.1021/ac3018795.

Dang, Lenny; White, David W.; Gross, Stefan; Bennett, Bryson D.; Bittinger, Mark A.; Driggers, Edward M. et al. (2009): Cancer-associated IDH1 mutations produce 2-hydroxyglutarate. In *Nature* 462 (7274), pp. 739–744. DOI: 10.1038/nature08617.

Dange, Manohar C.; Mishra, Vivek; Mukherjee, Bratati; Jaiswal, Damini; Merchant, Murtaza S.; Prasannan, Charulata B.; Wangikar, Pramod P. (2020): Evaluation of freely available software tools for untargeted quantification of 13C isotopic enrichment in cellular

metabolome from HR-LC/MS data. In *Metabolic engineering communications* 10, e00120. DOI: 10.1016/j.mec.2019.e00120.

DeBerardinis, Ralph J.; Chandel, Navdeep S. (2016): Fundamentals of cancer metabolism. In *Science advances* 2 (5), e1600200. DOI: 10.1126/sciadv.1600200.

Debik, Julia; Euceda, Leslie R.; Lundgren, Steinar; Gythfeldt, Hedda von der Lippe; Garred, Øystein; Borgen, Elin et al. (2019): Assessing Treatment Response and Prognosis by Serum and Tissue Metabolomics in Breast Cancer Patients. In *Journal of proteome research* 18 (10), pp. 3649–3660. DOI: 10.1021/acs.jproteome.9b00316.

Deininger, Sören-Oliver; Cornett, Dale S.; Paape, Rainer; Becker, Michael; Pineau, Charles; Rauser, Sandra et al. (2011): Normalization in MALDI-TOF imaging datasets of proteins: practical considerations. In *Analytical and bioanalytical chemistry* 401 (1), pp. 167–181. DOI: 10.1007/s00216-011-4929-z.

Dibble, Christian C.; Barritt, Samuel A.; Perry, Grace E.; Lien, Evan C.; Geck, Renee C.; DuBois-Coyne, Sarah E. et al. (2022): PI3K drives the de novo synthesis of coenzyme A from vitamin B5. In *Nature* 608 (7921), pp. 192–198. DOI: 10.1038/s41586-022-04984-8.

Dietmair, Stefanie; Hodson, Mark P.; Quek, Lake-Ee; Timmins, Nicholas E.; Gray, Peter; Nielsen, Lars K. (2012): A multi-omics analysis of recombinant protein production in Hek293 cells. In *PloS one* 7 (8), e43394. DOI: 10.1371/journal.pone.0043394.

Dietmair, Stefanie; Timmins, Nicholas E.; Gray, Peter P.; Nielsen, Lars K.; Krömer, Jens O. (2010): Towards quantitative metabolomics of mammalian cells. Development of a metabolite extraction protocol. In *Analytical biochemistry* 404 (2), pp. 155–164. DOI: 10.1016/j.ab.2010.04.031.

Dudek, Christian-Alexander; Reuse, Carsten; Fuchs, Regine; Hendriks, Janneke; Starck, Veronique; Hiller, Karsten (2020): MIAMI--a tool for non-targeted detection of metabolic flux changes for mode of action identification. In *Bioinformatics (Oxford, England)* 36 (12), pp. 3925–3926. DOI: 10.1093/bioinformatics/btaa251.

Dührkop, Kai; Fleischauer, Markus; Ludwig, Marcus; Aksenov, Alexander A.; Melnik, Alexey V.; Meusel, Marvin et al. (2019): SIRIUS 4. A rapid tool for turning tandem mass spectra into metabolite structure information. In *Nature methods* 16 (4), pp. 299–302. DOI: 10.1038/s41592-019-0344-8.

Ejigu, Bedilu Alamirie; Valkenborg, Dirk; Baggerman, Geert; Vanaerschot, Manu; Witters, Erwin; Dujardin, Jean-Claude et al. (2013): Evaluation of normalization methods to pave the way towards large-scale LC-MS-based metabolomics profiling experiments. In *Omics : a journal of integrative biology* 17 (9), pp. 473–485. DOI: 10.1089/omi.2013.0010.

Engelking, Larry R. (2015): Purine Biosynthesis. In : Textbook of Veterinary Physiological Chemistry: Elsevier, pp. 88–92.

Engelman, Jeffrey A. (2009): Targeting PI3K signalling in cancer. Opportunities, challenges and limitations. In *Nature reviews. Cancer* 9 (8), pp. 550–562. DOI: 10.1038/nrc2664.

Engelman, Jeffrey A.; Luo, Ji; Cantley, Lewis C. (2006): The evolution of phosphatidylinositol 3-kinases as regulators of growth and metabolism. In *Nature reviews. Genetics* 7 (8), pp. 606–619. DOI: 10.1038/nrg1879.

Epstein, Tamir; Gatenby, Robert A.; Brown, Joel S. (2017): The Warburg effect as an adaptation of cancer cells to rapid fluctuations in energy demand. In *PloS one* 12 (9), e0185085. DOI: 10.1371/journal.pone.0185085.

Errera, M.; Greenstein, J. P. (1949): Phosphate-activated glutaminase in kidney and other tissues. In *Journal of Biological Chemistry* 178 (1), pp. 495–502.

Faijes, Magda; Mars, Astrid E.; Smid, Eddy J. (2007): Comparison of quenching and extraction methodologies for metabolome analysis of Lactobacillus plantarum. In *Microbial cell factories* 6, p. 27. DOI: 10.1186/1475-2859-6-27.

Fan, Teresa W-M; El-Amouri, Salim S.; Macedo, Jessica K. A.; Wang, Qing Jun; Song, Huan; Cassel, Teresa; Lane, Andrew N. (2018): Stable Isotope-Resolved Metabolomics Shows Metabolic Resistance to Anti-Cancer Selenite in 3D Spheroids versus 2D Cell Cultures. In *Metabolites* 8 (3). DOI: 10.3390/metabo8030040.

Fan, Teresa W-M; Lane, Andrew N. (2016): Applications of NMR spectroscopy to systems biochemistry. In *Progress in nuclear magnetic resonance spectroscopy* 92-93, pp. 18–53. DOI: 10.1016/j.pnmrs.2016.01.005.

Faubert, Brandon; Tasdogan, Alpaslan; Morrison, Sean J.; Mathews, Thomas P.; DeBerardinis, Ralph J. (2021): Stable isotope tracing to assess tumor metabolism in vivo. In *Nature protocols* 16 (11), pp. 5123–5145. DOI: 10.1038/s41596-021-00605-2.

Fernandez, Charles A.; Des Rosiers, Christine; Previs, Stephen F.; David, France; Brunengraber, Henri (1996): Correction of13C Mass Isotopomer Distributions for Natural Stable Isotope Abundance. In *J. Mass Spectrom.* 31 (3), pp. 255–262. DOI: 10.1002/(SICI)1096-9888(199603)31:3<255::AID-JMS290>3.0.CO;2-3.

Fernández-García, Juan; Altea-Manzano, Patricia; Pranzini, Erica; Fendt, Sarah-Maria (2020): Stable Isotopes for Tracing Mammalian-Cell Metabolism In Vivo. In *Trends in biochemical sciences* 45 (3), pp. 185–201. DOI: 10.1016/j.tibs.2019.12.002.

Ferrer, Christina M.; Sodi, Valerie L.; Reginato, Mauricio J. (2016): O-GlcNAcylation in Cancer Biology: Linking Metabolism and Signaling. In *Journal of molecular biology* 428 (16), pp. 3282–3294. DOI: 10.1016/j.jmb.2016.05.028.

Fiehn, Oliver (2016): Metabolomics by Gas Chromatography-Mass Spectrometry. Combined Targeted and Untargeted Profiling. In *Current protocols in molecular biology* 114, 30.4.1-30.4.32. DOI: 10.1002/0471142727.mb3004s114.

Fruman, David A.; Chiu, Honyin; Hopkins, Benjamin D.; Bagrodia, Shubha; Cantley, Lewis C.; Abraham, Robert T. (2017): The PI3K Pathway in Human Disease. In *Cell* 170 (4), pp. 605–635. DOI: 10.1016/j.cell.2017.07.029.

Fu, Xiaorong; Deja, Stanisław; Kucejova, Blanka; Duarte, Joao A. G.; McDonald, Jeffrey G.; Burgess, Shawn C. (2019): Targeted Determination of Tissue Energy Status by LC-MS/MS. In *Analytical chemistry* 91 (9), pp. 5881–5887. DOI: 10.1021/acs.analchem.9b00217.

Fu, Zhuji; Runquist, Jennifer A.; Forouhar, Farhad; Hussain, Munif; Hunt, John F.; Miziorko, Henry M.; Kim, Jung-Ja P. (2006): Crystal structure of human 3-hydroxy-3-methylglutaryl-CoA Lyase: insights into catalysis and the molecular basis for hydroxymethylglutaric aciduria. In *Journal of Biological Chemistry* 281 (11), pp. 7526–7532. DOI: 10.1074/jbc.M506880200.

Gao, Xinxin; Lowry, Pamela R.; Zhou, Xin; Depry, Charlene; Wei, Zhikui; Wong, G. William; Zhang, Jin (2011): PI3K/Akt signaling requires spatial compartmentalization in plasma membrane microdomains. In *Proceedings of the National Academy of Sciences of the United States of America* 108 (35), pp. 14509–14514. DOI: 10.1073/pnas.1019386108.

Gauglitz, Julia M.; West, Kiana A.; Bittremieux, Wout; Williams, Candace L.; Weldon, Kelly C.; Panitchpakdi, Morgan et al. (2022): Enhancing untargeted metabolomics using metadata-based source annotation. In *Nature biotechnology* 40 (12), pp. 1774–1779. DOI: 10.1038/s41587-022-01368-1.

Gertsman, Ilya; Barshop, Bruce A. (2018): Promises and pitfalls of untargeted metabolomics. In *Journal of inherited metabolic disease* 41 (3), pp. 355–366. DOI: 10.1007/s10545-017-0130-7.

Gkiouli, Maria; Biechl, Philipp; Eisenreich, Wolfgang; Otto, Angela M. (2019): Diverse Roads Taken by 13C-Glucose-Derived Metabolites in Breast Cancer Cells Exposed to Limiting Glucose and Glutamine Conditions. In *Cells* 8 (10). DOI: 10.3390/cells8101113.

Gowda, G. A. Nagana; Djukovic, Danijel (2014): Overview of mass spectrometry-based metabolomics. Opportunities and challenges. In *Methods in molecular biology (Clifton, N.J.)* 1198, pp. 3–12. DOI: 10.1007/978-1-4939-1258-2_1.

Gowda, G. A. Nagana; Raftery, Daniel (Eds.) (2019): NMR-Based Metabolomics. New York, NY: Springer New York (Methods in Molecular Biology).

Grankvist, Nina; Watrous, Jeramie D.; Jain, Mohit; Nilsson, Roland (2020): Large-Scale Profiling of Cellular Metabolic Activities Using Deep 13C Labeling Medium. In *Methods in molecular biology (Clifton, N.J.)* 2088, pp. 73–92. DOI: 10.1007/978-1-0716-0159-4_5.

Greenstein, J. P.; Price, V. E. (1949): alpha-Keto acid-activated glutaminase and asparaginase. In *Journal of Biological Chemistry* 178 (2), pp. 695–705.

Grima-Reyes, Manuel; Martinez-Turtos, Adriana; Abramovich, Ifat; Gottlieb, Eyal; Chiche, Johanna; Ricci, Jean-Ehrland (2021): Physiological impact of in vivo stable isotope tracing on cancer metabolism. In *Molecular metabolism* 53, p. 101294. DOI: 10.1016/j.molmet.2021.101294.

Guasch-Ferré, Marta; Hruby, Adela; Toledo, Estefanía; Clish, Clary B.; Martínez-González, Miguel A.; Salas-Salvadó, Jordi; Hu, Frank B. (2016): Metabolomics in Prediabetes and Diabetes. A Systematic Review and Meta-analysis. In *Diabetes care* 39 (5), pp. 833–846. DOI: 10.2337/dc15-2251.

Gupta, Vineet K.; Sharma, Nikita S.; Durden, Brittany; Garrido, Vanessa T.; Kesh, Kousik; Edwards, Dujon et al. (2021): Hypoxia-Driven Oncometabolite L-2HG Maintains Stemness-Differentiation Balance and Facilitates Immune Evasion in Pancreatic Cancer. In *Cancer research* 81 (15), pp. 4001–4013. DOI: 10.1158/0008-5472.CAN-20-2562.

Gyamfi, Jones; Kim, Jinyoung; Choi, Junjeong (2022): Cancer as a Metabolic Disorder. In *International journal of molecular sciences* 23 (3). DOI: 10.3390/ijms23031155.

Haberland, Jörg; Bertz, Joachim; Wolf, Ute; Ziese, Thomas; Kurth, Bärbel-Maria (2010): German cancer statistics 2004. In *BMC cancer* 10, p. 52. DOI: 10.1186/1471-2407-10-52.

Han, Jingjing; Li, Qian; Chen, Yu; Yang, Yonglin (2021): Recent Metabolomics Analysis in Tumor Metabolism Reprogramming. In *Frontiers in molecular biosciences* 8, p. 763902. DOI: 10.3389/fmolb.2021.763902.

Hancox, Urs; Cosulich, Sabina; Hanson, Lyndsey; Trigwell, Cath; Lenaghan, Carol; Ellston, Rebecca et al. (2015): Inhibition of PI3Kβ signaling with AZD8186 inhibits growth of PTEN-deficient breast and prostate tumors alone and in combination with docetaxel. In *Molecular cancer therapeutics* 14 (1), pp. 48–58. DOI: 10.1158/1535-7163.MCT-14-0406.

Hansen, Aaron Richard; Shapiro, Geoffrey; Do, Khanh T.; Kumar, Rajiv; Martin-Liberal, Juan; Higano, Celestia S. et al. (2017): A first in human phase I study of AZD8186, a potent and selective inhibitor of PI3K in patients with advanced solid tumours as monotherapy and in

combination with the dual mTORC1/2 inhibitor vistusertib (AZD2014) or abiraterone acetate. In *JCO* 35 (15_suppl), p. 2570. DOI: 10.1200/JCO.2017.35.15_suppl.2570.

Harrieder, Eva-Maria; Kretschmer, Fleming; Böcker, Sebastian; Witting, Michael (2022): Current state-of-the-art of separation methods used in LC-MS based metabolomics and lipidomics. In *Journal of chromatography. B, Analytical technologies in the biomedical and life sciences* 1188, p. 123069. DOI: 10.1016/j.jchromb.2021.123069.

Heinrich, Paul; Kohler, Christian; Ellmann, Lisa; Kuerner, Paul; Spang, Rainer; Oefner, Peter J.; Dettmer, Katja (2018): Correcting for natural isotope abundance and tracer impurity in MS-, MS/MS- and high-resolution-multiple-tracer-data from stable isotope labeling experiments with IsoCorrectoR. In *Scientific reports* 8 (1), p. 17910. DOI: 10.1038/s41598-018-36293-4.

Heuillet, Maud; Bellvert, Floriant; Cahoreau, Edern; Letisse, Fabien; Millard, Pierre; Portais, Jean-Charles (2018): Methodology for the Validation of Isotopic Analyses by Mass Spectrometry in Stable-Isotope Labeling Experiments. In *Analytical chemistry* 90 (3), pp. 1852–1860. DOI: 10.1021/acs.analchem.7b03886.

Hiller, Karsten; Metallo, Christian M.; Kelleher, Joanne K.; Stephanopoulos, Gregory (2010): Nontargeted elucidation of metabolic pathways using stable-isotope tracers and mass spectrometry. In *Analytical chemistry* 82 (15), pp. 6621–6628. DOI: 10.1021/ac1011574.

Hoffmann, Friederike; Jaeger, Carsten; Bhattacharya, Animesh; Schmitt, Clemens A.; Lisec, Jan (2018): Nontargeted Identification of Tracer Incorporation in High-Resolution Mass Spectrometry. In *Analytical chemistry* 90 (12), pp. 7253–7260. DOI: 10.1021/acs.analchem.8b00356.

Hoffmann, G. F.; Langhans, C.-D.; Schulze, A. (2019): 3-Hydroxy-3-Methylglutarsäure. In Axel M. Gressner, Torsten Arndt (Eds.): Lexikon der Medizinischen Laboratoriumsdiagnostik. Berlin, Heidelberg: Springer Berlin Heidelberg (Springer Reference Medizin), pp. 1175–1176.

Hofmann, Ute; Maier, Klaus; Niebel, Anja; Vacun, Gabriele; Reuss, Matthias; Mauch, Klaus (2008): Identification of metabolic fluxes in hepatic cells from transient 13C-labeling experiments: Part I. Experimental observations. In *Biotechnology and bioengineering* 100 (2), pp. 344–354. DOI: 10.1002/bit.21747.

Horai, Hisayuki; Arita, Masanori; Kanaya, Shigehiko; Nihei, Yoshito; Ikeda, Tasuku; Suwa, Kazuhiro et al. (2010): MassBank. A public repository for sharing mass spectral data for life sciences. In *Journal of mass spectrometry : JMS* 45 (7), pp. 703–714. DOI: 10.1002/jms.1777.

Hosios, Aaron M.; Hecht, Vivian C.; Danai, Laura V.; Johnson, Marc O.; Rathmell, Jeffrey C.; Steinhauser, Matthew L. et al. (2016): Amino Acids Rather than Glucose Account for the

Majority of Cell Mass in Proliferating Mammalian Cells. In *Developmental cell* 36 (5), pp. 540–549. DOI: 10.1016/j.devcel.2016.02.012.

Hoxhaj, Gerta; Manning, Brendan D. (2020): The PI3K-AKT network at the interface of oncogenic signalling and cancer metabolism. In *Nature reviews. Cancer* 20 (2), pp. 74–88. DOI: 10.1038/s41568-019-0216-7.

Hsu, Ju-Yi; Chang, Chee-Jen; Cheng, Jur-Shan (2022): Survival, treatment regimens and medical costs of women newly diagnosed with metastatic triple-negative breast cancer. In *Scientific reports* 12 (1), p. 729. DOI: 10.1038/s41598-021-04316-2.

Huang, Xiaojing; Chen, Ying-Jr; Cho, Kevin; Nikolskiy, Igor; Crawford, Peter A.; Patti, Gary J. (2014): X13CMS: global tracking of isotopic labels in untargeted metabolomics. In *Analytical chemistry* 86 (3), pp. 1632–1639. DOI: 10.1021/ac403384n.

Isaacs, Jennifer S.; Jung, Yun Jin; Mole, David R.; Lee, Sunmin; Torres-Cabala, Carlos; Chung, Yuen-Li et al. (2005): HIF overexpression correlates with biallelic loss of fumarate hydratase in renal cancer: novel role of fumarate in regulation of HIF stability. In *Cancer cell* 8 (2), pp. 143–153. DOI: 10.1016/j.ccr.2005.06.017.

Ivanisevic, Julijana; Zhu, Zheng-Jiang; Plate, Lars; Tautenhahn, Ralf; Chen, Stephen; O'Brien, Peter J. et al. (2013): Toward 'omic scale metabolite profiling: a dual separation-mass spectrometry approach for coverage of lipid and central carbon metabolism. In *Analytical chemistry* 85 (14), pp. 6876–6884. DOI: 10.1021/ac401140h.

Jain, Mohit; Nilsson, Roland; Sharma, Sonia; Madhusudhan, Nikhil; Kitami, Toshimori; Souza, Amanda L. et al. (2012): Metabolite profiling identifies a key role for glycine in rapid cancer cell proliferation. In *Science (New York, N.Y.)* 336 (6084), pp. 1040–1044. DOI: 10.1126/science.1218595.

Jandera, Pavel; Janás, Petr (2017): Recent advances in stationary phases and understanding of retention in hydrophilic interaction chromatography. A review. In *Analytica chimica acta* 967, pp. 12–32. DOI: 10.1016/j.aca.2017.01.060.

Jang, Cholsoon; Chen, Li; Rabinowitz, Joshua D. (2018): Metabolomics and Isotope Tracing. In *Cell* 173 (4), pp. 822–837. DOI: 10.1016/j.cell.2018.03.055.

Janku, Filip; Yap, Timothy A.; Meric-Bernstam, Funda (2018): Targeting the PI3K pathway in cancer: are we making headway? In *Nature reviews. Clinical oncology* 15 (5), pp. 273–291. DOI: 10.1038/nrclinonc.2018.28.

Jazmin, Lara J.; Young, Jamey D. (2013): Isotopically nonstationary 13C metabolic flux analysis. In *Methods in molecular biology (Clifton, N.J.)* 985, pp. 367–390. DOI: 10.1007/978-1-62703-299-5_18.

Ježek, Petr (2020): 2-Hydroxyglutarate in Cancer Cells. In *Antioxidants & redox signaling* 33 (13), pp. 903–926. DOI: 10.1089/ars.2019.7902.

Jia, Shidong; Liu, Zhenning; Zhang, Sen; Liu, Pixu; Zhang, Lei; Lee, Sang Hyun et al. (2008): Essential roles of PI(3)K-p110beta in cell growth, metabolism and tumorigenesis. In *Nature* 454 (7205), pp. 776–779. DOI: 10.1038/nature07091.

Jones, Anthony E.; Sheng, Li; Acevedo, Aracely; Veliova, Michaela; Shirihai, Orian S.; Stiles, Linsey; Divakaruni, Ajit S. (2021): Forces, fluxes, and fuels: tracking mitochondrial metabolism by integrating measurements of membrane potential, respiration, and metabolites. In *American journal of physiology. Cell physiology* 320 (1), C80-C91. DOI: 10.1152/ajpcell.00235.2020.

Jung, Kyung-Ho; Lee, Jin Hee; Park, Jin Won; Da Kim, Hae; Moon, Seung-Hwan; Cho, Young Seok; Lee, Kyung-Han (2018): Targeted therapy of triple negative MDA-MB-468 breast cancer with curcumin delivered by epidermal growth factor-conjugated phospholipid nanoparticles. In *Oncology letters* 15 (6), pp. 9093–9100. DOI: 10.3892/ol.2018.8471.

Juvekar, Ashish; Hu, Hai; Yadegarynia, Sina; Lyssiotis, Costas A.; Ullas, Soumya; Lien, Evan C. et al. (2016): Phosphoinositide 3-kinase inhibitors induce DNA damage through nucleoside depletion. In *Proceedings of the National Academy of Sciences of the United States of America* 113 (30), E4338-47. DOI: 10.1073/pnas.1522223113.

Kamphorst, Jurre J.; Chung, Michelle K.; Fan, Jing; Rabinowitz, Joshua D. (2014): Quantitative analysis of acetyl-CoA production in hypoxic cancer cells reveals substantial contribution from acetate. In *Cancer & metabolism* 2, p. 23. DOI: 10.1186/2049-3002-2-23.

Kapoore, Rahul Vijay; Coyle, Rachael; Staton, Carolyn A.; Brown, Nicola J.; Vaidyanathan, Seetharaman (2015): Cell line dependence of metabolite leakage in metabolome analyses of adherent normal and cancer cell lines. In *Metabolomics* 11 (6), pp. 1743–1755. DOI: 10.1007/s11306-015-0833-4.

Kapoore, Rahul Vijay; Coyle, Rachael; Staton, Carolyn A.; Brown, Nicola J.; Vaidyanathan, Seetharaman (2017): Influence of washing and quenching in profiling the metabolome of adherent mammalian cells: a case study with the metastatic breast cancer cell line MDA-MB-231. In *The Analyst* 142 (11), pp. 2038–2049. DOI: 10.1039/c7an00207f.

Kaushik, Akash K.; DeBerardinis, Ralph J. (2018): Applications of metabolomics to study cancer metabolism. In *Biochimica et biophysica acta. Reviews on cancer* 1870 (1), pp. 2–14. DOI: 10.1016/j.bbcan.2018.04.009.

Kennedy, Luke; Sandhu, Jagdeep K.; Harper, Mary-Ellen; Cuperlovic-Culf, Miroslava (2020): Role of Glutathione in Cancer: From Mechanisms to Therapies. In *Biomolecules* 10 (10). DOI: 10.3390/biom10101429.

Khatami, Fatemeh; Aghamir, Seyed Mohammad Kazem; Tavangar, Seyed Mohammad (2019): Oncometabolites. A new insight for oncology. In *Molecular genetics & genomic medicine* 7 (9), e873. DOI: 10.1002/mgg3.873.

Kiefer, Patrick; Schmitt, Uwe; Müller, Jonas E. N.; Hartl, Johannes; Meyer, Fabian; Ryffel, Florian; Vorholt, Julia A. (2015): DynaMet: a fully automated pipeline for dynamic LC-MS data. In *Analytical chemistry* 87 (19), pp. 9679–9686. DOI: 10.1021/acs.analchem.5b01660.

Kind, Tobias; Fiehn, Oliver (2006): Metabolomic database annotations via query of elemental compositions. Mass accuracy is insufficient even at less than 1 ppm. In *BMC bioinformatics* 7, p. 234. DOI: 10.1145/41526.41528.

Knee, Jose M.; Rzezniczak, Teresa Z.; Barsch, Aiko; Guo, Kevin Z.; Merritt, Thomas J. S. (2013): A novel ion pairing LC/MS metabolomics protocol for study of a variety of biologically relevant polar metabolites. In *Journal of chromatography. B, Analytical technologies in the biomedical and life sciences* 936, pp. 63–73. DOI: 10.1016/j.jchromb.2013.07.027.

Koning, W. de; van Dam, K. (1992): A method for the determination of changes of glycolytic metabolites in yeast on a subsecond time scale using extraction at neutral pH. In *Analytical biochemistry* 204 (1), pp. 118–123. DOI: 10.1016/0003-2697(92)90149-2.

Kumar, Ashish; Misra, Biswapriya B. (2019): Challenges and Opportunities in Cancer Metabolomics. In *Proteomics* 19 (21-22), e1900042. DOI: 10.1002/pmic.201900042.

Küry, D.; Keller, U. (1991): Trimethylsilyl-O-methyloxime derivatives for the measurement of 6,6-2H2-D-glucose-enriched plasma samples by gas chromatography-mass spectrometry. In *Journal of chromatography* 572 (1-2), pp. 302–306. DOI: 10.1016/0378-4347(91)80494-w.

Lackner, Marcel; Neef, Sylvia K.; Winter, Stefan; Beer-Hammer, Sandra; Nürnberg, Bernd; Schwab, Matthias et al. (2022): Untargeted stable isotope-resolved metabolomics to assess the effect of PI3Kβ inhibition on metabolic pathway activities in a PTEN null breast cancer cell line. In *Frontiers in molecular biosciences* 9, p. 1004602. DOI: 10.3389/fmolb.2022.1004602.

Lam, Christine; Low, Jin-Yih; Tran, Phuoc T.; Wang, Hailun (2021): The hexosamine biosynthetic pathway and cancer: Current knowledge and future therapeutic strategies. In *Cancer letters* 503, pp. 11–18. DOI: 10.1016/j.canlet.2021.01.010.

Lane, Andrew N.; Higashi, Richard M.; Fan, Teresa W-M (2016): Preclinical models for interrogating drug action in human cancers using Stable Isotope Resolved Metabolomics (SIRM). In *Metabolomics : Official journal of the Metabolomic Society* 12 (7). DOI: 10.1007/s11306-016-1065-y.

Lane, Andrew N.; Higashi, Richard M.; Fan, Teresa W-M (2019): NMR and MS-based Stable Isotope-Resolved Metabolomics and Applications in Cancer Metabolism. In *Trends in analytical chemistry : TRAC* 120. DOI: 10.1016/j.trac.2018.11.020.

Lanning, Nathan J.; Castle, Joshua P.; Singh, Simar J.; Leon, Andre N.; Tovar, Elizabeth A.; Sanghera, Amandeep et al. (2017): Metabolic profiling of triple-negative breast cancer cells reveals metabolic vulnerabilities. In *Cancer & metabolism* 5, p. 6. DOI: 10.1186/s40170-017-0168-x.

Larsson J (2021): eulerr: Area-Proportional Euler and Venn Diagrams with Ellipses. Available online at https://CRAN.R-project.org/package=eulerr, checked on 3/15/2022.

Lawrence, Michael S.; Stojanov, Petar; Mermel, Craig H.; Robinson, James T.; Garraway, Levi A.; Golub, Todd R. et al. (2014): Discovery and saturation analysis of cancer genes across 21 tumour types. In *Nature* 505 (7484), pp. 495–501. DOI: 10.1038/nature12912.

Lee, W. N.; Boros, L. G.; Puigjaner, J.; Bassilian, S.; Lim, S.; Cascante, M. (1998): Mass isotopomer study of the nonoxidative pathways of the pentose cycle with 1,2-13C2glucose. In *The American journal of physiology* 274 (5), E843-51. DOI: 10.1152/ajpendo.1998.274.5.E843.

Leighty, Robert W.; Antoniewicz, Maciek R. (2011): Dynamic metabolic flux analysis (DMFA): a framework for determining fluxes at metabolic non-steady state. In *Metabolic engineering* 13 (6), pp. 745–755. DOI: 10.1016/j.ymben.2011.09.010.

Leuthold, Patrick; Schaeffeler, Elke; Winter, Stefan; Büttner, Florian; Hofmann, Ute; Mürdter, Thomas E. et al. (2017): Comprehensive Metabolomic and Lipidomic Profiling of Human Kidney Tissue. A Platform Comparison. In *Journal of proteome research* 16 (2), pp. 933–944. DOI: 10.1021/acs.jproteome.6b00875.

Levine, Arnold J.; Oren, Moshe (2009): The first 30 years of p53. Growing ever more complex. In *Nature reviews. Cancer* 9 (10), pp. 749–758. DOI: 10.1038/nrc2723.

Llufrio, Elizabeth M.; Cho, Kevin; Patti, Gary J. (2019): Systems-level analysis of isotopic labeling in untargeted metabolomic data by X13CMS. In *Nature protocols* 14 (7), pp. 1970–1990. DOI: 10.1038/s41596-019-0167-1.

López-López, Ángeles; López-Gonzálvez, Ángeles; Barker-Tejeda, Tomás Clive; Barbas, Coral (2018): A review of validated biomarkers obtained through metabolomics. In *Expert review of molecular diagnostics* 18 (6), pp. 557–575. DOI: 10.1080/14737159.2018.1481391.

Lorenz, Matthew A.; Burant, Charles F.; Kennedy, Robert T. (2011): Reducing time and increasing sensitivity in sample preparation for adherent mammalian cell metabolomics. In *Analytical chemistry* 83 (9), pp. 3406–3414. DOI: 10.1021/ac103313x.

Lorkiewicz, Pawel K.; Gibb, Andrew A.; Rood, Benjamin R.; He, Liqing; Zheng, Yuting; Clem, Brian F. et al. (2019): Integration of flux measurements and pharmacological controls to optimize stable isotope-resolved metabolomics workflows and interpretation. In *Scientific reports* 9 (1), p. 13705. DOI: 10.1038/s41598-019-50183-3.

Lynch, James T.; Polanska, Urszula M.; Delpuech, Oona; Hancox, Urs; Trinidad, Antonio G.; Michopoulos, Filippos et al. (2017): Inhibiting PI3Kβ with AZD8186 Regulates Key Metabolic Pathways in PTEN-Null Tumors. In *Clinical cancer research : an official journal of the American Association for Cancer Research* 23 (24), pp. 7584–7595. DOI: 10.1158/1078-0432.CCR-17-0676.

Lynch, James T.; Polanska, Urszula M.; Hancox, Ursula; Delpuech, Oona; Maynard, Juliana; Trigwell, Catherine et al. (2018): Combined Inhibition of PI3Kβ and mTOR Inhibits Growth of PTEN-null Tumors. In *Molecular cancer therapeutics* 17 (11), pp. 2309–2319. DOI: 10.1158/1535-7163.MCT-18-0183.

Ma, Eric H.; Verway, Mark J.; Johnson, Radia M.; Roy, Dominic G.; Steadman, Mya; Hayes, Sebastian et al. (2019): Metabolic Profiling Using Stable Isotope Tracing Reveals Distinct Patterns of Glucose Utilization by Physiologically Activated CD8+ T Cells. In *Immunity* 51 (5), 856-870.e5. DOI: 10.1016/j.immuni.2019.09.003.

Maier, Klaus; Hofmann, Ute; Bauer, Alexander; Niebel, Anja; Vacun, Gabriele; Reuss, Matthias; Mauch, Klaus (2009): Quantification of statin effects on hepatic cholesterol synthesis by transient (13)C-flux analysis. In *Metabolic engineering* 11 (4-5), pp. 292–309. DOI: 10.1016/j.ymben.2009.06.001.

Manning, Brendan D.; Toker, Alex (2017): AKT/PKB Signaling: Navigating the Network. In *Cell* 169 (3), pp. 381–405. DOI: 10.1016/j.cell.2017.04.001.

Mao, Gen-Hong; Lu, Ping; Wang, Ya-Nan; Tian, Chen-Guang; Huang, Xiao-Hui; Feng, Zong-Gang et al. (2017): Role of PI3K p110β in the differentiation of human embryonic stem cells into islet-like cells. In *Biochemical and biophysical research communications* 488 (1), pp. 109–115. DOI: 10.1016/j.bbrc.2017.05.018.

Martín-Blázquez, Ariadna; Díaz, Caridad; González-Flores, Encarnación; Franco-Rivas, Daniel; Jiménez-Luna, Cristina; Melguizo, Consolación et al. (2019): Untargeted LC-HRMS-based metabolomics to identify novel biomarkers of metastatic colorectal cancer. In *Scientific reports* 9 (1), p. 20198. DOI: 10.1038/s41598-019-55952-8.

Martínez-Reyes, Inmaculada; Chandel, Navdeep S. (2020): Mitochondrial TCA cycle metabolites control physiology and disease. In *Nature communications* 11 (1), p. 102. DOI: 10.1038/s41467-019-13668-3.

Matsumoto, I.; Kuhara, T. (1996): A new chemical diagnostic method for inborn errors of metabolism by mass spectrometry—rapid, practical, and simultaneous urinary metabolites analysis. In *Mass Spectrom. Rev.* 15 (1), pp. 43–57. DOI: 10.1002/(SICI)1098-2787(1996)15:1<43::AID-MAS3>3.0.CO;2-B.

Maynard, Juliana; Emmas, Sally-Ann; Blé, Francois-Xavier; Barjat, Hervé; Lawrie, Emily; Hancox, Urs et al. (2016): The use of (18)F-fluorodeoxyglucose positron emission tomography ((18)F-FDG PET) as a pathway-specific biomarker with AZD8186, a PI3Kβ/δ inhibitor. In *EJNMMI research* 6 (1), p. 62. DOI: 10.1186/s13550-016-0220-9.

Meyer, Hanna; Weidmann, Hendrikje; Lalk, Michael (2013): Methodological approaches to help unravel the intracellular metabolome of Bacillus subtilis. In *Microbial cell factories* 12, p. 69. DOI: 10.1186/1475-2859-12-69.

Meyer, Helmut E.; Fröhlich, Thomas; Nordhoff, Eckhard; Kuhlmann, Katja (2022): Massenspektrometrie. In Jens Kurreck, Joachim W. Engels, Friedrich Lottspeich (Eds.): Bioanalytik. Berlin, Heidelberg: Springer Berlin Heidelberg, pp. 359–414.

Miccheli, A.; Tomassini, A.; Puccetti, C.; Valerio, M.; Peluso, G.; Tuccillo, F. et al. (2006): Metabolic profiling by 13C-NMR spectroscopy: 1,2-13C2glucose reveals a heterogeneous metabolism in human leukemia T cells. In *Biochimie* 88 (5), pp. 437–448. DOI: 10.1016/j.biochi.2005.10.004.

Mishra, Rosalin; Patel, Hima; Alanazi, Samar; Kilroy, Mary Kate; Garrett, Joan T. (2021): PI3K Inhibitors in Cancer: Clinical Implications and Adverse Effects. In *International journal of molecular sciences* 22 (7). DOI: 10.3390/ijms22073464.

Molinaro, Angela; Becattini, Barbara; Mazzoli, Arianna; Bleve, Augusto; Radici, Lucia; Maxvall, Ingela et al. (2019): Insulin-Driven PI3K-AKT Signaling in the Hepatocyte Is Mediated by Redundant PI3Kα and PI3Kβ Activities and Is Promoted by RAS. In *Cell metabolism* 29 (6), 1400-1409.e5. DOI: 10.1016/j.cmet.2019.03.010.

Moseley, Hunter N. B.; Lane, Andrew N.; Belshoff, Alex C.; Higashi, Richard M.; Fan, Teresa W. M. (2011): A novel deconvolution method for modeling UDP-N-acetyl-D-glucosamine biosynthetic pathways based on (13)C mass isotopologue profiles under non-steady-state conditions. In *BMC biology* 9, p. 37. DOI: 10.1186/1741-7007-9-37.

Mullen, Andrew R.; Wheaton, William W.; Jin, Eunsook S.; Chen, Pei-Hsuan; Sullivan, Lucas B.; Cheng, Tzuling et al. (2011): Reductive carboxylation supports growth in tumour cells with defective mitochondria. In *Nature* 481 (7381), pp. 385–388. DOI: 10.1038/nature10642.

Munger, Joshua; Bajad, Sunil U.; Coller, Hilary A.; Shenk, Thomas; Rabinowitz, Joshua D. (2006): Dynamics of the cellular metabolome during human cytomegalovirus infection. In *PLoS pathogens* 2 (12), e132. DOI: 10.1371/journal.ppat.0020132.

Muschet, Caroline; Möller, Gabriele; Prehn, Cornelia; Angelis, Martin Hrabě de; Adamski, Jerzy; Tokarz, Janina (2016): Removing the bottlenecks of cell culture metabolomics. Fast normalization procedure, correlation of metabolites to cell number, and impact of the cell harvesting method. In *Metabolomics : Official journal of the Metabolomic Society* 12 (10), p. 151. DOI: 10.1007/s11306-016-1104-8.

Nakajima, Kazuki; Ito, Emi; Ohtsubo, Kazuaki; Shirato, Ken; Takamiya, Rina; Kitazume, Shinobu et al. (2013): Mass isotopomer analysis of metabolically labeled nucleotide sugars and N- and O-glycans for tracing nucleotide sugar metabolisms. In *Molecular & cellular proteomics : MCP* 12 (9), pp. 2468–2480. DOI: 10.1074/mcp.M112.027151.

Neef, Sylvia K.; Winter, Stefan; Hofmann, Ute; Mürdter, Thomas E.; Schaeffeler, Elke; Horn, Heike et al. (2020): Optimized protocol for metabolomic and lipidomic profiling in formalin-fixed paraffin-embedded kidney tissue by LC-MS. In *Analytica chimica acta* 1134, pp. 125–135. DOI: 10.1016/j.aca.2020.08.005.

Nilsson, Roland (2020): Validity of natural isotope abundance correction for metabolic flux analysis. In *Mathematical biosciences* 330, p. 108481. DOI: 10.1016/j.mbs.2020.108481.

Nonnenmacher, Yannic; Palorini, Roberta; Hiller, Karsten (2019): Determining Compartment-Specific Metabolic Fluxes. In *Methods in molecular biology (Clifton, N.J.)* 1862, pp. 137–149. DOI: 10.1007/978-1-4939-8769-6_10.

Nürnberg, Bernd; Beer-Hammer, Sandra (2019): Function, Regulation and Biological Roles of PI3Kγ Variants. In *Biomolecules* 9 (9). DOI: 10.3390/biom9090427.

Nürnberg, Bernd; Beer-Hammer, Sandra (2020): Phospholipid Kinases. In Stefan Offermanns, Walter Rosenthal (Eds.): Encyclopedia of Molecular Pharmacology. Cham: Springer International Publishing, pp. 1–8.

Nybo, S. Eric; Lamberts, Jennifer T. (2019): Integrated use of LC/MS/MS and LC/Q-TOF/MS targeted metabolomics with automated label-free microscopy for quantification of purine metabolites in cultured mammalian cells. In *Purinergic signalling* 15 (1), pp. 17–25. DOI: 10.1007/s11302-018-9643-2.

Oh, Sunhwa; Kim, Hyungjoo; Nam, KeeSoo; Shin, Incheol (2017): Glut1 promotes cell proliferation, migration and invasion by regulating epidermal growth factor receptor and integrin signaling in triple-negative breast cancer cells. In *BMB reports* 50 (3), pp. 132–137. DOI: 10.5483/bmbrep.2017.50.3.189.

Owusu-Brackett, Nicci; Zhao, Ming; Akcakanat, Argun; Evans, Kurt W.; Yuca, Erkan; Dumbrava, Ecaterina Ileana et al. (2020): Targeting PI3Kβ alone and in combination with chemotherapy or immunotherapy in tumors with PTEN loss. In *Oncotarget* 11 (11), pp. 969–981. DOI: 10.18632/oncotarget.27503.

Panchal, A. R.; Comte, B.; Huang, H.; Kerwin, T.; Darvish, A.; Des Rosiers, C. et al. (2000): Partitioning of pyruvate between oxidation and anaplerosis in swine hearts. In *American journal of physiology. Heart and circulatory physiology* 279 (5), H2390-8. DOI: 10.1152/ajpheart.2000.279.5.H2390.

Pang, Zhiqiang; Zhou, Guangyan; Ewald, Jessica; Le Chang; Hacariz, Orcun; Basu, Niladri; Xia, Jianguo (2022): Using MetaboAnalyst 5.0 for LC-HRMS spectra processing, multi-omics integration and covariate adjustment of global metabolomics data. In *Nature protocols* 17 (8), pp. 1735–1761. DOI: 10.1038/s41596-022-00710-w.

Pascual, J.; Turner, N. C. (2019): Targeting the PI3-kinase pathway in triple-negative breast cancer. In *Annals of oncology : official journal of the European Society for Medical Oncology* 30 (7), pp. 1051–1060. DOI: 10.1093/annonc/mdz133.

Patra, Krushna C.; Hay, Nissim (2014): The pentose phosphate pathway and cancer. In *Trends in biochemical sciences* 39 (8), pp. 347–354. DOI: 10.1016/j.tibs.2014.06.005.

Pearce, Oliver M. T.; Läubli, Heinz (2016): Sialic acids in cancer biology and immunity. In *Glycobiology* 26 (2), pp. 111–128. DOI: 10.1093/glycob/cwv097.

Perl, Andras; Hanczko, Robert; Telarico, Tiffany; Oaks, Zachary; Landas, Steve (2011): Oxidative stress, inflammation and carcinogenesis are controlled through the pentose phosphate pathway by transaldolase. In *Trends in molecular medicine* 17 (7), pp. 395–403. DOI: 10.1016/j.molmed.2011.01.014.

Peterson, Amanda L.; Walker, Adam K.; Sloan, Erica K.; Creek, Darren J. (2016): Optimized Method for Untargeted Metabolomics Analysis of MDA-MB-231 Breast Cancer Cells. In *Metabolites* 6 (4). DOI: 10.3390/metabo6040030.

Piovesan, Allison; Antonaros, Francesca; Vitale, Lorenza; Strippoli, Pierluigi; Pelleri, Maria Chiara; Caracausi, Maria (2019): Human protein-coding genes and gene feature statistics in 2019. In *BMC research notes* 12 (1), p. 315. DOI: 10.1186/s13104-019-4343-8.

Polat, Ibrahim H.; Tarrado-Castellarnau, Míriam; Bharat, Rohit; Perarnau, Jordi; Benito, Adrian; Cortés, Roldán et al. (2021): Oxidative Pentose Phosphate Pathway Enzyme 6-Phosphogluconate Dehydrogenase Plays a Key Role in Breast Cancer Metabolism. In *Biology* 10 (2). DOI: 10.3390/biology10020085.

Potter, Michelle; Newport, Emma; Morten, Karl J. (2016): The Warburg effect: 80 years on. In *Biochemical Society transactions* 44 (5), pp. 1499–1505. DOI: 10.1042/BST20160094.

Puchalska, Patrycja; Huang, Xiaojing; Martin, Shannon E.; Han, Xianlin; Patti, Gary J.; Crawford, Peter A. (2018): Isotope Tracing Untargeted Metabolomics Reveals Macrophage

Polarization-State-Specific Metabolic Coordination across Intracellular Compartments. In *iScience* 9, pp. 298–313. DOI: 10.1016/j.isci.2018.10.029.

Purwaha, Preeti; Lorenzi, Philip L.; Silva, Leslie P.; Hawke, David H.; Weinstein, John N. (2014): Targeted metabolomic analysis of amino acid response to L-asparaginase in adherent cells. In *Metabolomics : Official journal of the Metabolomic Society* 10 (5), pp. 909–919. DOI: 10.1007/s11306-014-0634-1.

R Core Team (2021): R: A language and environment for statistical computing. Version version 2021.9.0.351, Ghost Orchid: R Foundation of Statistical Computing.

Rahman, Md. Musfiqur; Abd El-Aty, A. M.; Choi, Jeong-Heui; Shin, Ho-Chul; Shin, Sung Chul; Shim, Jae-Han (2015): Basic Overview on Gas Chromatography Columns. In Veronica Pino, Jared L. Anderson, Alain Berthod, Apryll M. Stalcup (Eds.): Analytical Separation Science. Weinheim, Germany: Wiley-VCH Verlag GmbH & Co. KGaA, pp. 823–834.

Ritter, Joachim B.; Genzel, Yvonne; Reichl, Udo (2008): Simultaneous extraction of several metabolites of energy metabolism and related substances in mammalian cells: optimization using experimental design. In *Analytical biochemistry* 373 (2), pp. 349–369. DOI: 10.1016/j.ab.2007.10.037.

Robinson, David (2020): fuzzyjoin. fuzzyjoin: Join Tables Together on Inexact Matching. Version 0.1.6.

Roci, Irena; Gallart-Ayala, Hector; Schmidt, Angelika; Watrous, Jeramie; Jain, Mohit; Wheelock, Craig E.; Nilsson, Roland (2016): Metabolite Profiling and Stable Isotope Tracing in Sorted Subpopulations of Mammalian Cells. In *Analytical chemistry* 88 (5), pp. 2707–2713. DOI: 10.1021/acs.analchem.5b04071.

Roig, Bàrbara; Rodríguez-Balada, Marta; Samino, Sara; Lam, Eric W-F; Guaita-Esteruelas, Sandra; Gomes, Ana R. et al. (2017): Metabolomics reveals novel blood plasma biomarkers associated to the BRCA1-mutated phenotype of human breast cancer. In *Scientific reports* 7 (1), p. 17831. DOI: 10.1038/s41598-017-17897-8.

Salek, Reza M.; Steinbeck, Christoph; Viant, Mark R.; Goodacre, Royston; Dunn, Warwick B. (2013): The role of reporting standards for metabolite annotation and identification in metabolomic studies. In *GigaScience* 2 (1), p. 13. DOI: 10.1186/2047-217X-2-13.

San-Millán, Iñigo; Brooks, George A. (2017): Reexamining cancer metabolism: lactate production for carcinogenesis could be the purpose and explanation of the Warburg Effect. In *Carcinogenesis* 38 (2), pp. 119–133. DOI: 10.1093/carcin/bgw127.

Sapcariu, Sean C.; Kanashova, Tamara; Weindl, Daniel; Ghelfi, Jenny; Dittmar, Gunnar; Hiller, Karsten (2014): Simultaneous extraction of proteins and metabolites from cells in culture. In *MethodsX* 1, pp. 74–80. DOI: 10.1016/j.mex.2014.07.002.

Sargent, Mike; Harte, Rita; Harrington, Chris; Bedson, Peter (Eds.) (2002): Guidelines for Achieving High Accuracy in Isotope Dilution Mass Spectrometry (IDMS): Royal Society of Chemistry.

Schrimpe-Rutledge, Alexandra C.; Codreanu, Simona G.; Sherrod, Stacy D.; McLean, John A. (2016): Untargeted Metabolomics Strategies-Challenges and Emerging Directions. In *Journal of the American Society for Mass Spectrometry* 27 (12), pp. 1897–1905. DOI: 10.1007/s13361-016-1469-y.

Schultze, Simon M.; Hemmings, Brian A.; Niessen, Markus; Tschopp, Oliver (2012): PI3K/AKT, MAPK and AMPK signalling: protein kinases in glucose homeostasis. In *Expert reviews in molecular medicine* 14, e1. DOI: 10.1017/S1462399411002109.

Schwaiger-Haber, Michaela; Hermann, Gerrit; El Abiead, Yasin; Rampler, Evelyn; Wernisch, Stefanie; Sas, Kelli et al. (2019): Proposing a validation scheme for 13C metabolite tracer studies in high-resolution mass spectrometry. In *Analytical and bioanalytical chemistry* 411 (14), pp. 3103–3113. DOI: 10.1007/s00216-019-01773-7.

Schwaiger-Haber, Michaela; Stancliffe, Ethan; Anbukumar, Dhanalakshmi S.; Sells, Blake; Yi, Jia; Cho, Kevin et al. (2023): Using mass spectrometry imaging to map fluxes quantitatively in the tumor ecosystem. In *Nature communications* 14 (1), p. 2876. DOI: 10.1038/s41467-023-38403-x.

Schwentner, L.; Wolters, R.; Koretz, K.; Wischnewsky, M. B.; Kreienberg, R.; Rottscholl, R.; Wöckel, A. (2012): Triple-negative breast cancer. The impact of guideline-adherent adjuvant treatment on survival--a retrospective multi-centre cohort study. In *Breast cancer research and treatment* 132 (3), pp. 1073–1080. DOI: 10.1007/s10549-011-1935-y.

Sciacovelli, Marco; Frezza, Christian (2016): Oncometabolites. Unconventional triggers of oncogenic signalling cascades. In *Free radical biology & medicine* 100, pp. 175–181. DOI: 10.1016/j.freeradbiomed.2016.04.025.

Sellick, Christopher A.; Hansen, Rasmus; Maqsood, Arfa R.; Dunn, Warwick B.; Stephens, Gillian M.; Goodacre, Royston; Dickson, Alan J. (2009): Effective quenching processes for physiologically valid metabolite profiling of suspension cultured Mammalian cells. In *Analytical chemistry* 81 (1), pp. 174–183. DOI: 10.1021/ac8016899.

Sellick, Christopher A.; Knight, David; Croxford, Alexandra S.; Maqsood, Arfa R.; Stephens, Gill M.; Goodacre, Royston; Dickson, Alan J. (2010): Evaluation of extraction processes for intracellular metabolite profiling of mammalian cells. Matching extraction approaches to cell

type and metabolite targets. In *Metabolomics* 6 (3), pp. 427–438. DOI: 10.1007/s11306-010-0216-9.

Sen, Suvajit; Kawahara, Brain; Mahata, Sushil K.; Tsai, Rebecca; Yoon, Alexander; Hwang, Lin et al. (2016): Cystathionine. A novel oncometabolite in human breast cancer. In *Archives of biochemistry and biophysics* 604, pp. 95–102. DOI: 10.1016/j.abb.2016.06.010.

Seyfried, Thomas N.; Flores, Roberto E.; Poff, Angela M.; D'Agostino, Dominic P. (2014): Cancer as a metabolic disease. Implications for novel therapeutics. In *Carcinogenesis* 35 (3), pp. 515–527. DOI: 10.1093/carcin/bgt480.

Shestov, Alexander A.; Lee, Seung-Cheol; Nath, Kavindra; Guo, Lili; Nelson, David S.; Roman, Jeffrey C. et al. (2016): (13)C MRS and LC-MS Flux Analysis of Tumor Intermediary Metabolism. In *Frontiers in oncology* 6, p. 135. DOI: 10.3389/fonc.2016.00135.

Shi, Xiaojian; Xi, Bowei; Jasbi, Paniz; Turner, Cassidy; Jin, Yan; Gu, Haiwei (2020): Comprehensive Isotopic Targeted Mass Spectrometry: Reliable Metabolic Flux Analysis with Broad Coverage. In *Analytical chemistry* 92 (17), pp. 11728–11738. DOI: 10.1021/acs.analchem.0c01767.

Silva, Leslie P.; Lorenzi, Philip L.; Purwaha, Preeti; Yong, Valeda; Hawke, David H.; Weinstein, John N. (2013): Measurement of DNA concentration as a normalization strategy for metabolomic data from adherent cell lines. In *Analytical chemistry* 85 (20), pp. 9536–9542. DOI: 10.1021/ac401559v.

Smith, Colin A.; O'Maille, Grace; Want, Elizabeth J.; Qin, Chuan; Trauger, Sunia A.; Brandon, Theodore R. et al. (2005): METLIN. A metabolite mass spectral database. In *Therapeutic drug monitoring* 27 (6), pp. 747–751. DOI: 10.1097/01.ftd.0000179845.53213.39.

Smith, Colin A.; Want, Elizabeth J.; O'Maille, Grace; Abagyan, Ruben; Siuzdak, Gary (2006): XCMS: processing mass spectrometry data for metabolite profiling using nonlinear peak alignment, matching, and identification. In *Analytical chemistry* 78 (3), pp. 779–787. DOI: 10.1021/ac051437y.

Stancliffe, Ethan; Schwaiger-Haber, Michaela; Sindelar, Miriam; Murphy, Matthew J.; Soerensen, Mette; Patti, Gary J. (2022): An Untargeted Metabolomics Workflow that Scales to Thousands of Samples for Population-Based Studies. In *Analytical chemistry* 94 (50), pp. 17370–17378. DOI: 10.1021/acs.analchem.2c01270.

Statistisches Bundesamt (2024): Todesursachen nach Krankheitsarten - 2023. Available online at https://www.destatis.de/DE/Themen/Gesellschaft-Umwelt/Gesundheit/Todesursachen/_inhalt.html#235880, checked on 3/23/2025.

Statistisches Bundesamt (2025): Die 10 häufigsten Todesfälle durch Krebs in 2023. Available online at https://www.destatis.de/DE/Themen/Gesellschaft-Umwelt/Gesundheit/Todesursachen/Tabellen/sterbefaelle-krebs-insgesamt.html, checked on 3/23/2025.

Sumner, Lloyd W.; Amberg, Alexander; Barrett, Dave; Beale, Michael H.; Beger, Richard; Daykin, Clare A. et al. (2007): Proposed minimum reporting standards for chemical analysis Chemical Analysis Working Group (CAWG) Metabolomics Standards Initiative (MSI). In *Metabolomics : Official journal of the Metabolomic Society* 3 (3), pp. 211–221. DOI: 10.1007/s11306-007-0082-2.

Sun, Pu; Meng, Ling-hua (2020): Emerging roles of class I PI3K inhibitors in modulating tumor microenvironment and immunity. In *Acta pharmacologica Sinica* 41 (11), pp. 1395–1402. DOI: 10.1038/s41401-020-00500-8.

Tabata, Sho; Kojima, Yasushi; Sakamoto, Takeharu; Igarashi, Kaori; Umetsu, Ko; Ishikawa, Takamasa et al. (2023): L-2hydroxyglutaric acid rewires amino acid metabolism in colorectal cancer via the mTOR-ATF4 axis. In *Oncogene* 42 (16), pp. 1294–1307. DOI: 10.1038/s41388-023-02632-7.

Talwalkar, R. T.; Lester, R. L. (1973): The response of diphosphoinositide and triphosphoinostitide to perturbations of the adenylate energy charge in cells of Saccharomyces cerevisiae. In *Biochimica et biophysica acta* 306 (3), pp. 412–421. DOI: 10.1016/0005-2760(73)90180-X.

Tang, Dao-Quan; Zou, Ll; Yin, Xiao-Xing; Ong, Choon Nam (2016): HILIC-MS for metabolomics. An attractive and complementary approach to RPLC-MS. In *Mass spectrometry reviews* 35 (5), pp. 574–600. DOI: 10.1002/mas.21445.

Tang, W. H. Wilson; Wang, Zeneng; Levison, Bruce S.; Koeth, Robert A.; Britt, Earl B.; Fu, Xiaoming et al. (2013): Intestinal microbial metabolism of phosphatidylcholine and cardiovascular risk. In *The New England journal of medicine* 368 (17), pp. 1575–1584. DOI: 10.1056/NEJMoa1109400.

Tautenhahn, Ralf; Böttcher, Christoph; Neumann, Steffen (2008): Highly sensitive feature detection for high resolution LC/MS. In *BMC bioinformatics* 9, p. 504. DOI: 10.1186/1471-2105-9-504.

Teng, Quincy; Huang, Wenlin; Collette, Timothy W.; Ekman, Drew R.; Tan, Chalet (2009): A direct cell quenching method for cell-culture based metabolomics. In *Metabolomics* 5 (2), pp. 199–208. DOI: 10.1007/s11306-008-0137-z.

Tidwell, Tia R.; Røsland, Gro V.; Tronstad, Karl Johan; Søreide, Kjetil; Hagland, Hanne R. (2022): Metabolic flux analysis of 3D spheroids reveals significant differences in glucose

metabolism from matched 2D cultures of colorectal cancer and pancreatic ductal adenocarcinoma cell lines. In *Cancer & metabolism* 10 (1), p. 9. DOI: 10.1186/s40170-022-00285-w.

Tolosa, Jorge M.; Schjenken, John E.; Civiti, Theodora D.; Clifton, Vicki L.; Smith, Roger (2007): Column-based method to simultaneously extract DNA, RNA, and proteins from the same sample. In *BioTechniques* 43 (6), pp. 799–804. DOI: 10.2144/000112594.

Tolstikov, Vladimir; Moser, A. James; Sarangarajan, Rangaprasad; Narain, Niven R.; Kiebish, Michael A. (2020): Current Status of Metabolomic Biomarker Discovery: Impact of Study Design and Demographic Characteristics. In *Metabolites* 10 (6). DOI: 10.3390/metabo10060224.

Tomlinson, Ian P. M.; Alam, N. Afrina; Rowan, Andrew J.; Barclay, Ella; Jaeger, Emma E. M.; Kelsell, David et al. (2002): Germline mutations in FH predispose to dominantly inherited uterine fibroids, skin leiomyomata and papillary renal cell cancer. In *Nature genetics* 30 (4), pp. 406–410. DOI: 10.1038/ng849.

Trefely, Sophie; Ashwell, Peter; Snyder, Nathaniel W. (2016): FluxFix: automatic isotopologue normalization for metabolic tracer analysis. In *BMC bioinformatics* 17 (1), p. 485. DOI: 10.1186/s12859-016-1360-7.

Tsugawa, Hiroshi; Kind, Tobias; Nakabayashi, Ryo; Yukihira, Daichi; Tanaka, Wataru; Cajka, Tomas et al. (2016): Hydrogen Rearrangement Rules. Computational MS/MS Fragmentation and Structure Elucidation Using MS-FINDER Software. In *Analytical chemistry* 88 (16), pp. 7946–7958. DOI: 10.1021/acs.analchem.6b00770.

Vanhaesebroeck, Bart; Perry, Matthew W. D.; Brown, Jennifer R.; André, Fabrice; Okkenhaug, Klaus (2021): PI3K inhibitors are finally coming of age. In *Nature reviews. Drug discovery* 20 (10), pp. 741–769. DOI: 10.1038/s41573-021-00209-1.

Verbeke, Frederick; Bracke, Nathalie; Debunne, Nathan; Wynendaele, Evelien; Spiegeleer, Bart de (2020): LC-MS Compatible Antiadsorption Diluent for Peptide Analysis. In *Analytical chemistry* 92 (2), pp. 1712–1719. DOI: 10.1021/acs.analchem.9b01840.

Vettore, Lisa; Westbrook, Rebecca L.; Tennant, Daniel A. (2020): New aspects of amino acid metabolism in cancer. In *British journal of cancer* 122 (2), pp. 150–156. DOI: 10.1038/s41416-019-0620-5.

Vidal, Santiago; Bouzaher, Yanis Hichem; El Motiam, Ahmed; Seoane, Rocío; Rivas, Carmen (2022): Overview of the regulation of the class IA PI3K/AKT pathway by SUMO. In *Seminars in cell & developmental biology* 132, pp. 51–61. DOI: 10.1016/j.semcdb.2021.10.012.

Vučetić, Milica; Cormerais, Yann; Parks, Scott K.; Pouysségur, Jacques (2017): The Central Role of Amino Acids in Cancer Redox Homeostasis. Vulnerability Points of the Cancer Redox Code. In *Frontiers in oncology* 7, p. 319. DOI: 10.3389/fonc.2017.00319.

Wahl, Sebastian Aljoscha; Nöh, Katharina; Wiechert, Wolfgang (2008): 13C labeling experiments at metabolic nonstationary conditions: an exploratory study. In *BMC bioinformatics* 9, p. 152. DOI: 10.1186/1471-2105-9-152.

Wang, Jeffrey H.; Byun, Jaeman; Pennathur, Subramaniam (2010): Analytical approaches to metabolomics and applications to systems biology. In *Seminars in nephrology* 30 (5), pp. 500–511. DOI: 10.1016/j.semnephrol.2010.07.007.

Wang, Jun; Zhang, Ping; Zhong, Jie; Tan, Mingyue; Ge, Jifu; Le Tao et al. (2016): The platelet isoform of phosphofructokinase contributes to metabolic reprogramming and maintains cell proliferation in clear cell renal cell carcinoma. In *Oncotarget* 7 (19), pp. 27142–27157. DOI: 10.18632/oncotarget.8382.

Wang, Ruohong; Yin, Yandong; Li, Jingshu; Wang, Hongmiao; Lv, Wanting; Gao, Yang et al. (2022): Global stable-isotope tracing metabolomics reveals system-wide metabolic alternations in aging Drosophila. In *Nature communications* 13 (1), p. 3518. DOI: 10.1038/s41467-022-31268-6.

Wang, Wanyan; Cui, Jiayan; Ma, Hui; Lu, Weiqiang; Huang, Jin (2021): Targeting Pyrimidine Metabolism in the Era of Precision Cancer Medicine. In *Frontiers in oncology* 11, p. 684961. DOI: 10.3389/fonc.2021.684961.

Wang, Wei; Fridman, Alla; Blackledge, William; Connelly, Stephen; Wilson, Ian A.; Pilz, Renate B.; Boss, Gerry R. (2009): The phosphatidylinositol 3-kinase/akt cassette regulates purine nucleotide synthesis. In *The Journal of biological chemistry* 284 (6), pp. 3521–3528. DOI: 10.1074/jbc.M806707200.

Wang, Xiang; Ding, Jian; Meng, Ling-hua (2015): PI3K isoform-selective inhibitors. Next-generation targeted cancer therapies. In *Acta pharmacologica Sinica* 36 (10), pp. 1170–1176. DOI: 10.1038/aps.2015.71.

Wang, Xiongjun; Liu, Ruilong; Zhu, Wencheng; Chu, Huiying; Yu, Hua; Wei, Ping et al. (2019): UDP-glucose accelerates SNAI1 mRNA decay and impairs lung cancer metastasis. In *Nature* 571 (7763), pp. 127–131. DOI: 10.1038/s41586-019-1340-y.

Wang, Yingfeng; Sun, Wenting; Zheng, Jilin; Xu, Can; Wang, Xia; Li, Tianyi et al. (2018): Urinary metabonomic study of patients with acute coronary syndrome using UPLC-QTOF/MS. In *Journal of chromatography. B, Analytical technologies in the biomedical and life sciences* 1100-1101, pp. 122–130. DOI: 10.1016/j.jchromb.2018.10.005.

Wang, Zeneng; Klipfell, Elizabeth; Bennett, Brian J.; Koeth, Robert; Levison, Bruce S.; Dugar, Brandon et al. (2011): Gut flora metabolism of phosphatidylcholine promotes cardiovascular disease. In *Nature* 472 (7341), pp. 57–63. DOI: 10.1038/nature09922.

Warburg, Otto (1924): ber den Stoffwechsel der Carcinomzelle. In *Naturwissenschaften* 12 (50), pp. 1131–1137. DOI: 10.1007/BF01504608.

Wee, Susan; Wiederschain, Dmitri; Maira, Sauveur-Michel; Loo, Alice; Miller, Christine; deBeaumont, Rosalie et al. (2008): PTEN-deficient cancers depend on PIK3CB. In *Proceedings of the National Academy of Sciences of the United States of America* 105 (35), pp. 13057–13062. DOI: 10.1073/pnas.0802655105.

Wei, Siwei; Liu, Lingyan; Zhang, Jian; Bowers, Jeremiah; Gowda, G. A. Nagana; Seeger, Harald et al. (2013): Metabolomics approach for predicting response to neoadjuvant chemotherapy for breast cancer. In *Molecular oncology* 7 (3), pp. 297–307. DOI: 10.1016/j.molonc.2012.10.003.

Weibel, K. E.; Mor, J. R.; Fiechter, A. (1974): Rapid sampling of yeast cells and automated assays of adenylate, citrate, pyruvate and glucose-6-phosphate pools. In *Analytical biochemistry* 58 (1), pp. 208–216. DOI: 10.1016/0003-2697(74)90459-x.

Weindl, Daniel (2015): Non-targeted mass isotopolome analysis to gain insights into cancer cell metabolism. Dissertation. Unilu - University of Luxembourg, Luxembourg; FNR - Fonds National de la Recherche. Available online at https://hdl.handle.net/10993/21182, checked on 3/23/2025.

Weindl, Daniel; Cordes, Thekla; Battello, Nadia; Sapcariu, Sean C.; Dong, Xiangyi; Wegner, Andre; Hiller, Karsten (2016): Bridging the gap between non-targeted stable isotope labeling and metabolic flux analysis. In *Cancer & metabolism* 4, p. 10. DOI: 10.1186/s40170-016-0150-z.

Weindl, Daniel; Wegner, André; Jäger, Christian; Hiller, Karsten (2015): Isotopologue ratio normalization for non-targeted metabolomics. In *Journal of chromatography. A* 1389, pp. 112–119. DOI: 10.1016/j.chroma.2015.02.025.

Weinstein, I. Bernard; Case, Kathleen (2008): The history of Cancer Research: introducing an AACR Centennial series. In *Cancer research* 68 (17), pp. 6861–6862. DOI: 10.1158/0008-5472.CAN-08-2827.

Wickham, Hadley; Averick, Mara; Bryan, Jennifer; Chang, Winston; McGowan, Lucy; François, Romain et al. (2019): Welcome to the Tidyverse. In *JOSS* 4 (43), p. 1686. DOI: 10.21105/joss.01686.

Winnike, Jason H.; Stewart, Delisha A.; Pathmasiri, Wimal W.; McRitchie, Susan L.; Sumner, Susan J. (2018): Stable Isotope-Resolved Metabolomic Differences between Hormone-Responsive and Triple-Negative Breast Cancer Cell Lines. In *International journal of breast cancer* 2018, p. 2063540. DOI: 10.1155/2018/2063540.

Wise, David R.; Ward, Patrick S.; Shay, Jessica E. S.; Cross, Justin R.; Gruber, Joshua J.; Sachdeva, Uma M. et al. (2011): Hypoxia promotes isocitrate dehydrogenase-dependent carboxylation of α-ketoglutarate to citrate to support cell growth and viability. In *Proceedings of the National Academy of Sciences of the United States of America* 108 (49), pp. 19611–19616. DOI: 10.1073/pnas.1117773108.

Wishart, David S. (2015): Is Cancer a Genetic Disease or a Metabolic Disease? In *EBioMedicine* 2 (6), pp. 478–479. DOI: 10.1016/j.ebiom.2015.05.022.

Wishart, David S.; Guo, AnChi; Oler, Eponine; Wang, Fei; Anjum, Afia; Peters, Harrison et al. (2022): HMDB 5.0. The Human Metabolome Database for 2022. In *Nucleic acids research* 50 (D1), D622-D631. DOI: 10.1093/nar/gkab1062.

Wolf, Sebastian; Schmidt, Stephan; Müller-Hannemann, Matthias; Neumann, Steffen (2010): In silico fragmentation for computer assisted identification of metabolite mass spectra. In *BMC bioinformatics* 11, p. 148. DOI: 10.1186/1471-2105-11-148.

Wolfe, Robert R. (2005): Isotope tracers in metabolic research. Principles and practice of kinetic analysis / Robert R. Wolfe, David L. Chinkes. 2nd ed. Hoboken, NJ: Wiley.

Wu, Yiman; Li, Liang (2016): Sample normalization methods in quantitative metabolomics. In *Journal of chromatography. A* 1430, pp. 80–95. DOI: 10.1016/j.chroma.2015.12.007.

Yang, Ming; Soga, Tomoyoshi; Pollard, Patrick J.; Adam, Julie (2012): The emerging role of fumarate as an oncometabolite. In *Frontiers in oncology* 2, p. 85. DOI: 10.3389/fonc.2012.00085.

Zhang, Blake K.; Moran, Anne M.; Bailey, Charles G.; Rasko, John E. J.; Holst, Jeff; Wang, Qian (2019): EGF-activated PI3K/Akt signalling coordinates leucine uptake by regulating LAT3 expression in prostate cancer. In *Cell communication and signaling : CCS* 17 (1), p. 83. DOI: 10.1186/s12964-019-0400-0.

Zhang, Linwen; Vertes, Akos (2015): Energy Charge, Redox State, and Metabolite Turnover in Single Human Hepatocytes Revealed by Capillary Microsampling Mass Spectrometry. In *Analytical chemistry* 87 (20), pp. 10397–10405. DOI: 10.1021/acs.analchem.5b02502.

Publications

Parts of this work have been published within a peer-reviewed journal:

Lackner, Marcel; Neef, Sylvia K.; Winter, Stefan; Beer-Hammer, Sandra; Nürnberg, Bernd; Schwab, Matthias et al. (2022): Untargeted stable isotope-resolved metabolomics to assess the effect of PI3Kβ inhibition on metabolic pathway activities in a PTEN null breast cancer cell line. In *Frontiers in molecular biosciences* 9, p. 1004602. DOI: 10.3389/fmolb.2022.1004602.

Poster Presentations:

Lackner M, Hofmann U, Haag M, Schwab M, Beer-Hammer S, Nürnberg B. Untargeted stable isotope-resolved metabolomics to assess the effect of PI3Kβ inhibition on metabolic pathway activities in a PTEN null breast cancer cell line. 18th Annual Conference of the Metabolomic Society - Metabolomics 2022, Valencia, Spain, June 2022

Acknowledgements

First and foremost, I would like to thank my supervisors, Dr. Ute Hofmann and Dr. Mathias Haag for their unwavering support, guidance, and excellent mentorship during and after my time at the Dr. Margarete-Fischer Bosch Institute of Clinical Pharmacology (IKP). Their constructive input, patience, and expertise were invaluable and ultimately made this dissertation possible.

In addition, I would like to thank Prof. Dr. Matthias Schwab for giving me the opportunity to work at the IKP and for providing me with all the necessary resources to conduct my research and for supervising and evaluating this dissertation. I am also grateful to Prof. Dr. Lämmerhofer for overseeing and evaluating this work as part of the University of Tübingen. I am deeply grateful to my former working group for their exceptional technical assistance within the lab and constructive discussions outside the lab. Special thanks to Dr. Thomas Mürdter, Dr. Sylvia Neef, Monika Seiler, Ralf Barnaba, Georg Heinkele, Markus König.

Furthermore, I would like to thank all PhD students, staff of the IKP and friends who have accompanied, supported, and made my time both at work and in my free time pleasant over the past years. In particular, I would like to thank Dr. Isabel Maurus and Anika Fuhr, both of whom have supported and encouraged me throughout my dissertation.

I greatly appreciate the members of the Interfaculty Center for Phamacogenomics and Pharma Research (ICEPHA) for giving me the opportunity to work on this project. Especially Prof. Dr. Sandra Beer-Hammer and Prof. Dr. Bernd Nürnberg, who provided insightful comments, and valuable suggestions that have contributed to the completion of this project. I would like to thank the Robert-Bosch Stiftung for providing the necessary funding for this work.

I would like to express my deepest gratitude to Bianca. Her unconditional support, love, and patience over the past few years have been essential to the successful completion of this work.

Curriculum Vitae

The CV has been removed due to data protection

Eidesstattliche Erklärung

Ich erkläre hiermit, dass ich die zur Promotion eingereichte Arbeit mit dem Titel: „Establishment of Stable Isotope-resolved Metabolomics as Test System to assess Membrane-associated Drug Targets in Cancer" selbständig verfasst, nur die angegebenen Quellen und Hilfsmittel benutzt und wörtlich oder inhaltlich übernommene Stellen als solche gekennzeichnet habe.

Ich erkläre, dass die Richtlinien zur Sicherung guter wissenschaftlicher Praxis der Universität Tübingen (Beschluss des Senats vom 25.5.2000) beachtet wurden. Ich versichere an Eides statt, dass diese Angaben wahr sind und dass ich nichts verschwiegen habe. Mir ist bekannt, dass die falsche Abgabe einer Versicherung an Eides statt mit Freiheitsstrafe bis zu drei Jahren oder mit Geldstrafe bestraft wird.